Institut de Minéralogie et Géochimie (IMG)
Laboratoire de Géodynamique des Chaînes Alpines (LGCA)

The Mont Collon mafic complex (Austroalpine Dent Blanche nappe)

Permian evolution of the Western European mantle

Thèse de Doctorat

présentée à la Faculté des Géosciences et de l'Environnement
de l'Université de Lausanne

par

Philippe Monjoie

Géologue diplômé des Universités de Clermont-Ferrand - Lyon
- Saint Etienne (France)

Jury:

Professeur Henri Masson, Président
Professeur Giovanni B. Piccardo, Rapporteur
Professeur Alain Demant, Rapporteur
Docteur François Bussy, Expert
Professeur Pierre Tricart, Expert
Professeur Henriette Lapierre, Directeur de thèse
Professeur Hans-Rudolf Pfeifer, Directeur de thèse

Lausanne, 2004

A Chrys, Bastien, ma mère, mon père, ma sœur, mes p'tits beaufs (JC et JF) et belles-sœurs (Nath et Lilie), mes 4 petites puces (Marie, Sarah, Clémence et Auriane) et ma marraine Christiane

Avant-propos

Plusieurs parties de cette thèse ont été soumises dans divers journaux ou sont en cours de corrections par les différents co-auteurs avant soumission. Nous avons décidé de ne pas intégrer tels quels ces divers papiers, d'une part, dans un soucis d'éviter des répétitions pour les lecteurs du manuscrit et d'autre part, car les revues de ces papiers ne nous sont pas encore toutes revenues. Les parties de ce manuscrit soumises sont les suivantes:

1- Modeling of in situ crystallization processes in the Permian mafic layered intrusion of Mont Collon (Dent Blanche nappe, western Alps)

Philippe Monjoie, François Bussy, Henriette Lapierre et Hans-Rudolf Pfeifer

Soumise dans le volume spécial de Lithos: «Modeling of magma chambers». Acceptée avec révisions modérées. Ce papier intègre principalement les descriptions pétrographiques des cumulats, la modélisation de la cristallisation in-situ et du liquide parental.

2- Precise U/Pb and $^{40}Ar/^{39}Ar$ dating of the layered Permian Mafic Complex of the Mont Collon (Western Alps, Wallis, Switzerland)

Philippe Monjoie., François Bussy, Urs Schaltegger, Henriette Lapierre, Hans-Rudolf Pfeifer et Andreas Mulch

Soumis dans Schweizerische Mineralogische und Petrographische Mitteilungen. Ce papier inclut les âges U/Pb du gabbro pegmatitique et de la pegmatite quartzique et $^{40}Ar/^{39}Ar$ des filons dioritiques Fe-Ti.

3- Isotopic constraints on the mantle composition and geodynamic implications: insights from the Permian Mont Collon mafic complex (Austroalpine Dent Blanche nappe, Western Alps): titre non-définitif

Philippe Monjoie, François Bussy, Henriette Lapierre et Hans-Rudolf Pfeifer

En cours de corrections par les différents auteurs. Soumission prévue dans Chemical Geology. Ce papier comprend les descriptions pétrographiques des filons leucocrates et des filons mélanocrates Fe-Ti, les donnés isotopiques de tous les types de roches du complexe mafique du Mont Collon ainsi que les interprétations géodynamiques.

Remerciements

La première personne a remercié est bien sûr Chrystelle, pour m'avoir supporté pendant ces années de thèse et surtout lors de la rédaction de ce manuscrit.

Comment ne pas remercier mes directeurs de thèse, Henriette Lapierre et François Bussy pour leur encadrement de thèse, pour leur soutien et leur aide lors des diverses phases de la thèse (terrain, acquisition des données en laboratoire, interprétation et rédaction) ainsi que Hans-Rudolf Pfeifer pour avoir mis à ma disposition l'infracstructure du CAM et pour sa gestion de ma bourse de thèse.

Je tiens à remercier les examinateurs et experts de cette thèse (Pierre Tricart, Giovanni Piccardo et Alain Demant) pour m'avoir permis de la soutenir et pour leurs commentaires très instructifs sur mon travail.

Les nombreuses personnes que j'ai croisé durant cette thèse ont toutes leur place dans ces quelques lignes. Delphine Bosch pour son très sympathique accueil à Montpellier et les discussions que nous avons eu concernant les résultats isotopiques, Urs Schaltegger pour nous avoir ouvert sa salle blanche pour la préparation des datations U/Pb, Andreas Mulch pour les heures passées à analyser les amphiboles des filons dioritiques. Je n'oublie pas Laurie Reisberg et Catherine Zimmermann pour leur accueil au CRPG à Nancy, la mise à disposition de leur salle blanche et la qualité des analyses Re-Os.

Enfin, et la liste risque d'être longue, c'est pourquoi je citerais en vrac, ici, de nombreuses personnes qui savent (je l'espère) que je les apprécie beaucoup: Katchouchka et Dom, Jean-Claude (XRF Man), Marc et Fleurice, Alain, Loyc, François (dit Fanfouet), Jean-Cri, Mikki, Marion, Andrea, Super Tom-Tom, Vincenzo, Emile, Anne, etc, etc… Je n'oublie personne mais la liste est trop longue. Et que ceux qui ne sont pas dans ces quelques lignes m'excusent.

Ces travaux ont été financés dans leur majeure partie par le Fond National Suisse de Recherche (F.N.S.) ainsi que par une bourse Eurodoc accordée par la Région Rhône-Alpes (France) et l'Union Européenne. Je les remercie donc pour le soutien qu'ils ont apporté à mon travail de thèse.

Résumé

Le complexe du Mont Collon (nappe de la Dent Blanche, Austroalpin) est l'un des exemples les mieux préservés du magmatisme mafique permien des Alpes occidentales. Il est composé d'affleurements discontinus et d'une stratification magmatique en son centre (Dents de Bertol) et est composé à 95% de roches mafiques cumulatives (gabbros à olivine et/ou cpx, anorthositiques, troctolites, wehrlites et wehrlites à plagioclase) et localement de quelques gabbros pegmatitiques. Ces faciès sont recoupés par de nombreux filons acides (aplites, pegmatites quartziques, microgranodiorites et filons anorthositiques) et mafiques tardifs (dikes mélanocrates riches en Fe et Ti).

Les calculs thermométriques (équilibre olivine-augite) montrent des températures de 1070-1120 ± 6°C, tandis que le thermomètre amphibole-plagioclase indique une température de 740 ± 40°C à 0.5 GPa pour les amphiboles magmatiques tardives. La geobarométrie sur pyroxène donne des pressions moyennes de 0.3-0.6 GPa, indiquant un emplacement dans la croûte moyenne. De plus, les températures obtenues sur des amphiboles coronitiques indiquent des températures de l'ordre de 700 ± 40°C confirmant que les réactions coronitiques apparaissent dans des conditions subsolidus.

Les âges concordants U/Pb sur zircons de 284.2 ± 0.6 et 282.9 ± 0.6 Ma obtenus sur un gabbro pegmatitique et une pegmatitique quartzique, sont interprétés comme des âges de cristallisation. Les datations $^{40}Ar/^{39}Ar$ sur amphiboles des filons mélanocrates donnent un âge plateau de 260.2 ± 0.7 Ma, qui est probablement très proche de l'âge de cristallisation. Ainsi, cet age $^{40}Ar/^{39}Ar$ indique un second évènement magmatique au sein du complexe.

Les compositions des roches totales en éléments majeurs et traces montrent peu de variations, ainsi que le Mg# (75-80). Les éléments traces enregistrent le caractère cumulatif des roches (anomalie positive en Eu) et révèlent des anomalies négatives systématiques en Nb, Ta, Zr, Hf et Ti dans les faciès basiques. Le manque de corrélation entre éléments majeurs et traces est caractéristique d'un processus de cristallisation *in situ* impliquant une quantité variable de liquide interstitiel (L) entre les phases cumulus. Les distributions des éléments traces dans les minéraux sont homogènes, indiquant une rééquilibration subsolidus entre cristaux et liquide interstitiel. Un modèle quantitatif basé sur les équations de cristallisation *in situ* de Langmuir reproduisent correctement les concentrations en terres rares légères des minéraux cumulatifs montrant la présence de 0 à 35% de liquide interstitiel L pour des degrés de différenciation F de 0 à 45%, par rapport au faciès les moins évolués du complexe. En outre, les valeurs de L sont bien corrélées avec les proportions modales d'amphibole interstitielle et les concentrations en éléments incompatibles des roches (Zr, Nb). Le liquide parental calculé des cumulats du Mont Collon est caractérisé par un enrichissement relatif en terres rares légères et Th, un appauvrissement en terres rares lourdes typique d'une affinité transitionnelle (T-MORB) et une forte anomalie négative en Nb-Ta.

Les roches cumulatives montrent des compositions isotopiques en Nd-Sr proches de la terre globale silicatée (BSE), soit $-0.6<\varepsilon Nd_i<+3.2$, $0.7045<{}^{87}Sr/{}^{86}Sr_i<0.7056$. Les rapports initiaux en Pb indiquent une source dans le manteau enrichi subcontinental lithosphérique, préalablement contaminé par des sédiments océaniques. Les dikes mélanocrates Fe-Ti sont représentatifs de liquides et ont des spectres de terres rares enrichis, une anomalie positive en Nb-Ta et des εNd_i de +7, des $^{87}Sr/^{86}Sr_i$ de 0.703 et des rapports initiaux en Pb, similaires à ceux des basaltes d'île océanique, indiquant une source asthénosphérique modérément appauvrie. Ainsi, la fusion partielle du manteau lithosphérique subcontinental est induite par l'amincissement post-orogénique et la remontée de l'asthénosphère. Les filons mélanocrates proviennent, après délamination du manteau lithosphérique, de la fusion de l'asthénosphère.

Abstract

The early Permian Mont Collon mafic complex (Dent Blanche nappe, Austroalpine nappe system) is one of the best preserved examples of the Permian mafic magmatism in the Western Alps. It is composed of discontinuous exposures and a well-preserved magmatic layering (the Dents de Bertol cliff) crops out in the center part of the complex. It mainly consists of cumulative mafic rocks, which represent 95 vol-% of the mafic complex (ol- and cpx-bearing gabbros and rare anorthositic layers, troctolites, wehrlites and plagioclase-wehrlites) and locally pegmatitic gabbros. All these facies are crosscut by widespread acidic (aplites, quartz-rich pegmatites, microgranodiorites) and late mafic Fe-Ti melanocratic dikes.

Olivine-augite thermometric calculations yield a range of 1070-1120 ± 6°C, while amphibole-plagioclase thermometer yields a temperature of 740 ± 40°C at 0.5 GPa. Pyroxene geobarometry points to a pressure of 0.3-0.6 GPa, indicating a middle crustal level of emplacement. Moreover, temperature calculations on the Mont Collon coronitic amphiboles indicate temperatures of 700 ± 40°C, close to those calculated for magmatic amphiboles. These temperatures confirm that coronitic reactions occurred at subsolidus conditions.

ID-TIMS U/Pb zircon ages of 284.2 ± 0.6 and 282.9 ± 0.6 Ma obtained on a pegmatitic gabbro and a quartz-pegmatitic dike, respectively, were interpreted as the crystallization ages of these rocks. $^{40}Ar/^{39}Ar$ dating on amphiboles from Fe-Ti melanocratic dikes yields a plateau age of 260.2 ± 0.7 Ma, which is probably very close to the crystallization age. Consequently, this $^{40}Ar/^{39}Ar$ age indicates a second magmatic event.

Whole-rock major- and trace-element compositions show little variation across the whole intrusion and Mg-number stays within a narrow range (75-80). Trace-element concentrations record the cumulative nature of the rocks (e.g. positive Eu anomaly) and reveal systematic Nb, Ta, Zr, Hf and Ti negative anomalies for all basic facies. The lack of correlation between major and trace elements is characteristic of an *in situ* crystallization process involving variable amounts of interstitial liquid (L) trapped between the cumulus mineral phases. LA-ICPMS measurements show that trace-element distributions in minerals are homogeneous, pointing to subsolidus re-equilibration between crystals and interstitial melts. A quantitative modeling based on Langmuir's *in situ* crystallization equation successfully reproduced the Rare Earth Element (REE) concentrations in cumulitic minerals. The calculated amounts of interstitial liquid L vary between 0 and 35% for degrees of differentiation F of 0 to 45%, relative to the least evolved facies of the intrusion. Furthermore, L values are well correlated with the modal proportions of interstitial amphibole and whole-rock incompatible trace-element concentrations (e.g. Zr, Nb) of the tested samples. The calculated parental melt of the Mont Collon cumulates is characterized by a relative enrichment in Light REE and Th, a depletion in Heavy REE, typical of a transitional affinity (T-MORB), and strong negative Nb-Ta anomaly.

Cumulative rocks display Nd-Sr isotopic compositions close to the BSE ($-0.6 < \varepsilon Nd_i < +3.2$, $0.7045 < {}^{87}Sr/{}^{86}Sr_i < 0.7056$). Initial Pb ratios point to an origin from the melting of an enriched subcontinental lithospheric mantle source, previously contaminated at the source by oceanic sediments. The contrasted alkaline Fe-Ti melanocratic dikes are representative of liquids. They display enriched fractionated REE patterns, a positive Nb-Ta anomaly and εNd_i of +7, $^{87}Sr/^{86}Sr_i$ of 0.703 and initial Pb ratios, all reminiscent of Ocean Island Basalt-type rocks, pointing to a moderately depleted asthenospheric source. Thus, partial melting of an enriched lithospheric mantle is triggered by post-orogenic thinning and up-welling of hot asthenospheric mantle. The Fe-Ti melanocratic dikes originated, after the complete delamination of the lithospheric mantle, from the melting of the asthenospheric mantle.

Table of contents

References

Appendices

Chapter 1: General overview

Chapter 1: General overview

1.1. Introduction

The Pangea break-up during Jurassic times is synchronous with the opening of the Central Atlantic domain that led to the formation of the Tethyan Ocean. During the Mesozoic times, the Tethys Ocean covered a wide area (from the western Mediterranean to the eastern Himalaya) between African and Eurasian plates. The subduction of the Tethyan oceanic lithosphere beneath the African margin started some 110 Ma ago (e.g. Pfiffner, 1993), resulting from the beginning of the convergence between the Apulian (or Adriatic) and European plates. The Alpine chain resulted from the subsequent collision of the western parts of the European plate with the (African) Apulian microplate during the Mesozoic and Tertiary times (Coward et al., 1989). The convergence at Cretaceous times induced mostly (north) west-directed thrusting in the Eastern and Western Alps (de Graciansky, 1993), while the direction of the later Tertiary compressional phase is north-south.

Pre-Mesozoic basement units are widespread in central Europe (Fig. 1 and 2) and numerous exposures compose the framework of the Alps, actually scattered as a complex system among the Alpine structures. These pre-Mesozoic units are found in all the basement nappes of the Helvetic, Penninic and Austroalpine realms, as well as in the Southern Alps. In the Helvetic zone, the Variscan basement units are represented by the External Crystalline Massifs, the exposures of which form three main units, i.e., northern, middle and southern units, (i) the northern unit consists of the Mont Blanc and Aiguilles Rouges massifs, Aar-Gotthard massif, and Belledonne-Grandes Rousses located on an old Variscan lineament NE-SW aligned (de Graciansky, 1993), (ii) the middle unit is constituted principally by the NW-SE Pelvoux and Argentera-Mercantour massifs, (iii) the southern unit is represented by the Tanneron-Esterel-Maures massifs. In the Penninic Zone, the Variscan basement is represented by the Internal Crystalline Massifs. The latter include the Monte Rosa, Grand Paradis and Dora Maira massifs. The Austroalpine nappe system comprises large thrust sheets involving huge masses of the Variscan crystalline basement, i.e. granitoids from the Err-Bernina nappe (Spillman and Büchi, 1993 and ref. therein), the Valpelline and Arolla Series of the Austroalpine Dent Blanche nappe and the Sesia-Lanzo zone (e.g. Martinotti and Hunziker, 1984). Here we refer only to the western area of the Southern Alps, where the Palaeozoic granulite- to high-T amphibolite-facies metamorphics of the Ivrea-Verbano zone are tectonically juxtaposed with the amphibolite-facies Serie de Laghi (Boriani and Villa, 1997).

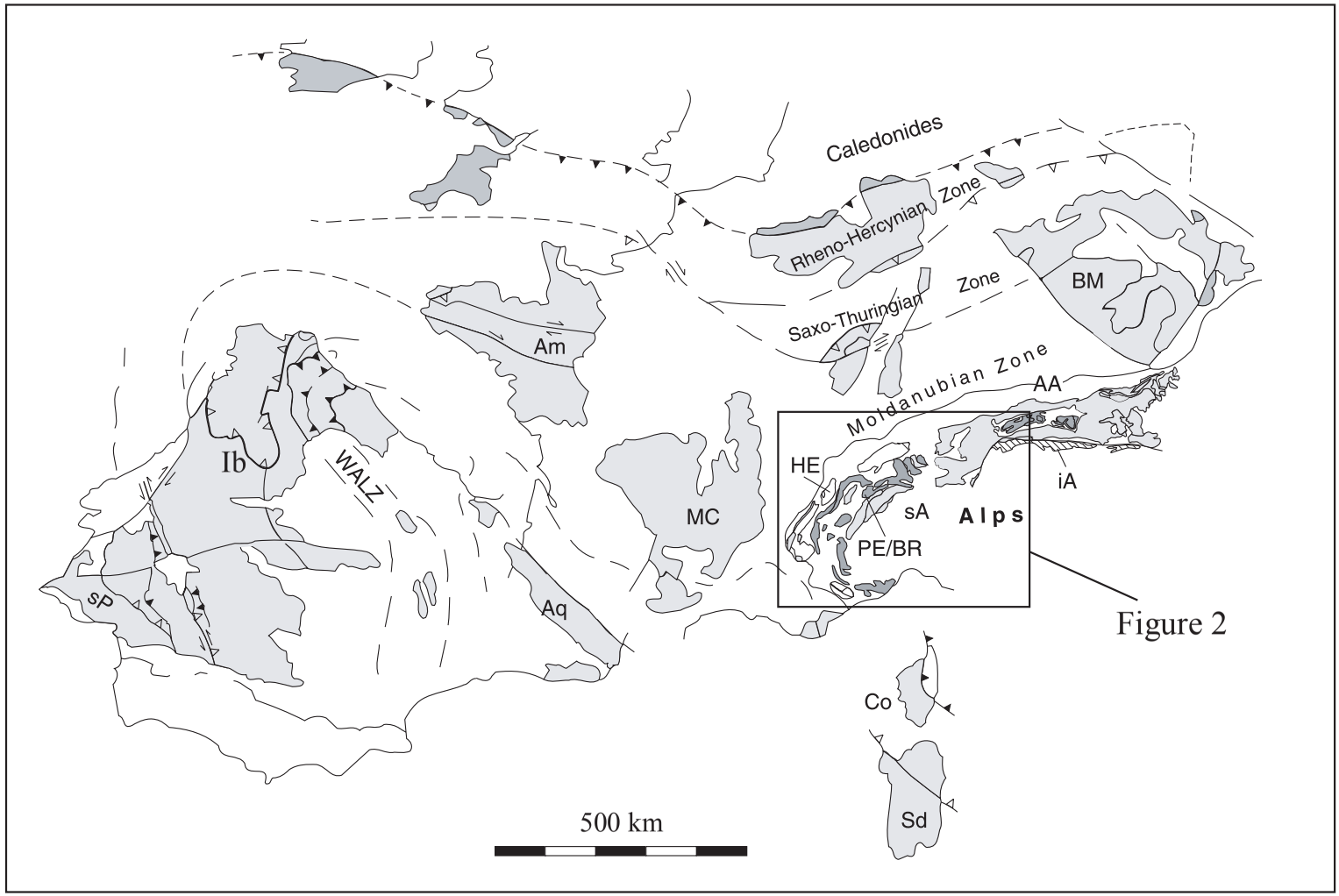

Fig. 1: Simplified geological map of Variscan basement areas in Central Europe after von Raumer et al. (2003) and based on Franke (1989), Martinez-Catalàn (1990), and Ribeiro and Sanderson (1996). AA: AustroAlpine; Am: Armorican Massif; Aq: Aquitaine-Pyrenees; BM: Bohemian Massif; Co: Corsica; HE: Helvetic Zone; iA: Intra-Alpine ; Ib: Iberia; MC: French Central Massif; PE/BR: Penninic/Briançonnais (dark grey); sA: Southalpine; Sd: Sardinia; sP: South Portuguese Zone; WALZ: West Asturias Leon Zone.

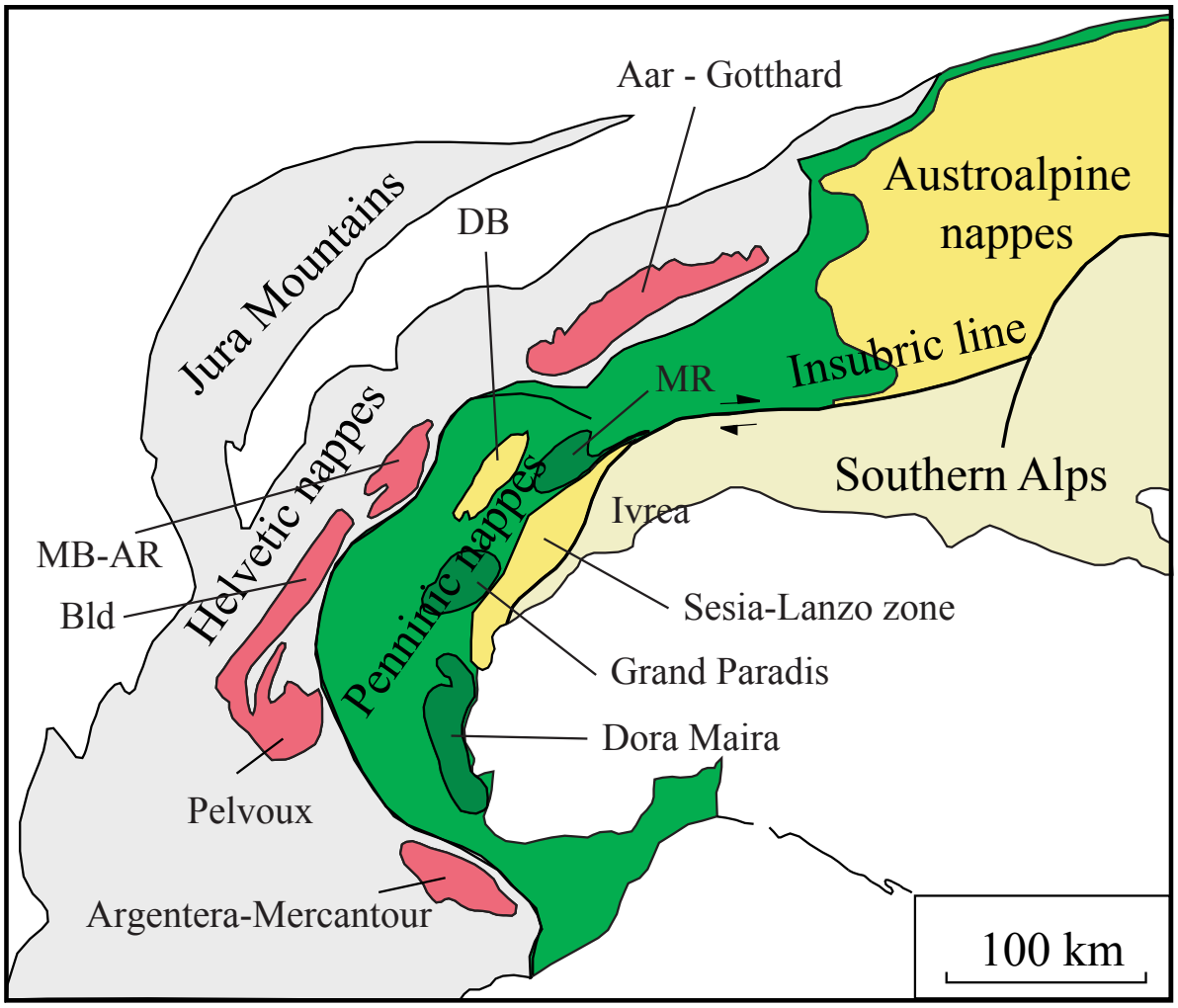

Fig. 2: Main tectonic units and Variscan crystalline massifs in the Alps. DB: Dent Blanche nappe, MR: Monte Rosa, MB-AR: Mont Blanc and Aiguilles Rouges massifs, Bld: Belledonne.

The above cited pre-Mesozoic basement units comprise large basic and/or acidic plutons and volcanic rocks related to numerous magmatic events of Variscan age. These magmatic events are the markers of the polyphased tectonic evolution of the long lasting build-up of the Variscan belt, each one associated with specific tectonic settings, i.e. pre-collisional, collisional and post-collisional tectonic events. Consequently, the study of the magmatic affinities of these igneous suites and the characterization of their mantle and/on continental sources enables to precise the geodynamic settings based on tectonic and paleomagnetism data, faunic correlations and palinspastic reconstructions. In addition, accurate age determinations are fundamental to replace the magmatic activity in its geodynamic context.

This Ph.D. thesis is focused on the Mont Collon-Dents de Bertol mafic complex (named as Mont Collon in the following sections), located in the Austroalpine Dent Blanche nappe (Western Alps, Switzerland). Few studies have been done on the Mont Collon mafic complex although it is probably one of the best preserved mafic complex of the Hercynian basement of the Alps. Indeed, this massif is affected only by a weak Alpine greenschist metamorphic overprint. Dal Piaz et al. (1977) dated the Mont Collon at ca. 250 Ma. This age was interpreted as the cooling age of the complex and relates the emplacement of the Mont Collon-Dents de Bertol mafic complex to a major phase of the tectonic evolution of Variscan belt, i.e. the post-collisional event, related to the collapse of the chain. Consequently, the Mont Collon complex must be more accurately dated. Furthermore, because of the well exposed cumulate rocks and their preserved magmatic layering at the Dents de Bertol area, the petrological and geochemical characterization of the complex will help to: (i) determine the differentiation process(es) that lead to the crystallization of the rock facies, (ii) characterize the affinities of the basic magmas related to the post-collisional event of the Variscan belt, (iii) precise the physical-chemical conditions of emplacement of the plutonic rocks, (iv) determine the type of mantle sources and possible involvement of the continental crust in the genesis of this complex.

1.2. The Variscan belt build-up

The Variscan belt was formed principally between the Devonian and the Carboniferous and is not a typical continent – continent collisional range. It was formed by successive accretions of several micro-continents detached from the Gondwana active margin (Stampfli and Borel, 2002). Different authors (e.g. von Raumer and Neubauer, 1993) proposed to subdivide the build-up of this belt in different periods: (i) the pre-collisional period (500 – 460 Ma), (ii) a major collisional event close to 380 Ma and (iii) a late to post -collisional stage, which started around 350 Ma and hold on roughly 30 Ma (von Raumer and Neubauer, 1993). At the late Carboniferous-early Permian, the Variscan chain collapsed, as the consequence of the slab roll-back of the Palaeo-Tethys (Stampfli and Borel, 2002).

The pre-collisional times were marked by the consecutive opening of the Rheic oceanic domain accompanied by the Palaeo-Tethys opening. Cambrian oceanic plagiogranites date the opening of the Rheic Ocean (von Raumer et al. 2003). At 440 Ma, the Avalonia continental fragment and associated satellites are already amalgamated to Laurussia in a short-lived orogenic pulse (von Raumer, 1998, Belka et al., 2002). The opening of the Palaeo-Tethys is interpreted as back-arc spreading related to the Gondwana-directed subduction of Rheic/Proto-Tethys. The northern active margin of the Gondwana was dismembered during the Silurian, generating the formation of several micro-continents and ribbon-like terranes (European Hunic terranes).

Fig. 3: Geodynamic reconstruction at the Late Permian (~280 Ma, Sakmarian). After Stampfli and Borel (2002).

The collision of the Gondwana-derived micro-continents with Laurasia took place from Late Devonian to Early Carboniferous time (~340 Ma) with the final closure of the Rhenohercynian domain (Stampfli and Borel, 2002), which ended up to ca. 320 Ma (von Raumer et al., 2003). The Palaeo-Tethys was still opened (Fig. 3) and at the time of emplacement of the Mont Collon mafic complex, the Variscan chain was supposed to collapse generating the development of pull-apart basins.

1.3. Magmatism related to the post-collisional stages of the Variscan belt

1.3.1. The External Crystalline Massifs of the Helvetic zone

The magmatism in the External Massifs units displays intermediate to acidic compositions. Parts of the Aar-Gotthard, Argentera, Belledonne and Aiguilles Rouges massifs are emplaced during the post-collisional stages of the Variscan belt.

The Aar massif displays different igneous suites (see a review in Schaltegger, 1994), i.e. (1) shoshonitic-ultrapotassic suites (diorites, monzonites, syenites and granites associated with high-K basic rocks) dated at 334 ± 2.5 Ma, (2) subordinate high-K calc-alkaline suites dated around 310 Ma (Schaltegger and Corfu, 1992), and (3) calc-alkaline to subalkaline granitic suites comprising granodiorite, granites and leucogranites of the Central Aar dated at 297 ± 2 Ma (Schaltegger and Corfu, 1992). Recently, new U/Pb dating on migmatites from the Aar massif yielded 290-300 Ma ages (Olsen et al., 2000). Granites in the Gotthard massif are coeval with those of the Aar massif and U/Pb concordant ages indicate (around 295-300 Ma, Sergeev and Steiger, 1993) that the Gotthard granites postdates also the Variscan collision.

In the External Crystalline Massifs, Debon and Lemmet (1999) distinguished two plutonic suites, one early, Visean and highly magnesian (~ 330-340 Ma), the other, Stephanian (~295-305 Ma) and more ferriferous. The Mg/Fe ratio variations are mainly related to the physical-chemical conditions of melting (P-T, fO_2) and the Late Variscan geodynamic setting. In the Argentera massif (332 Ma, Rubatto et al., 2001), plutonic granitic suites exhibits subalkaline magmatic affinity and magnesian character as well as in the Belledonne massif, the 340 Ma-old Saint Colomban, Sept Laux and La Lauzière granites show also an Al-enriched subalkaline affinities and magnesian character.

In the Aiguilles Rouges massif, subalkaline and magnesian quartz syenites, rich in mafic minerals, occurring in the Pormenaz monzonites, were dated at 332 ± 2 Ma by U/Pb on zircon (Bussy et al., 1998) whereas the Vallorcine granite is a peraluminous and magnesian-ferriferous and was dated by U/Pb on zircon and monazite at 307 ± 2 Ma (Bussy and Hernandez, 1997). They interpreted this Westphalian age as reflecting magmatic underplating beneath the crust.

The 304 Ma-old Mont Blanc granite displays an evolved metaluminous to slightly peraluminous K-rich magmatic affinity, with both alkaline and calc-alkaline characteristics (Bussy, 1990; Bussy and von Raumer, 1993). The emplacement of the Mont Blanc within the upper crust (10-15 km) occurred during transtensional strike-slip shearing context. By this way, the melting of a composite source was induced by a pressure release of a thickened thermally re-equilibrated lithosphere.

1.3.2. The Penninic domain: the Internal Crystalline Massifs

In this section, we focus on the geology of the Gran Paradiso and Monte Rosa massifs, which crop out in the northwestern Alps. Nevertheless, other igneous rocks are present in the Penninic zone, e.g. the Dora Maira massif and, the late Variscan granitoids of the Tauern window (Eastern Alps). Disregarding the pre-Alpine metamorphic overprint, the Monte Rosa and the Gran Paradiso massif protoliths are porphyritic granitoids (Dal Piaz, 2001). Engi et al. (2001) interpreted the 330 Ma-old monazites as the emplacement age of the main Monte Rosa granodiorite pluton and the 260 Ma dating obtained from monazites extracted from high-grade metapelites as the supposed response to the intrusion of minor granitic bodies.

1.3.3. The Southern Alps: the Ivrea-Verbano zone

Pin (1986) dated gabbroic and dioritic rocks, exposed in the Val Sesia and Val Mastallone, from the Main gabbro-diorite body (upper part of the Mafic Complex, Ivrea-Verbano zone). U/Pb zircon yields an age of 285 + 7 / -5 Ma, interpreted as the emplacement age of this mafic complex and the granulitic metamorphism exposed in the Val Strona area (north to the Val Sesia).

The early Permian age of the granulite metamorphism related to the underplating of the Mafic Complex in the Ivrea-Verbano zone has been confirmed by $^{40}Ar/^{39}Ar$ amphibole dating (Boriani and Villa, 1997). Ultramafic pipes intrude the Main Gabbro of the Mafic Complex and the roof metasediments of the Ivrea zone and have also an early Permian (287 ± 3 Ma) age. These ultramafic rocks are thought to represent the latest mantle-derived melts associated with the underplating event that has affected the Ivrea-Verbano zone during the transition from late Carboniferous to early Permian (Garuti et al., 2001).

1.3.4. The Austroalpine nappe system

The Austroalpine basement and the Helvetic realm are thought to represent Devonian passive and compressive margins, respectively, which accreted together during the Carboniferous. The magmatic rocks exposed in the Eastern domain of the Austroalpine zone of the Central Alps were more studied than those belonging to the several klippes of the Austroalpine nappes, e.g. the Dent Blanche nappe. Several basic intrusions have been dated close to the Carboniferous-Permian boundary as the Sondalo gabbroic complex: 290 Ma (Tribuzio et al., 1999), the Braccia gabbro and associated leucocratic anatexites: 281 ± 19 and 278.4 ± 2.6 Ma, respectively (Hansmann et al., 1996 and 2001, Müntener et al., 2000). The orthogneisses of the Arolla series, the surrounding rocks of the Mont Collon basic complex, were dated by Bussy et al. (1998) at 289 ± 2 Ma.

The magmatic affinity of the small granitoid bodies from the Sesia zone is interpreted as calc-alkaline, ranging in composition from granodiorite to quartz-monzodiorite. Zircon U/Pb dating indicates an age of the magmatic activity close to the Carboniferous-Permian boundary (293 ± 3 Ma, Bussy et al., 1998).

1.3.5. Chemical characteristics of the late Variscan magmatic events

Three distinct magmatic events characterized the end of the Variscan orogeny: early Carboniferous, late Carboniferous-early Permian, and late Permian. From the post-collisional stages to the late history of the Variscan belt (i.e. the collapse period), the magmatism ascribed to this long period, which lasted around 70 Ma, displays various geochemical characteristics. Each Variscan belt tectonic phase is related to specific magmatic events, which exhibit tholeiitic, (K-rich) calc-alkaline or subalkaline affinities.

In the early Carboniferous, acidic intrusions were emplaced along strike-slip fault zones in the basement areas of the Alpine realm (Bonin et al., 1993; von Raumer et al., 1993; Debon et al., 1994; Bussy et al., 2000). High-K calc-alkaline suites emplaced during the lower and middle Carboniferous are related with the post-collisional stage of the Variscan belt, which is characterized by uplift and erosion in a short-lived transtensional and/or transpressional regime. These calc-alkaline rocks are characterized by Nb and Ta negative anomalies which are not interpreted to be related to the contemporaneous subduction of an oceanic lithosphere.

The late Carboniferous and early Permian acidic intrusives and volcanics exhibit alkali-calcic affinities and like the previous calc-alkaline suites, Nb-Ta negative anomalies. These volcano-plutonic suites are thought to be emplaced in a major distensional regime, i.e. during the collapse of the Variscan belt.

Finally, the middle to late Permian-early Triassic period is characterized by the emplacement of anorogenic alkaline melts, characterized by the absence of Nb and Ta negative anomalies. These alkaline rocks are associated with the intra-continental extensional processes and crustal thinning, occurring at the end of the collapse of the Variscan range .

Therefore, from the post-collisional stages of the Variscan belt to the complete collapse of the chain, the mafic, as well as the acidic volcanic and plutonic rocks (lavas, small and large magmatic intrusions, lamprophyric dikes), share similar geochemical and isotopic characteristics, despite their different ages (lower, middle and late Carboniferous and early Permian), locations in the Variscan belt (European Alpine belt, Pyrenees Range, Corsica), and magmatic affinities (tholeiitic, calc-alkaline, subalkaline and shoshonitic). Thus, negative or near BSE εNd_i values and Nb-Ta negative anomalies are widespread in the Variscan post-collisional magmatism. These isotopic and trace-element features have been interpreted in different ways, i.e. as the effect of a crustal contamination and/or related to a subduction context. Nevertheless, another hypothesis can be proposed to explain the systematic Nb-Ta negative anomaly and the εNd_i values of all these magmas, such as the involvement of the subcontinental lithospheric mantle,

previously metasomatized by subduction-related fluids and/or contaminated by recycling of oceanic sediments.

Conversely, subsequent magmatism (mid- to late Permian) associated with the end of the extensional episode of the Variscan belt displays very different geochemical characteristics, i.e. positive Nb-Ta anomalies and positive εNd_i.

Thus, the petrological and geochemical (incompatible trace elements and Nd, Sr and Pb isotopes) studies of the Mont Collon mafic complex, which does not display typical calc-alkaline but rather (transitional) subalkaline characteristics, will bring new insights on the interpretation of the post-collisional magmatism related to the distensive episode that led to the collapse of the Variscan belt.

1.4. Previous studies on the Mont Collon mafic complex

Dal Piaz et al. (1977) associated the Mont Collon-Dents de Bertol mafic complex with the famous Matterhorn massif. They developed a mineralogical and petrographic study completed by some geochemical data. They also dated the massif as late Permian (ca 250 Ma), using Rb/Sr and K/Ar methods (on biotite) and interpreted this date as the cooling age of the Mont Collon complex. Moreover, the Mont Collon intrusion is cited several times in the literature as an example of a basic magmatism associated with the late tectonic extensional events concluding the history of the Variscan Range.

1.5. Geographical setting of the Mont Collon mafic complex

The Mont Collon mafic complex is located near the village of Arolla (Fig. 4), in the Southern Val d'Hérens (Wallis, Switzerland). It covers an area of approximately 14 km^2 and was labeled after the highest summit of the area, i.e. the Mont Collon. This mafic complex is composed of several discontinuous outcrops separated by glaciers and associated moraines (see Chapter 2). The principal exposure is the Dents de Bertol area, located in the central part of the intrusion, which exhibits a well-preserved magmatic layering.

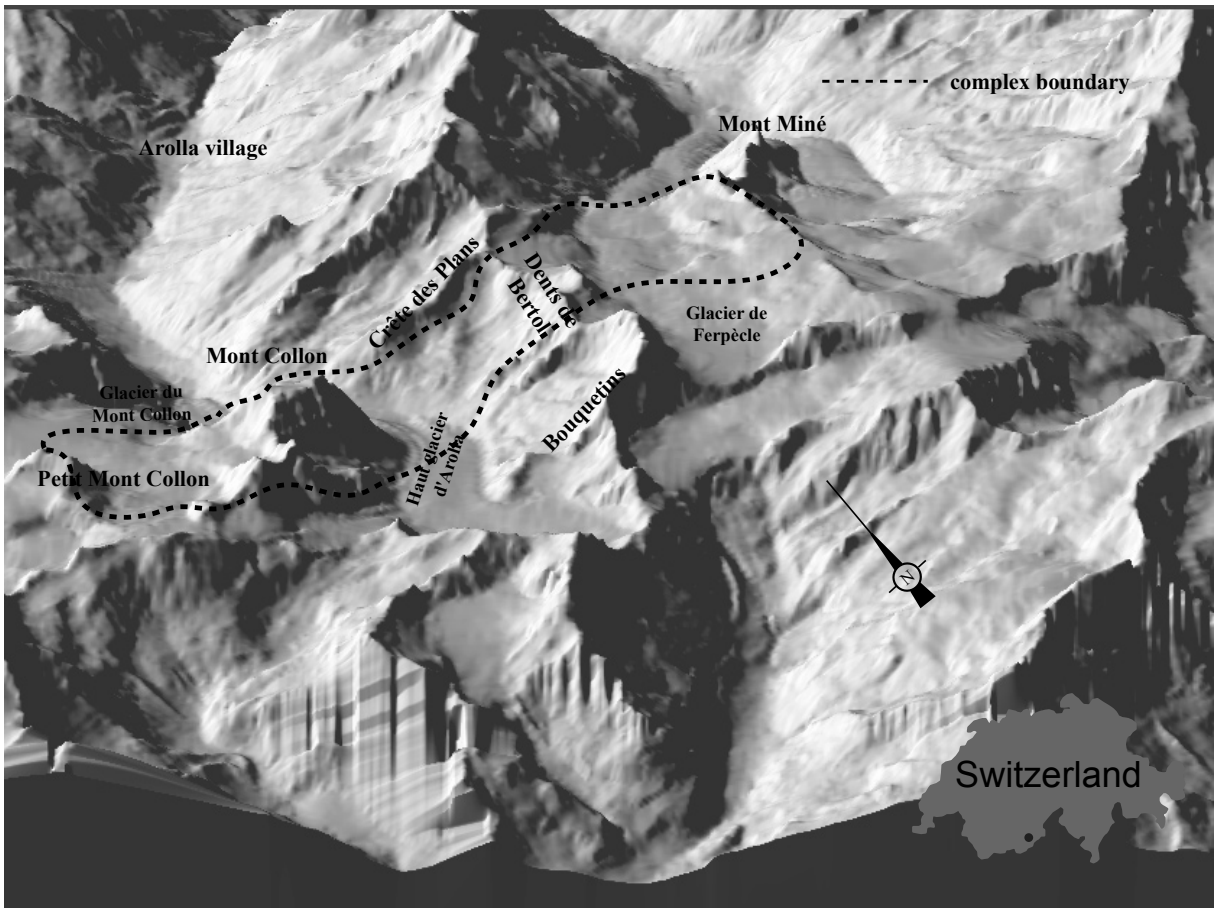

Fig. 4: Location of the Mont Collon mafic complex (dotted line) on a topographic elevation model (3D Atlas of Switzerland).

1.6. Aims and tools

1.6.1 Aims

The first aim of this work was to recognize, during the field work, the various rock types, their relationships in the complex and to obtain accurate ages of the main lithologies recognized in the Mont Collon complex, considering that the previously published data did not constrain the crystallization time. Moreover, the ages of the dikes intruding the plutonic rocks (i.e. the leucocratic and Fe-Ti melanocratic dikes) were still unknown, at that time this study started.

We have also to determine mineral and whole-rock chemistries of the magmatic suites (cumulates and dikes) in the Mont Collon mafic complex, in order to characterize the igneous processes which led to their genesis as well as the parental melt composition of the cumulates.

Mineral compositions will also allow to estimate the crystallisation depth of the Mont Collon complex.

Radiogenic isotopes (Nd-Sr, Pb and Re-Os and Hf) will help to (i) characterize the nature of the sources of the cumulates and dikes (crustal, lithospheric or asthenospheric), (ii) its possible evolution with time, and (iii) determine the potential involvement of the continental crust (contamination versus assimilation).

Finally, all the data obtained from this work (i.e. ages, geochemical and isotopic characteristics) will allow to replace the Mont Collon complex in its geodynamic context.

1.6.2 Tools

Rocks used for dating were a pegmatitic gabbro and a Qz-rich pegmatite for U/Pb on zircons and a Fe-Ti melanocratic dike for $^{40}Ar/^{39}Ar$ on amphibole. Both dating methods have been chosen considering the mineralogies of each rock type. U/Pb dating was also coupled with Hf isotopes analysis on the dated zircons. Zircon U/Pb dating was done at the ETH Zurich in the laboratory of the Prof. Urs Schaltegger while amphibole $^{40}Ar/^{39}Ar$ dating was done in the laboratory managed by Mike Cosca and Andreas Mulch, at the Institute of Mineralogy and Geochemistry (IMG, University of Lausanne).

Whole-rock major- and trace-element compositions were determined by X-Ray Fluorescence (major and trace elements) at the Centre for Mineral Analysis, directed by Hans-Rudolf Pfeifer (CAM, University of Lausanne) and ICPMS (trace elements), managed by Catherine Chauvel and Francine Keller (University of Grenoble). We refer to the appendix 3 for the detailed analysis procedures.

The mineral (clinopyroxene, plagioclase and amphibole) major- and trace-element chemistry were obtained using in-situ analysis methods: an electron microprobe CAMECA SX50 (major elements) and a Perkin-Elmer 6100 DRC Laser Ablation - Inductively Coupled Plasma Mass Spectrometer (LA-ICPMS: trace elements) in the laboratory managed by François Bussy, at the Institute of Mineralogy and Geochemistry (University of Lausanne). We refer to the appendix 4 for the detailed analysis procedures.

Nd and Sr radiogenic isotopes were measured by Pierre Brunet at the Laboratoire de Géochimie Isotopique de l'Université Paul Sabatier - Toulouse (France) on a Finnigan MAT261 multi-collector mass spectrometer and at the Institut des Sciences de la Terre, de l'Environnement et de l'Espace de Montpellier, managed by Delphine Bosch (ISTEEM, France), respectively. Pb radiogenic isotopes were analyzed on a VG Plasma 54 Multi-Collector - Inductively Coupled Plasma Mass Spectrometer (MC-ICP-MS), in the laboratory of Francis Albarède at the Ecole Normale Supérieure de Lyon (ENS, France). We refer to the appendix 5 for the detailed analysis procedures.

Chapter 2: Geological setting and petrology of the Mont Collon mafic complex

Chapter 2: Geological setting and petrology of the Mont Collon mafic complex

2.1. Introduction

The Mont Collon mafic complex is exposed within the Arolla Series on the external side of the Dent Blanche nappe (*s.s.*), which belongs to the Austroalpine nappe system. It represents one of the best preserved Permian mafic complexes of the Western Alps. It consists of a plutonic suite, crosscut by leucocratic and mafic dikes (Fig. 7). In this chapter, we will develop the geological background, the field relationship of the plutonic suites and intrusive rocks and their petrological features.

The Austroalpine nappe system originated from the stretched margin of the Adriatic microplate (Pfiffner, 1993) and was emplaced during the early Palaeogene period of the Mesoalpine orogeny (Dal Piaz et al., 1972; Hunziker et al., 1989), on the Penninic zone along a NW-vergent thrust system underlined by a SE-oriented stretching lineation. The latter was created by the underthrusting of the European plate below the Adriatic margin by ductile shear of the upper part of the European crust and the lower part of the Adriatic plate (Pfiffner, 1993; Steck and Hunziker, 1994).

The Dent Blanche nappe and the Sesia-Lanzo zone were concurrently scraped off the same paleostructural domain (Fig. 5; Dal Piaz, 1999). The Dent Blanche nappe was juxtaposed above the Penninic units subsequent to the high-pressure metamorphism in the latter during the Eocene-Oligocene (Avigad et al., 1993). The Arolla lower unit of the Dent Blanche nappe, containing the Mont Collon mafic complex, escaped the severe eclogitic overprint. According to Pfiffner (1993), the klippe-shape of the Dent Blanche nappe within the Penninic zone resulted from Tertiary extensive unroofing, uplift and erosion. Moreover, Ramsay (1967) proposed that the position of the Dent Blanche nappe resulted from a displacement (greater than 40 km) to the southwest along the ductile Simplon shear zone relative to the Verampio gneiss. This distance is based on a simple shear model with extension values measured by deformation markers in competent conglomerates and granitic gneiss. Steck (1980) proposed a displacement of the order of 80 km, postulating that deformation in the Mesozoic calcschists is much stronger.

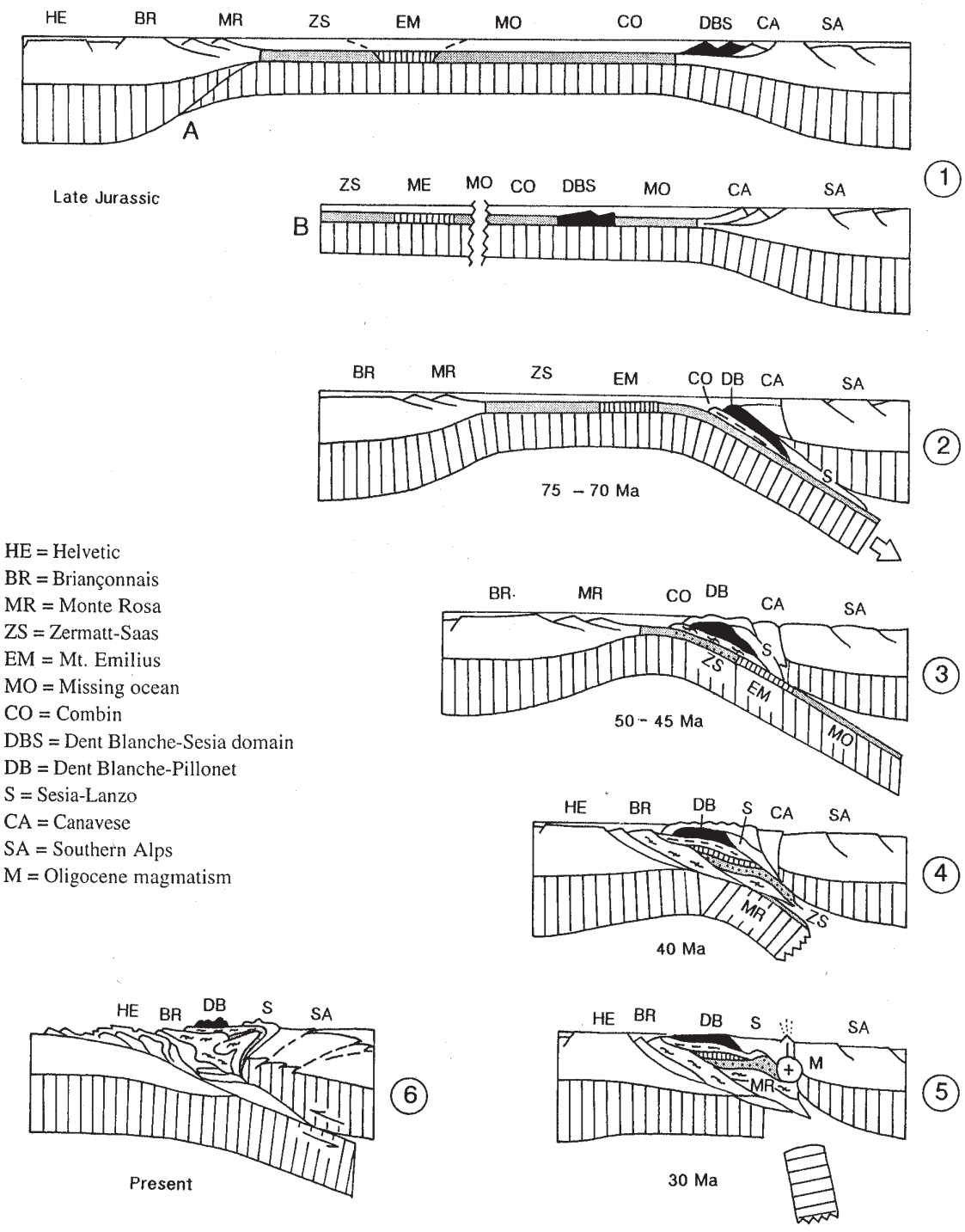

Fig. 5: Evolution of the Western Alps (after Dal Piaz, 1999). Stage 1 assumes asymmetric rifting, mantle denudation and one (A) or two (B) extensional allochthons within Piedmont-Ligurian ocean. Stages 2 to 5 show pre-collisional (2-3) to collisional contraction (4-5) from mid- Cretaceous onwards. Vertical rules: lithospheric mantle. Spreading ridges are omitted. The Dent Blanche nappe is underlined in black.

2.2. Geological background

In the western Alps, the Austroalpine nappe system (Martinotti and Hunziker, 1984, Ballèvre et al., 1986, Venturini et al., 1996, Dal Piaz, 1999) consists of several independent klippes belonging to the Dent-Blanche (s.l.) nappes system (on its external north-west side) and to the Sesia-Lanzo zone (on its internal southeast side) which are separated from the Ivrea-Verbano zone by the Insubric line (Fig. 6). The Sesia-Lanzo zone displays a wider distribution area than the Dent Blanche nappes system (s.l.) which, nevertheless, shows a noteworthy lithological consistency. The Dent-Blanche (s.l.) consists of several independent klippes, which systematically overlap the Piedmont nappes stack along a complicated thrust slices system. The main thrust sheets consist of the upper eclogitic-free northern unit (the Dent-Blanche (s.s.) - Mont Mary - Pillonet klippes) and the lower H-P eclogitic southern unit (the Mont Emilius - Glacier Raffray - Tour Ponton units). The east-west-trending Aosta-Ranzola fault system in the Aosta Valley separates these two units (Bistacchi et al., 2001).

The basement units of the upper Dent-Blanche nappe (*s.s.*) comprise the upper Valpelline and the lower Arolla Series, which are also exposed in the Mont-Mary, part of the Dent Blanche system (s.l.), (Fig. 6). The Valpelline Series consist of silicic to mafic granulites, high-T pelitic gneisses with interbedded marbles and tholeiitic amphibolites. The most common mineral assemblages of the granulites indicate metamorphic conditions of 8kbar / 750°C (Diehl, 1952). The Valpelline depression outlined the development of pull-apart structures during the oblique collision of Europe and Adria (Steck and Hunziker, 1994). In the Sesia-Lanzo zone, the second Diorite-Kinzigite zone (II DK zone) is coeval with the Valpelline Series. The II DK zone and the Valpelline Series display similar metamorphic assemblages and mica cooling ages ranging between 240 and 140 Ma (Hunziker, 1974, Hunziker et al. 1992). The lower tectonic unit of the Arolla Series is made of pre-granitic relics of high-grade paragneisses and fine-grained metabasites intruded by late Paleozoic metagranitoids (ca. 289 Ma, Bussy et al., 1998) affected by greenschist facies Alpine re-equilibration. The most common mineral assemblage of the Arolla Series orthogneisses consists of quartz, plagioclase, phengite, hornblende with brown cores, and minor amounts of chlorite, calcite and epidote (Hunziker, 1974). According to Compagnoni et al. (1977) and Martinotti and Hunziker (1984), the Gneiss Minuti complex is coeval with the Arolla Series in the Sesia-Lanzo zone. Instead, Ballèvre et al. (1986) assume that both the Valpelline and the Arolla Series are coeval with the Gneiss Minuti. The latter occurs throughout the external side of the Sesia-Lanzo zone as a continuous distributed sheet showing a prevailing greenschist overprint.

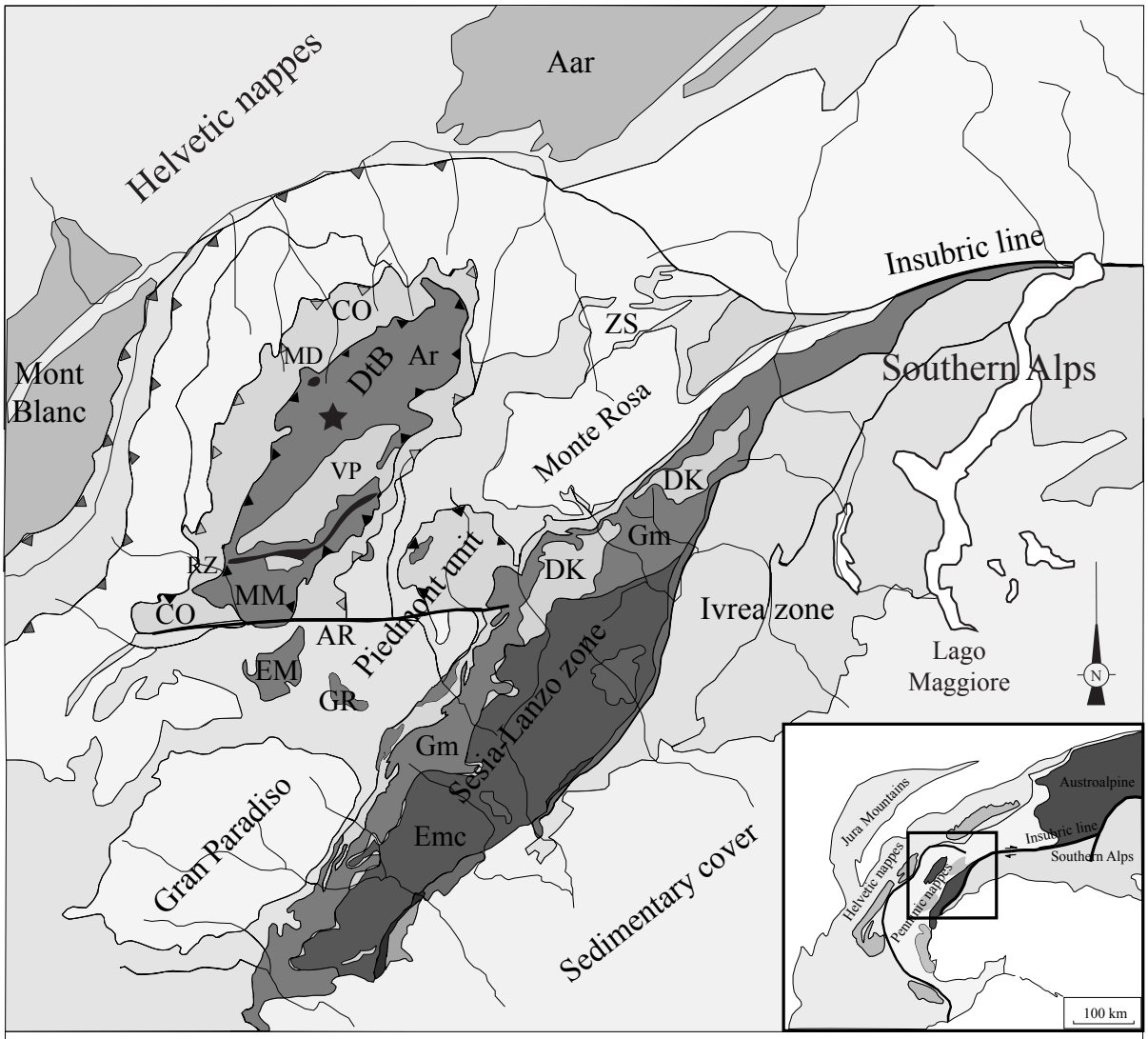

Fig. 6: Tectonic map of the northwestern Alps (after Bigi et al., 1990 and Dial Piaz et al., 1993 and 1999) showing the main tectonic units, i.e.: the Helvetic nappes, the External Crystalline Massifs (Mont Blanc, Aiguilles Rouges and Aar-Gotthard massifs), the klippe of the Dent Blanche nappe, the Piedmont units, the Internal Crystalline massifs of the Gran Paradiso and the Monte Rosa, the Sesia-Lanzo zone and the southern Alpine unit of Ivrea.

The Permian to Mesozoic monometamorphic metasedimentary rocks are locally preserved in the Dent-Blanche (s.l.) nappes system and constitute the two main units of the northern Mont Dolin Series (Weidmann and Zaninetti, 1974, Ayrton et al., 1982) and the southern Mont Roisan zone (Elter, 1960). They consist of Triassic siliceous clastics, Middle Triassic to Jurassic platform carbonates, syn-rift monogenic breccias and limestones, overlain by Cretaceous carbonates to terrigenous flysch-type metasediments (Ballèvre et al., 1986, Dal Piaz, 1999 and references therein). They are classically described as the cover sequence of the Austroalpine basement but Martinotti and Hunziker (1984) labeled the Mont Dolin Series and the Roisan zone with a more careful term of «detached remnants of a possible cover sequence». Mylonitic sheets of the orthogneisses of the Arolla Series separate the Mont Dolin-Roisan zone from the Valpelline Series. Several bodies of gabbros and related ultramafic cumulates have been described in the Dent Blanche nappe (Ballèvre et al., 1986; Dal Piaz, 1999). These rocks are affected by an important Alpine overprint (e.g. in the Pillonet klippe) but large well-preserved mafic complexes occur such as the Matterhorn or the Mont Collon-Dents de Bertol.

2.3. Field relationships

As shown in figure 7 and 10, the exposures are relatively discontinuous because they are partly hidden by three major glaciers (the Mont Collon, the Arolla and the Ferpècle glaciers) and associated moraines. The Mont Collon mafic complex consists of three major exposures and several small scattered outcrops.

The Mont Collon summit represents the main outcrop but it is hardly accessible on its southern and western sides. The Dents de Bertol exposures are located in the center of the complex (Fig. 7 and 10). A well-preserved magmatic layering is exposed almost continually over several hundred meters on its western wall (Fig. 8) while outcrops in the Mont Collon (s.s.) northeastern wall do not present asuch a preserved layered sequence. Thus, two groups of cumulates have been distinguished on the basis of their location, i.e. the group I encompassing the Mont Collon rocks and the group II, the Dents de Bertol layered sequence rocks (Fig. 7 and 8). The magmatic layering is sub-vertical and is related to a parallel rhythmic alternation of variable thickness of mafic rocks (Plate 1, Ph. 6). The rocks exhibit a mineral fabric, underlined by clinopyroxene and/or plagioclase, which is almost sub-parallel to the magmatic layering. The main facies observed in the layered sequence are olivine-bearing and clinopyroxene-bearing gabbros.

Rare thinner melanocratic layers (classified as plg-wehrlite according to their plagioclase, olivine and clinopyroxene modal contents) are also exposed at the northernmost extremity (near the contact with the surrounding rocks) and in the middle part of the layered sequence of the Dents de Bertol area. They have not been observed in other parts within the complex.

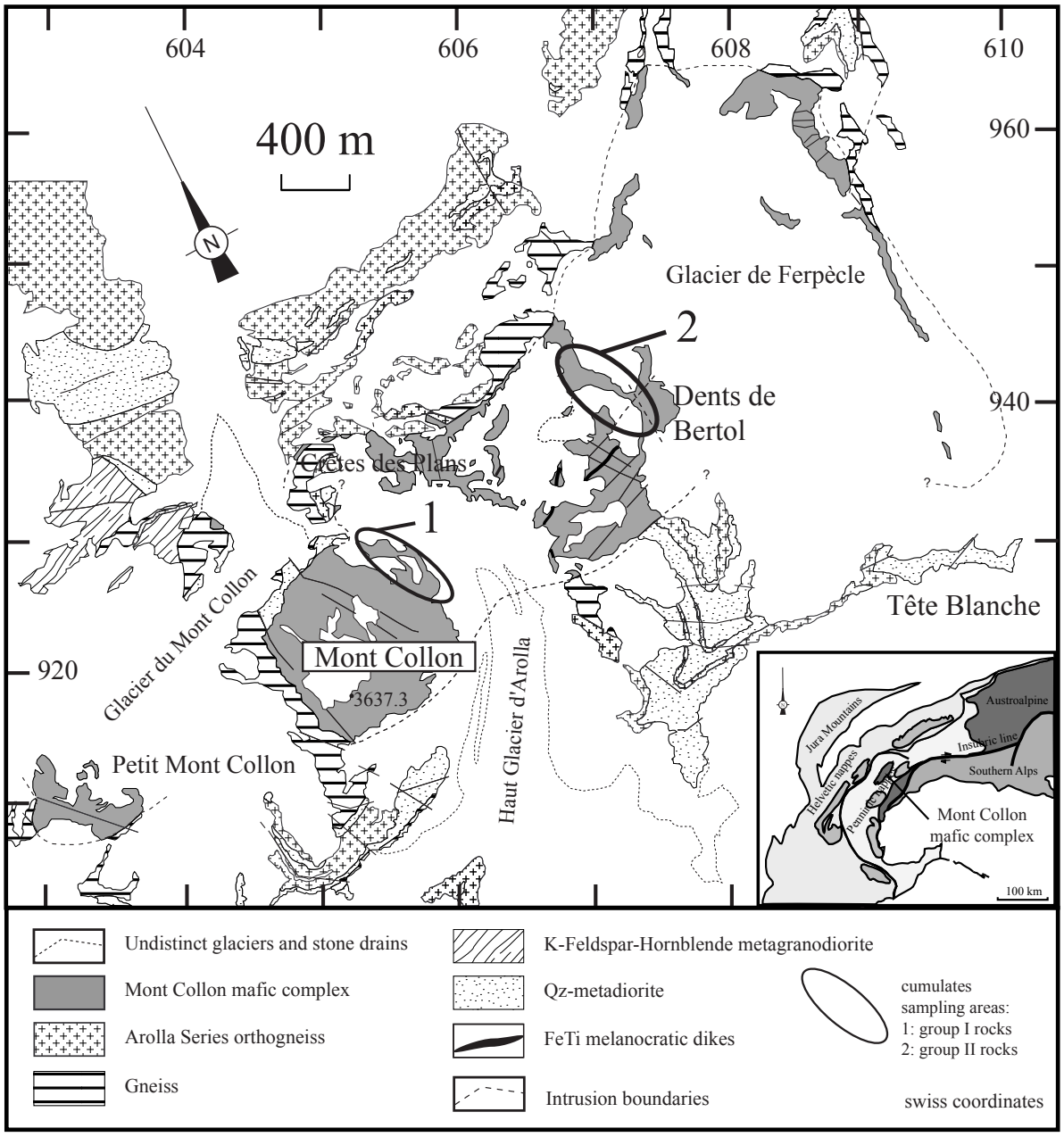

Fig. 7: a) Geological map of the Mont Collon area (scale: 1:25 000). Modified after Gouffon et al., 2003, map n°1317 Geological Atlas of Switzerland). b) Inset: main tectonic units of the Western European Alpine Belt (see also figure 2).

Fig. 8: Photograph of the well-preserved magmatic layering in the Dents de Bertol area. Scale: total length of the cliff is approximately 500 meters.

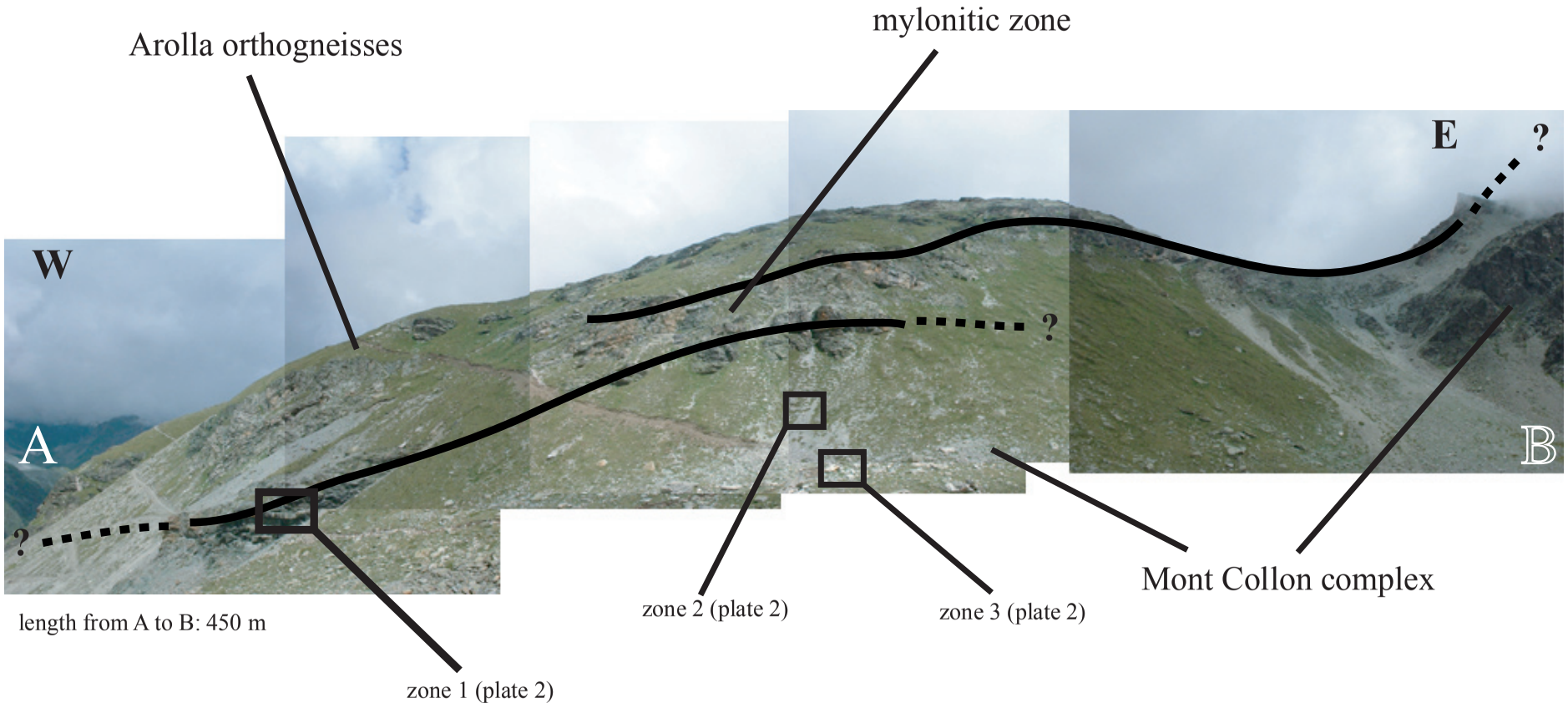

Fig. 9: Mylonitic contact between the Mont Collon complex and the Arolla orthogneisses exposed in the Crêtes des Plans area.

Two wehrlitic layers crop out also at the base of Crêtes des Plans (Plate 1, Photo. 1). These rocks occur only as sills within the gabbros, with sharp contact and they are not present in the preserved layered sequence. At the southernmost extremity of the Dents de Bertol area, a single anorthositic layer crops out with a magmatic layering parallel to the main orientation of the rhythmic sequence. Finally, the northeasternmost exposures are located on the eastern bank of the Glacier de Ferpècle. Patches of pegmatitic gabbros crop out at the base of the eastern wall of the Mont Collon or in the Dents de Bertol area.

Numerous centimeter- to decimeter-sized intermediate to acidic dikes are widespread in the Mont Collon intrusion (Plate 1, Photo. 2 to 5). The acidic dikes systematically crosscut the gabbroic facies and they exhibit various mineralogy. They consist of (i) quartz-rich pegmatites, (ii) microgranodiorites (iii) aplites and (iv) anorthositic dikes. The petrological characteristics of the dikes will be described in this chapter.

Fine-grained black dikes are exposed only in the Dents de Bertol area. They are never found in the surrounding orthogneisses of the Arolla series or in the other parts of the complex. They crosscut all the lithologies including the mafic cumulates and the leucocratic dikes with sharp contacts. The terminology, mineralogical and compositional characteristics used to name these dikes will be discuss in chapter 5. So, we will label these dikes as «Fe-Ti melanocratic dikes» as they are named by Dal Piaz et al. (1977).

The contact zone between the complex and its country rock (the orthogneisses of the Arolla Series) is several meter-thick (up to 70 m). It is clearly mylonitic and drastically folded with both the orthogneisses and the mafic cumulates by Alpine tectonic disturbances (Fig. 9 and plate 2). At the contact with the undeformed zone of the mafic complex, the gabbros (s.l.) display flaser texture (plate 2, zone 3). The contact can be followed along discontinuous exposures from the base of the Crêtes des Plans to the northern extremity of the Dents de Bertol where the magmatic layering zone is directly in contact with the mylonitic horizon (Fig. 10). Consequently, we cannot be sure whether the orthogneisses of the Arolla Series represent or not the original country rocks of the mafic complex.

The mafic cumulates of the Mont Collon complex display a weak metamorphic overprint of greenschist grade, which decreases from the mylonitic contact to the center of the complex (Dents de Bertol), where the magmatic textures and mineralogy are well-preserved. The weathering is discontinuous across the complex.

Plate 1: Microphotographs of field relationships

Photo 1: werhlite MP213 (Dents de Bertol area, swiss coordinates: 605650 / 093600)

Photo 2: anorthositic dike Crêtes des Plans (swiss coordinates: 605800 / 093420)

Photo 3: aplitic dike (Mont Collon NE wall, swiss coordinates: 605850 / 092850)

Photo 4: quartz pegmatite (Mont Collon NE wall, swiss coordinates: 605500 / 092800)

Photo 5: microgranodioritic dike (Crêtes des Plans, swiss coordinates: 605320 / 093550)

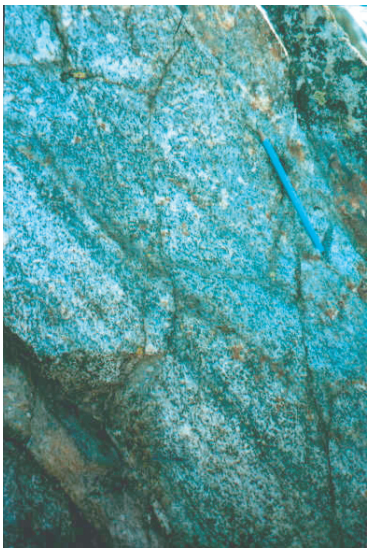

Photo 6: magmatic layering in the Dents de Bertol area (swiss coordinates: 607100 / 094210)

Plate 2: Microphotographs of successive zones within the contact area from the Arolla orthogneisses towards the Mont Collon complex

from the Arolla orthogneisses

zone 1: mylonitic rocks within the contact between the Mont Collon complex and the surrounding Arolla orthogneisses

zone 2: cumulates deformed near the contact with the Arolla orthogneisses

zone 3: flaser gabbro situated at the outermost zone of the contact, i.e. near the undeformed cumulates of the complex.

to the Mont Collon mafic complex

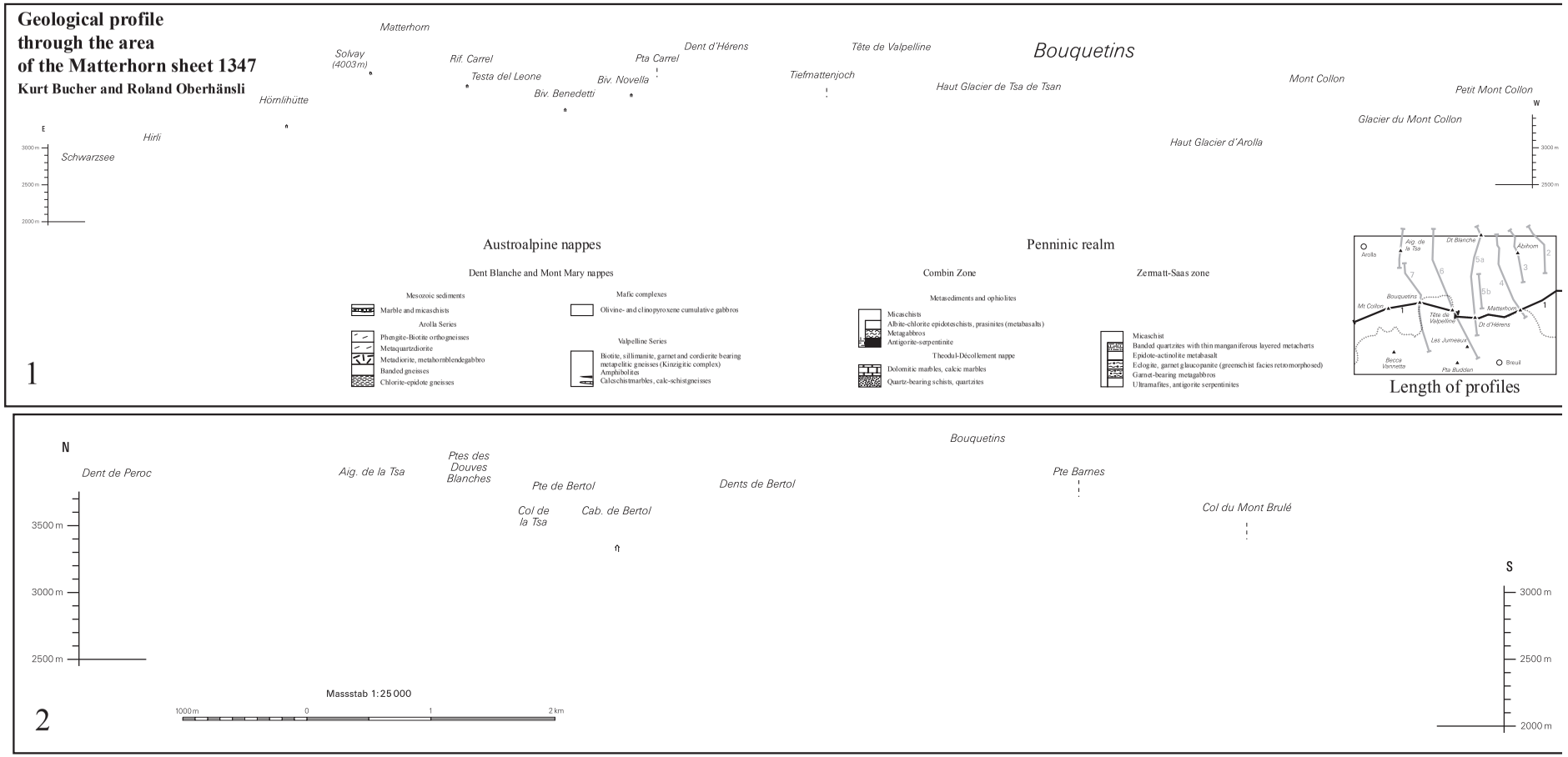

Fig. 10: Geological profiles through the Mont Collon and the Dents de Bertol (after Bucher et al., 2003 and 2004).

In the following presentation of each rock type, emphasis is on the chemical variations of their minerals. The bulk rock chemistry will be treated in chapter 4 (cumulate rocks) and chapter 6 (dikes).

2.4. The mafic cumulates and related rocks

Most rocks of the Mont Collon complex are medium- to coarse-grained cumulates displaying variable modal amounts of olivine, clinopyroxene and plagioclase as major mineral constituents (see major-element composition of minerals in Tables 1 to 4). Plagioclase-wehrlites, olivine- and clinopyroxene-bearing gabbros are the most common facies with some rare wehrlites and troctolites. They crop out as variable sized layers forming a well-defined cumulate sequence in the Dents de Bertol area (Fig. 8). Cumulitic textures are well-preserved and underlined by preferred mineral orientation. Olivine and clinopyroxene form the main cumulus phases and crystallize as eu- to subhedral grains, up to 2-3 mm long. Plagioclase forms tabular crystals, commonly with parallel alignment. Primary olivine crystal boundaries are systematically resorbed in olivine-bearing rocks by orthopyroxene and amphibole coronitic reactions (see chapter 3, Fig. 18). Late-magmatic Ti-amphibole dominates the intercumulus assemblage, occurring as overgrowths or more locally as patches surrounding clinopyroxenes. Accessory minerals are magnetite, ilmenite and sulphides; apatite is rare. With few exceptions, orthopyroxene occurs only as coronitic reaction rims between olivine and plagioclase in all olivine-bearing samples. Nevertheless, orthopyroxene could crystallize as a magmatic phase (1-2 vol-%) in some plagioclase-wehrlites.

2.4.1. Wehrlites

Wehrlites of the Mont Collon are ad- to mesocumulates with highly serpentinized olivine (up to 60 vol.%) and euhedral diopsidic clinopyroxene as cumulus phases. Intercumulus amphibole is a magnesio-hastingsitic hornblende, which is almost completely recrystallized into actinolite-tremolite.

2.4.2. Plagioclase-wehrlites (= plg-wehrlites)

Olivine is the main cumulus phase in plagioclase-bearing wehrlites. It displays a constant composition (Fo = 75.3 - 77.8) with Ni content between 450 and 630 ppm. MnO shows constant concentration close to 0.3 wt%. Euhedral to subhedral clinopyroxene represents 20 to 30% of the cumulus phases. Its composition varies from endiopside in the core to diopside in the rim (Fig. 11), i.e. Mg# decreases from 87 to 83 and CaO increases from 22.0 to 23.2 %, respectively. Clinopyroxene has a higher Al_2O_3 content than clinopyroxene in the gabbros. Al_2O_3 varies

from 2.9 % to 3.9 % and generally decreases from core to rim, while Na_2O and TiO_2 increase. Plagioclase appears as an intercumulus phase with variable modal proportions (10-30%). Its composition plots in the labradorite field ($An_{63.1}$ and $An_{69.2}$, Fig. 12). A significant amount of a magnesio-hastingsite magmatic amphibole (Fig.13) fills the interstices between plagioclase and clinopyroxene or occurs locally as large patches surrounding clinopyroxene and plagioclase. Accessories are essentially ilmenite and magnetite. Magnetite occurs as round-shaped grains, while ilmenite fills the interstices and is generally surrounded by magmatic amphibole. The ilmenite component is close to 90% with minor amount of geikielite (7.5%) and pyrophanite (2.5%). Magnetite is Mn, Cr and Mg poor. Its NiO content increases up to 1 wt%.

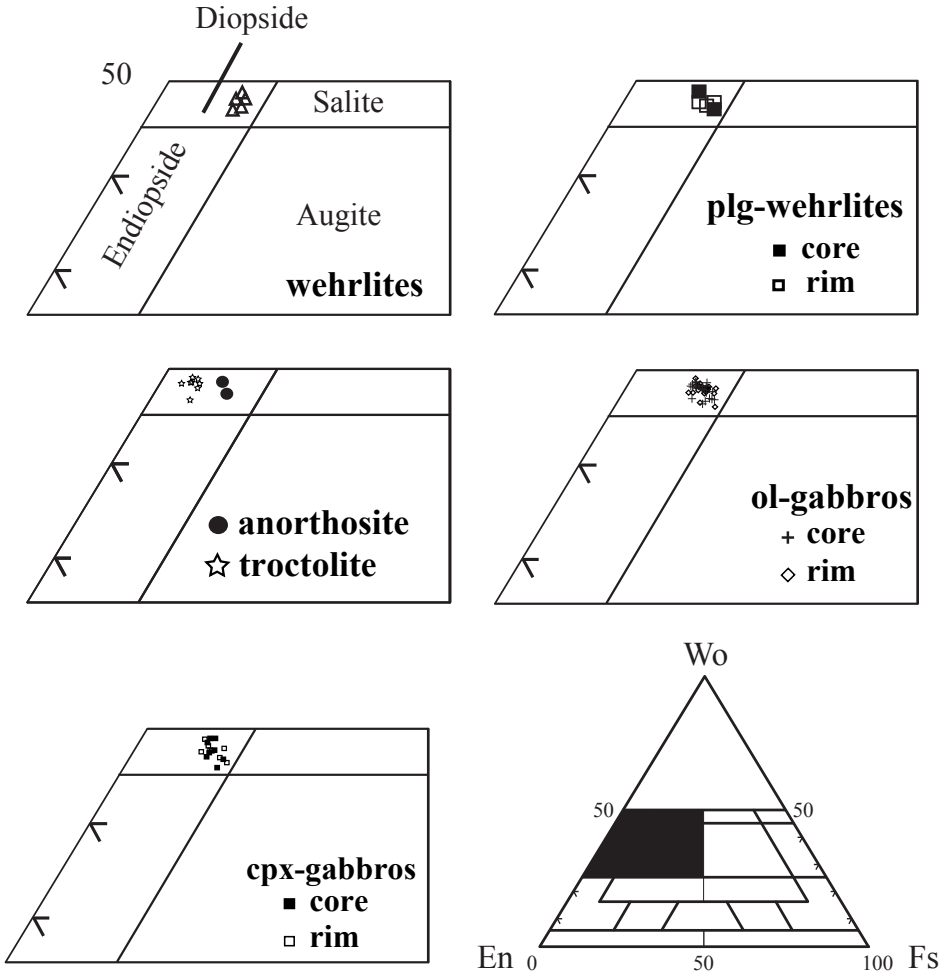

Fig. 11: Ternary diagrams for clinopyroxene from plagioclase-wehrlite, olivine- and clinopyroxene gabbros in the $Ca_2Si_2O_6$ (Wo) - $Mg_2Si_2O_6$ (En) - $Fe_2Si_2O_6$ (Fs) system (compositional fields after Morimoto et al., 1988).

Table 1: Representative major-element compositions of clinopyroxenes from wehrlites, plg-wehrlites, troctolite, ol- and cpx-gabbros and anorthosite used to the geobarometric calculations.

Rock types	wehrlites		plg-wehrlites						troctolite				ol-gabbros								cpx-gabbros						anorthosite	
Sample numbers	MP243		MP106		FB1094		FB1095		MP240				MP125		MP136		MP166				MP168				MP192		MP285	
	core	rim	core	core	core	rim	core	rim	core	rim	core	rim	core	rim	core	rim	core	rim	core	rim	core	rim	core	rim	core	rim	core	rim
SiO_2	50.6	51.3	51.6	51.7	51.0	52.7	51.7	52.5	51.5	52.1	51.9	51.5	53.2	52.4	51.20	52.64	53.5	52.2	51.6	52.2	52.4	52.4	51.8	51.7	52.7	53.1	51.5	50.0
TiO_2	0.74	0.71	0.72	0.87	1.26	0.75	0.72	0.54	0.87	0.58	0.70	0.71	0.21	0.48	0.84	0.64	0.36	0.45	0.72	0.68	0.63	0.72	0.71	0.71	0.58	0.57	0.55	0.76
Al_2O_3	3.5	2.8	3.4	3.3	3.4	2.9	3.9	3.1	3.5	2.8	3.2	3.2	1.2	2.4	3.5	2.7	1.9	3.0	3.0	2.7	3.0	2.9	3.1	3.0	2.9	3.1	3.3	4.1
Cr_2O_3	0.19	0.23	0.76	0.33	0.96	0.13	0.65	0.45	0.38	0.45	0.37	0.42	0.16	0.24	0.41	0.26	0.33	0.47	0.21	0.25	0.26	0.14	0.23	0.23	0.24	0.24	0.58	1.77
Fe_2O_3	1.89	1.85	1.01	0.39	0.70	0.65	0.81	0.65	1.13	0.54	0.58	2.02	1.53	1.26	1.79	0.30	0.00	0.33	1.78	0.06	0.00	0.00	0.83	1.13	0.00	0.00	0.34	1.81
FeO	3.9	3.3	5.0	5.0	5.4	4.3	3.9	4.4	3.7	4.1	4.5	2.9	3.4	3.8	3.4	5.0	4.7	5.1	4.2	5.6	5.3	5.3	4.4	4.5	5.0	5.4	5.1	3.9
MnO	0.19	0.14	0.18	0.17	0.20	0.15	0.14	0.19	0.16	0.19	0.18	0.17	0.20	0.19	0.21	0.26	0.18	0.18	0.19	0.21	0.15	0.14	0.16	0.20	0.18	0.17	0.16	0.21
MgO	15.8	15.3	14.6	14.9	14.9	15.7	15.0	15.2	15.3	15.2	16.0	15.8	16.0	15.5	15.3	15.2	16.0	15.2	15.1	15.4	16.3	16.2	15.9	15.5	15.4	15.0	15.6	15.0
CaO	21.2	23.1	22.3	22.6	22.0	23.2	22.8	23.0	22.6	23.3	21.6	22.5	23.4	23.2	22.5	22.8	22.5	22.3	22.7	22.0	20.8	21.0	22.0	22.3	21.6	22.0	21.5	22.0
Na_2O	0.36	0.37	0.56	0.41	0.39	0.32	0.54	0.45	0.46	0.35	0.39	0.46	0.29	0.38	0.49	0.43	0.21	0.39	0.44	0.35	0.32	0.29	0.34	0.35	0.56	0.42	0.32	0.31
Total	98.3	99.2	100.1	99.7	100.3	101.0	100.2	100.5	99.6	99.5	99.3	99.7	99.9	99.8	99.68	100.16	99.7	99.6	99.8	99.4	99.0	99.1	99.4	99.6	99.2	100.1	98.9	99.9
Si	1.887	1.902	1.901	1.909	1.882	1.916	1.894	1.919	1.895	1.922	1.912	1.895	1.956	1.927	1.887	1.932	1.962	1.926	1.903	1.930	1.931	1.934	1.910	1.909	1.946	1.944	1.912	1.850
Ti	0.021	0.020	0.020	0.024	0.035	0.020	0.020	0.015	0.024	0.016	0.019	0.020	0.006	0.013	0.023	0.018	0.010	0.012	0.020	0.019	0.018	0.020	0.020	0.020	0.016	0.016	0.015	0.021
Al^{IV}	0.113	0.098	0.099	0.091	0.118	0.084	0.106	0.081	0.105	0.078	0.088	0.105	0.044	0.073	0.113	0.068	0.038	0.074	0.097	0.070	0.069	0.066	0.090	0.091	0.054	0.056	0.088	0.150
Al^{VI}	0.040	0.026	0.049	0.051	0.029	0.044	0.064	0.052	0.047	0.042	0.050	0.032	0.007	0.031	0.040	0.048	0.045	0.054	0.032	0.048	0.062	0.058	0.045	0.039	0.070	0.079	0.054	0.029
Cr	0.006	0.007	0.022	0.010	0.028	0.004	0.019	0.013	0.011	0.013	0.011	0.012	0.005	0.007	0.012	0.007	0.010	0.014	0.006	0.007	0.007	0.004	0.007	0.007	0.007	0.007	0.017	0.052
Fe^{3+}	0.053	0.052	0.028	0.011	0.020	0.018	0.022	0.018	0.031	0.015	0.016	0.056	0.042	0.035	0.050	0.008	0.000	0.009	0.049	0.002	0.000	0.000	0.023	0.031	0.000	0.000	0.009	0.050
Fe^{2+}	0.122	0.103	0.153	0.154	0.166	0.131	0.120	0.134	0.114	0.127	0.138	0.089	0.103	0.116	0.105	0.153	0.145	0.157	0.128	0.171	0.163	0.164	0.134	0.139	0.155	0.166	0.158	0.121
Mn	0.006	0.004	0.006	0.005	0.006	0.005	0.004	0.006	0.005	0.006	0.006	0.005	0.006	0.006	0.007	0.008	0.006	0.006	0.006	0.007	0.005	0.004	0.005	0.006	0.006	0.005	0.005	0.006
Mg	0.880	0.844	0.803	0.820	0.820	0.851	0.821	0.830	0.842	0.834	0.881	0.865	0.877	0.850	0.838	0.830	0.875	0.838	0.831	0.849	0.896	0.892	0.874	0.850	0.849	0.821	0.863	0.824
Ca	0.847	0.919	0.880	0.895	0.868	0.904	0.892	0.900	0.893	0.921	0.851	0.887	0.934	0.914	0.890	0.897	0.886	0.882	0.896	0.872	0.820	0.829	0.869	0.882	0.855	0.861	0.854	0.873
Na	0.026	0.026	0.040	0.029	0.028	0.023	0.039	0.032	0.033	0.025	0.028	0.033	0.021	0.027	0.035	0.031	0.015	0.028	0.031	0.025	0.023	0.021	0.024	0.025	0.028	0.030	0.023	0.022
Wo	45.8	49.2	47.9	47.9	46.8	47.9	48.7	48.3	48.3	48.9	45.5	48.2	48.8	48.6	48.55	47.71	46.5	47.0	48.3	46.1	43.7	44.0	46.3	47.1	46.0	46.6	45.6	48.0
En	47.6	45.2	43.7	43.9	44.2	45.1	44.8	44.5	45.5	44.3	47.1	47.0	45.8	45.2	45.72	44.15	45.9	44.6	44.8	44.9	47.7	47.3	46.6	45.4	45.7	44.4	46.0	45.3
Fs	6.6	5.5	8.3	8.2	9.0	6.9	6.5	7.2	6.2	6.8	7.4	4.8	5.4	6.2	5.73	8.14	7.6	8.4	6.9	9.1	8.7	8.7	7.1	7.4	8.3	9.0	8.4	6.6
Mg#	87.8	89.1	84.0	84.2	83.2	86.7	87.3	86.1	88.1	86.8	86.4	90.7	89.5	88.0	88.9	84.4	85.8	84.2	86.6	83.2	84.6	84.5	86.7	85.9	84.6	83.2	84.5	87.2

Structural formula based on 4 cations, (n.d.): not determined.

Table 2: Representative major-element compositions of olivines from plg-wehrlites, troctolite, ol-gabbros.

Rock types	plg-wehrlite				troctolite				ol-gabbros					
Sample numbers	MP106		FB1095		MP240				MP125		MP136		MP161	
	core	rim	core	rim	core	rim	core	rim	core	rim	core	rim	core	rim
SiO_2	38.1	38.3	39.4	39.4	39.2	39.1	38.9	39.1	38.8	38.8	38.7	38.3	38.5	38.8
TiO_2	0.01	0.01	0.01	0.01	0.02	0.00	0.01	0.01	0.03	0.02	0.03	0.01	0.01	0.00
Al_2O_3	0.01	0.01	0.01	0.00	0.01	0.01	0.02	0.02	0.00	0.00	0.00	0.01	0.00	0.01
Cr_2O_3	0.01	0.02	0.00	0.02	0.02	0.01	0.02	0.02	0.06	0.01	0.04	0.00	0.01	0.02
FeO_T	22.6	22.2	20.7	20.6	19.3	19.8	19.9	19.8	19.3	19.6	20.6	21.1	21.9	21.9
MnO	0.35	0.41	0.32	0.32	0.26	0.26	0.29	0.28	0.31	0.30	0.30	0.31	0.34	0.34
MgO	38.6	39.2	40.6	40.4	41.6	41.9	41.3	41.4	41.7	41.7	41.3	41.1	39.7	39.9
CaO	0.04	0.03	0.07	0.06	0.03	0.00	0.01	0.03	0.00	0.01	0.02	0.07	0.04	0.05
NiO	0.07	0.05	0.05	0.06	0.06	0.05	0.06	0.07	0.04	0.02	0.08	0.07	0.04	0.07
Total	99.8	100.3	101.0	100.9	100.4	101.1	100.5	100.6	100.2	100.4	101.0	101.1	100.5	101.1
Si	0.996	0.995	1.004	1.005	1.000	0.994	0.995	0.997	0.994	0.993	0.989	0.982	0.994	0.996
Ti	0.000	0.000	0.000	0.000	0.000	0.000	0.000	0.000	0.001	0.000	0.000	0.000	0.000	0.000
Al^{IV}	0.000	0.000	0.000	0.000	0.000	0.000	0.001	0.001	0.000	0.000	0.000	0.000	0.000	0.000
Al^{VI}	0.000	0.000	0.000	0.000	0.000	0.000	0.000	0.000	0.000	0.000	0.000	0.000	0.000	0.000
Cr	0.000	0.000	0.000	0.000	0.000	0.000	0.000	0.000	0.001	0.000	0.001	0.000	0.000	0.000
Fe^{2+}	0.493	0.482	0.440	0.440	0.411	0.421	0.426	0.424	0.412	0.418	0.440	0.453	0.473	0.470
Mn	0.008	0.009	0.007	0.007	0.006	0.006	0.006	0.006	0.007	0.007	0.006	0.007	0.007	0.007
Mg	1.504	1.517	1.541	1.538	1.582	1.585	1.576	1.574	1.590	1.587	1.572	1.571	1.529	1.527
Ca	0.001	0.001	0.002	0.002	0.001	0.000	0.000	0.001	0.000	0.000	0.000	0.002	0.001	0.001
Ni	0.001	0.001	0.001	0.001	0.001	0.001	0.001	0.001	0.001	0.000	0.002	0.001	0.001	0.001
Fa	24.7	24.1	22.2	22.2	20.6	21.0	21.3	21.2	20.6	20.8	21.9	22.4	23.6	23.5
Fo	75.3	75.9	77.8	77.8	79.4	79.0	78.7	78.8	79.4	79.2	78.1	77.6	76.4	76.5

Structural formulae based on 3 cations. Olivines from wehrlites are all serpentinized and not included in this table.

Table 3: Representative major-element compositions of plagioclases from plg-wehrlites, troctolite, ol- and cpx-gabbros and anorthosite.

Rock types	plg-wehrlites				troctolite		ol-gabbros								cpx-gabbros		anorthosite	
Sample numbers	MP106		FB1095		MP240		MP125		MP136		MP166		FB1091		MP168	MP168	MP285	MP285
	core1	rim1	core3	rim3	core1	rim1	core1	rim1	core2	rim2	core5	rim5	core 5	rim 5	core1	rim1	core	rim
SiO_2	52.1	50.5	50.6	51.2	49.2	49.2	49.6	49.6	47.1	49.3	50.0	49.8	51.5	52.0	48.3	48.7	49.2	48.6
Al_2O_3	30.0	30.4	31.0	30.5	32.3	32.3	31.4	31.5	33.5	32.0	31.3	31.5	31.3	30.8	32.0	31.8	31.7	32.7
Fe_2O_3	0.23	1.35	0.18	0.20	0.12	0.11	0.23	0.22	0.10	0.13	0.25	0.23	0.13	0.17	0.15	0.16	0.02	0.15
MgO	0.01	0.44	0.00	0.00	0.01	0.00	0.01	0.02	0.00	0.00	0.00	0.00	0.01	0.00	0.00	0.00	0.01	0.01
CaO	12.8	12.8	14.2	13.5	15.5	15.6	14.7	14.8	16.6	15.0	14.8	14.5	13.8	13.6	14.8	14.7	14.9	15.4
Na_2O	4.10	3.63	3.46	3.67	2.89	2.94	3.02	3.18	1.92	2.94	2.89	3.17	3.29	3.70	3.04	3.00	3.04	2.71
K_2O	0.04	0.03	0.05	0.07	0.01	0.03	0.04	0.04	0.00	0.01	0.06	0.08	0.38	0.39	0.02	0.01	0.07	0.03
Total	99.30	99.10	99.45	99.16	100.02	100.16	98.95	99.33	99.15	99.33	99.44	99.34	100.35	100.62	98.25	98.40	98.95	99.58
Si	2.379	2.320	2.315	2.345	2.247	2.247	2.284	2.280	2.177	2.263	2.293	2.285	2.330	2.349	2.245	2.257	2.268	2.229
Al^{IV}	1.614	1.644	1.674	1.648	1.740	1.737	1.703	1.704	1.822	1.733	1.693	1.706	1.673	1.640	1.751	1.740	1.725	1.771
Al^{VI}	0.000	0.000	0.000	0.000	0.000	0.000	0.000	0.000	0.000	0.000	0.000	0.000	0.000	0.000	0.000	0.000	0.000	0.000
Fe^{3+}	0.008	0.047	0.006	0.007	0.004	0.004	0.008	0.008	0.003	0.004	0.009	0.008	0.004	0.006	0.005	0.006	0.001	0.005
Mg	0.001	0.030	0.000	0.000	0.001	0.000	0.000	0.001	0.000	0.000	0.000	0.000	0.001	0.000	0.000	0.000	0.001	0.001
Ca	0.625	0.631	0.695	0.663	0.759	0.761	0.728	0.728	0.821	0.737	0.724	0.715	0.668	0.659	0.736	0.731	0.737	0.755
Na	0.363	0.323	0.307	0.326	0.256	0.260	0.270	0.283	0.172	0.261	0.256	0.282	0.289	0.324	0.274	0.270	0.272	0.241
K	0.002	0.002	0.003	0.004	0.001	0.002	0.002	0.002	0.000	0.000	0.004	0.005	0.022	0.022	0.001	0.001	0.004	0.002
Ab	36.6	33.8	30.5	32.8	25.2	25.5	27.0	27.9	17.4	26.2	26.1	28.2	29.5	32.2	27.1	26.9	26.8	24.1
An	63.1	66.0	69.2	66.8	74.7	74.4	72.8	71.8	82.6	73.8	73.6	71.4	68.3	65.6	72.8	73.0	72.8	75.7
Or	0.2	0.2	0.3	0.4	0.1	0.2	0.2	0.2	0.0	0.0	0.4	0.5	2.2	2.2	0.1	0.1	0.4	0.2

Structural formula based on 5 cations.

Table 4: Representative major-element compositions of amphiboles from wehrlites, plg-wehrlites, troctolite, ol- and cpx-gabbros and anorthosite. Amphibole names after Leake et al. (1997).

Rock types	wehrlite	plg-wehrlites		troctolite		ol-gabbros					cpx-gabbros			anorthosite
Sample numbers	MP243	FB1095		MP240		MP125		MP136	MP166		MP168	MP192		MP285
SiO_2	42.5	43.3	43.1	43.1	44.6	42.4	42.6	51.0	41.9	42.6	42.9	43.3	42.5	46.3
TiO_2	1.80	0.03	2.13	1.44	1.09	0.02	0.15	0.61	2.33	2.42	3.68	2.37	3.53	1.58
Al_2O_3	13.8	16.0	13.3	14.5	13.3	17.1	15.8	5.9	13.6	12.8	12.0	13.2	12.8	10.9
Cr_2O_3	0.15	0.00	0.09	0.17	0.13	0.03	0.09	0.26	0.10	0.11	0.27	0.12	0.18	0.07
Fe_2O_3	1.3	6.5	3.2	4.5	4.0	6.8	8.4	3.1	3.7	4.5	2.1	2.5	1.9	2.6
FeO	7.2	1.5	4.5	2.9	3.7	1.8	0.7	6.3	6.3	5.8	7.8	6.5	6.8	7.5
MnO	0.06	0.19	0.14	0.05	0.16	0.10	0.14	0.19	0.06	0.13	0.09	0.10	0.11	0.21
MgO	15.4	15.7	16.1	16.1	16.0	15.0	15.6	17.0	14.3	14.5	14.3	14.7	14.7	14.3
CaO	11.9	11.8	12.2	12.2	12.1	12.2	11.9	12.7	12.0	11.8	12.0	11.9	11.9	12.0
Na_2O	2.50	2.55	2.46	2.31	2.19	2.27	2.30	0.67	1.86	1.88	1.76	2.30	2.05	1.06
K_2O	n.d.	0.66	0.92	0.58	0.50	0.37	0.58	0.10	1.21	1.11	1.16	0.77	1.03	0.74
OH	2.01	2.12	2.09	2.10	2.11	2.62	2.51	2.12	2.06	2.07	2.07	2.08	2.07	2.08
Total	99.5	100.5	100.2	99.9	99.8	100.7	100.8	100.1	99.4	99.7	100.1	99.88	99.5	99.2
Si	6.338	6.114	6.173	6.148	6.355	6.016	6.038	7.226	6.112	6.187	6.226	6.250	6.176	6.685
Al^{IV}	1.662	1.886	1.827	1.852	1.645	1.984	1.962	0.774	1.888	1.813	1.774	1.750	1.824	1.315
Al^{VI}	0.756	0.786	0.426	0.579	0.584	0.868	0.680	0.218	0.455	0.382	0.280	0.497	0.370	0.534
Ti	0.202	0.003	0.229	0.154	0.117	0.002	0.016	0.065	0.256	0.264	0.402	0.257	0.385	0.172
Cr	0.018	0.000	0.010	0.019	0.015	0.004	0.011	0.029	0.012	0.013	0.032	0.014	0.020	0.008
Fe^{3+}	1.051	0.696	0.350	0.487	0.433	0.727	0.897	0.332	0.404	0.490	0.227	0.267	0.207	0.282
Fe^{2+}	0.000	0.178	0.538	0.344	0.437	0.210	0.082	0.742	0.765	0.705	0.944	0.784	0.820	0.905
Mn	0.008	0.022	0.017	0.006	0.019	0.012	0.016	0.023	0.007	0.016	0.011	0.012	0.014	0.026
Mg	3.426	3.315	3.430	3.410	3.395	3.177	3.298	3.592	3.101	3.129	3.104	3.171	3.184	3.073
Ca	1.897	1.790	1.866	1.857	1.842	1.846	1.804	1.932	1.877	1.832	1.861	1.837	1.845	1.857
Na	0.722	0.699	0.684	0.638	0.605	0.624	0.630	0.183	0.526	0.529	0.494	0.643	0.576	0.297
K	n.d.	0.119	0.168	0.105	0.091	0.066	0.104	0.018	0.225	0.206	0.215	0.142	0.191	0.136
OH*	2	2	2	2	2	2	2	2	2	2	2	2	2	2
Total cations	16.08	15.61	15.72	15.60	15.54	15.54	15.54	15.13	15.63	15.57	15.57	15.62	15.61	15.29
Amphibole names	magnesio-hastingsitic-hornblende	pargasite	pargasite	pargasite	pargasitic hornblende	pargasite	magnesio-hastingsite	magnesio-hastingsite	titanian-pargasite	titanian-magnesio-hastingsite	titanian pargasite	titanian pargasite	titanian pargasite	magnesio-hornblende

Structural formula based on 23 oxygens.

2.4.3. Troctolites

Troctolites are medium-grained ortho- to mesocumulates, consisting of anhedral olivine (35 vol%; Fo = 78.7 - 79.4) and variable sized laths of bytownitic plagioclase (65 vol%, An_{74}, Fig. 12). Plagioclase crystallizes as euhedral tabular grain underlying the cumulative texture of the rock. Clinopyroxene is scarce and frequently absent at the thin section scale (< 3 %). It is diopsidic (mean of 9 analyses: $En_{45.5}Fs_{6.5}Wo_{48}$, Fig. 11); the CaO content increases systematically from core (>21.6 wt%) to rim (max. 23.3 wt%). Al_2O_3 ranges from 3.2 to 3.5 wt%, but does not present coherent variations between core and rim. Na_2O remains constant close to 0.3 wt%. Rare magnesio-hornblende fills the interstices between plagioclases (Fig. 13). Accessory oxides are extremely rare and fill the interstices between plagioclase grains.

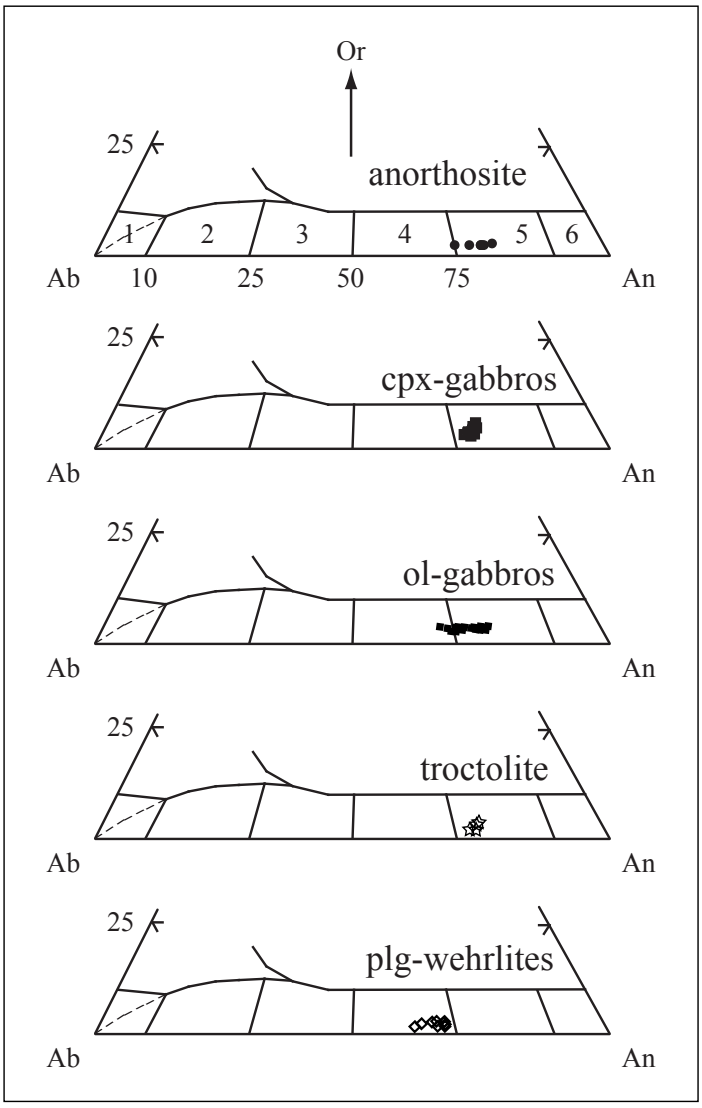

Fig. 12: Compositions of plagioclase from plagioclase-wehrlite, troctolite, olivine- and clinopyroxene gabbros, anorthosite. Compositional fields after Smith and Brown (1988).
1: albite, 2: oligoclase, 3: andesite, 4: labradorite, 5: bytownite, , 6: anorthite.

2.4.4. Olivine gabbros (= ol-gabbros)

Olivine gabbros display ortho- to mesocumulate textures. Modal proportions of cumulus phases are slightly variable and plagioclase is generally dominant. Olivine is anhedral and displays a more homogeneous composition (Fo = 76.4 - 79.4) than in plagioclase-wehrlites, but similar Ni contents. MnO is rather constant with mean concentrations close to 0.3 wt%. Diopside crystallizes as euhedral to anhedral grains of variable size (Fig. 11), indicating an early-stage magmatic crystallization. Mg# ranges from 84 to 89 and remains rather constant between core and rim. CaO content shows limited variations (22.0 < CaO < 23.4). Clinopyroxene is characterized by a wide range in Al content, which is rather low (1.2 < Al_2O_3 < 3.5 wt%). Na_2O (0.21 to 0.49 wt%) is positively correlated with Al_2O_3 as does TiO_2. Plagioclase is tabular and preferentially oriented in the layering plane. It is chemically zoned (Fig. 12) with bytownitic cores (up to $An_{82.6}$) and labradoritic rims ($An_{65.6}$). Magmatic amphibole occurs as interstitial phase between plagioclase and / or clinopyroxene or patches riming clinopyroxene. Its distribution is not spatially uniform at the scale of a thin section. It displays three main compositions: Ti-rich pargasite, magnesio-hastingsite and magnesio-hornblende (Fig. 13). The Al^{VI} content is anti-correlated with Ti. Their Mg# is the highest observed in all Mont Collon basic rocks. Actinolitic hornblende, actinolite and tremolite appear as spatially limited retromorphic products of magmatic amphibole during Alpine greenschist metamorphism. Ilmenite is rare and magnetite represents the most common non-silicate mineral present in this rock facies.

2.4.5. Clinopyroxene gabbros (= cpx-gabbros)

Olivine-free **clinopyroxene gabbros** are essentially composed of cumulitic clinopyroxene and plagioclase in equal proportions. They contain variable amounts of Ti-rich magmatic amphibole as intercumulus phase (up to 8 %). Both plagioclase and clinopyroxene crystallized as euhedral grain, showing preferred orientation. Clinopyroxene composition plots in the diopside field (Fig. 11). It is characterized by low Al_2O_3 (< 3.1 wt%) and Na_2O (0.29 to 0.56 wt%) contents. Rims are generally depleted in Al_2O_3 and TiO_2 with respect to the cores. Clinopyroxene displays relatively constant Mg# close to 85. Compositional features are very similar to those of clinopyroxene crystallizing in the other rock types. Plagioclase crystallizes as equigranular crystals and exhibits commonly bytownitic composition (Fig. 12). Plagioclase (An_{73}) is commonly unzoned. Magmatic amphibole is a Ti-rich pargasite (Fig. 13), surrounding clinopyroxene and/or oxides. Its Mg# is the lowest among magmatic amphiboles in the massif. Extremely rare oxides are closely associated with amphiboles.

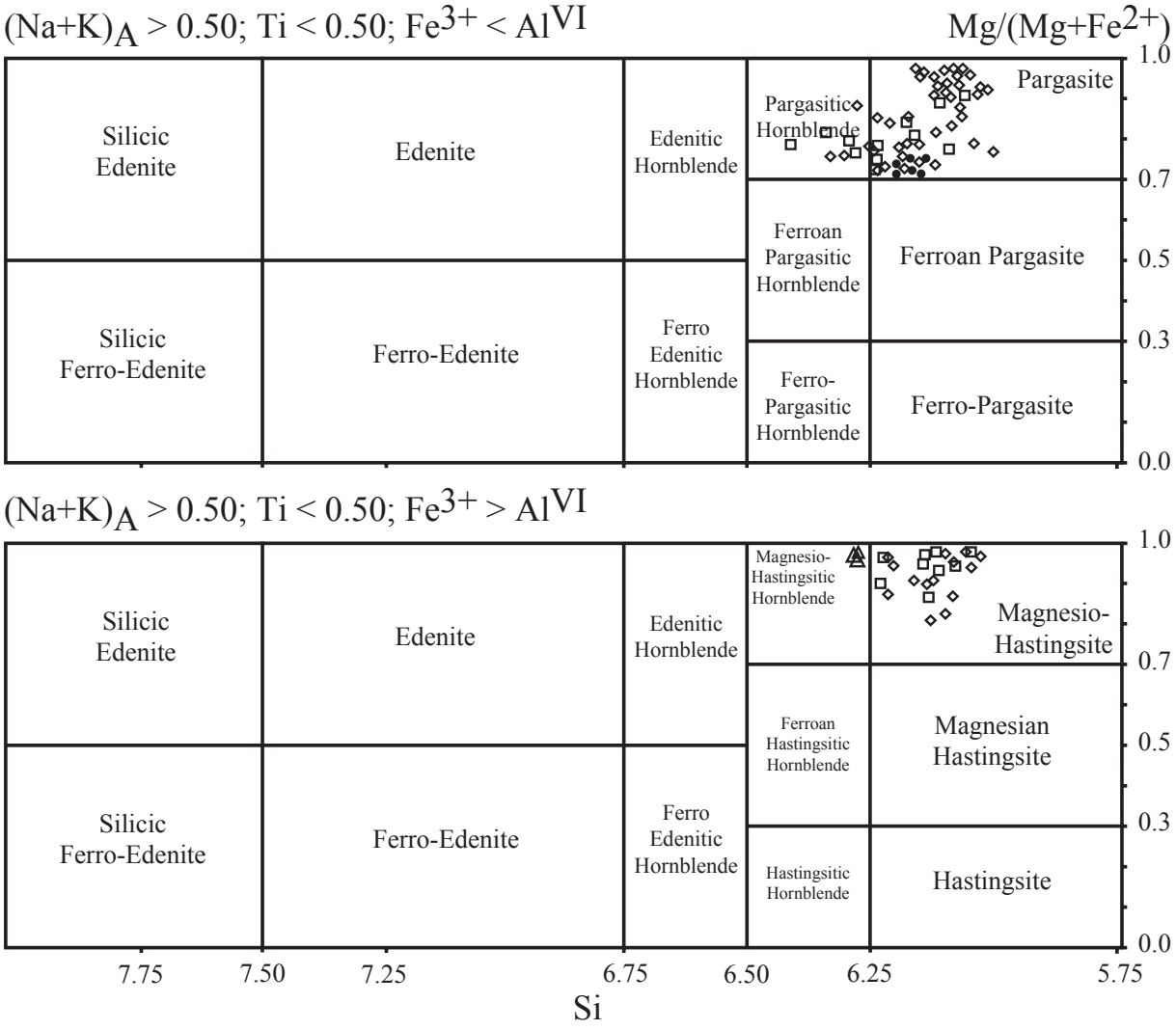

Fig. 13: Compositions of amphibole of cumulative rocks. Nomenclature of calcic amphiboles $(Ca+Na)_B > 1.34$; $Na_B < 0.67$) according to Leake et al. (1997).

2.4.6. Anorthosite

The unique anorthositic layer observed in the Dents de Bertol area is essentially constituted of tabular grains of unzoned bytownitic plagioclase (Fig. 12) without preferential orientation; although a weak fabric is visible at the outcrop scale. There is also a small amount of clinopyroxene (4 –5 vol.-%) and amphibole (< 1 vol.-%). Rare clinopyroxene displays diopsidic composition (Fig. 11) similar to that of other rocks and amphibole is commonly a magnesio-hornblende (Fig. 13) with relatively high TiO_2 content (up to 1.58 wt%).

2.4.7. Pegmatitic gabbros

The pegmatitic gabbros have rather preserved magmatic assemblages, although their magmatic texture are still preserved. They are partly recrystallized under greenschist facies conditions. This metamorphic overprint is explained by the sampling location, which is in an outermost position (i.e. at the base of the Mont Collon), more affected by Alpine greenschist metamorphism, whereas the cumulates crop out in the innermost well-preserved part of the complex (i.e. the Dents de Bertol). They consist of large crystals (up to several cm long) of plagioclase, which are mainly completely recrystallized as albite (Ab_{98}). A primary magmatic amphibole is replaced by a pale green polycrystalline secondary amphibole (actinolite). Fe-oxides are scarce and represent less than 1 vol-%.

2.5. The leucocratic dikes and the Arolla orthogneisses

The leucocratic rocks crop out as centimeter- to decimeter thick dikes. Four types of dikes can be distinguished on the basis of their mineralogy: (i) K-feldspar-quartz pegmatites, (ii) K-feldspar-quartz aplites, (iii) microgranodiorites, and (iv) anorthositic dikes. The other leucocratic rocks exposed in the Mont Collon area are the surrounding Arolla orthogneisses. Feldspar and amphibole compositions are given in Tables 5 and 6, respectively.

2.5.1. Aplites

Aplites are fine-grained dikes essentially composed of K-feldspar and quartz. These dikes are mostly deformed and crystals show intracrystalline deformation. Feldspar is seldom preserved and replaced by sericite. Preserved crystals display orthoclase composition (Or_{90-97}, Fig. 14). Na_2O varies from 0.29 to 0.95 wt%. Feldspars are characterized by low major-element variations between the core and the rim ($63 < SiO_2 < 64$ wt%, Al_2O_3 close to 18.2 wt%). Epidote is common, whereas white mica (muscovite), pyrite and Fe oxides are rare.

2.5.2. Quartz-rich pegmatites

The quartz-rich pegmatites differ from the aplite by the large size and anhedral shape of the crystals. The acid pegmatites consist of large K-feldspar and quartz (up to 5 centimeter-sized). As aplitic dikes, the K-feldspar exhibits orthoclase (Or_{96}, Fig. 14) composition.

2.5.3. Microgranodiorites

The microgranodiorites consist of eu- to subhedral tabular-shaped feldspars, euhedral biotite and xenomorphic quartz. Feldspars show oligoclase ($An_{28}Ab_{72}$) and sanidine ($Ab_{4-15}Or_{85-96}$) compositions (Fig. 14) and crystallize before (or probably contemporaneously) with biotite. Biotite is characterized by low K_2O (8.7-9.3 wt%), relatively high MnO and TiO_2 (up to 5 wt% and 3.7-4.8 wt%, respectively) contents. SiO_2, Al_2O_3, FeO_T exhibit low variations (29-30 wt%, 16.8 wt% and around 26 wt%, respectively). Biotite can be completely recrystallized into chlorite and feldspar replaced by sericite. Textural evidences (e.g. biotite and feldspar included within quartz, xenomorphic shape) show that quartz is the latest crystallizing phase. Quartz occurs occasionally as poikilitic crystals. From the core to the margin of the dikes, modal proportions of quartz increase whereas biotite decreases. Epidote is the most common accessory mineral with apatite. The former is closely related to biotite and the latter is always included within feldspars.

2.5.4. Anorthositic dikes

Plagioclase is the major component of the anorthositic dikes (90 vol-%). Apatite is widespread and represented as inclusions in plagioclase. It is difficult to determine the exact apatite modal proportion. Nevertheless, several percents (up to 5 vol-%) could be a right estimate. Amphibole crystallizes also as interstitial grains (2-5 vol-%), and displays more or less important chlorite recrystallization at its rim.

2.5.5. The Arolla orthogneisses

The common mineral assemblage of the Arolla orthogneisses consists of quartz, plagioclase, phengite, hornblende with brown cores, and minor amounts of chlorite, calcite and epidote (Hunziker, 1974; this study).

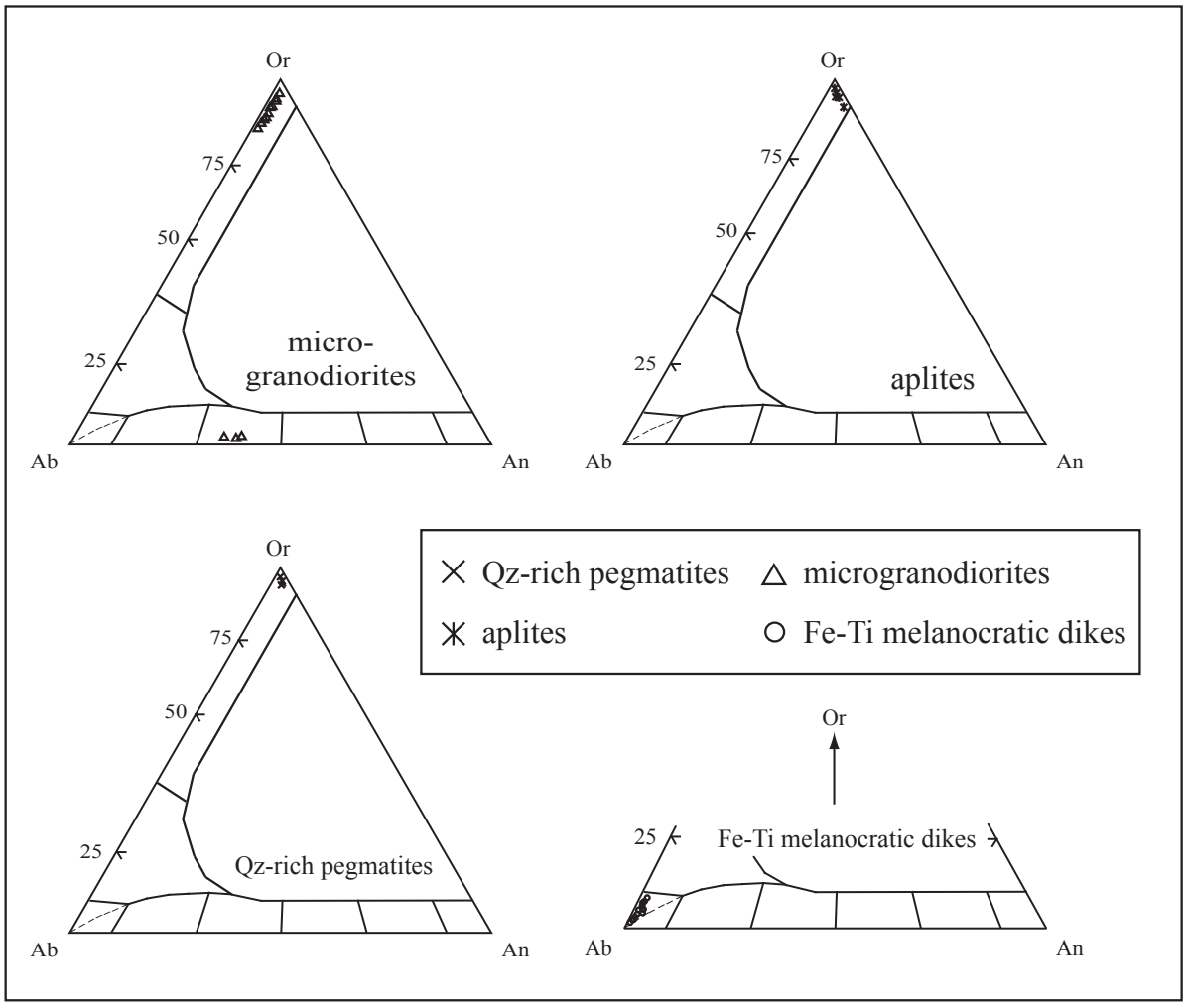

Fig. 14: Compositions of plagioclase from leucocratic and Fe-Ti melanocratic dikes. Compositional fields after Smith and Brown (1988).

Table 5: Representative major-element compositions of k-feldspars from leucocratic dikes exposed in the Mont Collon mafic complex.

Rock types	microgranodiorite			aplite					Qz-pegmatite	
Sample numbers	MP132			MP141					MP2	
SiO_2	61.2	64.4	64.1	64.3	64.4	64.1	63.7	65.1	64.5	64.2
Al_2O_3	24.1	18.2	18.2	18.3	18.1	18.2	18.2	18.4	18.2	18.2
Fe_2O_3	0.06	0.07	0.03	0.00	0.08	0.12	0.00	0.00	0.02	0.04
MgO	0.02	0.01	0.00	0.00	0.00	0.00	0.00	0.01	0.00	0.00
CaO	5.64	0.00	0.00	0.18	0.02	0.01	0.06	0.04	0.04	0.03
Na_2O	8.27	0.43	1.63	0.95	0.36	0.31	0.29	0.34	0.36	0.34
K_2O	0.06	16.07	14.57	15.33	16.29	16.34	16.13	16.59	16.23	16.23
Total	99.38	99.17	98.58	99.03	99.22	99.09	98.43	100.46	99.41	99.09
Si	2.732	2.998	2.993	2.993	3.001	2.994	2.994	2.998	3.001	2.998
Al^{IV}	1.267	1.000	1.003	1.005	0.995	1.002	1.007	0.998	0.998	1.001
Al^{VI}	0.000	0.000	0.000	0.000	0.000	0.000	0.000	0.000	0.000	0.000
Fe^{3+}	0.002	0.003	0.001	0.000	0.003	0.004	0.000	0.000	0.001	0.001
Mg	0.001	0.000	0.000	0.000	0.000	0.000	0.000	0.001	0.000	0.000
Ca	0.270	0.000	0.000	0.009	0.001	0.000	0.003	0.002	0.002	0.001
Na	0.715	0.039	0.148	0.086	0.033	0.028	0.026	0.030	0.032	0.031
K	0.004	0.955	0.868	0.911	0.969	0.974	0.967	0.975	0.962	0.966
Ab	72.3	3.9	14.6	8.5	3.2	2.8	2.6	3.0	3.2	3.1
An	28.0	0.0	0.0	0.9	0.1	0.1	0.3	0.2	0.2	0.1
Or	0.4	96.1	85.4	90.6	96.7	97.2	97.0	96.8	96.6	96.8

Structural formula based on 5 cations.

Table 6: Representative major-element compositions of kaersutites from Fe-Ti melanocratic dikes exposed in the Mont Collon mafic complex. Amphibole names after Leake et al. (1997).

Rock types	Fe-Ti melanocratic dikes												
Sample numbers	MP177							MP249					
SiO_2	38.60	39.81	38.82	38.35	38.53	39.13	38.52	38.39	39.00	39.22	38.68	39.97	40.08
TiO_2	4.99	4.91	5.52	6.79	5.86	5.62	6.08	5.81	6.60	6.76	6.64	6.06	4.61
Al_2O_3	13.49	12.81	13.07	13.46	13.43	13.22	13.33	12.13	13.94	13.67	13.96	12.25	12.61
FeO	17.31	15.20	13.21	12.60	12.83	12.25	11.94	16.82	11.52	10.65	11.65	13.62	14.90
MnO	0.29	0.29	0.22	0.21	0.21	0.20	0.24	0.24	0.20	0.13	0.15	0.20	0.23
MgO	8.40	9.85	10.93	10.87	10.66	11.52	11.35	8.35	11.36	12.21	11.54	10.45	9.80
CaO	11.13	11.13	11.30	11.59	11.15	11.16	11.14	11.97	11.47	11.10	11.21	11.52	10.74
Na_2O	2.90	2.79	2.67	2.56	2.94	2.86	2.78	2.60	2.84	2.79	2.59	2.39	3.26
K_2O	1.17	1.07	1.20	1.17	1.14	1.17	1.12	1.18	1.25	1.08	1.17	0.98	1.11
H_2O*	1.97	1.99	1.98	2.00	1.98	2.00	2.00	1.95	2.02	2.02	2.01	2.00	1.98
Total	100.25	99.88	98.90	99.60	98.75	99.37	99.30	99.44	100.20	99.63	99.60	99.44	99.32
Si	5.87	6.00	5.87	5.76	5.83	5.87	5.79	5.90	5.78	5.81	5.76	6.00	6.06
Al^{IV}	2.13	2.00	2.13	2.24	2.17	2.13	2.21	2.10	2.22	2.19	2.24	2.00	1.94
Al^{VI}	0.29	0.27	0.20	0.14	0.23	0.20	0.15	0.09	0.22	0.20	0.21	0.17	0.31
Ti	0.57	0.56	0.63	0.77	0.67	0.63	0.69	0.67	0.74	0.75	0.74	0.68	0.52
Fe^{2+}	2.20	1.92	1.67	1.58	1.62	1.54	1.50	2.16	1.43	1.32	1.45	1.71	1.89
Mn	0.04	0.04	0.03	0.03	0.03	0.03	0.03	0.03	0.03	0.02	0.02	0.03	0.03
Mg	1.90	2.21	2.46	2.43	2.40	2.57	2.54	1.91	2.51	2.70	2.56	2.34	2.21
Ca	1.81	1.80	1.83	1.86	1.81	1.79	1.79	1.97	1.82	1.76	1.79	1.85	1.74
Na	0.85	0.82	0.78	0.75	0.86	0.83	0.81	0.77	0.82	0.80	0.75	0.70	0.96
K	0.23	0.21	0.23	0.22	0.22	0.22	0.21	0.23	0.24	0.20	0.22	0.19	0.21
OH*	2.00	2.00	2.00	2.00	2.00	2.00	2.00	2.00	2.00	2.00	2.00	2.00	2.00
Total	17.89	17.81	17.84	17.77	17.84	17.82	17.72	17.84	17.79	17.75	17.75	17.67	17.87
Amphibole names	ferro-kaersutite	kaersutite	kaersutite	kaersutite	kaersutite	kaersutite	kaersutite	ferro-kaersutite	kaersutite	kaersutite	kaersutite	kaersutite	kaersutite

Structural formula based on 23 oxygens.

Table 7: Representative major-element compositions of clinopyroxenes from Fe-Ti melanocratic dikes exposed in the Mont Collon mafic complex.

Rock type	Fe-Ti melanocratic dikes													
Sample numbers	MP177				MP244					MP249				
	core	rim	core	rim	core	rim	core	core	rim	core	rim	core	intermediate	rim
SiO_2	51.0	50.9	49.3	49.6	50.1	48.5	50.2	49.7	48.0	50.7	49.1	50.5	49.2	50.1
TiO_2	1.51	1.55	2.09	2.10	1.89	2.17	1.74	1.79	2.66	1.44	2.00	1.58	2.17	1.74
Al_2O_3	3.45	3.67	4.71	4.87	4.12	4.69	3.89	3.98	5.52	3.57	4.92	3.80	5.14	4.13
Cr_2O_3	0.44	0.27	0.04	0.02	0.21	0.03	0.36	0.26	0.02	0.44	0.01	0.20	0.02	0.14
Fe_2O_3	1.0	0.8	1.6	1.0	1.2	2.0	0.7	1.8	2.1	1.2	2.1	1.5	2.0	1.8
FeO	5.4	6.2	6.6	7.2	6.1	5.9	5.5	5.0	5.4	5.3	5.5	5.5	5.9	5.5
MnO	0.11	0.13	0.21	0.19	0.13	0.14	0.15	0.15	0.13	0.14	0.17	0.15	0.19	0.11
MgO	15.0	14.5	13.6	13.4	14.1	13.4	14.3	14.5	12.8	14.9	13.7	14.6	13.4	14.3
CaO	21.8	21.7	20.9	21.1	21.7	21.4	22.0	21.7	21.9	21.4	21.6	21.6	21.5	21.7
Na_2O	0.47	0.52	0.63	0.65	0.52	0.54	0.50	0.51	0.73	0.53	0.61	0.52	0.70	0.55
Total	100.1	100.2	99.7	100.1	100.1	98.9	99.4	99.3	99.3	99.7	99.7	99.9	100.1	100.0
Si	1.880	1.880	1.837	1.843	1.857	1.825	1.869	1.853	1.800	1.878	1.829	1.868	1.824	1.855
Ti	0.042	0.043	0.059	0.059	0.053	0.062	0.049	0.050	0.075	0.040	0.056	0.044	0.061	0.048
Al^{IV}	0.120	0.120	0.163	0.157	0.143	0.175	0.131	0.147	0.200	0.122	0.171	0.132	0.176	0.145
Al^{VI}	0.030	0.040	0.045	0.057	0.037	0.033	0.040	0.028	0.044	0.034	0.044	0.034	0.049	0.035
Cr	0.013	0.008	0.001	0.001	0.006	0.001	0.011	0.008	0.000	0.013	0.000	0.006	0.000	0.004
Fe^{3+}	0.027	0.023	0.045	0.029	0.032	0.058	0.020	0.049	0.059	0.034	0.060	0.042	0.056	0.050
Fe^{2+}	0.167	0.190	0.207	0.222	0.190	0.185	0.172	0.155	0.170	0.163	0.171	0.170	0.181	0.169
Mn^{2+}	0.004	0.004	0.006	0.006	0.004	0.004	0.005	0.005	0.004	0.004	0.005	0.005	0.006	0.004
Mg	0.825	0.797	0.756	0.740	0.777	0.753	0.793	0.802	0.713	0.822	0.758	0.806	0.740	0.790
Ca	0.859	0.858	0.836	0.840	0.863	0.864	0.875	0.866	0.881	0.851	0.860	0.855	0.856	0.859
Na	0.033	0.037	0.046	0.047	0.038	0.040	0.036	0.037	0.053	0.038	0.044	0.037	0.050	0.040
Wo	46.4	46.5	46.5	46.6	47.1	47.9	47.6	47.5	49.9	46.4	48.1	46.7	48.2	47.2
En	44.6	43.2	42.0	41.1	42.5	41.8	43.1	44.0	40.4	44.8	42.4	44.0	41.6	43.4
Fs	9.0	10.3	11.5	12.3	10.4	10.3	9.3	8.5	9.7	8.9	9.5	9.3	10.2	9.3

Structural formula based on 4 cations.

2.6. The Fe-Ti melanocratic dikes

The Fe-Ti melanocratic dikes are mainly composed of amphibole, clinopyroxene and plagioclase associated with apatite and Fe-Ti oxides (magnetite and ilmenite). The grain size of these Fe-Ti rich dikes decreases from the core to the margin. The latter exhibits microcrystalline texture and includes pyroxene and olivine xenocrysts belonging to the cumulate host rocks.

Euhedral amphibole is the main component (55 - 60 vol.-%) and displays a kaersutite composition (Leake et al., 1997; Fig. 15). The kaersutite is Fe- ($10.65 < FeO^* \% < 15.20$), Ti- ($4.85 < TiO_2 < 6.79$ wt%) and alkali-rich ($3.4 < [Na_2O + K_2O] < 4.4$ wt%). Some amphibole grains show higher FeO* (up to 17.31 %) and lower MgO (< 8.5 wt%) contents and thus, can be named ferro-kaersutites. The Fe enrichment is related to the ($Fe^{2+} + Fe^{3+}$) substitution of Mg.

Clinopyroxene crystallizes as euhedral or round-shaped small grain (6 to 8 vol-% modal proportions). Primary compositions plot within the diopside field (Fig. 16, Table 7), although some clinopyroxenes tend toward the salite compositional field. The latter exhibit high Al_2O_3 content (between 6.2 and 7.5 wt%) compared to diopside (3.45-5.52 wt%). The CaO content does not display a regular evolution from core to rim and remain relatively constant (20.9-22-3 wt%). Fe and Ti increase systematically from core to rim and the TiO_2 content reaches 2.66 wt% in the most enriched rim (sample MP244d) with the exception of clinopyroxenes, which tend to the wollastonite field (TiO_2 content up to 3.45 wt%). They display low Na_2O (0.47-0.73 wt%), Cr_2O_3 and MnO contents (lesser than 0.44 wt% and 0.21 wt%, respectively).

Anhedral Na-rich ($Ab_{94.5-95.2}An_{4.5-5.2}Or_{0.1-0.2}$) plagioclase (25-28 vol-%) fills the spaces left between the kaersutite, clinopyroxene and oxides grains, and shows a Na enrichment from core to rim (range between Ab_{90} and Ab_{96}; Fig. 14). This albitic composition is surprising, considering the chemistry of these dikes (see chapter 3), which present ultrabasic characteristics ($SiO_2 <$ 45 wt%). It is noteworthy that Dal Piaz et al. (1977) obtain a range of An_{70-55} for plagioclase of melanocratic dikes from the Matterhorn-Mont Collon massifs and especially, an An_{68} composition for a plagioclase of a melanocratic dike from the Dents de Bertol (sample DBL 605). So, the albitic composition of the plagioclase from the melanocratic dikes sampled for this study is not in agreement with those given by Dal Piaz et al. (1977). They could be related either to the Alpine metamorphic overprint or to deuteric transformations although, other constituent minerals remain remarkably preserved and not affected by secondary reactions. Another explanation can be given for the Na-rich composition of the plagioclase. The FeO/MgO ratios of the melanocratic dikes indicate that they are evolved rocks (FeO/MgO ~ 1.59). Consequently, the plagioclase composition could be related to the differentiated character of these dikes.

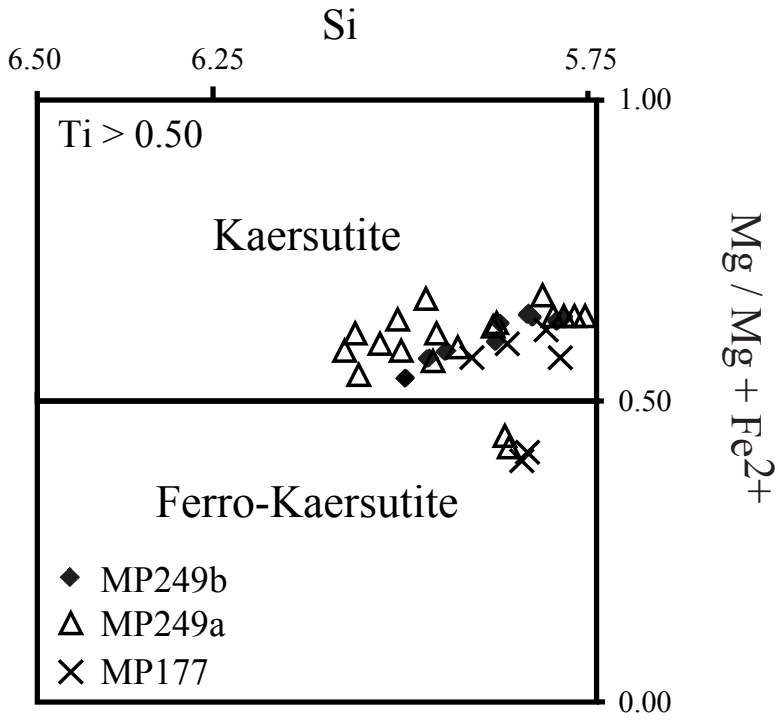

Fig. 15: Compositions of amphiboles of the Fe-Ti melanocratic dikes. Nomenclature according to Leake et al. (1997). MP177, MP249a and b refer to sample numbers.

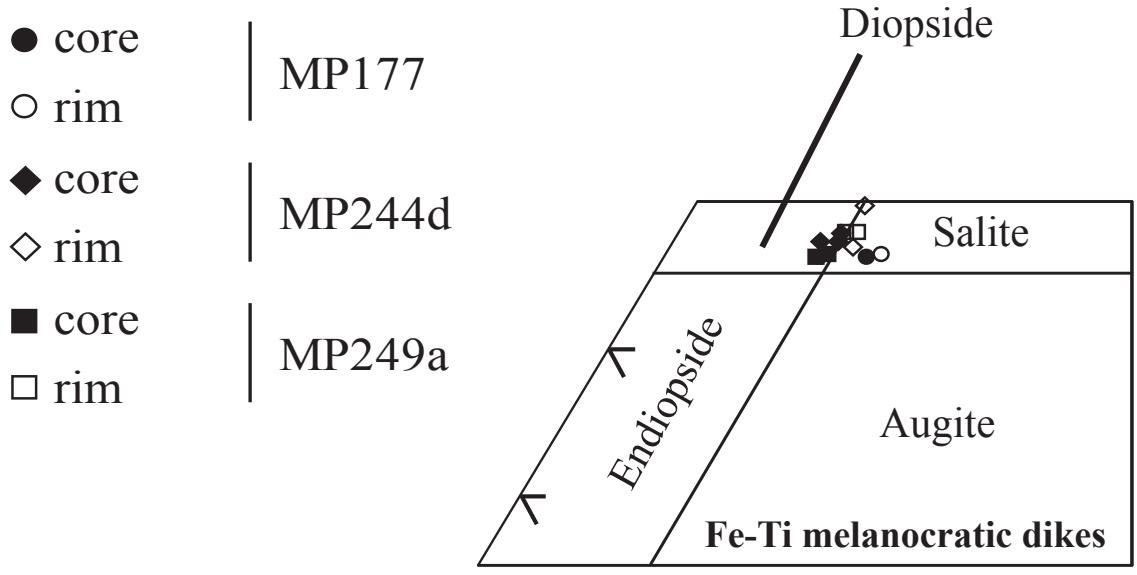

Fig. 16: Ternary diagrams for clinopyroxene from Fe-Ti melanocratic dikes in the $Ca_2Si_2O_6$ (Wo) - $Mg_2Si_2O_6$ (En) - $Fe_2Si_2O_6$ (Fs) system (compositional fields after Morimoto et al., 1988).

Euhedral ilmenite and magnetite represent approximately 3-5 vol-% of the modal proportions and precipitated before albite. They crystallize as euhedral grains, commonly associated with the amphibole or as isolated grain within feldspar.

Needle-shaped apatite (~ 2 vol-%) is included in the albite grains. Titanite, zircon and pyrite are rare at the scale of a thin section. Calcite is common, crystallizing in thin veins. These dikes are also characterized by the presence of miarolitic vesicles. The occurrence of these vesicles and the apatite habitus suggest a rapid cooling at shallow depth.

2.7. Conclusion

Mineral evolution in the cumulitic sequence

The crystallization sequence in the cumulates of the Mont Collon mafic complex is variable. Olivine is the first phase to crystallize, followed either by plagioclase or clinopyroxene (e.g. in troctolites and wehrlites, respectively) depending on the lithologies and probably the location within the magma chamber (i.e. variation in space and time of parameters such as PH_2O, fO_2, magma replenishment). Ilmenite and/or magnetite crystallize subsequently, whereas Ti-amphibole is the last phase to form together with accessory apatite. Mineral compositions are surprisingly homogeneous among the different rock types. The most primitive olivine composition (Fo = 78.7-79.4) is found in the troctolites, but it is barely different in others lithologies (Fo = 74 - 77). The overall plagioclase compositional range is An_{83-63}, not much larger than zoning in individual crystals in olivine-gabbros (An_{83-65}). Clinopyroxene is diopsidic, but shows some weak elemental variations in plagioclase-wehrlites, where less calcic composition (endiopside-augite joint) are locally found in crystal cores. Rims are often slightly more calcic (by 0.1-0.5 wt% CaO) than the core of the crystals. Aluminum exhibits larger variations; the Al_2O_3 content of clinopyroxene ranges from 1 to 5 wt% over the pluton, with up to 1 wt% Al_2O_3 increase (in plagioclase-wehrlites) or decrease (in clinopyroxene-gabbros) between core and rim within a single clinopyroxene crystal and up to 2 wt% within a sample. Small scale variations probably reflect fluctuation in the silica activity of the melt (Deer, Howie and Zussmann, 1992) in the vicinity of crystallizing grains in relation with the nature of surrounding phases. Composition of interstitial amphibole does not vary significantly, except for its Ti content (from 0 to 3.5 wt% TiO_2 over the massif), which is in direct relationship with the presence or absence of ilmenite/magnetite in the sample. The $Mg\#_{cpx}$ and $Mg\#_{ol}$ of cumulates are positively correlated (Fig. 17a), whereas a poorly defined negative correlation is observed between the $Mg\#_{cpx}$ and the mean An content of plagioclase (Fig. 17c). Anorthite content (An) of plagioclase from the Dents de Bertol rocks is distinctly higher than in plg-wehrlites and ol-gabbros collected in the moraine close to the Mont Collon (i.e. MP106, FB1094 and FB1095). In general, there is no systematic evolution in the An content, the $Mg\#_{cpx}$ and the $Mg\#_{ol}$ of cumulates in the Dents de Bertol sequence (Fig. 17b and c).

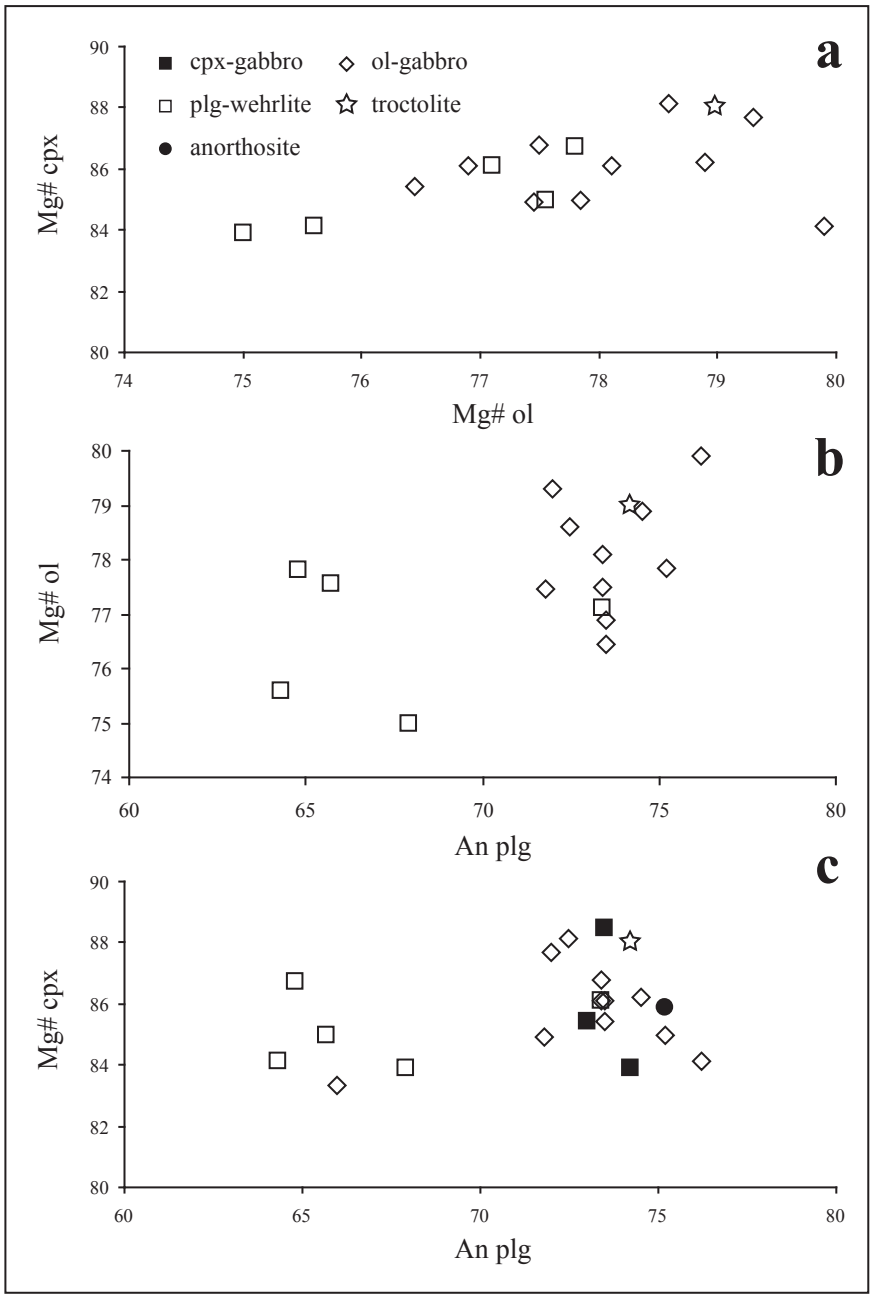

Fig. 17a-c: Variation diagrams using $Mg\#_{cpx}$, $Mg\#_{ol}$ and anorthite content of plagioclase (An_{plg}) of the Mont Collon cumulates.

Leucocratic and Fe-Ti melanocratic dikes

Leucocratic dikes display three main mineral assemblages: (i) K-feldspar and quartz, (ii) plagioclase, K-feldspar, biotite and quartz, and (iii) rather solely plagioclase. Thus, quartz-pegmatites and aplites differ only by their grain sizes. The occurrence of biotite in the microgranodiorites suggests the presence of water which appears to be absent in the other leucocratic dikes. Anorthositic dikes are different from the other leucocratic dikes as they contain only plagioclase, showing that they originated probably from less Si enriched melt than the others.

The Fe-Ti melanocratic dikes are characterized by a contrasted mineralogy, compared to the mafic cumulates and leucocratic dikes. The main feature of the Fe-Ti melanocratic dike is the presence of kaersutite, ilmenite and ± titanite and Na-rich plagioclase. This mineral assemblage is typical of alkaline hydrous melts.

2.8. Thermo-barometric conditions of emplacement of the Mont Collon mafic complex

2.8.1. Introduction

The pressure and temperature conditions of crystallization and/or emplacement of the Mont Collon mafic complex were still unknown, up to the current study. However, these parameters are helpful to discuss the geodynamic setting of this complex. Moreover, accurate pressure and temperature will allow us to calculate specific partition coefficients between clinopyroxene and melt, which will be used in chapter 4 for the modeling of the differentiation process of the Mont Collon mafic cumulates. As the contact with the country rock is tectonic, the Arolla orthogneiss mineralogy does not give any clue.

The geobarometers and geothermometers calibrated and available for basic magmas are scarce in the literature. Published geothermometers (e.g. Lindsey, 1983) need specific mineralogical assemblages, most of the time with both orthopyroxene and clinopyroxene and provide only estimates of the temperature. But, orthopyroxene is absent as a primary phase in most of the Mont Collon cumulates. Nevertheless, some geothermometers are applicable to the basic rocks containing olivine and clinopyroxene, such as the olivine-augite geothermometer of Loucks (1996). The most adapted geobarometer available is the one developed by Nimis and Ulmer (1998) for anhydrous and hydrous basic magmas based on the mineralogical structure of clinopyroxene. However, this geobarometer requires an accurate temperature, considering its sensitivity to this parameter. Temperature on interstitial amphiboles will be also estimated using thermometer B of Holland and Blundy (1994).

2.8.2. Thermo-barometric conditions of emplacement

2.8.2.1 Thermometric calculations

Geothermometric calculations were made on the Mont Collon olivine- and clinopyroxene-bearing rocks. As mentioned above, we have to calculate accurate crystallization temperatures, which, then, will be introduced in the geobarometer of Nimis and Ulmer (1998). We propose to use the thermometer developed by Loucks (1996) based on the Fe-Mg exchanges between coexisting augite and olivine calculated on the basis of the $Kd_{Fe/Mg}^{ol/aug} = (Fe/Mg)_{ol} / (Fe^{2+}/Mg)_{aug}$. This geothermometer can be applied within a wide range of temperatures (800-1250°C) and for mineral assemblages including olivine + augite + plagioclase ± pigeonite or orthopyroxene. Experimental studies described by Loucks (1996) suggest that the calculations are valid up to 1 GPa. The geothermometer is reliable up to 2wt% H_2O in the melt, which covers most of the range of relevant natural olivine-bearing assemblages. Computation for thermal calculations were performed using Wolfran© Mathematica© software (ver. 4) in order to extract the temperature T from the equation proposed by Loucks. The obtained temperatures range from 1070 to 1120 ± 6 °C.

Calculations were then made on interstitial magmatic amphiboles crystallizing in the mafic cumulates using the geothermometer B of Holland and Blundy (1994) based on amphibole/plagioclase compositions. This geothermometer can be applied to silica-undersaturated rocks in the range of 400-1000°C for pressures between 0.1 to 1.5 GPa. It can be applied for a wide range of amphibole compositions using the following parameters: amphibole atom per formula contents for $Na_{(M4)} > 0.03$, $Al^{VI} < 1.8$, $6.0 < Si < 7.7$ and the anorthite content of plagioclase has to lie between 0.1 and 0.9. The calculated temperatures are close to 740 ± 40°C for a pressure of 0.5 GPa. This temperature indicates clearly that the development of these amphiboles took place during igneous conditions of crystallization. However, the obtained temperatures are rather related to cooling conditions. This value must be very close to the solidus temperature of the considering magmatic system at 1GPa, according to experimental work on partial melting of (meta)basalts and gabbros at $P_{H_2O} < P_{tot}$ (Holloway and Burnham, 1972; Springer and Seck, 1997).

2.8.2.2. Barometric calculations

Several geobarometers taking into account the Al content in hornblende (s.l) are available in the literature (Hammarstrom and Zen, 1986, Johnson and Rutherford, 1989, Schmidt, 1992), but none of them are well calibrated for undersaturated rocks. So, we used parameters defined by Nimis (1995) and Nimis and Ulmer (1998) for geobarometric calculations on clinopyroxenes. Firstly, Nimis (1995) developed a barometer based on the volume of cell (V_{cell}) and of the M1-site (V_{M1}) which are negatively correlated for a given pressure (P) corresponding

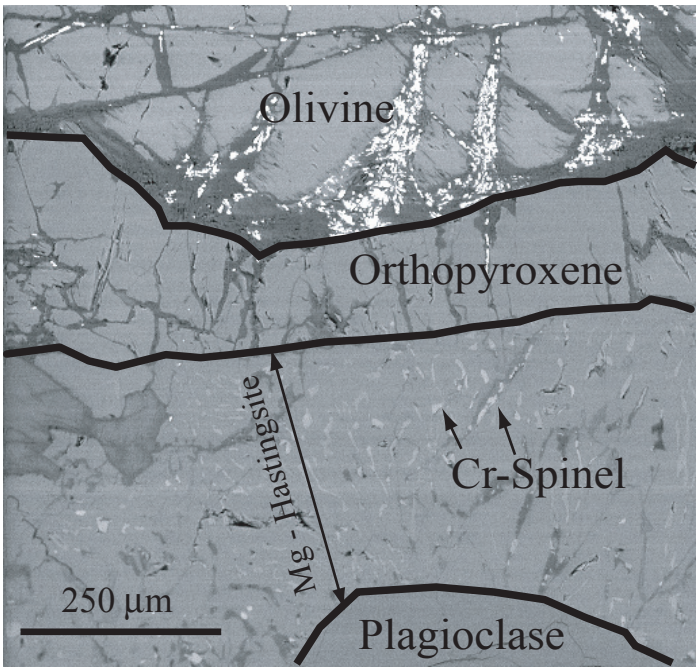

Fig. 18: Backscattered electron image (BSE) of olivine-gabbro coronitic texture (magnification x150). Primary assemblage of olivine-gabbro : olivine + clinopyroxene + plagioclase + spinelle. Corona assemblage: orthopyroxene+amphibole+Cr-spinel.

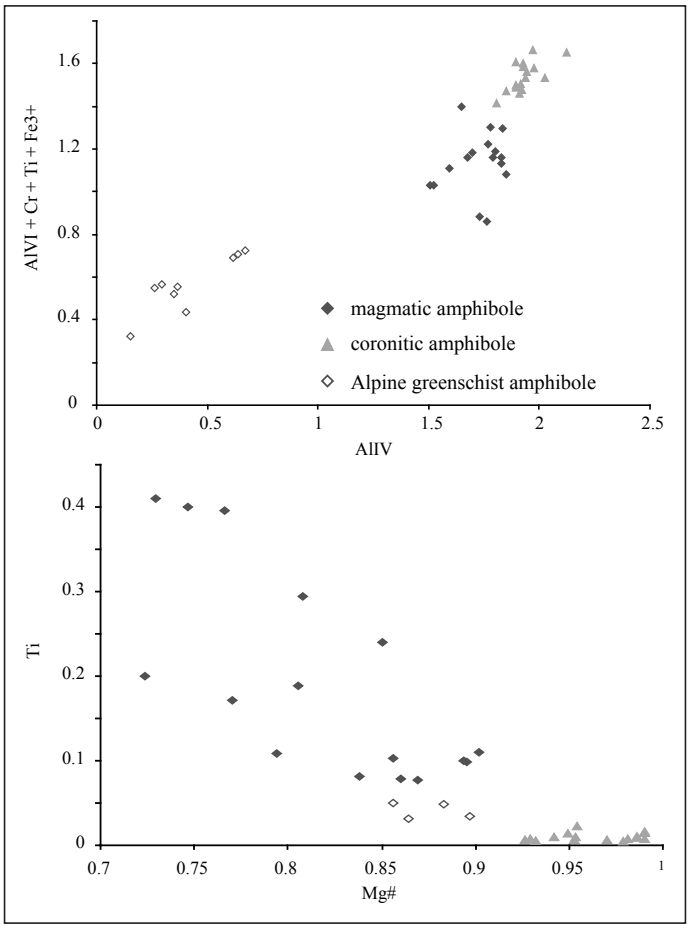

Fig. 19: Variation diagrams for amphibole of selected elements (Al, Ti Cr and Fe^{3+} in atom per formulae). Mg# = molar (Mg / (Fe_T + Mg) x100 ratio.

with the extent of the Tschermak-type substitutions depending on the activities of SiO_2 and CaO. Moreover, both these parameters decrease linearly as P increases. Thus, this barometer is applicable to near-liquidus C2/c clinopyroxene crystallizing from a basaltic anhydrous melt in the absence of garnet. Nimis and Ulmer (1998) expanded a second T-depend barometer for both anhydrous and hydrous melts to obtain corrections for thermal expansivity on unit-cell and M1-site. This geobarometer closely agrees with the pressures calculated by independent methods on the Adamello batholith. Nimis and Ulmer (1998) developed a MS-DOS software to facilitate the barometric calculations «CpxBar» (available at http//dmp.unipd.it). This program excludes clinopyroxene which do not display the calibrated compositions ($Mg\#_{cpx}$ = 0.7-0.9, (Ca + Na) > 0.5 and basaltic melt with Al_2O_3 = 18%). The Nimis and Ulmer (1998) geobarometer needs accurate temperatures with an error lower than 20°C. Reporting the calculated temperatures into the Nimis and Ulmer (1998) clinopyroxene geobarometer yields pressures ranging from 0.3 to 0.6 ± 0.17 GPa (=1σ).

2.8.3. Coronitic reactions

Coronitic layers occur systematically between olivine and plagioclase in the mafic cumulates. They consist of two or three distinct shells (Fig. 18). The first shell is adjacent to the olivine and is composed of colorless 20-50 μm thick orthopyroxene. The second shell is a corona of amphibole-Cr-spinel of variable width. Amphibole composition ranges from pargasite to magnesio-hastingsite (nomenclature of Leake et al., 1997), while the fine exsolution of Al-Mg spinel exhibits hercynite composition. The third shell consists of spinel-free amphibole with the same composition as in the second shell. The orthopyroxene and the first amphibole layers are optically continuous single crystals. Coronitic and magmatic amphiboles display markedly different major- and trace-element compositions. Coronitic amphiboles display higher Mg# and Al^{VI} and lower Ti, Na, Cr contents and similar Si contents (Fig. 19). Grantham et al. (1993) described coronitic reactions modeled with the software Thermocalc in the Proterozoic olivine melanorite of the Equeefa Suite (Natal Metamorphic Province, South Africa).

The coronitic reaction is as following:

$$2\ Ab + 12\ Fo + 4\ An + 2\ H_2O = 7\ En + 2\ Parg + 2\ Sp$$

The activity of water is supposed to be less than 1.0 and reaction occurs at around 800°C (at 0.7 GPa). Grantham et al. (1993) interpreted this reaction as a partial hydration of the mafic rocks at high temperature and pressure, probably shortly after crystallization. Temperature calculations were also made on the Mont Collon coronitic amphiboles using the geothermometer of Holland and Blundy (1994) based on amphibole-plagioclase pair.

The calculated temperatures of 700 ± 40°C are close to those calculated for magmatic amphiboles (740 ± 40°C, see section 3.2.1). Thus, this temperature confirms that coronitic reactions occurred at subsolidus conditions. Similar coronas have been described in many gabbroic intrusions (Grieve and Gittins, 1975; Claeson, 1998 and ref. therein) and are also interpreted as subsolidus reaction products, which developed during deep-seated slow cooling. The undeformed nature of the Mont Collon gabbro suggests that there is no need for a metamorphic overprint to trigger the development of coronas.

2.8.4. Concluding remarks

The temperature and pressure (mean values: 1100°C and 0.45 GPa) show conditions of emplacement in the middle crust. This temperature is consistent with a cotectic precipitation of the mineralogical assemblage ol+plg+cpx from a basaltic magma containing some water (Green and Ringwood, 1967). This low pressure of intrusion is also compatible with (i) the absence of orthopyroxene, (ii) the widespread presence of olivine and plagioclase, (iii) the Na contents of clinopyroxene and (iv) the relatively high An content of plagioclase.

Comparison with some other mafic intrusions ascribed to the post-collisional extension of the Variscan belt at the Carboniferous-Permian boundary illustrates that mafic magmas emplaced at the mantle/crust boundary and at different crustal levels (Fig. 20). P/T intrusion conditions of the Val Malenco (Müntener et al., 2000) and gabbros of the Ivrea-Verbano zone (Maronni et al., 1998) based on primary mineralogical assemblages reflect deeper emplacement depths for these Permian Mafic Complexes (PMC) than the Mont Collon mafic complex, i.e. at the crust-mantle boundary. Despite any accurate calculations on the gabbros, Tribuzio et al. (1999) proposed a similar level of emplacement for the Sondalo gabbroic complex to that of the Mont Collon complex, i.e. the middle crust, based on the P/T conditions deduced from the minerals assemblages of the surrounding rocks.

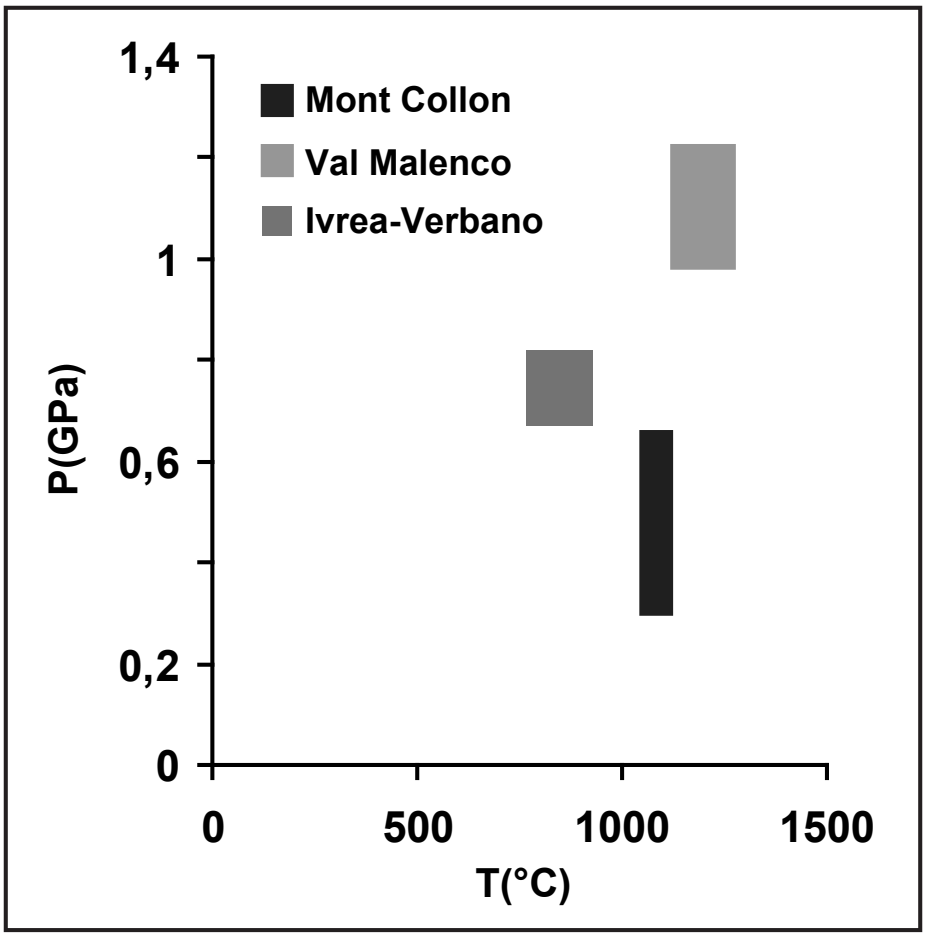

Fig. 20: Comparison of the calculated P/T conditions of emplacement of the Mont Collon mafic complex (this study), the Braccia gabbro (Val Malenco, Hermann et al., 1997) and the Ivrea-Verbano zone (Marroni et al., 1998).

Chapter 3: Modeling of in situ crystallization processes in the Permian mafic layered intrusion of Mont Collon

Chapter 3: Modeling of in situ crystallization processes in the Permian mafic layered intrusion of Mont Collon

3.1. Introduction

Large parts of the Variscan belt have been involved in the Alpine orogeny and some of them underwent high-grade metamorphic recrystallization (granulite, eclogite and/or Alpine greenschist overprints) and deformations (Variscan and/or Alpine). In contrast, the Mont Collon mafic complex displays remarkably well-preserved magmatic structures and mineral assemblages (especially in the Dents de Bertol area), which allow detailed investigation and modeling of crystallization processes in an intra-continental mafic magma chamber.

This chapter focuses on the whole-rock and mineral (clinopyroxene, plagioclase and amphibole) major- and trace-element geochemistry of mafic cumulates. Monotonous major-element compositions throughout the Mont Collon mafic intrusion coupled to highly variable trace-element distribution are better explained by an *in situ* crystallization model (Langmuir, 1989) than by a classical fractional crystallization process. Interstitial residual liquid is involved during crystallization of mafic cumulates and the relative proportion of interstitial residual liquid can be computed by modeling the mineral trace-element contents. Interstitial melt tends to re-equilibrate with early cumulus minerals (clinopyroxene, plagioclase). Such re-equilibration leads to enrichments in incompatible trace elements in these phases. So, this enrichment could be erroneously interpreted as the effects of magmatic differentiation, rather than the involvement of interstitial liquid.

Modeling indicates a transitional MORB-type affinity for the Mont Collon cumulate melt, showing that transitional MORB are not restricted to oceanic context, but can occur in intra-continental settings.

3.2. Whole-rock major- and minor-element chemistry

Chemical data are reported in Tables 8a-c and 8a-d. Major- and trace-element distributions are illustrated in figures 22 to 29 as well as in figure 30 for the specific chemical evolution of the Dents de Bertol cumulative sequence. Iron is recalculated as total iron (FeO^*) following the recommendations of Irvine and Baragar (1971). CIPW norm calculation has been restricted to unmetamorphosed samples, as it is very sensitive to potentially mobile elements (e.g. Na) during metamorphism or alteration processes. Rocks are olivine and hypersthene normative and plot in the olivine tholeiite field (Ol-Hy-Di triangle; Fig. 21) of Ne-Di-Ol-Hy-Q diagram Thompson (1984).

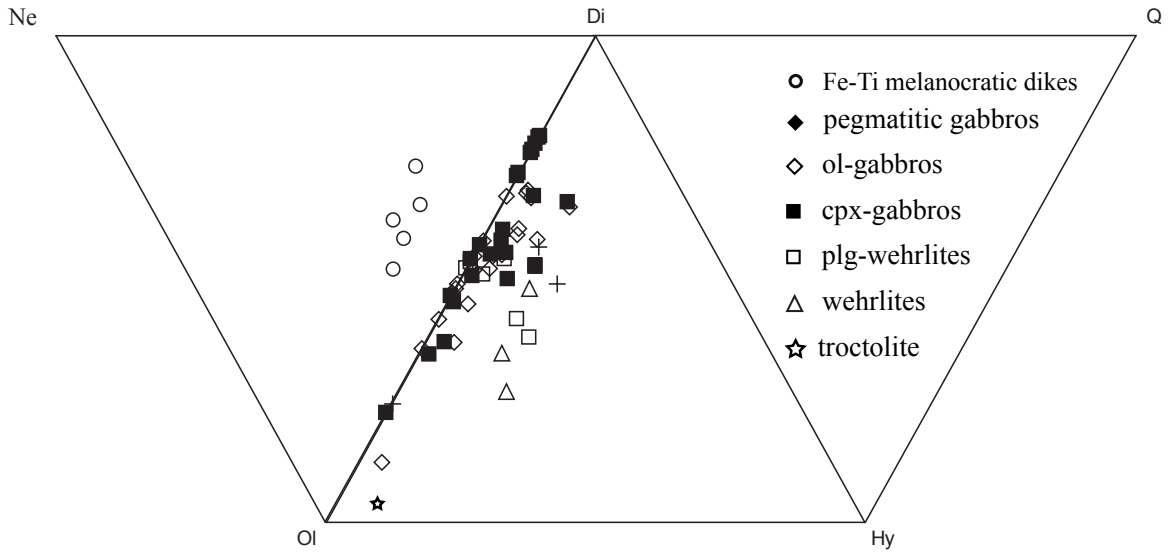

Fig. 21: Classification of the Mont Collon mafic cumulates and Fe-Ti melanocratic dikes based on their CIPW normative compositions expressed as Ne-Ol-Di, Ol-Di-Hy and Di-Hy-Q (after Thompson, 1984).

The Mg# (molar Mg / (Mg+Fe_T) x 100 ratio) shows remarkably small variation (73-80) over the whole rock suite (Fig. 30), pointing to concomitant decrease of FeO^* and MgO (see the good correlation in the MgO vs. FeO^* diagram of Fig. 22b).

The major elements plotted against MgO reveal two distinct groups of rocks (Fig. 22a-c): ultramafic cumulates, i.e. wehrlites and plagioclase-bearing wehrlites, with MgO contents ranging between 13 and 27 wt% on the one hand and mafic cumulates, i.e. olivine- and clinopyroxene-bearing gabbros, with lower MgO contents (5-13 wt%), on the other hand. Compositional fields of olivine and clinopyroxene gabbros generally overlap without significant chemical differences. The olivine- and clinopyroxene-gabbros display similar and large variations in Al_2O_3 (14.2 - 23.1 wt%, 12.6 - 23.6 wt%, respectively) and SiO_2 (43.8 - 47.6 wt%, 43.8 - 49.4 wt%, respectively). Clinopyroxene-gabbros are generally higher in K_2O (up to 0.63 wt%) than all other rock types. Plagioclase-wehrlites have weak variations in Al_2O_3 (10.6-12.2 wt%). P_2O_5 and TiO_2 do not show well-defined correlations with MgO. TiO_2 generally increases with decreasing MgO in plg-wehrlites, and scatter in the other cumulitic facies. MnO stays relatively constant (0.14-0.17 wt%) in wehrlites and plagioclase-wehrlites, then tend to decrease from 0.14 wt% to 0.06 wt% in olivine- and clinopyroxene-bearing gabbros.

The anorthosite displays the highest content in Al_2O_3 (28.5 wt%) and Na_2O (2.30 wt%) and the lowest one in TiO_2 (0.11 wt%), FeO^* (2.1 wt%), MnO and P_2O_5 (0.02-0.03 wt%), both close to the detection limits (0.01 wt%). These compositional features are in good agreement with the mineralogy of anorthosite, dominated by plagioclase accumulation.

The whole-rock chemistry of pegmatitic gabbros does not largely differ from that of olivine- and clinopyroxene-gabbros. They display similar FeO^* and Al_2O_3 contents, are enriched in TiO_2, Na_2O and K_2O and depleted in CaO, compared to the olivine and clinopyroxene gabbros. Off-trend values for Na, K and Ca might partly result from remobilization during greenschist facies recrystallization.

The whole-rock MgO content basically reflects the cumulus character of the various rocks (i.e. the modal abundances of cumulus olivine and/or clinopyroxene) and cannot be used as a differentiation index in the interpretation of figure 22 diagrams, as it would be for volcanic rocks. The same is true for Al_2O_3, CaO and Na_2O, whose concentrations are strongly related to the plagioclase modal proportions in these rocks. This is well illustrated by a clear negative correlation between MgO and Al_2O_3 contents, which results from the complementary proportions of clinopyroxene (Mg tank) and plagioclase (Al tank) in the cumulitic rocks.

As mentioned in chapter 2 (section 2.7), MgO cannot be used as a differentiation index for cumulitic rocks. Alternatively, the mg-number (Mg#) of cumulus minerals should reflect the degree of differentiation of the melt from which they crystallized. Mg# of the clinopyroxene ($Mg\#_{cpx}$; Fig. 17a) shows a relatively good correlation with that of olivine ($Mg\#_{ol}$) and will tentatively be used as a proxy for the degree of differentiation of the Mont Collon cumulates. $Mg\#_{cpx}$ has been preferred to $Mg\#_{ol}$, as pyroxene is less prone to post-solidus re-equilibration than olivine and because it allows involvement of olivine-free rocks.

First of all, the $Mg\#_{cpx}$ lies within a very narrow range (83-89), as does the whole-rock Mg#, which confirms that the Mont Collon cumulitic rocks record very little magmatic differentiation at all. No significant (if any) trend can be observed when $Mg\#_{cpx}$ is plotted against major elements (e.g. CaO, Al_2O_3 or MgO; Fig. 23), with the possible exception of TiO_2, which tends to increase with increasing differentiation (i.e. decreasing $Mg\#_{cpx}$), as in classical tholeiitic differentiation. Interestingly, analytical points do not plot in the same way as in binary diagrams using MgO as index (Fig. 22a-c). For example, plagioclase wehrlites and wehrlites, which are very high in MgO and would be considered the less evolved rocks if MgO was used as a differentiation index, now plot totally differently, some being on the differentiated side (i.e. low $Mg\#_{cpx}$) of the diagram. This definitely demonstrates that whole-rock MgO is not a proxy for the degree of evolution of the magmatic system.

In general, $Mg\#_{cpx}$ are higher in wehrlites ($Mg\#_{cpx}$ = 88.5-6), troctolite ($Mg\#_{cpx}$ = 88), ol- and cpx-gabbros ($Mg\#_{cpx}$ = 84.9 - 88.5) and anorthosite ($Mg\#_{cpx}$ = 89.5) than in plg-wehrlites (with two exceptions, most samples have $Mg\#_{cpx} \leq 85$; Fig. 17a). Analytical points for major elements plot according to their cumulus mineralogy; e.g. wehrlites and plg-wehrlites plot on the low Al_2O_3, but high FeO or MgO side. This indicates that Fe-Mg mineral phases are dominant in these rock types, conversely, that plagioclase (the only Al-rich phase with c. 30% Al_2O_3) is less abundant (and subsidiary less aluminous; see Fig. 17) than in ol- and cpx-gabbros, whatever the degree of differentiation of the rocks.

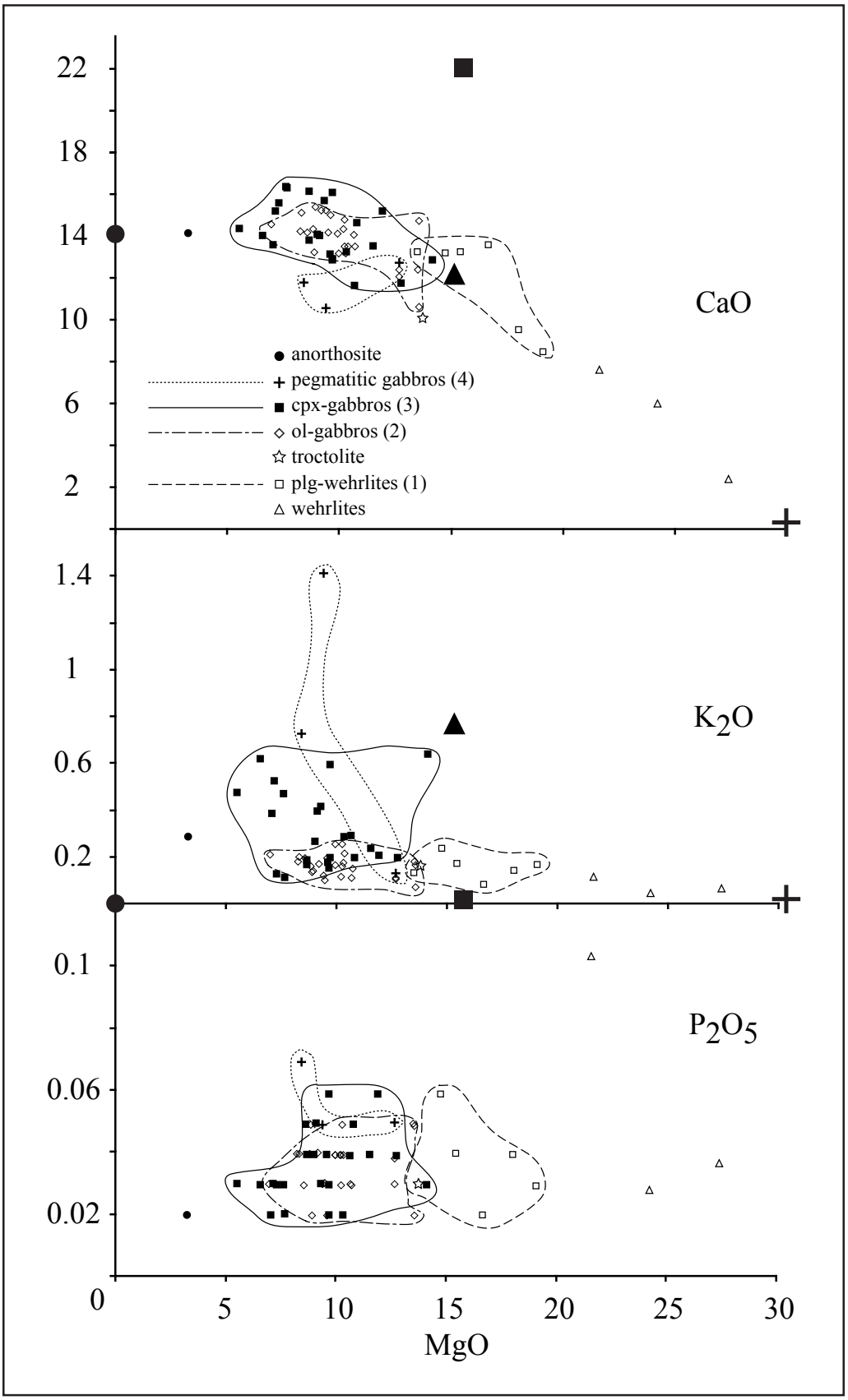

Fig. 22a: Variation diagrams for major elements versus MgO (in wt%) for cumulative rocks of the Mont Collon.

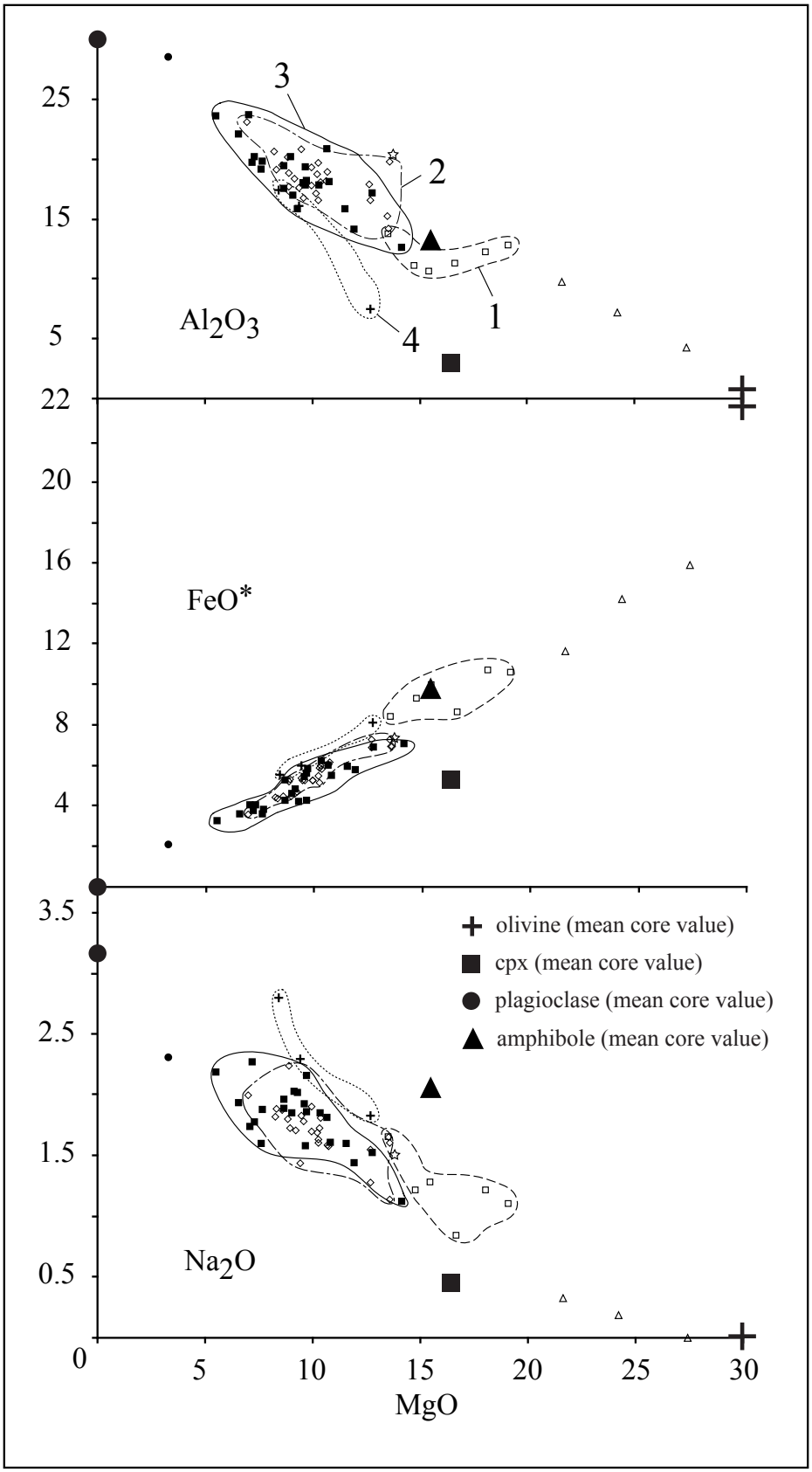

Fig. 22b: Variation diagrams for major elements versus MgO (in wt%) for cumulative rocks of the Mont Collon. Same legend as figure 22a.

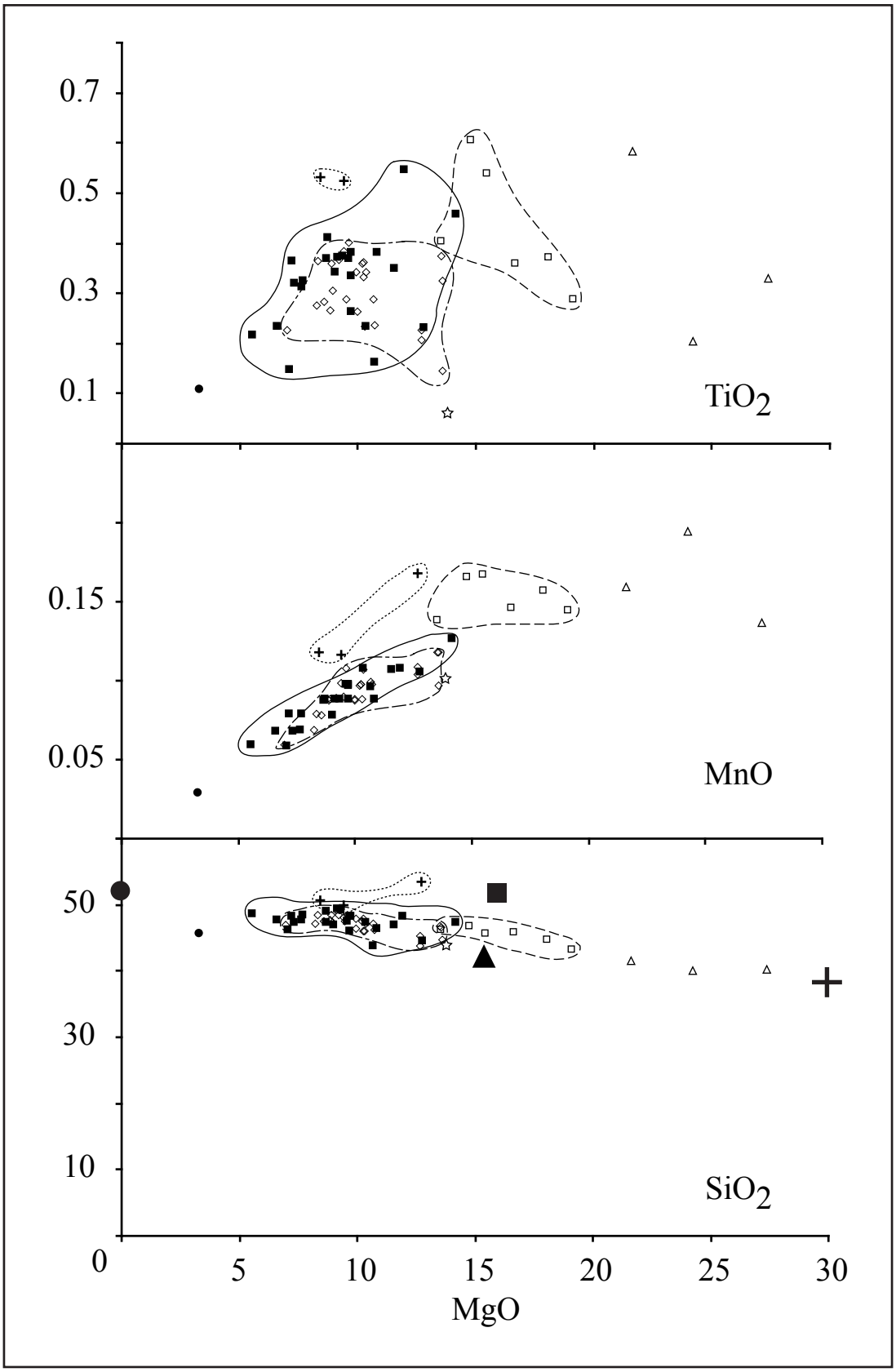

Fig. 22c: Variation diagrams for major elements versus MgO (in wt%) for cumulative rocks of the Mont Collon. Same legend as figure 22a.

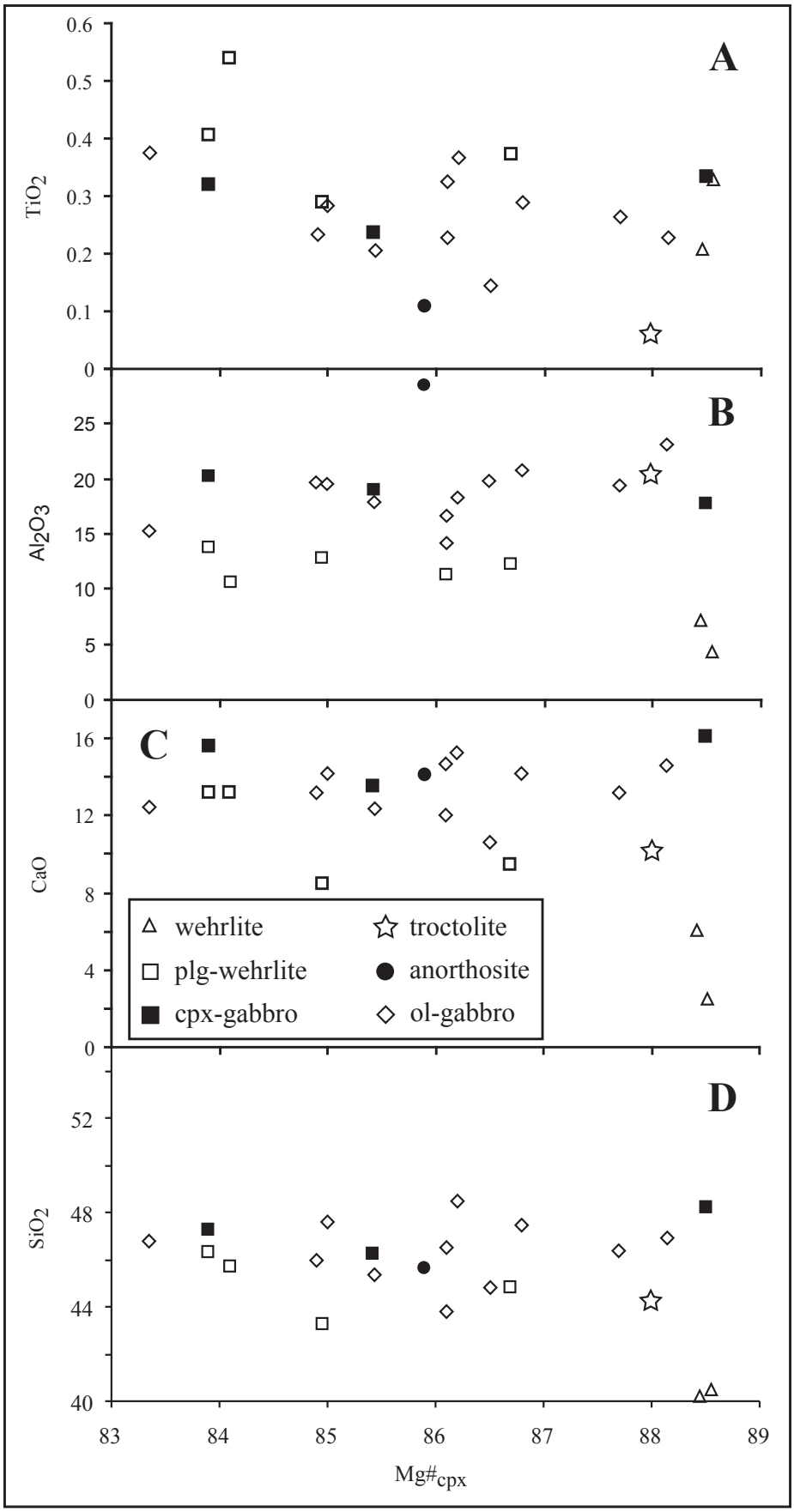

Fig. 23: Variation diagrams for major elements (in wt%) versus $Mg\#_{cpx}$ for cumulative rocks of the Mont Collon.

Table 8a: Representative major-element compositions of whole-rocks (wehrlites, plg-wehrlites, troctolite, ol- and cpx-gabbros pegmatitic gabbros and anorthosite).

Rock type	wehrlites			plg-wehrlites						pegmatitic gabbros			troctolite	anorthosite
Sample numbers	MP213	MP243	MP278	FB1094	FB1095	MP106	MP107	MP108	MP155	MP4	MP113	MP265a	MP240	MP285
SiO_2	40.3	40.1	41.5	43.3	44.8	45.7	46.7	46.3	45.8	50.6	53.4	49.9	44.2	45.7
TiO_2	0.33	0.20	0.58	0.29	0.37	0.54	0.60	0.40	0.36	0.53	1.17	0.53	0.06	0.11
Al_2O_3	4.2	7.2	9.7	12.8	12.2	10.6	11.0	13.8	11.2	17.4	7.5	16.1	20.2	28.5
FeO_T	15.9	14.2	11.6	10.6	10.7	9.9	9.3	8.4	8.6	5.5	8.1	6.0	7.3	2.1
MnO	0.14	0.19	0.16	0.14	0.16	0.17	0.17	0.14	0.15	0.12	0.17	0.12	0.10	0.03
MgO	27.4	24.2	21.6	19.1	18.1	15.5	14.8	13.5	16.7	8.4	12.7	9.4	13.7	3.3
CaO	2.4	6.0	7.6	8.4	9.5	13.2	13.2	13.2	13.6	11.8	12.7	10.6	10.1	14.1
Na_2O	0.00	0.19	0.33	1.10	1.21	1.28	1.21	1.65	0.84	2.79	1.83	2.30	1.49	2.30
K_2O	0.06	0.05	0.11	0.16	0.14	0.17	0.23	0.13	0.08	0.73	0.13	1.41	0.16	0.28
P_2O_5	0.04	0.03	0.10	0.03	0.04	0.04	0.06	0.03	0.02	0.07	0.05	0.05	0.03	0.02
LOI	8.66	7.39	6.05	3.64	2.08	1.80	2.52	1.35	2.70	1.68	1.30	2.71	1.75	2.38
Total	99.50	99.77	99.54	99.66	99.29	99.15	99.99	99.11	100.17	99.68	99.10	99.14	99.09	98.75
Mg#	75.5	75.3	76.8	76.3	75.1	73.5	74.0	74.2	77.5	73.1	0.0	73.6	77.0	73.9

Table 8b: continued.

Rock type	ol-gabbros										
Sample numbers	FB1091	FB1090	FB1093	MP125	MP127	MP135	MP136	MP150	MP152	MP156	MP157
SiO_2	46.80	47.50	46.04	46.37	47.86	48.46	47.60	46.94	44.80	47.37	46.51
TiO_2	0.37	0.36	0.33	0.26	0.34	0.36	0.28	0.23	0.15	0.30	0.32
Al_2O_3	15.28	17.10	18.76	19.34	17.75	19.15	19.49	23.08	19.79	18.86	14.23
FeO_T	7.25	5.48	5.88	5.25	5.25	4.38	4.46	3.60	6.92	4.49	6.93
MnO	0.12	0.10	0.10	0.09	0.09	0.08	0.08	0.06	0.10	0.09	0.12
MgO	13.51	10.20	10.24	9.97	9.96	8.32	8.57	6.98	13.59	8.94	13.57
CaO	12.41	14.35	13.49	13.15	14.13	15.09	14.17	14.56	10.59	15.37	14.71
Na_2O	1.65	1.68	1.60	1.90	1.69	1.88	1.88	1.99	1.60	1.72	1.14
K_2O	0.18	0.12	0.25	0.25	0.17	0.20	0.20	0.21	0.16	0.14	0.07
P_2O_5	0.05	0.04	0.04	0.04	0.04	0.04	0.03	0.03	0.05	0.02	0.02
LOI	1.56	2.77	2.44	2.47	2.19	1.53	2.24	1.41	2.11	1.68	1.89
Total	99.24	99.75	99.21	99.14	99.56	99.57	99.05	99.16	99.88	99.13	99.66
Mg#	76.9	76.8	75.6	77.2	77.2	77.2	77.4	77.6	77.8	78.0	77.7

Rock type	ol-gabbros										
Sample numbers	MP159	MP160	MP161	MP166	MP176	MP188	MP190	MP191	MP221	MP227	MP242
SiO_2	47.23	47.73	45.33	45.98	47.46	47.18	48.02	43.77	48.46	47.09	48.47
TiO_2	0.29	0.27	0.21	0.23	0.29	0.27	0.38	0.23	0.40	0.34	0.37
Al_2O_3	18.21	20.14	17.88	19.69	20.79	20.65	17.58	16.59	16.73	18.04	18.34
FeO_T	6.02	5.20	7.26	5.95	5.25	4.44	5.39	6.87	5.27	5.81	4.70
MnO	0.10	0.09	0.11	0.09	0.09	0.07	0.10	0.10	0.11	0.11	0.09
MgO	10.68	8.83	12.68	10.29	9.49	8.24	9.40	12.69	9.60	10.37	9.19
CaO	14.08	14.35	12.36	13.15	14.18	14.20	15.20	12.03	15.02	13.50	15.25
Na_2O	1.59	1.80	1.55	1.72	1.82	1.81	1.43	1.27	1.78	1.80	1.71
K_2O	0.11	0.16	0.11	0.18	0.10	0.18	0.12	0.10	0.20	0.21	0.17
$_2O_5$	0.03	0.04	0.03	0.05	0.03	0.04	0.03	0.04	0.02	0.04	0.04
LOI	0.87	1.37	1.57	2.23	0.39	1.95	1.35	5.52	2.17	2.50	0.61
Total	99.29	100.06	99.15	99.61	100.06	99.11	99.09	99.31	99.89	99.93	99.03
Mg#	76.0	75.2	75.7	75.5	76.3	76.8	75.7	76.7	76.4	76.1	77.7

Table 8c: continued.

Rock type	cpx-gabbros											
Sample numbers	MP120	MP122	MP124	MP131	MP134	MP138	MP148	MP149	MP154	MP168	MP169	MP171
SiO_2	49.28	46.95	44.61	49.06	46.94	47.71	48.55	46.14	48.52	46.26	45.96	47.30
TiO_2	0.37	0.35	0.23	0.41	0.34	0.23	0.22	0.15	0.33	0.24	0.26	0.23
Al_2O_3	15.78	15.78	17.11	17.51	20.17	22.02	23.58	23.64	19.77	18.93	19.30	17.82
FeO_T	4.18	5.95	6.90	4.23	4.59	3.59	3.22	4.04	3.82	6.15	5.58	6.19
MnO	0.09	0.11	0.11	0.09	0.08	0.07	0.06	0.06	0.08	0.10	0.10	0.11
MgO	9.34	11.57	12.79	8.71	9.03	6.59	5.55	7.09	7.70	10.73	9.71	10.36
CaO	15.67	13.51	11.72	16.13	14.03	13.98	14.31	13.54	16.30	13.50	12.89	13.22
Na_2O	2.02	1.59	1.52	1.89	1.85	1.93	2.18	1.73	1.87	1.58	1.86	1.85
K_2O	0.41	0.23	0.19	0.19	0.26	0.61	0.47	0.38	0.11	0.15	0.59	0.28
P_2O_5	0.03	0.04	0.04	0.04	0.04	0.03	0.03	0.02	0.02	0.03	0.03	0.02
LOI	1.68	2.94	3.85	1.28	2.29	2.38	1.25	1.96	1.37	2.04	2.77	2.27
Total	99.03	99.12	99.13	99.64	99.67	99.20	99.49	98.79	100.03	99.75	99.11	99.70
Mg#	79.9	77.6	76.8	78.6	77.8	76.6	75.4	75.8	78.2	75.7	75.6	74.9

Rock type	cpx-gabbros											
Sample numbers	MP180	MP181	MP184	MP187	MP189	MP192	MP194	MP223	MP225	MP230	MP247	FB1092
SiO_2	49.38	47.42	48.23	47.76	43.79	47.27	48.26	47.58	48.20	47.25	46.41	48.30
TiO_2	0.37	0.46	0.33	0.31	0.16	0.32	0.37	0.37	0.38	0.37	0.38	0.55
Al_2O_3	16.94	12.57	17.77	19.09	20.84	20.17	19.69	17.97	18.22	19.38	18.08	14.11
FeO_T	4.79	7.07	4.26	3.58	5.97	4.04	3.77	5.40	5.79	5.27	5.45	5.77
MnO	0.09	0.13	0.09	0.07	0.10	0.07	0.08	0.10	0.10	0.09	0.09	0.11
MgO	9.14	14.18	9.70	7.64	10.69	7.32	7.20	9.61	9.74	8.68	10.82	11.96
CaO	13.98	12.81	16.07	16.36	11.59	15.56	15.14	13.13	12.83	13.80	14.58	15.16
Na_2O	2.02	1.12	1.57	1.59	1.81	1.77	2.26	1.92	2.15	1.95	1.60	1.44
K_2O	0.39	0.63	0.15	0.47	0.29	0.13	0.52	0.18	0.20	0.17	0.20	0.21
P_2O_5	0.05	0.03	0.02	0.03	0.04	0.03	0.03	0.04	0.06	0.05	0.05	0.06
LOI	1.85	2.48	1.65	2.31	3.81	2.95	1.82	2.64	2.22	2.76	2.26	2.32
Total	99.10	99.08	100.02	99.42	99.11	99.69	99.28	99.01	99.94	99.82	100.24	100.05
Mg#	77.3	78.1	80.2	79.2	76.1	76.4	77.3	76.0	75.0	74.6	78.0	78.7

3.3. Trace-element chemistry

3.3.1. Compatible-element evolution

The trace-element behavior in the Mont Collon cumulitic rocks is quite variable (trace-element contents are given in Tables 9a-c). Compatible elements such as Ni, Co, Zn with K_D values >1 for early crystallizing minerals (olivine, clinopyroxene) usually show a good positive correlation when plotted against MgO. Others like Sr, Ba or Ga are negatively correlated with MgO (Fig. 24), which reflects the dominant role of plagioclase in the cumulitic sequence when ferromagnesian minerals are less abundant. V, Cr and Y display a more complex, chevron-like evolution; with maximum concentrations at ca. 15 wt% MgO (Fig. 24), which is the limit between the gabbros (s.l.) and the wehrlites.

Some compatible trace elements (e.g. Ni) exhibit no clear correlation with $Mg\#_{cpx}$, some a crude negative one (e.g. Cr), which might again be linked to cumulus effects (Fig. 25). Most incompatible elements (Fig. 26) do not display systematic variations with $Mg\#_{cpx}$; for example Zr and Y contents remain constant with decreasing $Mg\#_{cpx}$. Nevertheless, some incompatible elements, such as Nb or REE (e.g. La; Fig. 26), increase with decreasing $Mg\#_{cpx}$.

3.3.2. Incompatible trace-element binary diagrams

On the other hand, incompatible elements (not incorporated in the dominant cumulitic phases) such as Zr, Nb, Hf behave more erratically and yield scattered plots, as illustrated by the MgO-Zr diagram (Fig. 27a). Consequently, classical binary diagrams using Zr as differentiation index are mostly scattered, with few exceptions like for Ti (Fig. 27b) or other incompatible elements such as Nb (Fig. 28). The Zr vs Nb diagram (Fig. 28) is particularly interesting; if the troctolite MP240 plots as expected in the low concentration part of the diagram, the sample MP106 (plagioclase-wehrlite) is relatively Zr-rich. In other words, the incompatible trace-element content of the Mont Collon lithologies is not solely controlled by their cumulitic mineralogy, or by their degree of differentiation, but rather by the amount and composition of trapped interstitial liquid, as will be demonstrated later on by quantitative modeling. Absence of correlation between the degree of differentiation of the lithologies and their incompatible trace-element content is also illustrated in the well-preserved cumulitic sequence of the Dents de Bertol area (Fig. 30). Concentrations in incompatible elements like Zr, Y or Ba fluctuate largely and independently from Mg#.

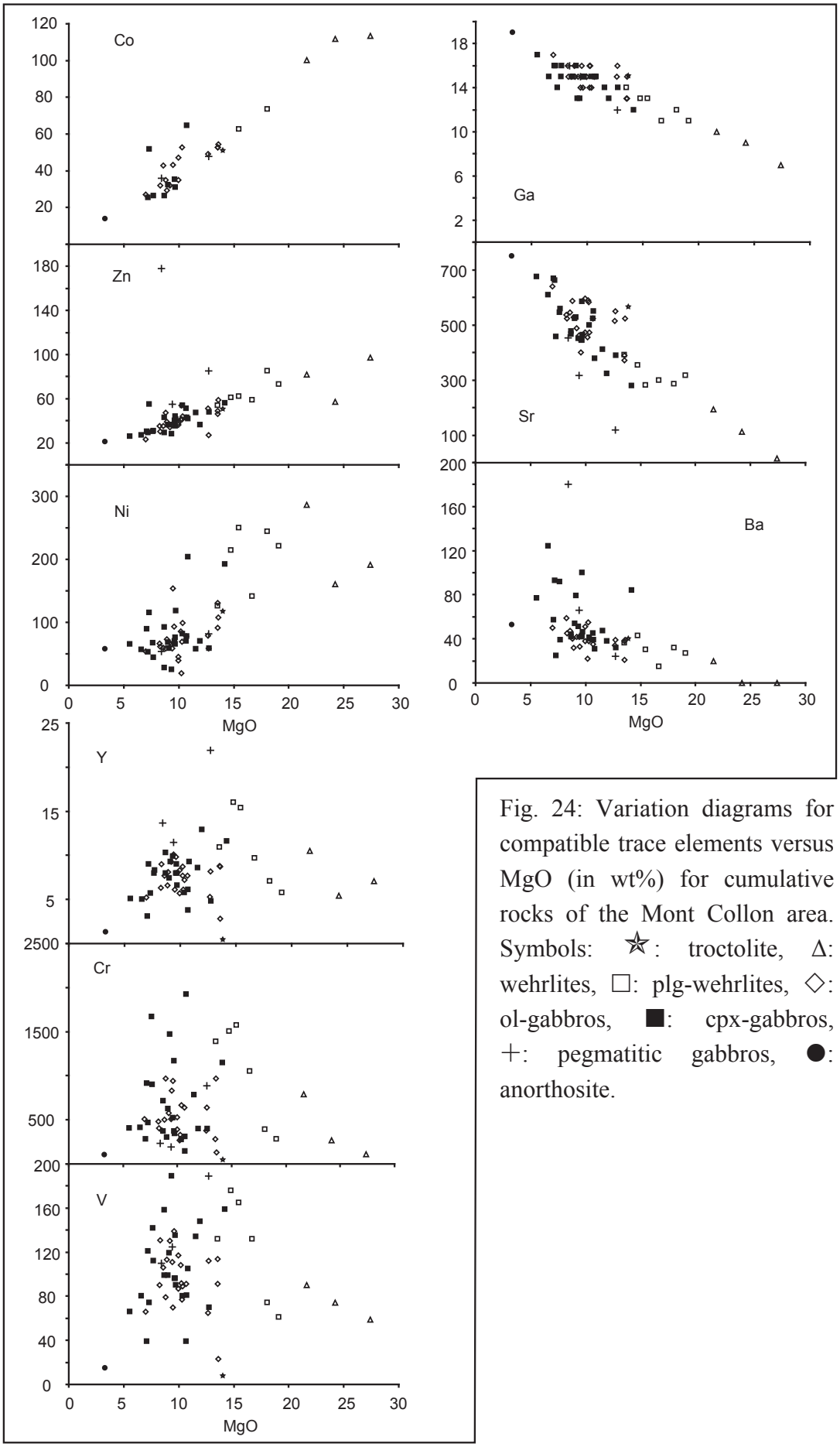

Fig. 24: Variation diagrams for compatible trace elements versus MgO (in wt%) for cumulative rocks of the Mont Collon area. Symbols: ✡: troctolite, Δ: wehrlites, □: plg-wehrlites, ◇: ol-gabbros, ■: cpx-gabbros, +: pegmatitic gabbros, ●: anorthosite.

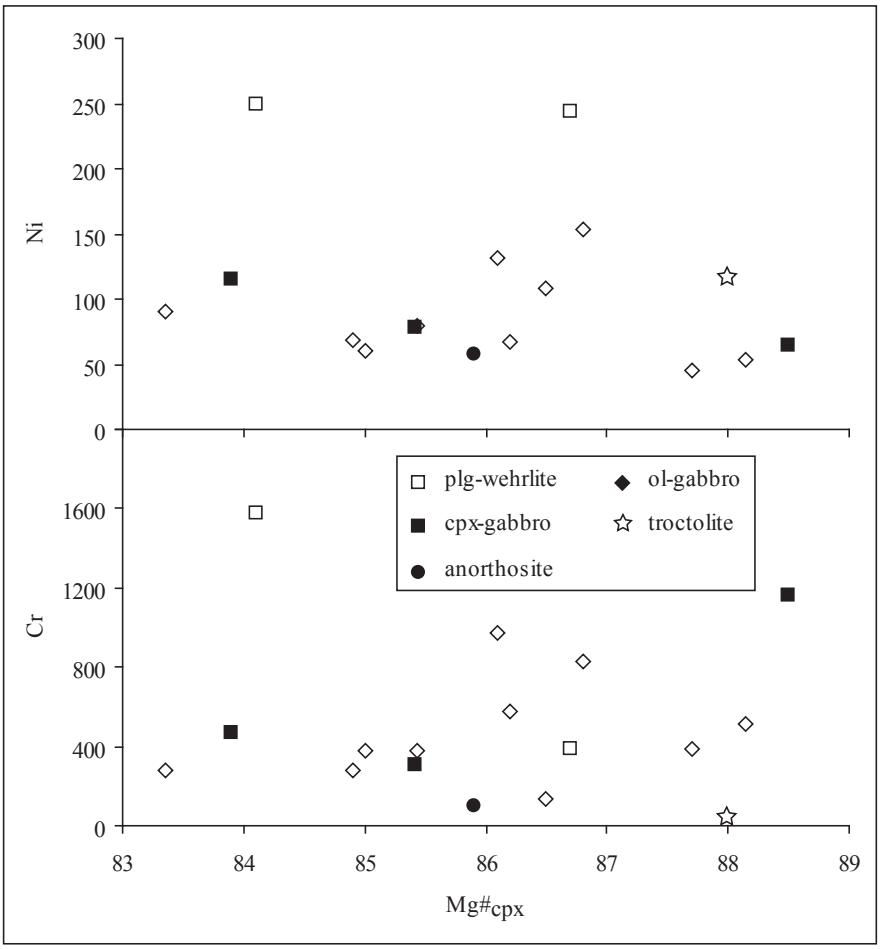

Fig. 25: Variation diagrams for compatible trace elements (in ppm) versus $Mg\#_{cpx}$ for cumulative rocks of the Mont Collon.

Sr displays the same behavior as Ba. In a Sr-La correlation diagram (Fig. 29), all rocks show relatively similar Sr contents with the exception of a plagioclase-free wehrlite. Focusing on the well-preserved cumulative sequence of the Dents de Bertol area, the incompatible trace-element abundances fluctuate largely and without a specific trend along the cumulate pile. Figure 30 illustrates the variations of the trace-element abundances with respect to the stratigraphic distribution of cumulates within the complex. Only well preserved rocks with unaltered magmatic mineralogy are represented in this stratigraphic column. Y ranges between 2.8 to 11.6 ppm and the lowest contents characterize the olivine and cpx gabbros located between 250-200 m. Nb shows a discrepancy from 0.18 to 1.32 ppm; the olivine gabbros located between 350 and 300 m are the most Nb-depleted. Zr ranges between 26 and 46 ppm while Ba exhibits the larger range (from 15 to 124 ppm).

Overall, major- and trace-element distribution do not show any well defined evolutionary trend over the small differentiation range expressed by the Mg# of clinopyroxene. This is due to the absence of substantial differentiation in this magmatic system and above all to the blurring effect of cumulus phases.

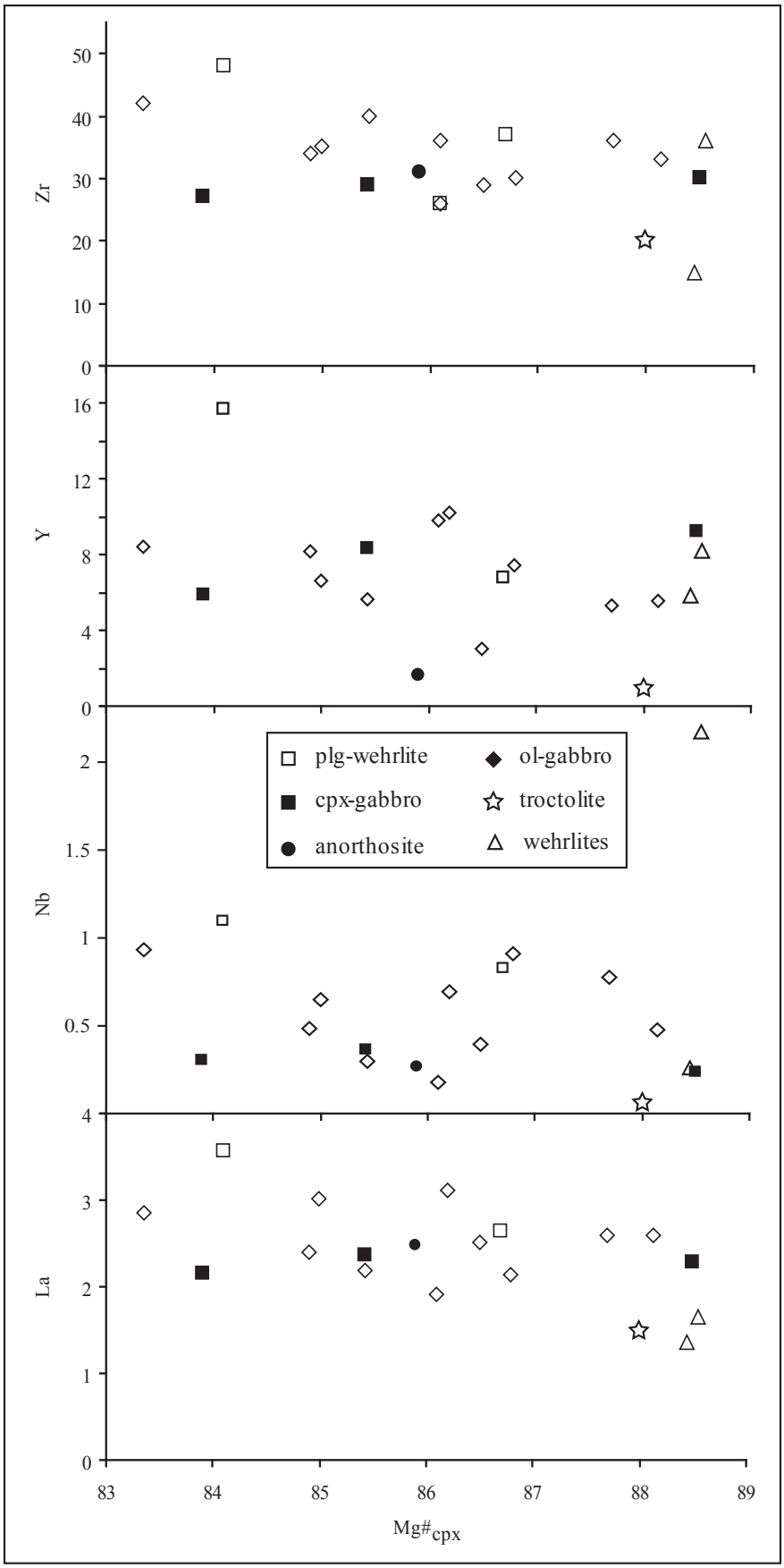

Fig. 26: Variation diagrams for incompatible trace elements (in ppm) versus $Mg\#_{cpx}$ for cumulative rocks of the Mont Collon.

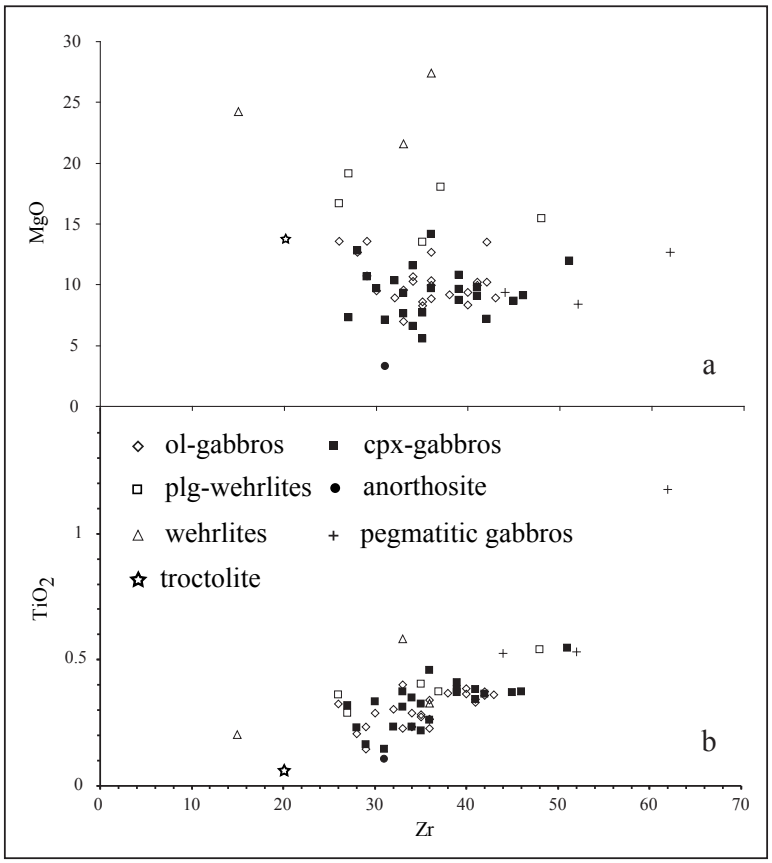

Fig. 27: Variation diagrams using Zr (ppm) as differentiation index versus a) MgO and b) TiO_2 (in wt%).

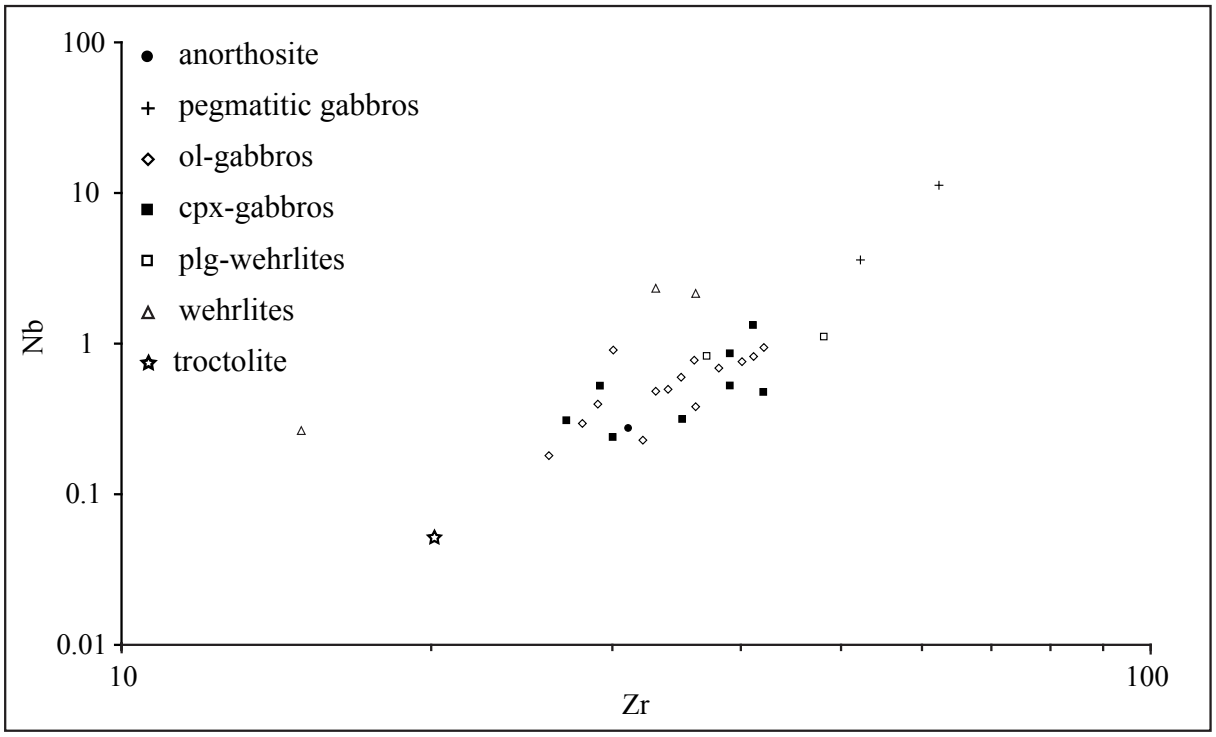

Fig. 28: Variation diagram using Zr (in ppm) as differentiation index versus Nb (in ppm).

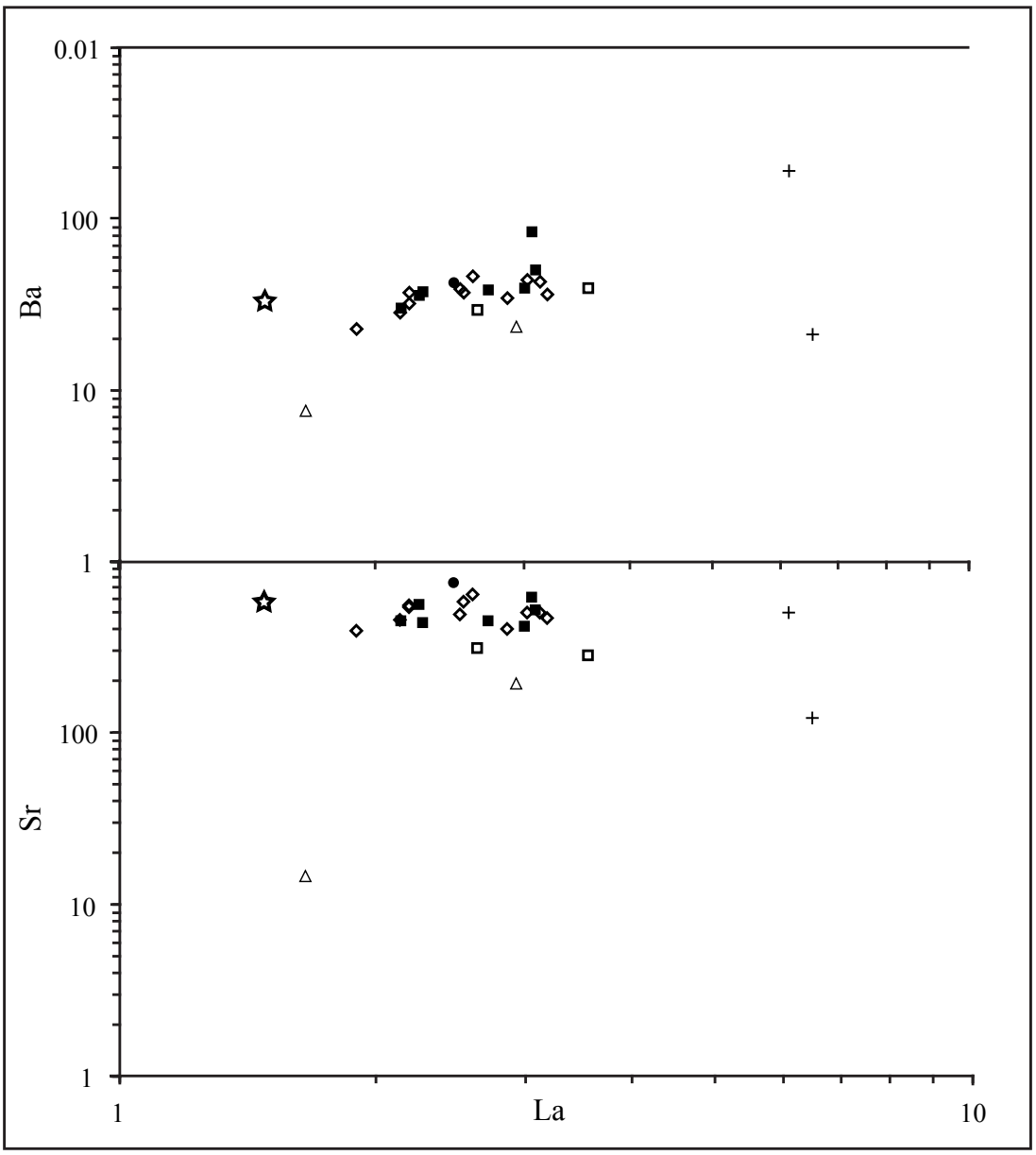

Fig. 29: Logarithmic binary diagrams using La (ppm) as differentiation index versus Ba and Sr (in ppm). Same legend as figure 28.

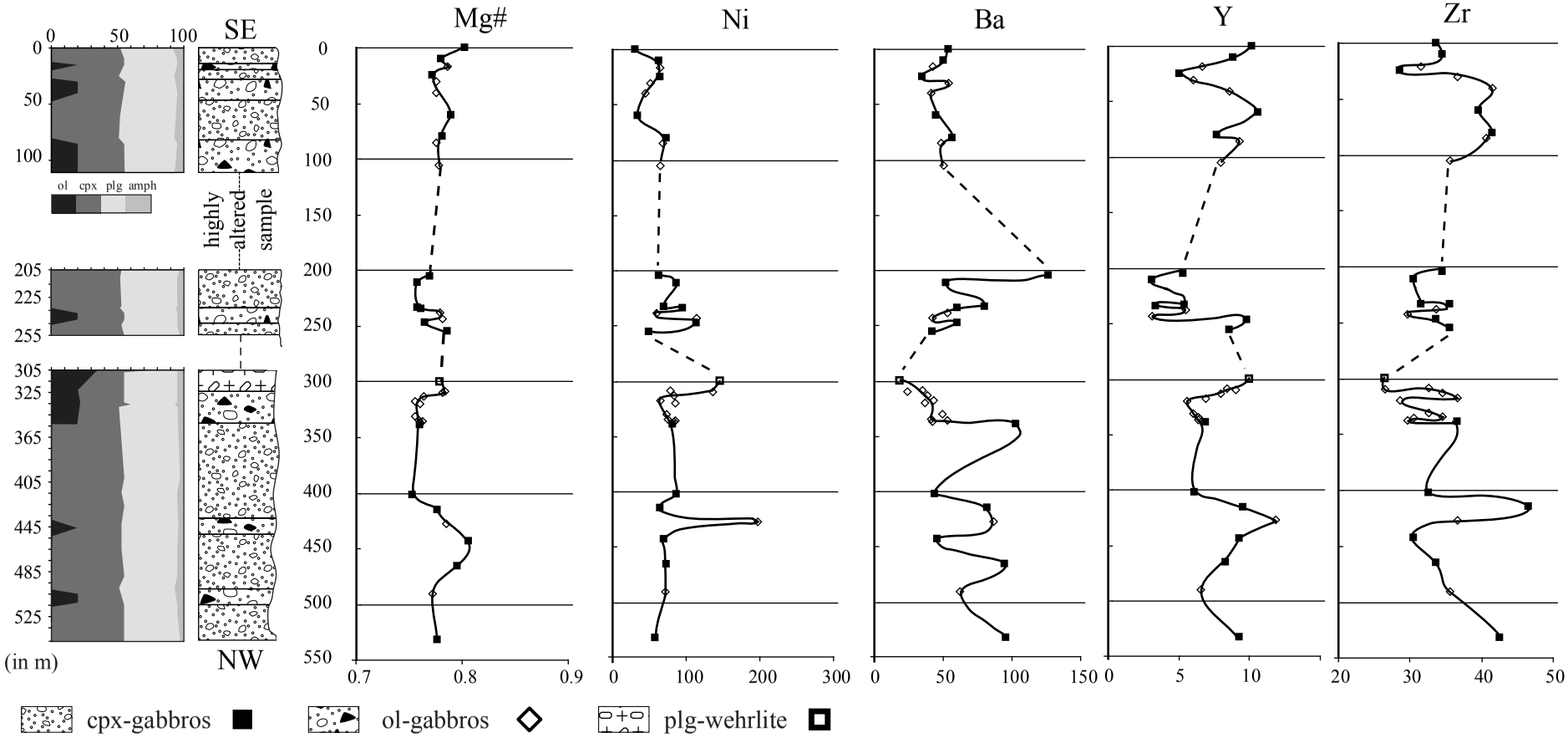

Fig. 30: Variations of selected elements along the cumulate pile of the Dents de Bertol area (cf. Fig. 8; group 2 cumulates). Mg# = molar (Mg / (Fe_T + Mg) x100 ratio, elements are given in ppm.

Table 9a: Representative trace-element analyses of whole-rocks (wehrlites, plagioclase-wehrlites, troctolite, olivine-gabbros, clinopyroxene-gabbros and anorthosite). (*) XRF trace-element analysis using classical “short time” procedure. (**) XRF analysis using «Rhodes» long time procedure. (-): under detection limits. (n.d.): not determined. Other trace elements have been analyzed by ICPMS.

Rock types	wehrlites			plg-wehrlites	
Sample numbers	MP213	MP243	MP278	FB1095	MP106
Cu*	n.d.	14	n.d.	15	83
S*	n.d.	-	n.d.	-	5823
Sc*	n.d.	78	n.d.	62	97
As*	n.d.	-	n.d.	-	5
V**	59	74	90	74	165
Cr**	110	270	793	390	1574
Ni**	191	161	287	244	250
Ga**	7	9	10	12	13
Zn**	97	57	82	85	62
Co	113	103	100	74	63
Cs	0.26	0.44	0.43	0.32	0.40
Rb	2	1	2	3	4
Ba	8	6	22	29	39
Th	0.69	0.04	0.14	0.36	0.28
U	0.15	0.03	0.04	0.09	0.05
Nb	2.17	0.26	2.31	0.82	1.09
Ta	0.14	0.15	0.12	0.06	0.07
Pb	0.54	0.94	1.01	1.21	1.01
Sr	15	111	196	309	278
Zr	23.6	9.3	24.4	24.4	37.3
Hf	0.59	0.41	0.74	0.60	1.17
Y	8.2	5.8	11.9	6.8	15.7
La	1.66	1.37	2.93	2.64	3.56
Ce	4.97	3.19	8.57	6.17	10.10
Pr	0.82	0.50	1.43	0.88	1.63
Nd	4.01	2.70	7.20	3.99	8.05
Sm	1.19	0.69	1.98	1.03	2.40
Eu	0.15	0.37	0.55	0.51	0.79
Gd	1.37	0.97	2.12	1.19	2.73
Tb	0.24	0.18	0.34	0.20	0.45
Dy	1.38	1.13	1.99	1.17	2.81
Ho	0.29	0.21	0.40	0.25	0.58
Er	0.77	0.66	1.10	0.69	1.62
Yb	0.66	0.51	0.85	0.59	1.32
Lu	0.09	0.08	0.13	0.09	0.19

Rock types	pegmatitic gabbros		troctolite	anorthosite
Sample numbers	MP4	MP113	MP240	MP285
Cu*	18	n.d.	11	n.d.
S*	69	n.d.	247	n.d.
Sc*	35	n.d.	14	n.d.
As*	-	n.d.	-	n.d.
V**	110	189	7	15
Cr**	233	886	36	102
Ni**	54	82	117	58
Ga**	16	12	15	19
Zn**	178	85	50	21
Co	36	48	51	14
Cs	0.36	0.04	0.32	0.24
Rb	30	2	3	11
Ba	188	21	33	42
Th	0.90	3.35	0.07	0.10
U	0.70	1.48	0.02	0.02
Nb	3.56	11.24	0.05	0.27
Ta	0.23	0.72	0.00	0.02
Pb	38.18	1.57	0.68	1.13
Sr	504	121	564	737
Zr	52.1	62.2	20.0	5.5
Hf	0.67	2.29	0.08	0.14
Y	16.1	24.7	0.9	1.7
La	6.11	6.51	1.47	2.47
Ce	15.36	17.62	2.72	4.61
Pr	2.18	2.73	0.32	0.59
Nd	9.39	12.36	1.25	2.42
Sm	2.48	3.69	0.22	0.45
Eu	0.77	0.86	0.35	0.54
Gd	2.60	3.83	0.15	0.40
Tb	0.43	0.64	0.03	0.06
Dy	2.51	4.05	0.14	0.31
Ho	0.51	0.84	0.03	0.06
Er	1.41	2.31	0.07	0.16
Yb	1.14	2.05	0.08	0.12
Lu	0.17	0.29	0.01	0.02

Table 9b: conitnued

Rock types	ol gabbro													
Sample numbers	FB1091	MP125	MP127	MP135	MP136	MP150	MP152	MP156	MP157	MP160	MP161	MP166	MP176	MP242
Cu*	15	15	16	30	31	24	18	40	86	38	23	25	49	39
S*	40	992	6022	4717	1058	498	281	200	1234	765	892	1964	675	1647
Sc*	50	34	35	27	27	32	20	50	57	18	42	46	28	19
As*	-	-	4	-	-	4	-	-	4	-	-	5	-	5
V**	91	87	117	131	106	66	23	113	114	79	65	77	70	130
Cr**	283	390	532	405	375	510	133	966	970	503	380	282	829	574
Ni**	91	45	39	62	60	54	108	73	131	59	79	69	154	67
Ga**	13	15	15	15	15	17	15	15	13	16	15	16	16	15
Zn**	49	36	38	30	35	23	59	39	46	47	51	41	36	34
Co	53	46	35	32	41	27	54	29	53	35	49	48	43	32
Cs	0.84	0.24	0.13	0.20	0.17	0.19	0.33	0.12	0.16	0.17	0.26	0.22	0.13	0.14
Rb	4	6	3	4	5	7	3	4	1	3	2	4	2	3
Ba	35	52	36	44	42	47	39	37	23	37	32	40	28	43
Th	0.31	0.31	0.38	0.39	0.48	0.16	0.18	0.12	0.08	0.19	0.12	0.29	0.15	0.28
U	0.08	0.09	0.09	0.08	0.16	0.03	0.05	0.03	0.02	0.04	0.03	0.05	0.05	0.07
Nb	0.93	0.78	0.82	0.76	0.65	0.48	0.40	0.23	0.18	0.38	0.30	0.49	0.91	0.69
Ta	0.06	0.28	0.05	0.04	0.37	0.03	0.02	0.02	0.02	0.02	0.02	0.31	0.09	0.04
Pb	1.01	1.82	1.44	0.99	1.84	1.18	1.25	0.98	0.65	1.07	0.86	2.33	1.13	1.07
Sr	401	594	474	502	531	647	494	551	399	582	546	568	461	503
Zr	25.9	14.2	23.7	23.3	16.0	12.8	17.1	16.1	14.1	14.8	10.7	15.7	17.2	31.2
Hf	0.69	0.67	0.67	0.66	0.35	0.37	0.41	0.51	0.52	0.44	0.34	0.58	0.49	0.88
Y	8.5	5.3	8.9	9.3	6.6	5.6	3.0	7.5	9.8	6.7	5.6	8.2	7.4	10.2
La	2.85	2.58	3.18	3.02	3.01	2.59	2.51	2.19	1.90	2.53	2.19	2.40	2.14	3.11
Ce	6.84	6.18	7.65	7.32	6.78	5.69	5.17	5.38	5.22	5.87	5.04	5.55	5.16	7.59
Pr	1.01	0.85	1.12	1.11	1.11	0.82	0.68	0.82	0.86	0.85	0.72	0.78	0.79	1.17
Nd	4.81	4.00	5.15	5.38	5.32	3.71	2.81	4.12	4.48	4.11	3.28	4.37	3.73	5.49
Sm	1.32	0.62	1.44	1.49	1.19	0.94	0.59	1.21	1.49	1.11	0.92	0.88	1.02	1.60
Eu	0.59	0.65	0.68	0.72	0.76	0.60	0.49	0.63	0.63	0.64	0.60	0.46	0.58	0.79
Gd	1.49	1.05	1.63	1.70	1.62	1.09	0.58	1.36	1.64	1.24	1.00	1.26	1.28	1.82
Tb	0.24	0.16	0.26	0.27	0.21	0.16	0.09	0.22	0.28	0.19	0.16	0.16	0.21	0.30
Dy	1.47	1.15	1.58	1.62	1.59	0.96	0.51	1.35	1.75	1.18	1.01	0.95	1.24	1.76
Ho	0.30	0.21	0.32	0.33	0.21	0.19	0.11	0.27	0.35	0.23	0.19	0.22	0.27	0.36
Er	0.83	0.36	0.87	0.91	0.80	0.53	0.28	0.74	0.91	0.66	0.52	0.71	0.71	1.00
Yb	0.68	0.47	0.72	0.72	0.34	0.41	0.28	0.59	0.77	0.49	0.44	0.47	0.61	0.83
Lu	0.10	0.10	0.10	0.10	0.12	0.06	0.04	0.08	0.11	0.08	0.06	0.06	0.09	0.11

Table 9c: conitnued

Rock types	cpx-gabbros							
Sample numbers	MP131	MP134	MP154	MP168	MP184	MP192	MP194	MP223
Cu*	20	35	25	31	33	45	n.d.	28
S*	1027	303	66	1830	5	1393	n.d.	71
Sc*	19	28	21	42	45	50	n.d.	29
As*	-	-	-	3	5	4	n.d.	4
V**	158	99	112	81	135	74	121	96
Cr**	711	300	900	310	1166	467	912	525
Ni**	28	68	44	78	65	115	53	70
Ga**	15	16	16	15	15	14	16	15
Zn**	29	36	31	43	35	55	29	40
Co	26	32	27	57	31	52	25	35
Cs	0.09	0.16	0.09	0.20	0.11	0.35	0.26	0.09
Rb	3	6	2	4	3	2	16	9
Ba	38	50	36	37	37	29	83	39
Th	0.24	0.38	0.12	0.13	0.21	0.12	0.23	0.35
U	0.09	0.08	0.03	0.05	0.05	0.02	0.07	0.11
Nb	0.52	1.33	0.31	0.37	0.24	0.31	0.47	0.85
Ta	0.03	0.08	0.02	0.76	0.02	0.02	0.05	0.06
Pb	1.04	2.10	2.10	1.31	1.05	1.18	1.29	1.45
Sr	452	521	550	543	434	445	611	418
Zr	51.6	23.0	15.0	12.2	15.4	11.2	18.0	31.6
Hf	1.32	0.61	0.52	0.26	0.58	0.37	0.60	0.86
Y	11.3	8.2	8.9	8.3	9.2	5.9	9.1	8.9
La	2.72	3.08	2.26	2.36	2.28	2.15	3.05	2.99
Ce	7.01	7.45	5.65	4.86	5.70	5.06	7.31	7.38
Pr	1.11	1.10	0.92	0.65	0.90	0.73	1.10	1.09
Nd	5.73	4.94	4.58	4.68	4.58	3.53	5.23	5.09
Sm	1.66	1.34	1.35	0.95	1.40	0.95	1.50	1.46
Eu	0.72	0.69	0.71	0.76	0.66	0.52	0.70	0.62
Gd	1.95	1.57	1.55	2.07	1.61	1.03	1.63	1.57
Tb	0.31	0.24	0.27	0.15	0.26	0.17	0.26	0.26
Dy	1.95	1.44	1.62	1.19	1.60	1.05	1.59	1.51
Ho	0.40	0.29	0.32	0.23	0.33	0.21	0.32	0.32
Er	1.07	0.79	0.87	0.65	0.92	0.57	0.84	0.83
Yb	0.92	0.64	0.69	0.64	0.71	0.48	0.70	0.76
Lu	0.13	0.09	0.10	0.09	0.10	0.07	0.11	0.11

3.3.3. Rare earth elements chondrite-normalized patterns

In the whole-rock plots of figure 31, wehrlites exhibit smooth REE patterns with low and variable contents (ΣREE ranges from 17.58 to 29.59 ppm), and a more or less marked negative Eu anomaly (Fig. 31d), which could be interpreted as plagioclase fractionation before wehrlites crystallization. Plg-wehrlites show relatively flat patterns ($1.84 < La_N/Yb_N < 1.93$; $0.89 < La_N/Sm_N < 0.95$, and $Sm_N/Yb_N = 2$; Fig. 31d) with slightly higher concentrations (9 to 15 times the chondrite). The troctolite is characterized by the lowest REE content (ΣREE = 6.85 times the chondritic abundances. Fig 31b) and the strongest positive Eu anomaly (Eu/Eu* = 5.77). This rock is enriched in LREE ($La_N/Yb_N = 13.20$, $La_N/Sm_N = 4.27$) and displays a relative flat M- to HREE pattern ($Sm_N/Yb_N = 3.08$). The total REE content of the cumulate gabbros correlates positively with SiO_2 and represents about 10 times the chondritic abundances. Ol- and cpx-gabbros display similar REE patterns (Fig. 31b and c), slightly LREE-enriched (La_N/Yb_N up to 3.67) and characterized by more or less marked positive Eu anomalies, showing the important role of plagioclase accumulation in the genesis of these rocks. Among the olivine gabbros (Fig. 31b), sample MP152 differs from the others by a significant LREE enrichment ($La_N/Yb_N = 6.48$) and lower REE contents (ΣREE = 14.13 ppm), making it more similar to the troctolite than to olivine-gabbros. Plagioclase accumulation, which represents the most significant feature of the anorthositic layer (Fig. 31a), is reflected by the marked positive Eu anomaly (Eu/Eu* = 3.87), which nevertheless is lower than in the troctolite. Anorthosite differs from the gabbros by a REE pattern which is enriched in LREE [(La/Yb) = 14.24]. Pegmatitic gabbros exhibit REE patterns similar to those of the other gabbros (Fig. 31a), but with higher (and highest) REE contents (average ΣREE = 51.43 ppm), and a small Eu negative anomaly (Eu/Eu* close to 1).

3.3.4. Multi-element primitive mantle-normalized diagrams

The various Mont Collon lithologies have very similar multi-element primitive mantle-normalized diagrams (Fig. 32). Typical features are negative anomalies in Nb-Ta, Zr-Hf, and Ti, and positive anomalies in Sr and Eu. All cumulitic rocks are more or less enriched in Th, U and LILE and depleted in HREE and Y. The pegmatitic gabbros differ from the ultramafic (wehrlites) and mafic (gabbros s.l.) cumulates by the absence of the Nb, Ta, Zr, Hf and Ti negative anomalies, a significant enrichment in U, Th and a marked depletion in LILE (Ba, Rb).

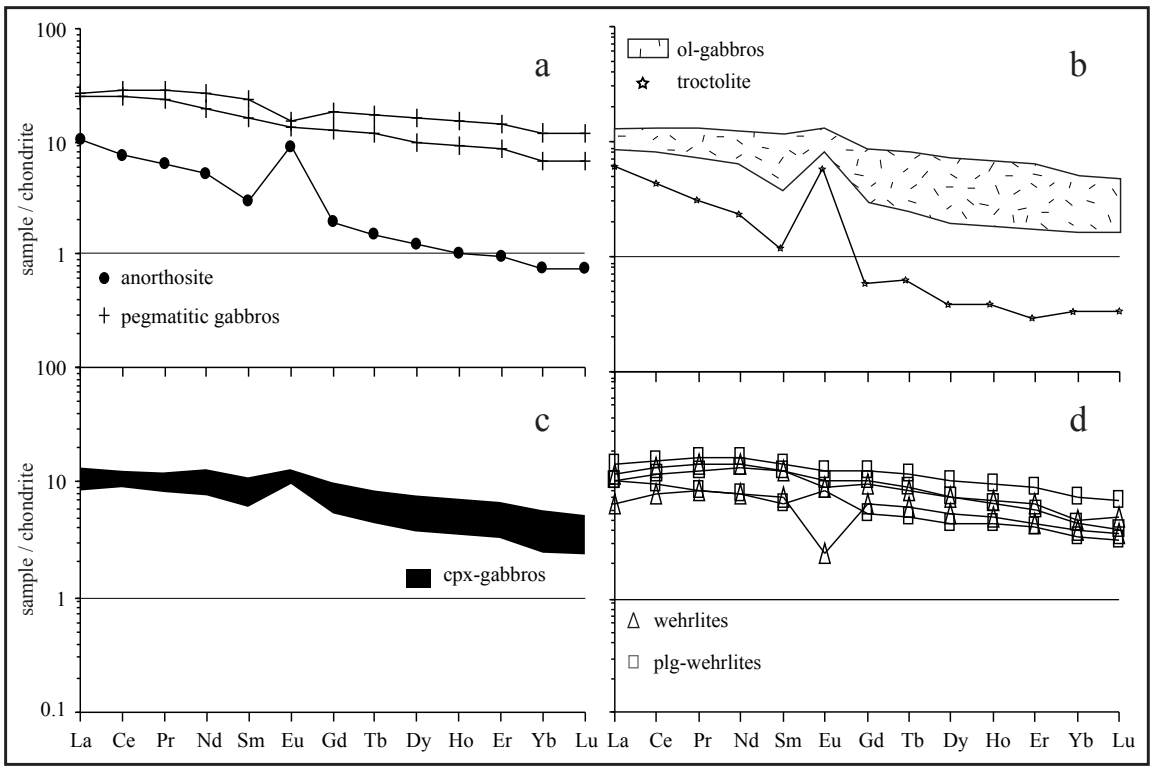

Fig. 31: Chondrite-normalized REE content of whole-rocks of the Mont-Collon mafic cumulates, pegmatitic gabbros and anorthosite. Normalization to the C1 chondrite (Sun and McDonough, 1989).

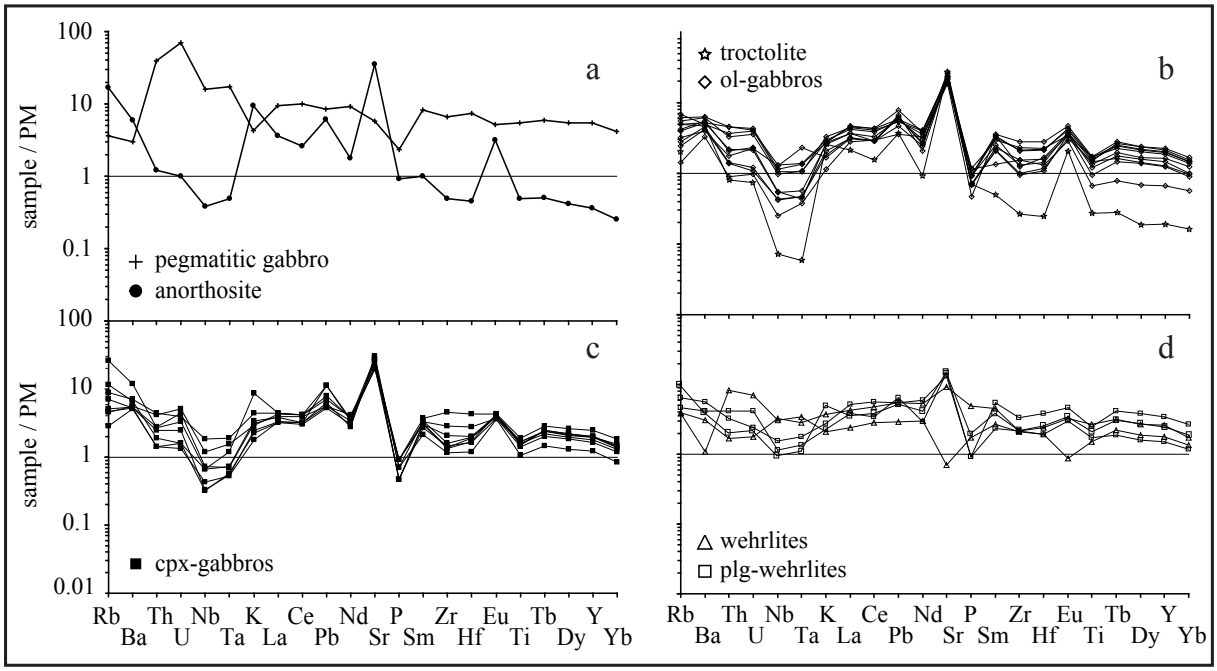

Fig. 32: Primitive Mantle (PM) normalized trace-element patterns of whole rocks of the Mont Collon mafic cumulates, pegmatitic gabbros and anorthosite. Normalization values are taken from Sun and McDonough (1989).

3.4. Trace-element mineral chemistry

3.4.1. Clinopyroxene

Chemical data are reported in Table 10. The REE contents (about 10 times the chondritic abundances) and patterns of clinopyroxenes are very similar whatever the rock type (Fig. 33a). They are depleted in La and Ce, and enriched in Nd and Sm. Gabbro clinopyroxenes (cpx) exhibit a marked negative Eu anomaly, which is less important in clinopyroxenes from ultramafic cumulates. There is no correlation between REE content and the Eu anomaly. The main difference in the cpx REE patterns lies in the Nd and Sm enrichment, which appears to be more important in some gabbros (MP191, MP150, MP168). Clinopyroxenes from troctolites display REE patterns similar to those of the olivine-bearing gabbros. Multi-element primitive mantle-normalized diagrams of clinopyroxene do not show differences related to the rock-type and are characterized, like those for whole-rocks (Fig. 32), by (i) Nb, Ta, Zr, Hf negative anomalies, (ii) a depletion in LILE, HREE and Y, and (iii) an enrichment in Th (Fig. 33b). The only difference lies in the presence of Sr and Eu negative anomalies in the clinopyroxenes. These geochemical similarities between clinopyroxenes and whole-rock show that clinopyroxene is a major host for trace elements in the Mont Collon cumulates. Moreover, these clinopyroxenes with humped, convex-upward REE patterns, with a significant negative fractionation of the most incompatible REE are significantly differents from those crystallizing from a N-MORB melt.

3.4.2. Plagioclase

HREE in plagioclases (from Ho to Lu) are always below detection limits. REE patterns of plagioclase are characterized more important La and Ce contents, relative to Nd and Sm, (La_N/Sm_N = 27.6) and a higher (La_N/Dy_N) ratio (Fig. 34a-e). All analyzed plagioclases exhibit a large positive Eu anomaly. Multi-element primitive mantle-normalized diagrams exhibit a systematic negative Nb anomaly, like in the clinopyroxenes and whole-rocks (Fig. 34f-j). Interestingly, plagioclases from plagioclase-wehrlite are enriched in Rb (up to 10 times the primitive mantle) with respect to other rock types.

Table 10: Trace-element contents of the minerals used to constraint the in-situ crystallization model (in ppm).

Rock types	wehrlite	plg-wehrlite			troctolite			ol-gabbros								cpx-gabbro			anorthosite		
Sample numbers	MP243	MP106			MP240			MP125		MP136			MP166			MP168			MP285		
Mineral types	cpx	cpx	plg	amph	cpx	plg	amph	cpx	plg	cpx	plg	amph	cpx	plg	amph	cpx	plg	amph	cpx	plg	amph
Rb	0.05	0.09	2.31	16.45	0.27	<0.04	7.96	0.16	<0.014	0.09	0.13	13.20	0.80	<0.04	15.51	0.07	0.17	11.77	0.15	0.18	61.41
Ba	2.2	1.1	80.7	131.6	0.3	41.6	63.2	0.6	42.8	1.1	37.9	98.4	0.1	46.9	60.5	0.7	9.7	80.9	2.2	47.0	7.7
Th	0.24	0.37	-	1.13	0.32	<0.02	0.38	0.48	0.14	0.48	0.04	1.14	0.88	-	2.47	0.29	<0.03	0.62	0.22	-	0.71
Nb	-	0.06	-	20.38	<0.04	<0.03	8.21	<0.04	<0.02	<0.05	-	28.27	<0.04	-	16.72	<0.04	0.08	8.78	0.22	0.04	12.06
Ta	-	<0.01	-	1.48	<0.01	-	0.72	-	-	-	-	1.54	<0.01	-	1.03	<0.01	-	0.67	0.08	-	0.56
Pb	0.16	0.18	2.88	1.35	0.07	1.26	0.49	0.13	1.15	0.12	1.97	0.94	0.29	1.30	0.61	0.09	0.73	0.40	<0.02	1.28	0.45
Sr	31.6	26.7	1054.0	171.0	30.7	793.4	101.4	37.9	837.3	29.2	879.5	214.1	34.8	908.9	101.7	33.4	37.9	146.9	25.4	854.8	97.4
Zr	22.5	49.1	-	222.8	19.7	0.1	64.7	19.0	0.8	25.5	0.1	173.7	22.3	-	173.1	23.4	0.1	98.6	31.5	-	149.6
Hf	0.97	1.23	0.11	7.31	0.87	-	1.92	0.93	-	0.80	<0.02	6.04	0.85	-	4.28	1.01	-	3.51	1.09	-	3.11
Ti	4252	4618	48	21612	4287	383	11908	3897	n.d.	2998	n.d.	4563	4376	168	14735	2815	-	13957	5190	143	16680
Y	18.1	24.1	0.3	66.9	16.9	0.3	21.1	15.4	0.9	16.4	0.2	44.6	16.7	0.1	29.4	17.6	0.2	46.8	18.8	0.2	30.6
K	n.d.	75	855	8117	36	398	5212	n.d.	275	n.d.	111	1477	n.d.	501	9340	n.d.	363	7230	163	605	6008
La	2.00	3.02	3.68	12.32	1.39	1.68	2.81	1.73	2.43	1.56	3.42	8.06	1.86	3.05	6.81	1.91	2.87	6.77	1.24	2.81	5.10
Ce	6.56	10.67	5.95	36.65	5.98	3.14	13.08	6.40	3.27	6.79	5.40	29.78	7.72	4.86	24.48	7.82	4.77	21.79	7.22	4.91	23.14
Pr	1.41	2.09	0.55	6.13	1.13	0.37	2.55	1.27	0.49	1.47	0.46	5.59	1.41	0.42	4.26	1.50	0.49	4.15	1.68	0.51	4.20
Nd	8.08	11.06	1.93	33.71	6.59	1.49	13.87	7.56	1.63	8.09	1.50	28.73	8.05	1.25	23.41	9.13	1.60	24.58	8.48	1.71	22.88
Sm	2.62	3.36	0.19	10.17	2.28	0.21	5.00	2.60	0.32	2.70	0.22	8.39	2.88	0.19	7.19	3.14	0.24	8.28	2.99	0.24	6.32
Eu	0.83	0.85	0.41	2.60	0.69	0.54	1.80	0.69	0.55	0.77	0.53	2.30	0.90	0.56	2.20	0.84	0.68	2.28	0.83	0.48	1.98
Gd	3.22	3.79	0.22	11.80	2.65	0.25	4.91	2.77	0.12	2.86	0.17	8.38	2.95	0.05	6.99	3.22	0.18	9.26	3.53	0.16	6.45
Tb	0.54	0.69	-	2.00	0.45	-	0.67	0.56	<0.03	0.59	<0.01	1.45	0.49	<0.02	1.18	0.60	<0.02	1.61	0.66	0.03	0.99
Dy	3.66	4.53	-	11.84	2.95	-	4.71	2.83	0.06	3.31	0.06	8.61	3.13	-	7.45	3.78	0.06	9.19	3.41	0.10	6.30
Ho	0.77	0.98	-	2.41	0.46	-	0.82	0.52	-	0.74	-	1.59	0.67	-	1.51	0.77	-	1.82	0.75	-	1.16
Er	1.78	2.58	-	6.74	1.54	-	2.14	1.66	-	1.74	-	4.33	1.90	-	3.91	1.97	-	4.99	2.02	-	3.54
Yb	1.40	2.29	-	5.41	1.57	-	1.78	1.43	-	1.66	-	3.20	1.54	-	3.12	1.78	-	4.42	1.85	-	3.61
Lu	0.19	0.31	-	0.77	0.18	-	0.23	0.18	-	0.23	-	0.63	0.22	-	0.41	0.23	-	0.68	0.23	-	0.38

(-): under detection limits. (n.d.): not determined.

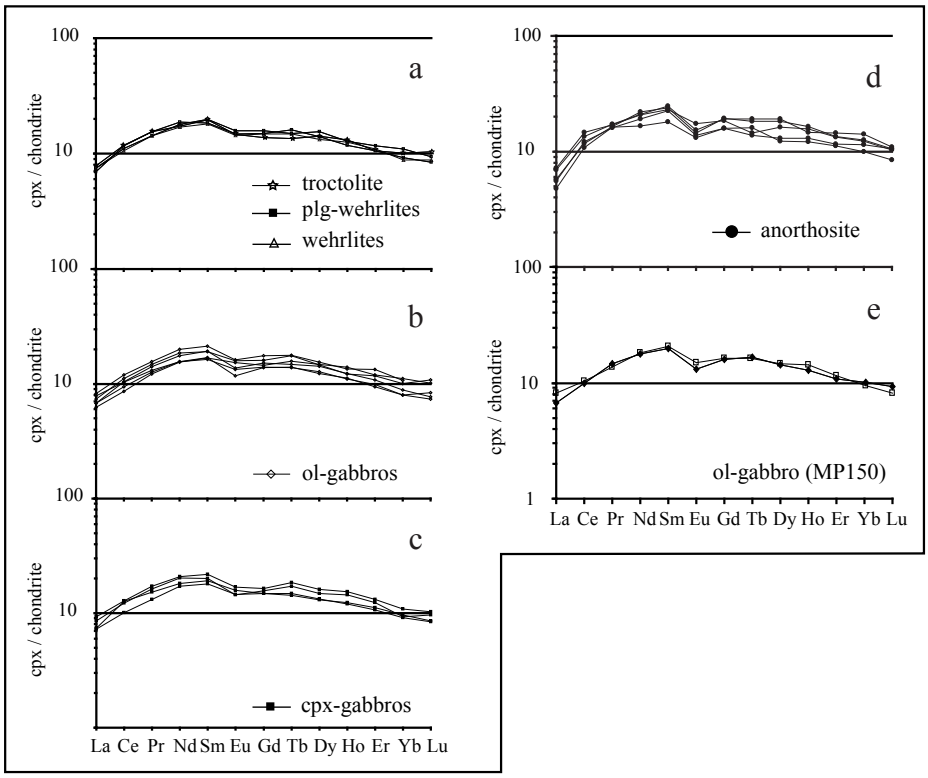

Fig. 33a: Selected REE patterns of clinopyroxenes of cumulate rocks (a-d) and example of REE variations within a single clinopyroxene of the ol-gabbro MP150 (e). Normalization values after Sun and McDonough (1989).

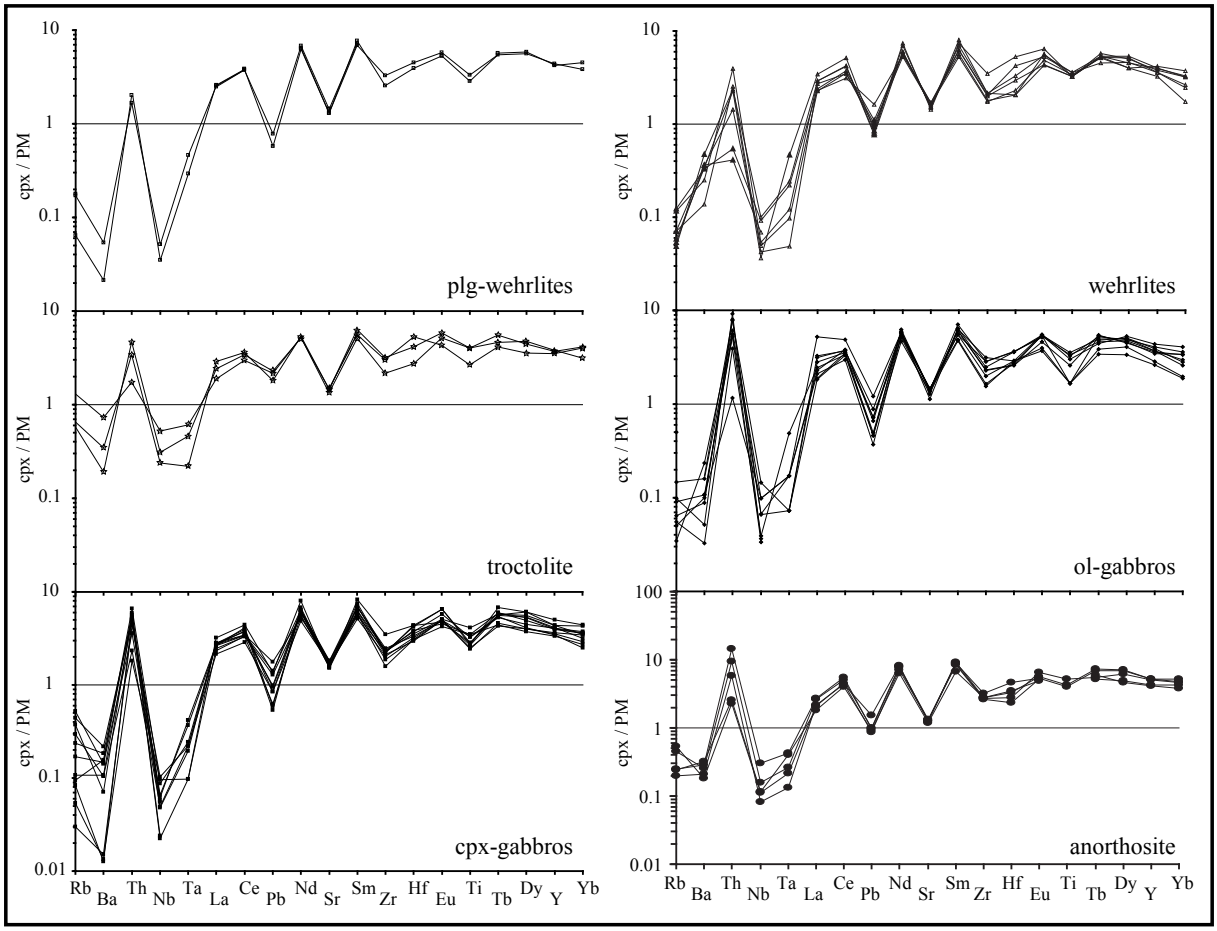

Fig. 33b: Primitive Mantle (PM) normalized trace-element patterns of representative clinopyroxenes. Normalization values after Sun and McDonough (1989).

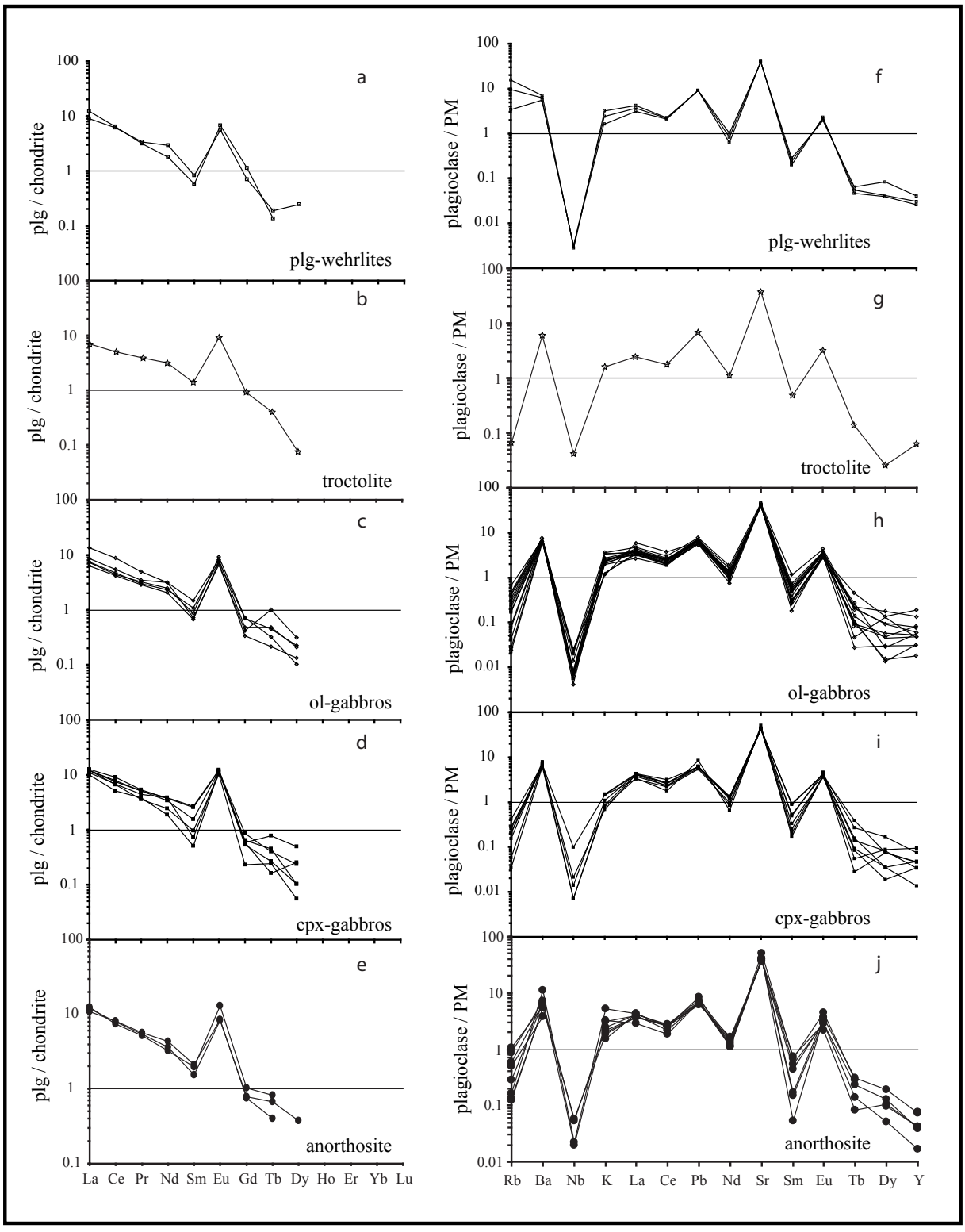

Fig. 34: (a-e) Chondrite-normalized REE patterns of representative plagioclase (C1 chondrite values after Sun and McDonough, 1989) and (f-j) Primitive Mantle (PM) normalized trace-element patterns of magmatic amphibole (normalization values are taken from Sun and McDonough, 1989).

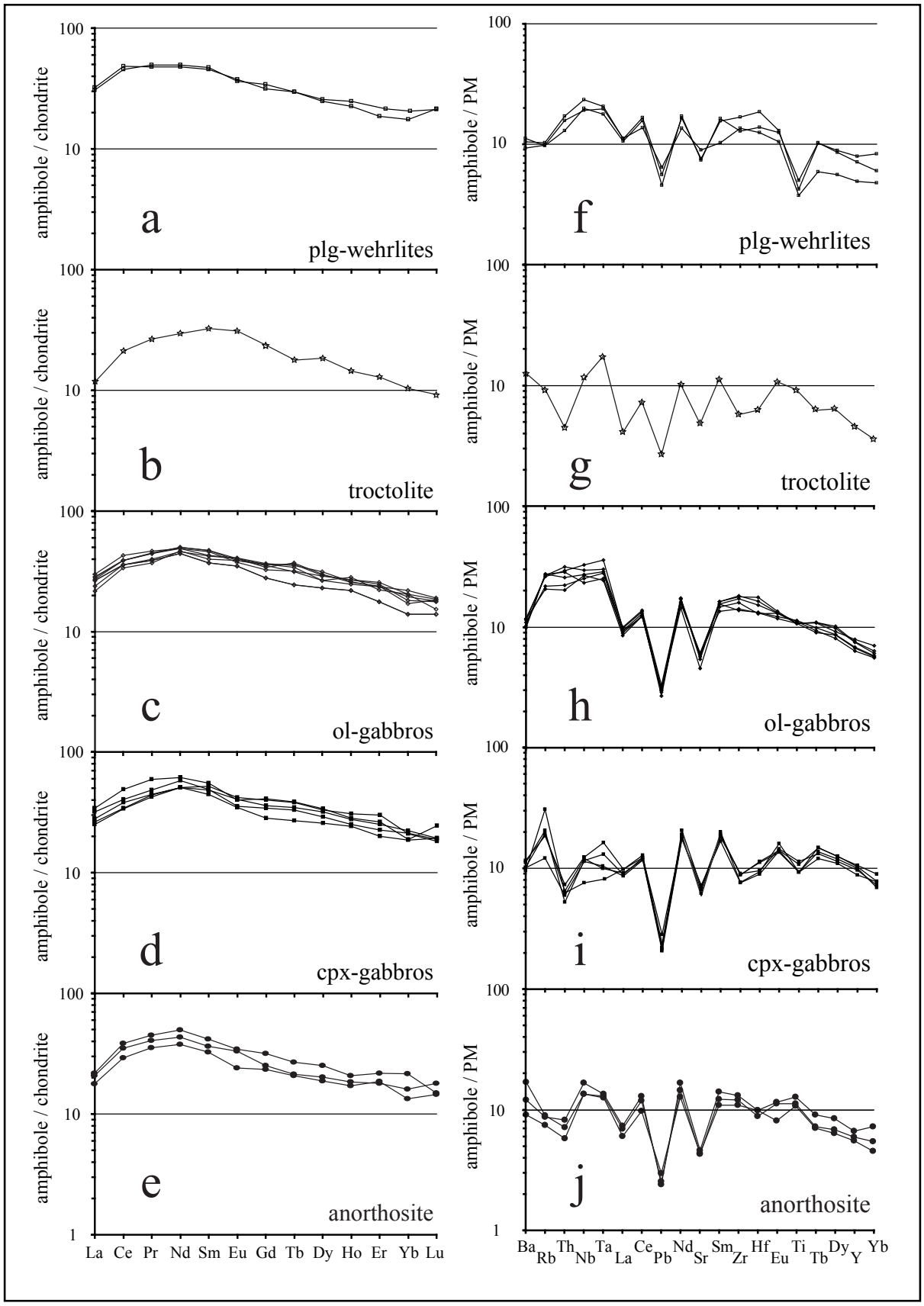

Fig. 35: Chondrite-normalized REE patterns of magmatic amphibole (C1 chondrite values after Sun and McDonough, 1989) and Primitive Mantle normalized trace-element patterns of plagioclase (normalization values are taken from Sun and McDonough, 1989).

3.4.3. Amphibole

Amphiboles have higher REE contents than clinopyroxenes (about 30 times the chondrite; Fig. 35a-e). Their REE patterns are similar and do not depend on the rock type. Multi-element primitive mantle-normalized diagrams are very different from those of clinopyroxenes, because they show positive Nb, Ta, Zr and Hf anomalies, as expected from the high distribution coefficients of these elements in amphiboles (Fig. 35f-j). Conversely, Sr is relatively depleted, as in clinopyroxenes, because this element has a higher affinity for plagioclase.

3.5. Modeling of *in-situ* crystallization process

Although strongly layered, the Mont Collon mafic complex does not show clear differentiation trends. As illustrated by the Dents de Bertol sequence (Fig. 30), major-element contents of the main lithologies do not vary systematically and largely overlap. The Mg# is monotonous and the modal abundance of major minerals remains roughly constant. At the same time, concentrations in incompatible elements like Zr, Nb, Y, Ba, and REE vary considerably. As stated by Langmuir (1989), this feature is typical for *in-situ* crystallization, where gabbros form in a solidification zone with an unknown proportion of cumulates and interstitial liquid. In this situation, the major-element composition of a gabbroic cumulate would be close to that of the magma from which it crystallizes and remain constant during differentiation, whereas incompatible trace-element contents would be controlled by a variable amount of interstitial liquid. In the Mont Collon cumulitic sequence, water-rich interstitial liquid is documented by intercumulus Ti-pargasite with high concentrations of incompatible elements. Laser ablation ICP-MS micro-analysis show that there is no trace-element zoning in minerals (but contents might vary from one crystal to the other within a sample), which means that they locally re-equilibrated with the interstitial liquid at subsolidus conditions (Hermann et al., 2001). In other words, the trace-element composition of mineral phases directly records the presence and the proportion of a former interstitial liquid.

To quantify this process, we thereafter use the model of *in-situ* crystallization developed by Hermann et al. (2001). The idea is to calculate REE patterns of all mineral phases in a given sample starting from a primitive liquid and using the equation of Langmuir (1989). These calculated patterns are then fitted to actual LA-ICP-MS data in adjusting the parameters F (degree of differentiation) and L (proportion of interstitial liquid) in equation (4). For each set of mineral data, a best fit can be calculated with corresponding F and L values.

3.5.1. Parameters used for the *in-situ* crystallization model

Partition coefficients

The first step is to determine REE partition coefficients between minerals and melt, starting with those for clinopyroxene ($D_{cpx/Melt}$). Unfortunately, available data sets in the literature are either incomplete or are not applicable to our clinopyroxene compositions, which are high in CaO (up to 23 wt%) and low in Al_2O_3 (<4 wt%). We therefore used the predictive model of Wood & Blundy (1997) with analysis MP157cpx3-2, selected for its lowest REE content (ΣREE = 25.08 ppm), its high Mg# (87.8), its weak Eu negative anomaly (Eu/Eu* ~ 0.95) and the low Nb-Zr content of the host rock. Calculations were done using a $K^{ol}_{Fe\text{-}Mg}$ of 0.30, and the pressure and temperature calculated in the above P/T section (chapter 3). $D_{pl/M}$, $D_{ol/M}$ and $D_{amph/M}$ (for plagioclase, olivine and amphibole) are then calculated using mineral/cpx partition coefficients, according to equations (1a-c) (the REE content of each mineral is measured by LA-ICP-MS):

$$REE_{pl} / REE_{cpx} = D_{pl/M} / D_{cpx/M} = cste \quad \Rightarrow D_{pl/M} = D_{cpx/M} * REE_{pl} / REE_{cpx} \qquad (1a)$$

$$REE_{amph} / REE_{cpx} = D_{amph/M} / D_{cpx/M} = cste \quad \Rightarrow D_{amph/M} \qquad (1b)$$

$$REE_{ol} / REE_{cpx} = D_{ol/M} / D_{cpx/M} = cste \quad \Rightarrow D_{ol/M} \qquad (1c)$$

The bulk rock partition coefficient $D_{rock/M}$ is calculated (2a) assuming the modal content of MP157 olivine-gabbro (48% clinopyroxene, 35% plagioclase, 15% olivine and 2% pargasite). To calculate the enrichment of elements in the residual melt, we introduce the $D'_{rock/M}$ parameter (2b) in the «Rayleigh fractionation» part of the *in-situ* crystallization equation, which takes into account that an average of 10% of melt is trapped during differentiation (this parameter does not affect drastically the modeled REE contents).

$$D_{rock/M} = 0.40\ D_{cpx/M} + 0.20\ D_{pl/M} + 0.35\ D_{ol/M} + 0.05\ D_{amph/M} \qquad (2a)$$

$$D'_{rock/M} = 0.90\ D_{rock/M} + 0.10 \qquad (2b)$$

Calculation of the initial magma composition

The starting liquid L_o is obtained using the REE composition of the «reference» clinopyroxene (i.e. with lowest REE content, MP157cpx3-2, Fig 36):

$$L_o = REE_{cpx} / D_{cpx/M} \quad (3)$$

Estimation of the degree of differentiation (F) and proportion of intercumulus liquid (L)

The whole-rock REE content (REE_{rock}) can be expressed as the sum of cumulus phases and interstitial liquid, given by Langmuir equation (4), or as the sum of the different mineral contributions (5). Boundary limits for equation (4) are set by L=0 (pure cumulate) and L=100% (frozen liquid).

$$REE_{rock} = \text{cumulus phase} + \text{interstitial melt}$$

$$= L_o (1 - F)^{D'rock/M - 1} [D_{rock/M} (1 - L) + L] \quad (4)$$

$$= 0.48\ REE_{cpx} + 0.35\ REE_{pl} + 0.15\ REE_{ol} + 0.02\ REE_{amph} \quad (5)$$

Combining equations (4) and (5) with (1a-c) (i.e. $REE_{pl} = REE_{cpx} * (D_{pl/M} / D_{cpx/M})$, etc), we extract the calculated REE content of clinopyroxene ($REEc_{cpx}$, equation 6a) and subsequently that of other mineral species (equations 6b-c).

$$\Rightarrow (6a)\ REEc_{cpx} = \frac{[L_o (1 - F)^{D'rock/M - 1} * [D_{rock/M} (1 - L) + L]}{0.48 + 0.35(D_{pl/M} / D_{cpx/M}) + 0.15(D_{ol/M} / D_{cpx/M}) + 0.02(D_{amph/M} / D_{cpx/M})}$$

$$\Rightarrow REEc_{pl} = REEc_{cpx} * (D_{pl/M} / D_{cpx/M}) \quad (6b)$$

$$\Rightarrow REEc_{amph} = REEc_{cpx} * (D_{amph/M} / D_{cpx/M}) \quad (6c)$$

The calculated $REEc_{mineral}$ are then compared with and fitted to the real LA-ICP-MS mineral data of tested sample in adjusting F and L by a trial and error procedure (Fig. 36).

3.5.2. Results and limitations of the model

Examples of measured vs. modeled mineral compositions are given in figure 36 for a wehrlite (MP243), a plg-wehrlite (MP106), ol-gabbros (MP125, MP136, and MP166), a cpx-gabbro (MP168), the troctolite (MP240) and the anorthosite (MP285). Measured compositions are means of several LA-ICP-MS analyses for all mineral species. Because of the structure of equation (4), L and F do not influence the calculated mineral REE contents in the same way. For instance, L has a much stronger effect on the LREE contents of low $D_{min/melt}$ minerals such as clinopyroxene than F. Thus, clinopyroxenes with highest amounts of Sm or Nd are modeled with the highest L values. More generally, the higher the REE contents of minerals, the higher is the proportion of calculated trapped liquid L. As a consequence of the differentiated effect of F and L in equation (4), we found in most cases unique sets of F and L values to fit accurately the measured mineral compositions. A notable exception is wehrlite MP243, for which REE clinopyroxene contents can be modeled with F = 0% and L = 20% or better with F = 35% and L = 0% (Fig. 36 and 37). This duality is certainly related to the absence of plagioclase and amphibole in the sample, which usually provide additional constraints to the fitting procedure. The main difference between the two calculations resides in a higher LREE content for F = 0% / L = 20% than for F = 35% / L = 0%, which further illustrates that F is less sensitive than L to (Light)REE concentrations. Apart from plg-wehrlite MP243, the calculated degree of fractionation F is comprised within a narrow range of 0 to 20% for all tested samples. Anorthosite MP285 displays an F value of 10%, suggesting that segregation of anorthositic material might occur early in the magma chamber. This result is in agreement with field and petrological data, but deserves confirmation, as the measured REE contents of the rare crystals of amphibole and clinopyroxene found in anorthosite MP285 cannot be fitted simultaneously (Fig. 36). The REE content of the modeled amphibole is too high, while that of the clinopyroxene is too low with a given set of F and L values. MP285 anorthosite mainly consists of plagioclase (95%-vol), which means that the measured clinopyroxenes and amphiboles might not be statistically representative. There is no clear correlation between the calculated degree of differentiation F and the differentiation index of the tested samples expressed by their $Mg\#_{cpx}$ (Fig. 38). Nevertheless, F values of 0% plot preferentially on the high $Mg\#_{cpx}$ side of the diagram, as expected for weakly differentiated rocks. Additional data would be necessary to confirm this trend, but in any case, F values between 0 and 20% are geologically reasonable within the observed range of $Mg\#_{cpx}$. The calculated proportion of trapped liquid L is more variable than F. Some samples are modeled as pure cumulates, without interstitial liquid (L=0%, i.e. troctolite MP240), whereas the maximum L is 35% (plg-wehrlite MP106). These values are consistent with mineralogical and chemical features. There is a good correlation between L values and the modal proportions of magmatic amphibole (Fig. 39a), which makes this mineral a good proxy for the proportion of interstitial melt. L is also consistent with whole-rock concentrations of incompatible trace elements such as Zr and REE (Fig. 39b and 40), unlike F (Fig. 39c). This confirms our assumption that incompatible trace-element distribution is essentially controlled by the proportion of interstitial liquid L rather than by the degree of differentiation F.

The proportion of trapped liquid L is not correlated with the $Mg\#_{cpx}$ of the tested samples (Fig. 38), which is not surprising, as the proportion of interstitial melt in a cumulitic sequence is decoupled from the degree of evolution of the latter in a given range of magma composition. It must be pointed out that a large L might shift down $Mg\#_{cpx}$ by a few hundredth of unit through reequilibration between interstitial melt and cumulus clinopyroxene (Barnes, 1986). Interestingly, plagioclase core composition is somehow correlated with L values. Samples with lowest L contain the most anorthositic plagioclase (MP136 (L=5%): plg_{core} An = 82.6; MP125 (L=10%): plg_{core} An = 72.8; MP168 (L=10%): plg_{core} An = 72.8), whereas plagioclase in plg-wehrlite MP106 (L=35%) is significantly more sodic (plg_{core} An = 63.1-69.2). This feature agrees well with the late intercumulus (thus more sodic) nature of plagioclase in plg-wehrlites.

The in-situ crystallization model reaches its limitations with rock containing high content of REE-bearing minerals (i.e. apatite or zircon), which strongly influence the REE budget. Mineral alteration and high modal proportion of zircon in pegmatitic gabbros prevents any quantitative modeling. But we suspect that these rocks represent almost pure, fluid-rich melts, differentiated, although without much plagioclase subtraction.

In this model, all non-cumulitic material has been considered as local interstitial melt L, trapped in the solidification zone. But field observation of veinlets of anorthositic composition locally crosscutting the layered lithologies evidence that some melt must have migrated through the cumulitic sequence and eventually been trapped in a more or less distant place. Such situations are open systems with mixing of intercumulus liquids of different origins and possibly contrasting composition. The proposed model is not able to resolve these complex open systems, which are not well enough constrained, but migrating liquids could be partly responsible for the observed dispersion of points in some correlation diagrams like L vs Zr (Fig. 39).

Absence of significant differentiation in the cumulitic pile of Dents de Bertol, which is several hundred meters high, raise the question of how this sequence built up. Recurrent lithologies with similar cumulus mineral compositions point to an efficiently convective magma chamber, with possible periodic replenishment. Heterogeneities within initial Sr isotopic ratios (Monjoie et al, in prep) strongly support the latter mechanism.

Fig. 36 (previous page): a) partition coefficient values ($D_{cpx/melt}$) for clinopyroxene based on the predictive model of Wood and Blundy (1997). Partition coefficients for plagioclase and amphibole are calculated from $D_{cpx/M}$. $D_{rock/M}$ = bulk partition coefficient considering any trapped liquid and $D'_{rock/M}$ = bulk partition coefficient with 10% of liquid remaining in the cumulate pile, b) Chondrite-normalized REE pattern of the reference clinopyroxene used for in-situ crystallization modeling. c-j) Comparison of measured (filled symbol) and calculated (open symbol) chondrite-normalized REE patterns of clinopyroxene (■), plagioclase (●) and amphibole (▲). F = degree of differentiation with respect to the reference clinopyroxene and L = the amount of trapped liquid.

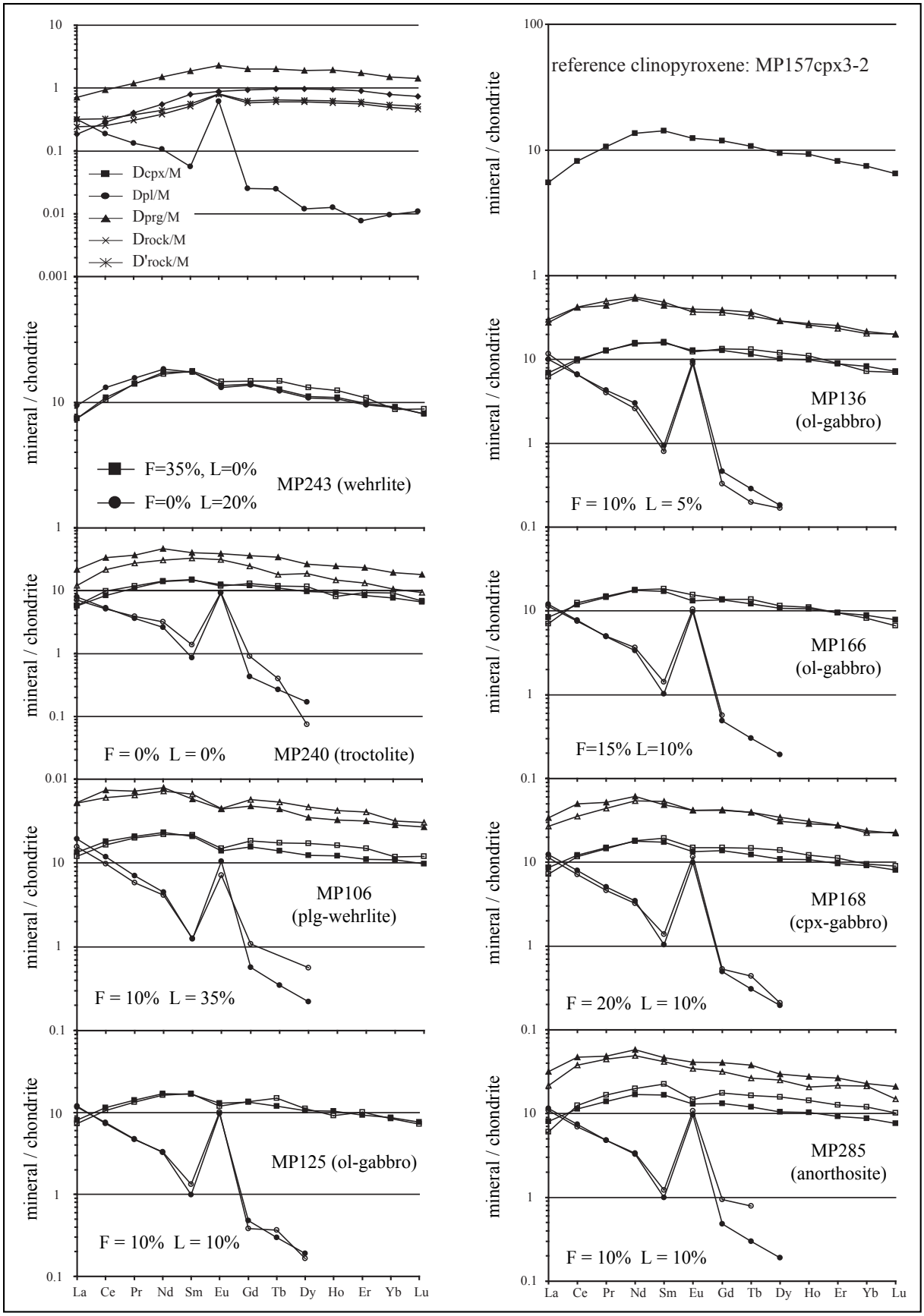

Fig. 36: legend on the next page.

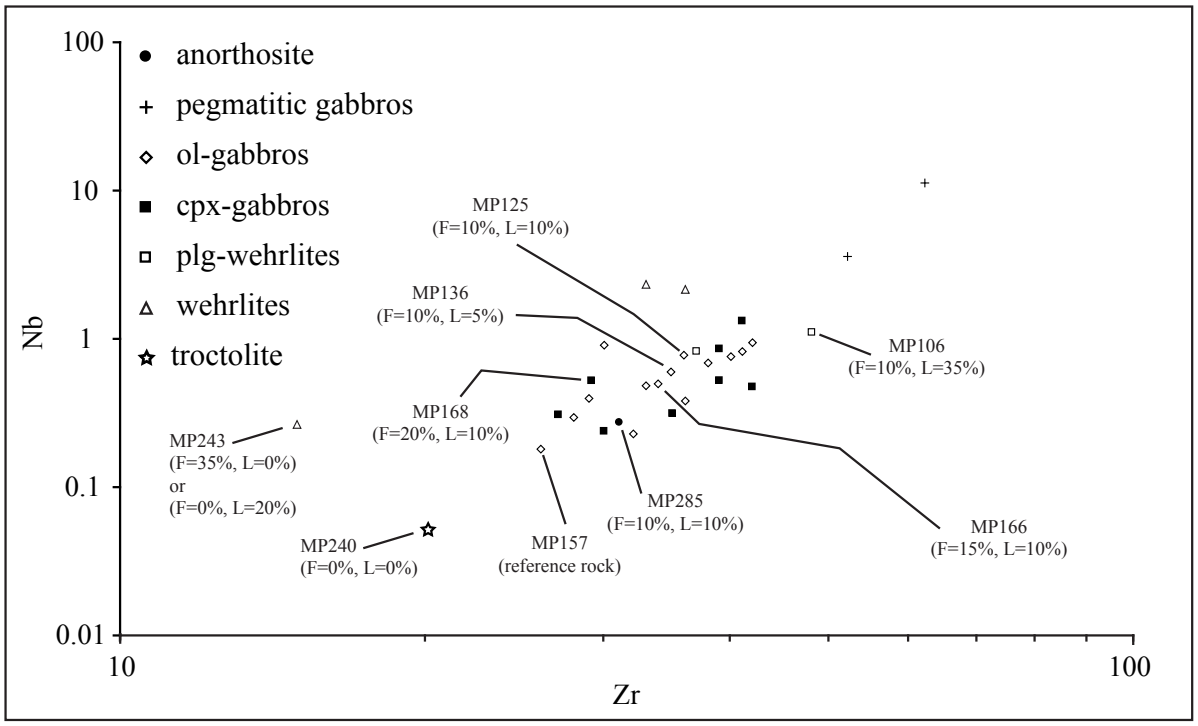

Fig. 37: Variation binary diagrams using Zr as differentiation index versus Nb (in ppm). Sample numbers are indicated with the modeled F and L parameters.

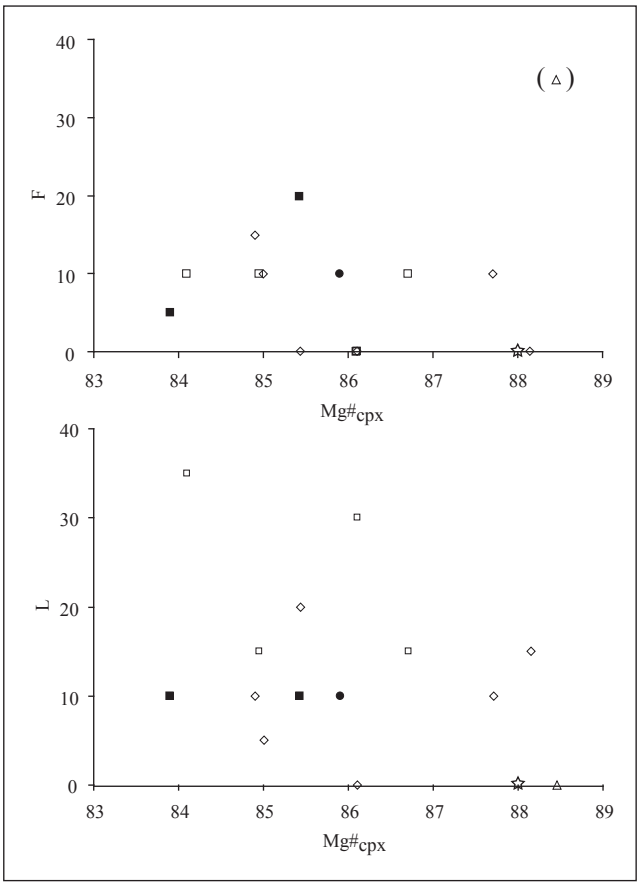

Fig. 38: Variation diagrams between the percentage of interstitial liquid (L) and the degree of differentiation F (%) versus the $Mg\#_{cpx}$ for cumulative rocks of the Mont Collon.

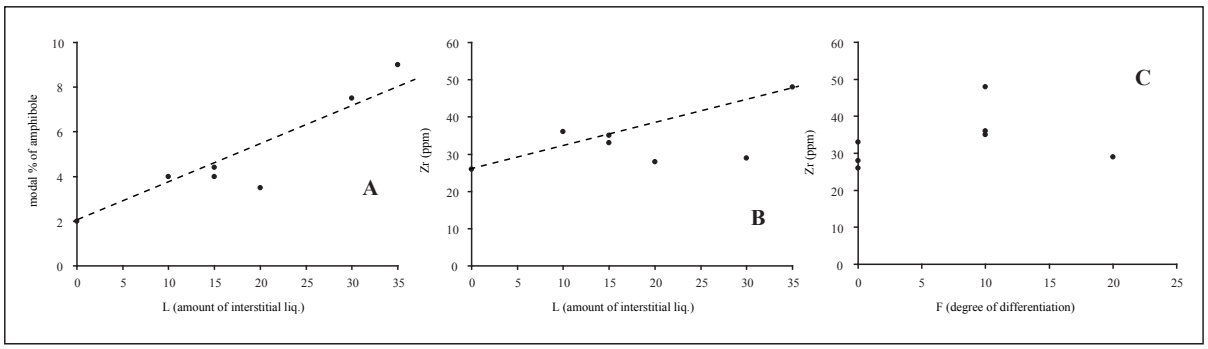

Fig. 39: Variation diagrams between the percentage of interstitial liquid (L) and the modal amount of interstitial magmatic amphibole and the Zr (ppm) content (a-b), and the degree of differentiation F (%) and the Zr (ppm) content (c) in the modeled rocks.

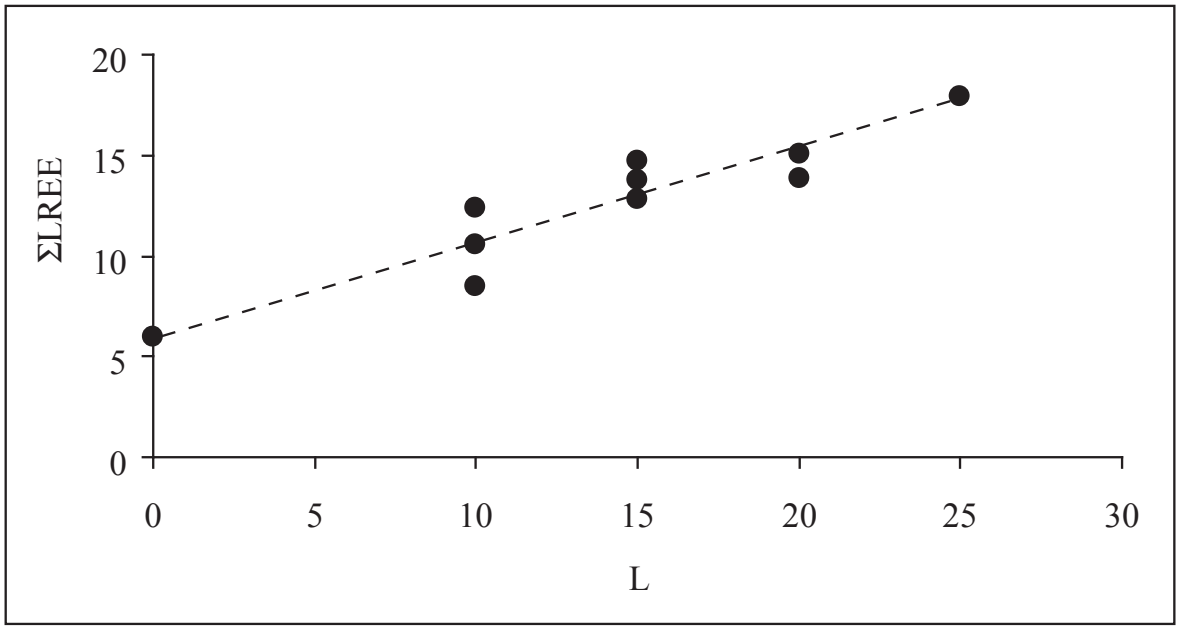

Fig. 40: Variation diagrams between the percentage of interstitial liquid (L) and the total REE content (ppm) in the modeled rocks.

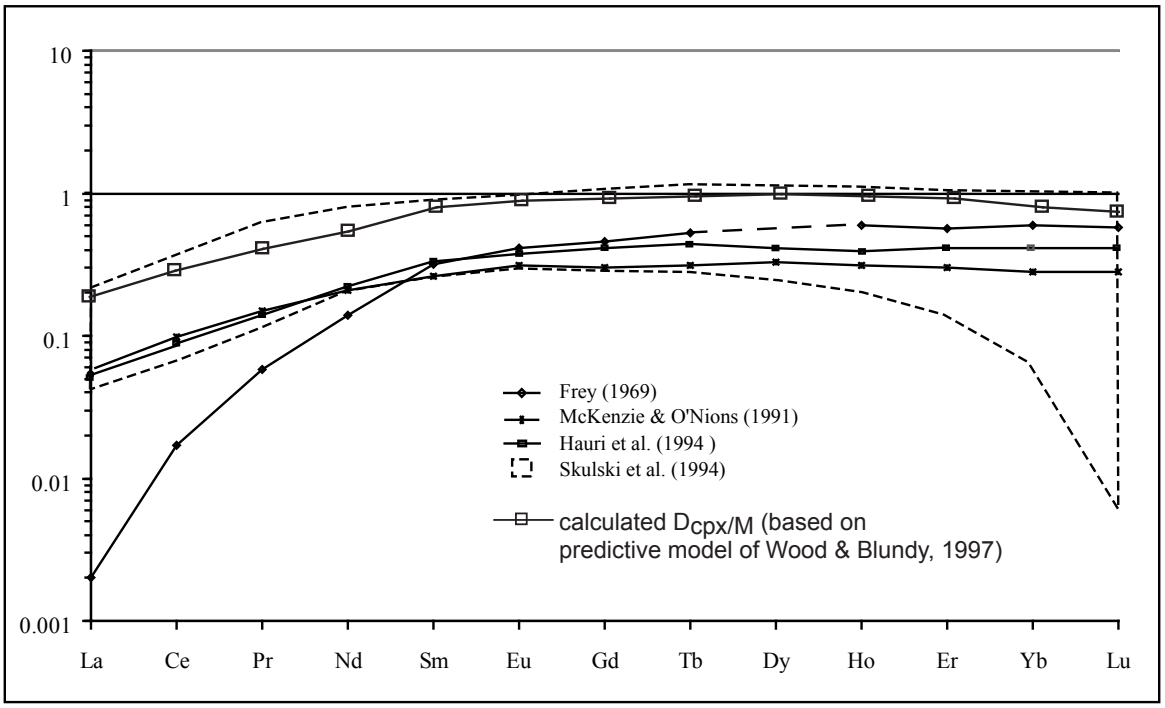

Fig. 41: Compilation of different clinopyroxene / melt partition coefficients from the literature. □: calculated $D_{cpx/M}$ from the reference clinopyroxene based on the predictive model of Wood and Blundy (1997).

Table 11: Calculated with the method of Wood and Blundy, 1997 (a) and published (b) partition coefficients between clinopyroxene and melt (lower and upper values are given when available).

a	$D_{cpx/M}$	$D_{pl/M}$	$D_{amph/M}$	$D_{ol/M}$	$D_{rock/M}$	$D'_{rock/M}$
La	0.204	0.294	0.804	0.000012	0.217	0.295
Ce	0.312	0.204	1.281	0.000024	0.247	0.322
Pr	0.445	0.151	1.545	0.000061	0.298	0.368
Nd	0.597	0.115	2.028	0.000305	0.367	0.431
Sm	0.862	0.051	2.415	0.000549	0.480	0.532
Eu	0.954	0.708	2.985	0.0015	0.766	0.789
Gd	1.021	0.037	3.115	0.0031	0.566	0.609
Tb	1.057	0.026	3.350	0.0042	0.584	0.626
Dy	1.060	0.019	3.001	0.0079	0.577	0.619
Ho	1.034	0.044	2.776	0.0118	0.569	0.612
Er	0.987	0.030	2.829	0.029000	0.545	0.591
Yb	0.868	0.015	2.269	0.0469	0.474	0.527
Lu	0.807	0.020	2.219	0.076	0.450	0.505

b	Frey (1969)	Skulski et al. (1994)		McKenzie & O'Nions (1991)	Irving & Frey (1984)		Hauri et al. (1994)
		Lower values	Higher values		Lower values	Higher values	
La	0.002	0.041	0.212	-	0.02	0.10	0.05
Ce	0.02	-	-	0.10	0.03	0.20	0.09
Pr	0.06	0.11	0.63	0.15	0.04	0.30	0.14
Nd	0.14	0.20	0.80	0.21	0.07	0.50	0.22
Sm	0.32	-	-	0.26	0.10	0.80	0.33
Eu	0.41	-	-	0.31	0.20	0.70	0.37
Gd	0.46	-	-	0.30	0.20	0.80	0.41
Tb	0.53	0.28	1.12	0.31	0.30	0.90	0.41
Dy	-	-	-	0.33	0.30	0.90	0.41
Ho	0.60	-	-	0.31	0.30	1.00	0.41
Er	0.57	-	-	0.30	0.30	1.00	0.41
Yb	0.60	-	-	0.28	0.20	0.90	0.41
Lu	0.58	0.01	0.96	0.28	0.10	0.90	0.41

The calculated $D_{cpx/M}$ using the model of Wood & Blundy (1997) largely differs from most published values (calculated and some published D values are given in figure 41 and Tables 11a and b). Nevertheless, they are close to the upper values recommended by Skulski et al. (1994) for clinopyroxene from alkali olivine basalt. These differences have important consequences for the *in-situ* crystallization model, which is very sensitive to $D_{cpx/M}$. For example, modeled clinopyroxenes indicate a lower F value at constant L using lower $D_{cpx/M}$ than those calculated with the model of Wood and Blundy (1997).

3.6. Parental melt of the Mont Collon cumulative rocks

The parental melt composition of the Mont Collon intrusion is unknown and can hardly be deduced from whole-rock analyses, as all are cumulates (L max = 35% in the model calculations) and any rock has been modeled as a pure liquid (L = 100%). The initial liquid L_0 calculated in the model (equation 3) is only a first order approximation, because (i) it relies on a reference clinopyroxene composition prone to re-equilibration with interstitial liquid after crystallization, (ii) the Mg# of the cumulates look too low (< 78) to consider these rocks as the products of a primitive magma. It is highly probable that L_0 corresponds to a magma which underwent some degree of differentiation before intrusion in the magma chamber and/or that the earliest cumulates of the system are not outcropping (e.g. absence of dunites). To account for this, we tentatively tried to back calculate the effect of some differentiation on L_0, assuming that olivine first reached the liquidus, followed by the two pyroxenes (orthopyroxene was probably present especially if P was higher than in the magma chamber) and plagioclase (i.e. a gabbronorite assemblage). In a first approximation, we consider that about 10% of dunite (90% ol and 10% cpx) and 10% of ol-gabbronorite (20% cpx, 40% plg, 15% ol and 25% opx) were extracted before crystallization of the outcropping gabbroic rocks (i.e. before the liquid reaches composition L_0 of equation 3). The resulting liquid (parental melt in Fig. 42) is similar to L_0, with lower REE concentrations and virtually no Eu anomaly. The calculated parental melt is enriched in LREE (up to 20 times the chondritic abundances) and comparatively depleted in HREE (<10 times the chondritic values), with La_N/Sm_N = 1.5 and Sm_N/Yb_N = 1.9. The LREE values and fractionation pattern are close to the upper bound of the transitional MORB range (Fig. 42a), but distinctly lower in HREE, which might be due to the presence of garnet in the mantle source. The most striking feature of the parental melt composition lies in its strong negative Nb anomaly when normalized to the primitive mantle (Fig. 42b), as also observed in whole-rock and mineral analyses. A weak positive Sr anomaly is noticeable; calculations show that this anomaly in the melt is more sensitive to the contribution of the clinopyroxene than of the plagioclase. Compared to the classical basalt types, the calculated parental melt is intermediate between T-MORBs and more alkaline basalts. This is not a typical tholeiitic melt, as it is hydrated, high in Zr (26-46 ppm) and relatively low in Fe and Ti; this is not an alkaline melt either with its low contents in Na_2O, K_2O and its negative Nb-Ta anomalies. The Mont Collon parental melt thus appear to be of transitional affinity.

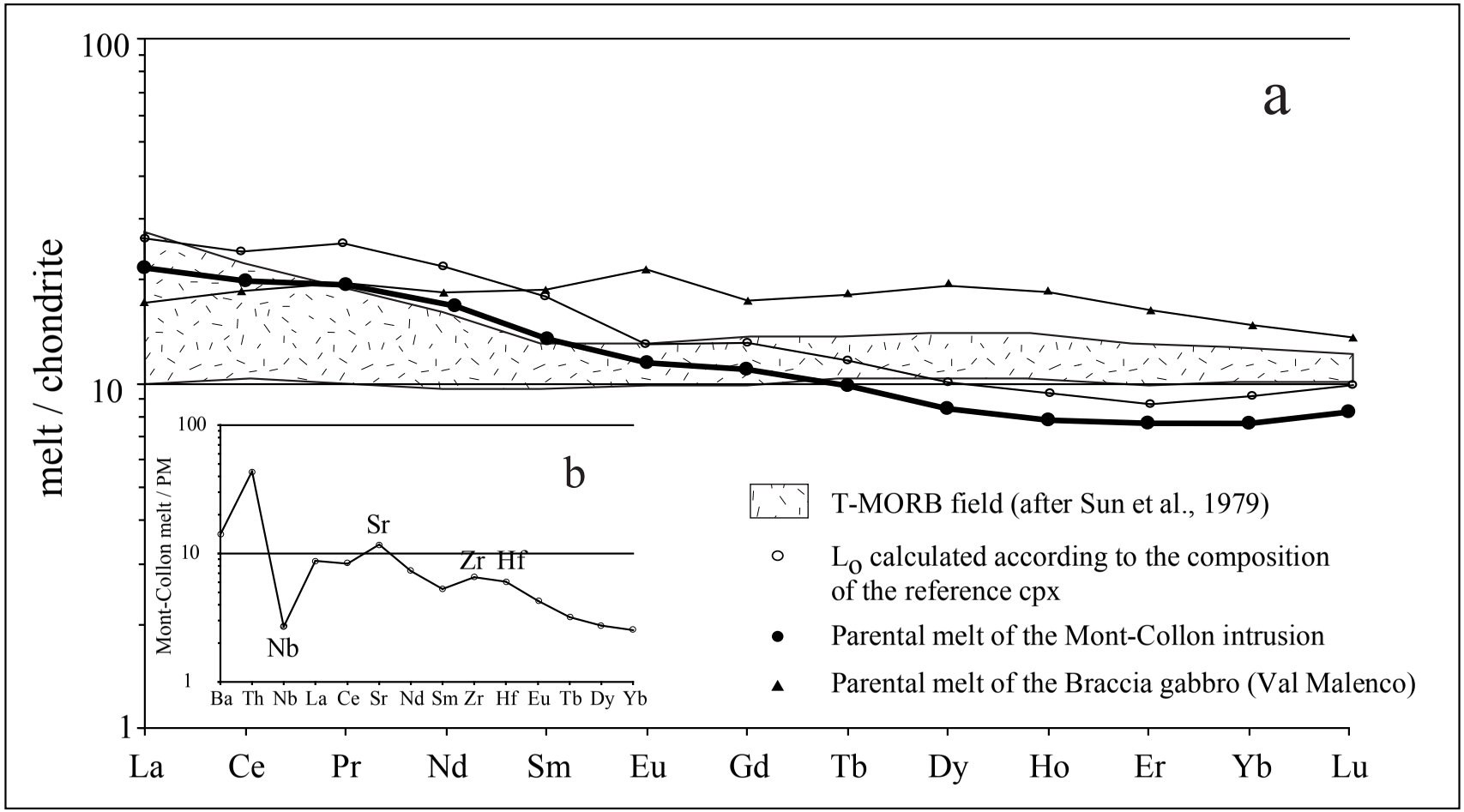

Fig. 42: a) Chondrite-normalized comparison of the calculated parental melt of the Mont-Collon intrusion with T-MORB (grey field, after Sun et al., 1979), the Braccia gabbro (Hermann et al., 2001). L_o is the calculated melt in equilibrium with the reference clinopyroxene. Normalizing values after Sun and McDonough (1989). b) Primitive normalized trace-elements pattern of the calculated parental melt of the Mont Collon mafic complex (normalization values are taken from Sun and McDonough, 1989)

3.7. Discussion

Despite its layered structure, the Mont Collon intrusion is a weakly differentiated pluton. Isotopic data indicate (see chapter 6) that the numerous acidic dikes originate by partial melting of the country rock (back-dyking), whereas the few high Fe-Ti melanocratic dikes are much younger (260 Ma, chapter 5 and Monjoie et al., submitted) and do not belong to the same magmatic system. About 95% of the outcropping facies are made of an assemblage of olivine, plagioclase, clinopyroxene and a little amphibole. Anorthosites are extremely rare and evolved facies like Fe-Ti melanocratic dikes have not been found; either they have been eroded, are buried or never existed. As stated by Langmuir (1989), this lack of differentiation, coupled with highly variable concentrations in incompatible trace elements, is typically expected for in situ crystallization in the bottom and margins of a convecting magma chamber. Whether other processes like periodic replenishment of the magma chamber took place or not is difficult to assess. In the Dents de Bertol layered sequence, no chemical or isotopic evidence support such a mechanism, but it should be kept in mind that large part of the former inner magma chamber disappeared by erosion. The pegmatitic gabbros represent the only mafic facies without cumulitic features. They are randomly distributed in the massif as meter-sized pockets. These gabbros are characterized by the highest REE and LILE concentrations ever found in the complex, except for Rb and Ba (Fig. 32), which were probably remobilized by late-magmatic fluids (plagioclase is always heavily altered). REE patterns are moderately fractionated (La_N/Yb_N = ~ 2) and the negative Eu anomaly is small to absent. Mineral alteration prevents any quantitative modeling, but we suspect that these rocks represent almost pure, fluid-rich melts, differentiated, although without much plagioclase subtraction.

At the Carboniferous-Permian boundary, the Variscan Range collapse is marked by the emplacement of mantle-derived mafic complexes related to intra-continental extension and crustal thinning (e.g. Dal Piaz, 1993). In the Western Alps, this magmatism is essentially represented by the Austroalpine and South alpine Permian Mafic Complexes (=PMC) of Val Malenco (281 ± 19 Ma, Müntener et al., 2000; Hermann et al., 2001), Sondalo (300 ± 12 and 280 ± 10 Ma, Tribuzio et al., 1999), Ivrea-Verbano (285-290 Ma, Rivalenti et al., 1980; Sinigoi et al., 1994; Mulch et al., 2002) and Mont Collon (284 ± 0.6 Ma, chapter 5 and Monjoie et al., submitted). The Mont Collon complex shares common features with these contemporaneous Austroalpine mafic complexes, but also significant differences. The Braccia pluton (Val Malenco) displays the chemical and mineralogical characteristics of a deeper, drier, more tholeiitic and more differentiated intrusion than the Mont Collon. It intruded at the crust-mantle boundary (Müntener et al., 2000) and shows a much wider range of Mg# (from 80 to 50) and REE contents from olivine gabbronorites (Mg-gabbros) to ilmenite gabbronorites (Fe-gabbros) (Hermann et al., 2001). Olivine is rare and orthopyroxene quite widespread (deeper and drier magma than in the Mont Collon). Clinopyroxene is systematically higher in Al_2O_3 (pressure effect) and FeO*, and exhibits a wider range of REE contents. Plagioclase has lower anorthite

component (labradorite, drier magma), but displays large REE variations. Ti-pargasite is a minor interstitial magmatic phase and the main accessory mineral is ilmenite. Reaction coronas are well developed like in the Mont Collon (Müntener et al., 2000). In situ crystallization is thought to be the dominant magmatic process (Hermann et al, 2001).

The calculated REE pattern of the Braccia parental melt (Hermann et al, 2001) is rather flat, similar to that of a transitional tholeiitic MORB with La_N/Yb_N close to 1.2 (Fig. 42). It is much less depleted in HREE than the parental melt of the Mont Collon intrusion, which led the above-mentioned authors to favor a spinel-peridotite mantle source. Although Hermann et al. (2001) do not model the Nb-Ta content of their parental melt, it probably exhibits a negative anomaly similar to that of the Mont Collon, considering the composition of the reference clinopyroxene they used for their modeling.

The Sondalo complex (Northern Italian Alps, Tribuzio et al., 1999) is mainly composed of troctolites and gabbronorites, intruded at mid-crustal level like the Mont Collon. Major- and trace-element chemistry of clinopyroxene and plagioclase (a bit less calcic) is very similar to that of the Mont Collon intrusion, despite the abundance of orthopyroxene in the assemblage. Tribuzio et al. (1999) calculated a melt composition on the basis of a poikilitic clinopyroxene, which cannot represent a parental melt. They suggest that the primary melt of the Sondalo complex should have a tholeiitic affinity with a slight REE enrichment relative to N-MORBs.

In summary, all major Permian mafic intrusions from the Austroalpine domain have a tholeiitic or transitional magmatic affinities. Mineral chemistry is partly controlled by the level of intrusion and water content of the magmas. These factors are also responsible for the restricted development of orthopyroxene in the Mont Collon (low P and high water content). Compared to Braccia and Sondalo, the Mont Collon parental magma is slightly enriched in LREE and LILE and substantially more REE fractionated. The latter feature might be related to crustal contamination and/or a characteristic of the mantle source. In the latter case, an enriched lithospheric mantle would be a suitable candidate, which will be confirmed by isotope data (chapter 6 and sMonjoie et al., in prep.).

3.8. Conclusion

The well-preserved Mont Collon pluton results from the intrusion at mid-crustal level (ca. 0.6 GPa) of a basic magma with transitional affinity into a magma chamber. The parental melt is characterized by a relative enrichment in LREE and Th, depletion in HREE (La_N/Yb_N=2.85), and strong negative Nb-Ta anomalies when normalized to primitive mantle. Other Permian mafic complexes in the Alps derive from comparatively less enriched magmas.

Uncoupling between monotonous major-element chemistry and highly variable incompatible trace-element concentrations across this well layered, but poorly differentiated intrusion, is best explained by an in situ crystallization process. Quantitative modeling points to 0 to 35% of interstitial liquid (L) in the cumulates for a maximum differentiation rate (F) of 45%, relative to the less evolved composition outcropping in the massif. L is quite variable along a cumulitic sequence, pointing to irregular convection (?) efficiency in the magma chamber. Rare pegmatitic gabbros might represent the only pure, fluid-rich liquids within the massif.

Chapter 4: U/Pb and $^{40}Ar/^{39}Ar$ dating

Chapter 4: U/Pb and $^{40}Ar/^{39}Ar$ dating

4.1. Introduction

The end of the Variscan orogeny is characterized by three distinct magmatic events: Early Carboniferous, Late Carboniferous-Early Permian, and Late Permian. In the Early Carboniferous, acid intrusions were emplaced during an extensional event related to strike-slip faults in the basement areas of the Alps such as the External Crystalline Massifs and the Penninic domain (von Raumer et Ménot, 1989; Dal Piaz, 1993; von Raumer et al., 1993; Debon et al., 1994; Ménot et al., 1994). At the Carboniferous-Permian boundary, the Variscan Range collapse is marked by the emplacement of several mafic complexes and K-rich magmas related to intra-continental extension and crustal thinning. In the European Alpine belt, the late Carboniferous-Early Permian mafic magmatism is essentially distributed in the Austroalpine and South Alpine domains and brings good evidence for a major melting event. It must be distinguished from the ophiolitic gabbros of the Jurassic Tethyan rifting (Rampone et al., 1998; Costa and Caby, 2001) and clearly dated. The Permian Mafic Complexes (=PMC) of Val Malenco (Müntener et al., 2000; Hermann et al., 2001), Sondalo (Tribuzio et al., 1999), Ivrea-Verbano zone (Rivalenti et al., 1980; Sinigoi et al., 1994) and Mont Collon mafic complex (Dal Piaz et al., 1977 and this study) are likely related to this Late Carboniferous-Early Permian event. Some of these complexes are dated e.g. Val Malenco (ca. 281 ± 19 Ma), Sondalo (ca. 300 ± 12 Ma and 280 ± 10 Ma), others not (the Mont Collon mafic complex).

The pre-Triassic basements, including sedimentary and magmatic rocks belonging to the Variscan cycle, exposed in the Alpine belt have underwent severe metamorphic conditions and deformation phases. In contrast, the Mont Collon mafic complex is remarkably well-preserved. Dating this complex will allow adding new constraints on the evolution of the Variscan orogeny. Thus, the aim of this chapter is to obtain accurate ages for the emplacement of the mafic and acid rocks, and the Fe-Ti Fe-Ti melanocratic dikes exposed in the Dents de Bertol area in order to confirm that a late-Variscan basic magmatism occurred at the Permo-Carboniferous boundary in this segment of the belt, i.e. the Austroalpine Dent Blanche nappe. So, we present here new ages on the Mont Collon based on U/Pb zircon and $^{40}Ar/^{39}Ar$ amphibole dating.

4.2. Previous age determinations for the Mont Collon intrusion

Dal Piaz et al. (1977) dated the Mont Collon and Matterhorn intrusions. They analyzed biotites extracted from pegmatitic pyroxenite outcropping in the Matterhorn area, and fine grained quartz diorite and pegmatitic plagioclase veins exposed in the Dents de Bertol area. They obtained ages ranging from 246 ± 8 Ma (by K/Ar method) to 257 ± 6 Ma (Rb/Sr corrected age), which were interpreted as cooling ages.

4.3. Ages of other Permian Mafic Complexes

The literature provides several other dating on this crucial period of the Variscan cycle. Bussy et al. (1998) dated a metagranitoid, sampled south of the Matterhorn (Swiss coordinates: 616900/89250/2600) and similar to that of the Mont Collon country rocks (see in chapter 2, the petrological description of the Arolla orthogneisses). It yielded small euhedral, pink zircons with some resorption features. Two multigrain fractions (8 short prisms [9] and 4 needles [10], Table 14) yielded the same age of 289 ± 2 Ma (Fig. 43), interpreted by Bussy et al. (1998) as the intrusion age of the metagranite.

The Sermenza gabbroic and dioritic masses belong to the internal unit of the polycyclic basement of the Sesia zone (Venturini et al., 1996). The main rock type of this basement unit is a layered cumulitic high Mg-, low Ti-gabbro. It consists of plagioclase, hornblende, clinopyroxene, magnetite ± zoisite, white mica, and chlorite and is geochemically similar (Venturini et al., 1996) to the Dent Blanche/Sesia Mg-rich metagabbros. The dated metagabbro sample (913az, for sample location, description and chemical composition, see Venturini et al., 1996) yielded large pink zircon fragments from which three multigrain fractions were selected [11] and [13], see Table 14) which yielded an age of 288 + 2 / 4 Ma (Fig. 43). This age was proposed for the intrusion of the Sermenza mafic stock (Bussy et al., 1998), which is contemporaneous (within errors) with the Val Mastallone gabbroic mass from the neighboring Ivrea zone (285 + 7 / - 5 Ma, Pin, 1986). The Braccia gabbro (Val Malenco), which is petrologically and geochemically similar to the Mont Collon complex, has been dated at 281 ± 19 Ma (Hansmann et al., 1996 and 2001).

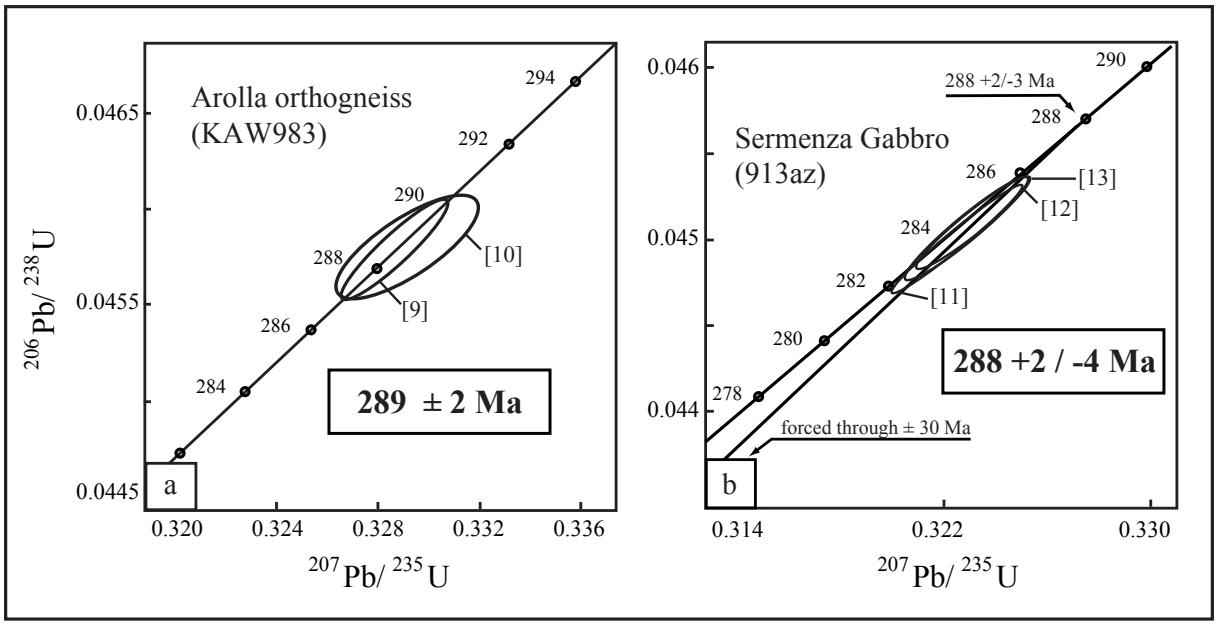

Fig. 43: U/Pb Concordia diagram for the Arolla Series orthogneisses and the Sermenza gabbro. Error ellipses are given at the 95% confidence level). Numbers in [ ] refer to the mineral fraction listed in table 13.

4.4. Sampling and analytical procedures

4.4.1. Samples choice for U/Pb on zircon dating

We sampled the two rock types that are the most suitable to hosted zircons, i.e. a pegmatitic gabbro and a quartz-rich pegmatitic dike. Pegmatitic gabbros provide some good samples for U/Pb dating because of their higher zircon content than the other mafic rocks (i.e. the cumulates). The sampled pegmatitic gabbro MP4 is exposed at the base of the Mont Collon on its northern side (Fig. 44). The quartz-rich pegmatite MP2 occurs as a decimeter-thick dike crosscutting the magmatic fabric of the pegmatitic gabbro MP4 (Fig. 45). Major- and trace-element contents of whole rocks are given in Table 12.

4.4.2. Sample preparations

Zircons were extracted from 30 - 40 kilograms of samples according to the procedure described in Bussy and Cadoppi (1996). Selected crystals were air-abraded (Krogh, 1982) to suppress post-magmatic overgrowths and to reduce the uncertainties for the common lead corrections. From a population of approximately 250 suitable zircons, we selected crystals by hand picking under a binocular microscope without impurities (as mineral inclusions), cracks, central canals or inherited cores to obtain the most concordant ages in order to follow closely the procedures described in Schaltegger et al. (1999). Isotopic measurements were done on a

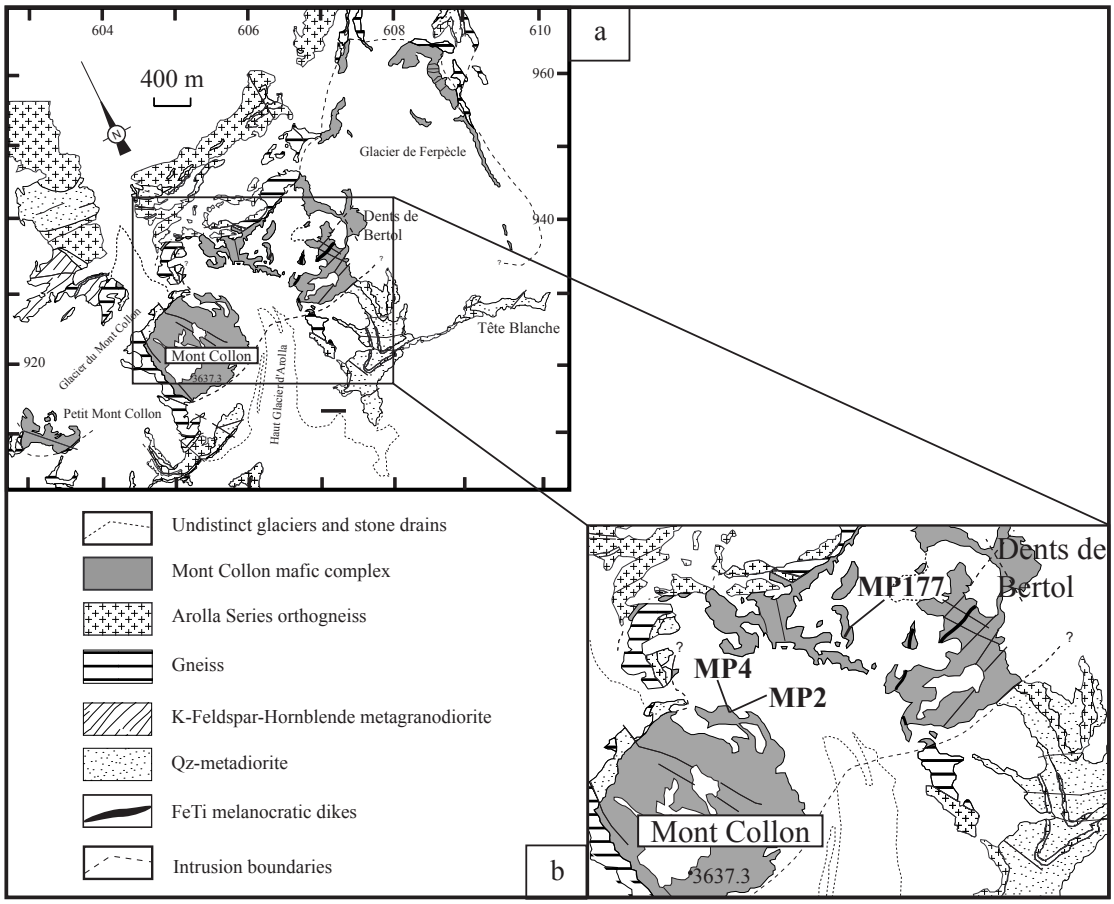

Fig. 44: Localization of the dated samples MP2 (quartz-rich pegmatite), MP4 (pegmatitic gabbro) for the U/Pb zircons dating, and MP177 (Fe-Ti melanocratic dike) for the $^{40}Ar/^{39}Ar$ amphibole dating).

Finnigan MAT 262 mass spectrometer at the ETH (Zurich). Data reduction was done using the Isoplot software of Ludwig (1998). Errors are reported at the 95% confidence level (2σ). Decay constants are those reported by Jaffrey et al. (1971).

4.4.3. Choice of samples for $^{40}Ar/^{39}Ar$ on amphibole dating

The Fe-Ti melanocratic dike MP177 chosen for dating, is exposed in the Dents de Bertol area and crosscuts all the rocks facies of the intrusion (Fig. 44 and 45b-c, composition is given in Table 12). The melanocratic dikes are poor in zircons and extracted zircons appeared too small to provide accurate U/Pb dating. Then, we selected the $^{40}Ar/^{39}Ar$ amphibole dating, considering the high modal amount of kaersutite in these dikes (selected mineral major- and trace-element contents are given in Table 13).

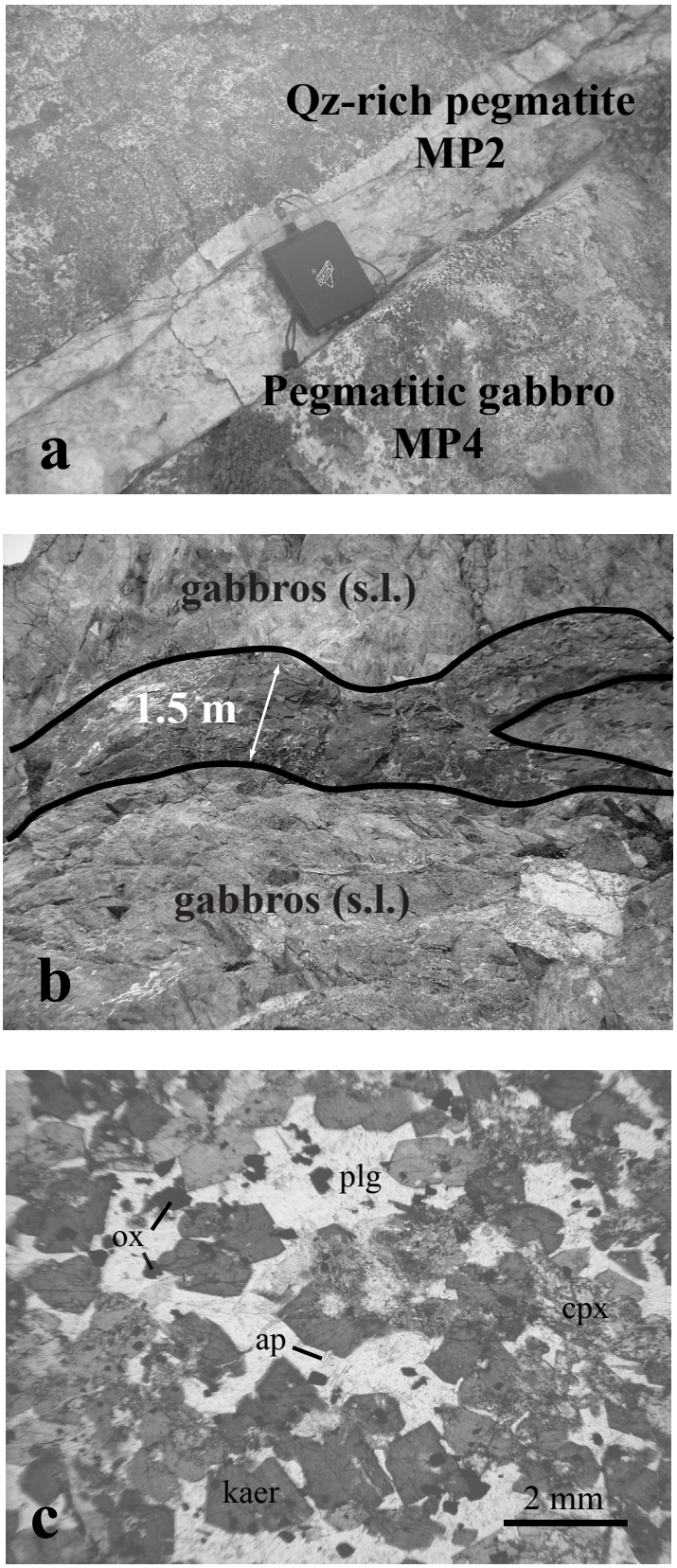

Fig. 45: a) field relationship between MP4 (pegmatitic gabbro) and MP2 (quartz pegmatite) on the northern wall of the Mont Collon, b) example of Fe-Ti melanocratic dike (located on the Dents de Bertol), c) thin section detail of the Fe-Ti melanocratic dike MP177 (kaer = kaersutite, cpx = clinopyroxene, plg = plagioclase (An3-15), ox = Fe-Ti oxides, ap = apatite).

Table 12: Major- (in wt% oxides) and trace-element (in ppm) compositions of dated rocks.

Rock types	pegmatitic gabbro	Qz-rich pegmatite	Fe-Ti melanocratic dike
Sample numbers	MP4	MP2	MP177
SiO_2	50.6	61.0	41.6
TiO_2	0.53	0.14	3.32
Al_2O_3	17.4	22.1	12.2
FeO_T	5.5	0.87	14.2
MnO	0.12	0.01	0.19
MgO	8.4	0.63	10.5
CaO	11.8	6.7	10.2
Na_2O	2.79	5.59	2.90
K_2O	0.73	1.48	0.51
P_2O_5	0.07	0.11	0.72
LOI	1.7	1.3	2.8
Total	99.68	100.05	99.14
Mg#	73.1	56.5	56.9
in ppm			
Cu*	18	6	61
S*	69	80	1351
Sc*	35	7	34
V**	110	15	267
Cr**	233	8	256
Ni**	54	14	246
Ga**	16	26	24
Zn**	178	16	131
Co	36	13	50
Cs	0.36	0.82	0.43
Rb	29.6	47.2	2.6
Ba	188.4	275.2	92.2
Th	0.90	14.67	3.84
U	0.70	0.88	1.30
Nb	3.56	11.50	69.98
Ta	0.23	0.66	3.94
Pb	38.18	6.07	2.01
Sr	503.9	492.3	442.9
Zr	20.9	20.0	290.2
Hf	0.67	0.60	5.87
Y	16.1	4.0	29.8
La	6.11	61.40	35.44
Ce	15.36	108.64	72.77
Pr	2.18	11.13	9.06
Nd	9.39	35.46	37.99
Sm	2.48	4.58	8.20
Eu	0.77	1.41	2.54
Gd	2.60	2.45	7.69
Tb	0.43	0.25	1.13
Dy	2.51	0.87	5.73
Ho	0.51	0.13	1.02
Er	1.41	0.32	2.60
Yb	1.14	0.25	1.93
Lu	0.17	0.04	0.26

Table 13: Major- and trace-element analyses of the $^{40}Ar/^{39}Ar$ dated kaersutites (wt%). The structural formulae are calculated on the basis on 23 oxygens.

Sample	MP177			
Type	kaersutite			
SiO_2	39.81	39.53	38.35	38.97
TiO_2	4.91	5.42	6.79	6.02
Al_2O_3	12.81	12.79	13.46	13.30
FeO	15.20	13.87	12.60	11.83
MnO	0.29	0.24	0.21	0.17
MgO	9.85	10.22	10.87	11.82
CaO	11.13	11.26	11.59	11.28
Na_2O	2.79	2.82	2.56	2.83
K_2O	1.07	1.08	1.17	1.13
OH	1.99	1.99	2.00	2.00
Total	99.88	99.21	99.60	99.43
Si	6.00	5.97	5.76	5.83
Al^{IV}	2.00	2.03	2.24	2.17
Al^{VI}	0.27	0.24	0.14	0.17
Ti	0.56	0.62	0.77	0.68
Fe^{2+}	1.92	1.75	1.58	1.48
Mn	0.04	0.03	0.03	0.02
Mg	2.21	2.30	2.43	2.64
Ca	1.80	1.82	1.86	1.81
Na	0.82	0.83	0.75	0.82
K	0.21	0.21	0.22	0.22
OH*	2.00	2.00	2.00	2.00
Total	17.81	17.80	17.77	17.83

4.4.4. Sample preparations

20 - 30 mg amphiboles were separated using conventional methods. Minerals were selected by hand picking under binocular microscope for their euhedral shape and free of retromorphosed rims (i.e. green amphibole overgrowths). The samples and closely spaced standards were irradiated for 20 hours in the central thimble position of the USGS TRIGA reactor in Denver (CO), USA (Dalrymple et al. 1981). The neutron flux was monitored using the standard MMHB1 assuming an age of 523.1 ±4.6 Ma (Renne et al. 1998). J value for the irradiation was 0.00301 ±0.0001 for bulk mineral separate. Furnace step-heating analyses were performed using a double vacuum resistance furnace. After furnace step-heating, the gas was exposed to a metal cold finger at temperatures of approximately –130°C and gettered using a SAES AP50 getter for an additional 180 seconds to remove all active gases. Following cleanup, the gas was expanded into a modified MAP 215-50 mass spectrometer for isotopic analysis. Eight scans per analysis were made over the mass range of 40 to 36 and peak heights extrapolated back to inlet time. Furnace blanks ranged for m/e=40 from 2 x 10^{-14} moles at 1500°C to 5 x 10^{-15}

moles below 1000°C. Blank values for m/e (36-39) were below 2 x 10^{-16} moles. Peak heights were corrected for background, mass discrimination, and for decay of interfering isotopes of argon derived from Ca, K, and Cl. The apparent ages were calculated using an assumed initial $^{40}Ar/^{36}Ar$ ratio of 295.5 and decay constants recommended by Steiger and Jäger (1977).

4.5. Results

Five zircon fractions of the pegmatitic gabbro and three zircon fractions of the pegmatitic dike yielded the ID-TIMS U/Pb mean concordant ages of 284.2 ± 0.6 Ma and 282.9 ± 0.6 Ma (Fig. 46a-b, Table 14). These ages are interpreted as the crystallization age of the gabbroic complex and the emplacement of the associated acid magmatism, respectively.

We obtain an integrated age of 255.4 ± 2.0 Ma (Fig. 47) on the amphiboles separates from the Fe-Ti melanocratic dike. Argon isotopic incremental measurements are given in appendix 7. As shown in figure 47, during argon heating of kaersutitic amphiboles, the first five heating steps differed markedly from the other ones by giving a higher Ca/K ratio, interpreted as the degassing of another minor phases as plagioclase inclusions. Thus, we omitted the first analytical steps, and we prefer to choose the plateau age of 260.2 ± 0.7 Ma (Fig. 47).

4.6. Discussion

Zircons extracted from the pegmatitic gabbro and the quartz-rich pegmatite display all concordant ellipses. In both cases, the zircons show no evidences of inheritance. Thus, the obtained dating can be considered as the crystallization ages of the main gabbroic intrusion and associated felsic dikes. These results show that basic and acid magmatisms are nearly contemporaneous and emplaced at the Permian-Carboniferous boundary. If we postulate that the orthogneisses of the Arolla series (ca. 289 Ma) are the original country rocks of the intrusion, the several acidic dikes and dikelets exposed in the Mont Collon intrusion could arise by back-diking processes as the emplacement of the basic magmas provide enough heat for partial melting of the country rocks. The magmatic processes leading to the formation of the intermediate to acidic dikes will be discussed in chapter 6. Nevertheless, field observations do not bring evidences for the mentioned hypothesis because the contact between the Mont Collon intrusion and its present day country rocks is strongly reworked by the Alpine tectonics. Moreover, dikes coming directly from the Arolla orthogneisses have not been observed near the contact.

Table 14: Analytical isotopic results U/Pb: *: radiogenic Pb, a) frg = fragment, ndl = needle, pr = prism, b) in mol-% relative to total radiogenic Pb, c) corrected for spike Pb and for fractionation, d) corrected for fractionation, spike, U and Pb blanks and initial common lead, error estimates (95% confidence level) refer to the last significant digits of the isotopic ratios and reflect the reproducibility of standards, measurement errors and uncertainties in the common lead correction. [-] refers in the text to the label of analyzed zircon grain or fractions.

fraction		Description		Nb	Zircon	Concentrations				Atomic ratios								Apparent ages		
number		a)		of grains	weight (mg)	U ppm	Pb* ppm	^{208}Pb* b)		206/204 c)	206/238 d)	Error 2s	207/235 d)	Error 2s	207/206 d)	Error 2s		206/238	207/235	207/206
Mont Collon pegmatitic gabbro - MP4																				
1		big pr		1	0.0102	285	14	14		4401	0.04511	30	0.3236	21	0.05203	26		284.4	284.7	286.9
2		big pr		2	0.022	1051	47	9		38024	0.04506	25	0.3232	18	0.05201	10		284.1	284.3	285.9
3		smll pr		2	0.013	743	34	11		12686	0.04499	27	0.3229	19	0.05206	16		283.7	284.1	288.0
4		small pr		3	0.0156	520	25	14		7036	0.04504	19	0.3229	15	0.05200	18		284.0	284.1	285.2
5		small pr		4	0.008	477	22	11		9476	0.04505	26	0.3226	19	0.05193	10		284.1	283.9	282.3
Mont Collon Qz pegmatite - MP2																				
6		acicular pr		1	0.012	1188	51	6		20137	0.04477	16	0.3205	13	0.05192	6		282.4	282.3	281.9
7		rounded gr		2	0.013	441	20	10		6430	0.04497	20	0.3222	16	0.05197	10		283.6	283.6	284.0
8		pr		2	0.0148	290	13	9		11455	0.04490	18	0.3215	11	0.05194	10		283.1	283.1	282.8
Sermenza gabbro - 913az																				
9		big frg		4	0.039	501	25	18		19433	0.04497	24	0.3226	18	0.05202	8		283.6	283.9	286.5
10		frg		24	0.029	672	33	17		27969	0.04503	24	0.3232	18	0.05205	8		283.9	284.4	287.8
11		frg		8	0.042	261	13	17		8157	0.04509	24	0.3236	18	0.05204	10		284.3	284.6	287.3
Arolla orthogneiss - KAW983																				
12		small pr		8	0.004	580	27	12		6610	0.04579	20	0.3287	18	0.05206	10		288.6	288.6	288.2
13		ndl		4	0.004	141	7	11		2722	0.04580	22	0.3292	22	0.05213	24		288.7	288.9	291.1

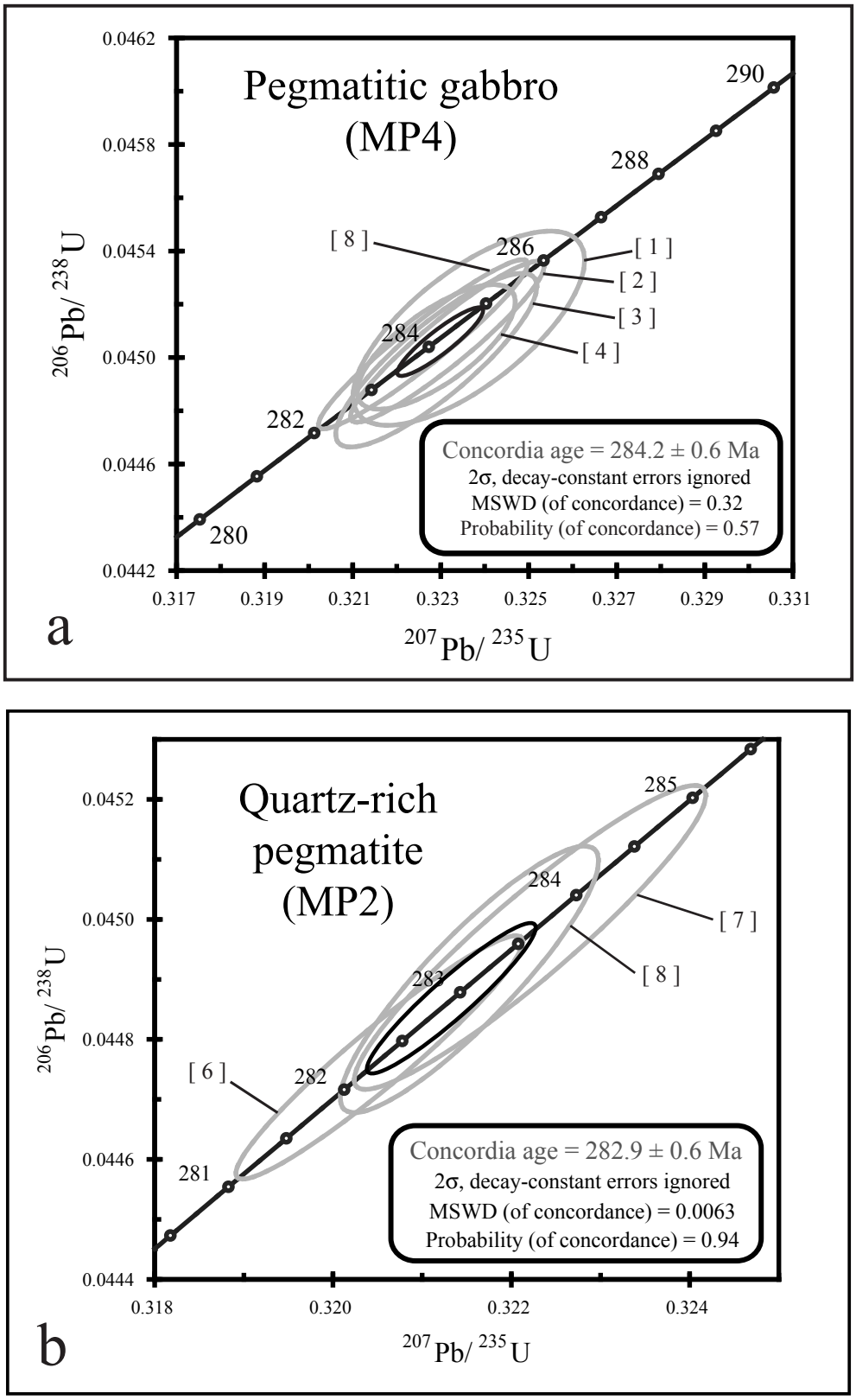

Fig. 46: a) U/Pb Concordia diagram for 1 to 3-grain zircon fractions of a pegmatitic gabbro and for b) 2 to 3-grain zircon fractions of a quartzitic pegmatite from the Mont Collon northern face (error ellipses are given at the 2σ confidence level). Black ellipse represents the mean Concordia age. Number in [ ] refers to the mineral fraction listed in table 14.

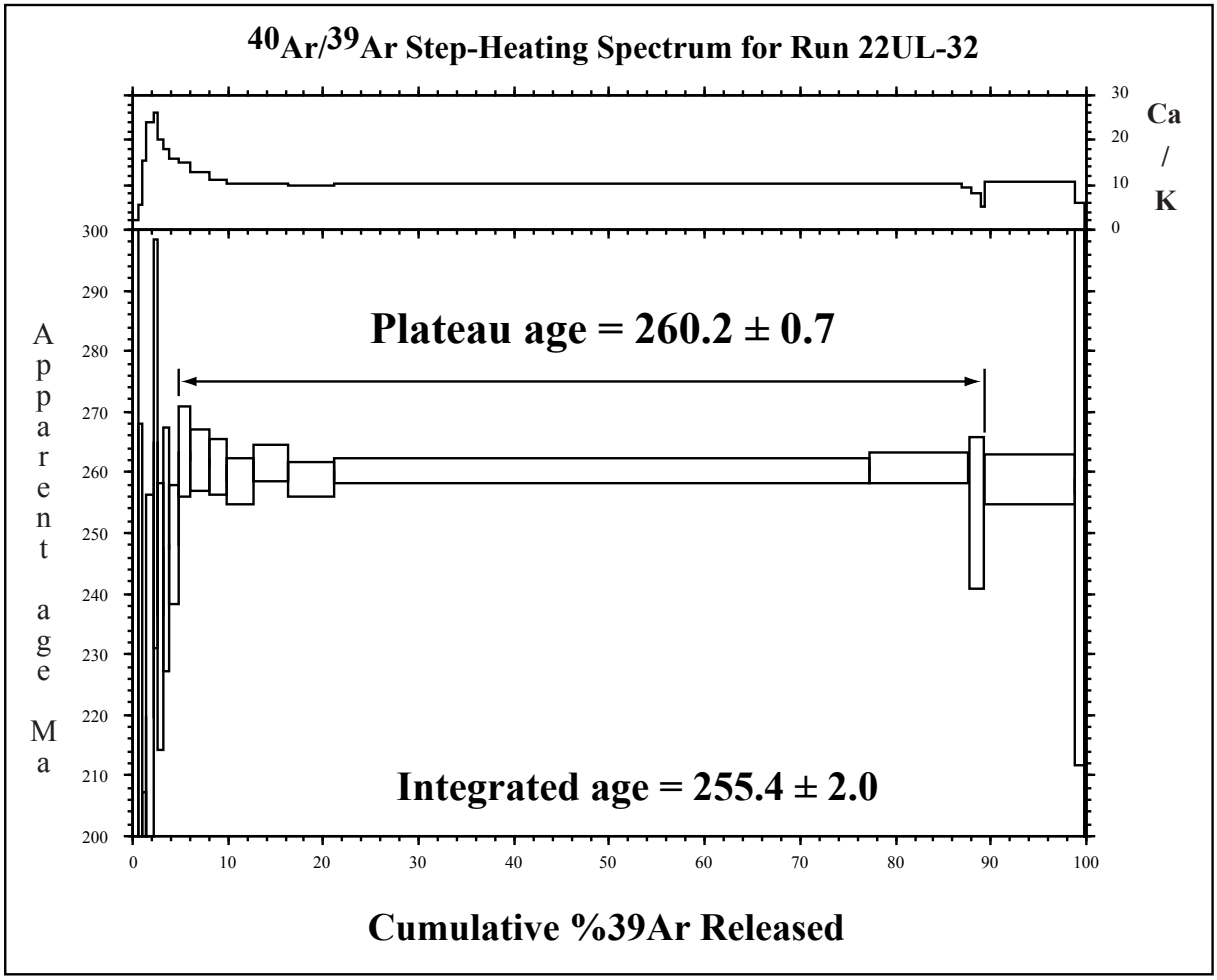

Fig. 47: Ca/K and $^{40}Ar/^{39}Ar$ step-heating spectrum vs. cumulative %39Ar released diagram for the sample MP177 (Fe-Ti melanocratic dike).

The Early Permian Mont Collon complex is contemporaneous with other gabbros of the Alpine domain (i.e., Sermenza .gabbro-diorite mass (Val Anzasca), Braccia (Val Malenco) and Sondalo gabbros, the main gabbro-diorite body in the Ivrea-Verbano zone; Fig. 48). It is noteworthy that, as the Mont Collon gabbros and Arolla orthogneisses association, many gabbroic intrusions of the Alpine domain are in space and time related with granitoid bodies. Near the Sondalo complex, several small granitoid bodies have been dated between 282 and 259 Ma using Rb/Sr method on muscovites (Del Moro and Notarpietro, 1987). A similar association was dated in the Val Malenco. The age of the acid magmatism associated with the Braccia gabbro yields an U/Pb zircon age of 278.4 ± 2.6 Ma (Hansmann et al., 1996 and 2001).

The Fe-Ti melanocratic dikes represent probably a distinct and later magmatic event with respect to the early Permian Mont Collon complex cumulates. The $^{40}Ar/^{39}Ar$ dating of these dikes yields a surprisingly younger plateau age than what we expected. The $^{40}Ar/^{39}Ar$ dating shows that it is not the case. According to McDougall and Harrison (1988), the closure temperatures of amphiboles range between 450 to 500°C and these minerals are known for their important retentiveness of argon during cooling. But other parameters have to be taken

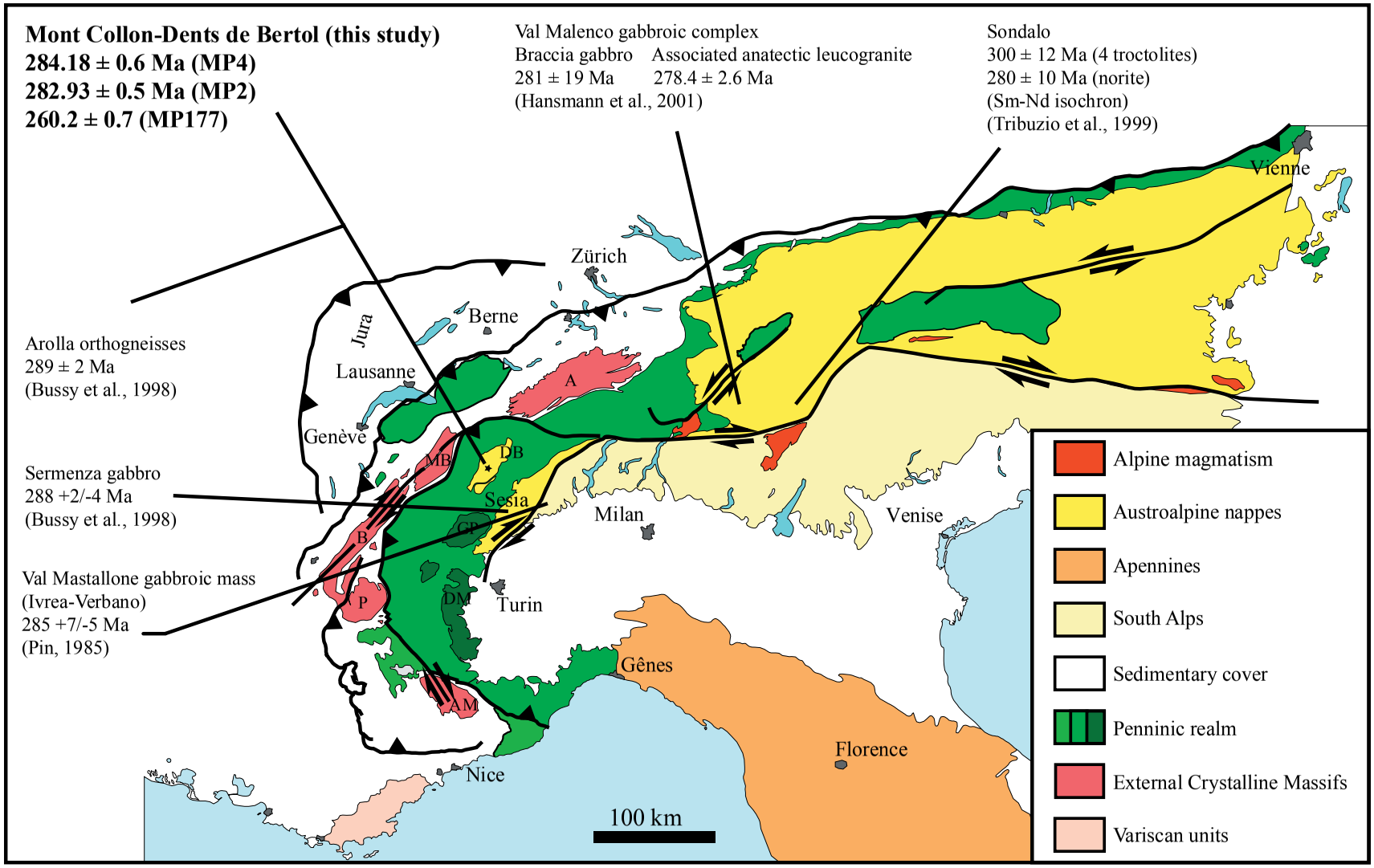

Fig. 48: Distribution map of some Permian Mafic Complexes with comparable ages in the Alps. All ages were determinate using a zircons U/Pb method except for Tribuzio et al., 1999 which obtain Sm/Nd ages on separate minerals.

into account as the grain size, the diffusion length scale and the Mg content in the MP177 sample kaersutites (MgO = 9.85 - 11.82 wt%, table 13). Pressures of 0.3 - 0.6 GPa calculated applying the geobarometer of Nimis and Ulmer (1998) for hydrous basaltic magmas based on clinopyroxene compositions indicate that the Mont Collon complex was emplaced into the middle crust (see chapter 3). Inversely, some structural and petrographical characteristics of the Fe-Ti melanocratic dikes (i.e. miarolitic voids indicating a fluid exsolution, very fine apatite needles) suggest an emplacement and a quenching at shallower levels than the gabbroic rocks. Then, a fast cooling and the relatively high Mg content of the analyzed kaersutites probably balance the effects of their small grain sizes and possibly prevent Ar loss which could yield a younger age than the effective age of the sample. Consequently, the obtained $^{40}Ar/^{39}Ar$ age is probably very close to the age of crystallization of the dike.

The presence of such contrasting dikes suggests a second magmatic event, distinct from the early Permian magmatic event related to the Mont Collon cumulates emplacement. The conditions of mantle melting and the tectonic processes which led to this emplacement will be discussed in the following chapters.

Chapter 5: Geochemical constraints on the magma sources

Chapter 5: Geochemical constraints on the magma sources

5.1. Introduction

The Mont Collon mafic complex consists mainly of ultramafic and mafic cumulates intruded by two types of rocks: (i) leucocratic and (ii) Fe-Ti melanocratic dikes. U/Pb dating (chapter 5 and Monjoie et al., submitted) on zircons show that the leucocratic (283 Ma) dikes are contemporaneous with the cumulates (284 Ma), while the Fe-Ti melanocratic ones are younger (260 Ma, $^{40}Ar/^{39}Ar$ amphibole dating, Monjoie et al., submitted). The leucocratic dikes are widespread within the whole intrusion, whereas the Fe-Ti melanocratic dikes are restricted to the Dents de Bertol area.

The aim of this chapter is to present and discuss the whole-rock petrology, chemistry and above all the isotopic (Nd, Sr, Pb and Re-Os) compositions of the main rock types (i.e. cumulates, leucocratic and Fe-Ti melanocratic dikes) in order to characterize their magmatic affinities and sources.

5.2. Summary of the the Mont Collon cumulates elemental characteristics

5.2.1. Major- and trace-element chemistry

The chemical variations from wehrlites to gabbros, through plagioclase-wehrlites is marked by an increase of Al_2O_3, CaO and Na_2O. Ol- and cpx-gabbros are geochemically similar and display wider variations in Al_2O_3 and SiO_2 than the other cumulates (Fig. 22a-c). Compared to the other mafic cumulates, cpx-gabbros are generally enriched in K_2O. TiO_2, Na_2O and CaO increase with increasing SiO_2.

5.2.2. Chondrite-normalized rare earth element patterns

All cumulates (Fig. 31), whatever the rock type, display similar LREE-enriched patterns ($1.84 < La_N/Yb_N < 3.67$) with variable REE contents and more or less marked Eu negative anomalies. The troctolite displays a relative flat Medium (M) to HREE pattern (Sm_N/Yb_N = 3.08), compared to the other cumulates. Anorthosites differ from the gabbros by a larger LREE enrichment [(La_N/Yb_N) = 14.24]. Compared to the cumulate gabbros, the pegmatitic gabbros exhibit the highest REE contents and a small Eu negative anomaly (Eu/Eu* = 0.70 - 0.93).

5.2.3. Primitive mantle-normalized multi-element plots

The primitive mantle-normalized (Sun and Mc Donough, 1989) multi-element plots of the Mont Collon ultramafic and mafic cumulates and anorthosite layer are very similar (Fig. 32, Tables 9a-d). These plots are characterized by (i) LILE enrichment, (ii) Nb-Ta (La/Nb = 1.27 - 10.50), Zr-Hf, and Ti negative anomalies and (iii) HREE and Y depletions. The Sr and Eu positive anomalies are linked to plagioclase accumulation. The pegmatitic gabbros differ by the absence of Nb and Ta negative anomalies (La/Nb = 0.57; sample MP113).

5.2.4. Nd, Sr and Pb isotope compositions

The cumulates have a wide range of εNd_i (3.2 to -0.6, Table 15a) which are not related to the rock types (Fig. 49). The groups distinguished on the basis of their sampling locations (Fig. 7; chapter 2 section 2.3.) have been also differentiated according to their $^{87}Sr/^{86}Sr_i$ values, and to a lesser extent, their εNd_i. Group I, which consists of rocks sampled in different locations of the Mont Collon massif is characterized by $^{87}Sr/^{86}Sr_i$ lower than 0.705 (about 0.70481) and εNd_i ranging between +1.2 to +3.2. Group II encompasses all the cumulates collected along the Dents de Bertol cliff and differs from group I by higher $^{87}Sr/^{86}Sr_i$ (> 0.705) and comparatively lower and homogeneous εNd_i values near 0. These low values of the εNd_i are in the range of those of the Bulk Silicate Earth (BSE). It is noteworthy that this two groups can not be distinguished on the base of their whole-rock and mineral compositions.

The subdivision into two groups, mentioned above, can be also applied on the basis of the $^{207}Pb/^{204}Pb_i$ and $^{208}Pb/^{204}Pb_i$ ratios (Table 15b). In the enlarged plot (Fig. 50), group I differs from group II by lower $^{207}Pb/^{204}Pb_i$ and $^{208}Pb/^{204}Pb_i$ ratios, but both groups have similar $^{206}Pb/^{204}Pb_i$. $^{207}Pb/^{204}Pb_i$ and $^{208}Pb/^{204}Pb_i$ ratios display a positive linear correlation with $^{206}Pb/^{204}Pb_i$. In the $^{207}Pb/^{204}Pb_i$ - $^{206}Pb/^{204}Pb_i$ diagrams (Fig. 51a), group II exhibits a linear trend parallel to the $^{206}Pb/^{204}Pb_i$ axis and plots near the Atlantic sediments field. Similarly, in the $^{208}Pb/^{204}Pb_i$ - $^{206}Pb/^{204}Pb_i$ diagram (Fig. 51b), the Mont Collon cumulates fall close to the Atlantic sediments field (values after Ben Othman et al., 1989). Despite its higher Pb isotopic signature, the pegmatitic gabbro (MP4) is aligned with the cumulates. The $^{87}Sr/^{86}Sr_i$ - $^{206}Pb/^{204}Pb_i$ plot well illustrates the distinction into two groups (Fig. 52). In the $^{207}Pb/^{204}Pb_i$ versus $^{206}Pb/^{204}Pb_i$ and Nd ratio versus $^{206}Pb/^{204}Pb_i$ diagrams (Fig. 51a and 53), the cumulates plot also close to the BSE field.

The subdivision into two groups could be explained by either variable crustal contamination (by assimilation of wall-rocks or at the source) or two melt batches exhibiting slightly different isotopic composition (heterogeneity of the mantle source?). The hypothesis of two (or more) melt batches is consistent with the lack of differentiation within the whole complex, i.e. the poorly variation in the rocks facies (no occurrences of differentiated rock types).

Table 15a: Nd and Sr isotopic compositions of the Mont Collon cumulate groups I and II (plg-wehrlites, ol- and cpx-gabbros, troctolite and anorthosite) and the pegmatitic gabbro MP4.

Sample type	Sample number	Age (Ma)	$^{143}Nd/^{144}Nd$	2σ	$^{143}Nd/^{144}Nd_i$	εNd_i	$^{87}Sr/^{86}Sr$	2σ	$^{87}Sr/^{86}Sr_i$	εSr_i
Group I										
plg-wehrlite	FB1095	284	0.51268	0.000006	0.51239	+2.3	0.70464	0.000006	0.70453	+5.2
ol-gabbro	MP176	284	0.51275	0.000004	0.51244	+3.2	0.70464	0.000013	0.70458	+6.0
	FB1091	284	0.51269	0.000005	0.51238	+2.2	0.70481	0.000007	0.70469	+7.4
cpx-gabbro	MP223	284	0.51266	0.000007	0.51233	+1.2	0.70474	0.000015	0.70449	+4.6
Group II										
plg-wehrlite	MP106	284	0.51261	0.000006	0.51227	0.0	0.70585	0.000015	0.70567	+21.4
troctolite	MP240	284	0.51247	0.000011	0.51227	0.0	0.70545	0.000008	0.70539	+17.4
ol-gabbro	MP127	284	0.51257	0.000005	0.51226	-0.3	0.70541	0.000006	0.70533	+16.5
	MP135	284	0.51259	0.000012	0.51228	+0.1	0.70539	0.000008	0.70530	+16.1
	MP152	284	0.51260	0.000007	0.51237	+1.9	0.70530	0.000007	0.70524	+15.2
	MP156	284	0.51258	0.000017	0.51225	-0.5	0.70543	0.000008	0.70534	+16.7
	MP157	284	0.51263	0.000006	0.51225	-0.4	0.70542	0.000012	0.70540	+17.5
	MP160	284	0.51255	0.000009	0.51225	-0.5	0.70541	0.000008	0.70536	+16.9
	MP161	284	0.51261	0.000006	0.51229	+0.4	0.70543	0.000009	0.70539	+17.4
	MP242	284	0.51260	0.000008	0.51228	+0.1	0.70535	0.000010	0.70527	+15.7
cpx-gabbro	MP131	284	0.51262	0.000007	0.51230	+0.5	0.70543	0.000009	0.70535	+16.8
	MP134	284	0.51256	0.000005	0.51226	-0.3	0.70545	0.000014	0.70532	+16.4
	MP150	284	0.51258	0.000005	0.51229	+0.4	0.70561	0.000012	0.70548	+18.7
	MP154	284	0.51257	0.000003	0.51224	-0.6	0.70552	0.000014	0.70548	+18.7
	MP184	284	0.51260	0.000007	0.51226	-0.3	0.70549	0.000010	0.70541	+17.6
	MP192	284	0.51258	0.000006	0.51228	+0.1	0.70544	0.000009	0.70540	+17.5
	MP194	284	0.51257	0.000008	0.51224	-0.6	0.70582	0.000011	0.70551	+19.0
pegmatitic gabbro	MP4	284	0.51256	0.000004	0.51226	-0.2	0.70592	0.000016	0.70523	+15.1

Table 15b: Lead isotopic compositions of the Mont Collon cumulate groups I and II (plg-wehrlites, ol- and cpx-gabbros, troctolite and anorthosite) and the pegmatitic gabbro MP4.

		measured Pb ratios										corrected Pb ratios		
Sample type	Sample number	206/204	2σ	207/204	2σ	208/204	2σ	207/206	2σ	208/206	2σ	206/204i	207/204i	208/204i
Group I														
plg-wehrlite	FB1095	18.575	0.020	15.636	0.013	38.578	0.018	0.842	0.007	2.077	0.004	18.350	15.620	38.296
ol-gabbro	MP176	18.627	0.005	15.655	0.007	38.455	0.008	0.841	0.003	2.065	0.004	18.489	15.644	38.324
	FB1091	-	-	-	-	-	-	-	-	-	-	-	-	-
cpx-gabbro	MP223	18.498	0.005	15.640	0.005	38.509	0.007	0.846	0.003	2.082	0.005	18.267	15.623	38.275
Group II														
plg-wehrlite	MP106	18.568	0.005	15.659	0.006	38.663	0.008	0.843	0.003	2.082	0.004	18.417	15.657	38.428
troctolite	MP240	18.424	0.008	15.663	0.008	38.471	0.009	0.850	0.003	2.088	0.003	18.336	15.654	38.366
ol-gabbro	MP127	18.577	0.008	15.653	0.007	38.642	0.010	0.843	0.003	2.080	0.003	18.386	15.645	38.405
	MP135	18.553	0.003	15.657	0.005	38.654	0.065	0.844	0.004	2.084	0.003	18.296	15.643	38.300
	MP152	18.422	0.006	15.654	0.006	38.476	0.007	0.850	0.003	2.089	0.004	18.297	15.646	38.348
	MP156	18.500	0.006	15.663	0.006	38.557	0.007	0.847	0.003	2.084	0.004	18.473	15.651	38.515
	MP157	18.487	0.008	15.667	0.007	38.559	0.008	0.848	0.004	2.086	0.004	18.386	15.656	38.446
	MP160	18.522	0.007	15.658	0.008	38.591	0.010	0.845	0.002	2.083	0.003	18.386	15.648	38.427
	MP161	18.481	0.007	15.660	0.008	38.540	0.010	0.847	0.002	2.085	0.004	18.379	15.653	38.409
	MP242	18.519	0.007	15.662	0.008	38.595	0.009	0.846	0.002	2.084	0.002	18.300	15.645	38.343
cpx-gabbro	MP131	18.519	0.005	15.656	0.006	38.583	0.008	0.845	0.003	2.083	0.004	18.249	15.642	38.381
	MP134	18.554	0.004	15.654	0.005	38.642	0.006	0.844	0.002	2.083	0.002	18.430	15.646	38.485
	MP150	18.468	0.004	15.652	0.006	38.512	0.007	0.848	0.003	2.085	0.004	18.371	15.646	38.390
	MP154	18.527	0.005	15.655	0.005	38.565	0.006	0.845	0.002	2.082	0.003	18.383	15.661	38.454
	MP184	18.528	0.005	15.664	0.006	38.565	0.007	0.845	0.003	2.081	0.003	18.367	15.651	38.370
	MP192	18.489	0.008	15.667	0.006	38.567	0.008	0.847	0.003	2.086	0.003	18.415	15.659	38.463
	MP194	18.519	0.005	15.662	0.006	38.536	0.006	0.846	0.002	2.081	0.002	18.346	15.648	38.363
pegmatitic gabbro	MP4	18.982	0.011	15.672	0.012	38.690	0.012	0.826	0.002	2.038	0.004	18.922	15.674	38.686

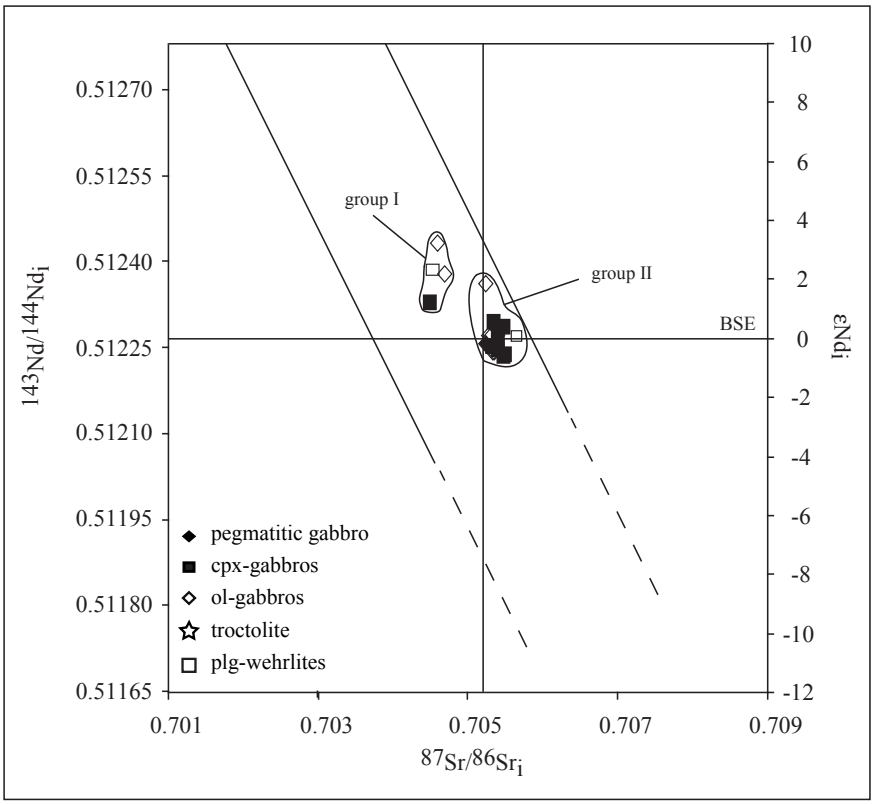

Fig. 49: εNd_i, $^{143}Nd/^{144}Nd_i$ and $^{87}Sr/^{86}Sr_i$ diagram for the Mont Collon cumulates showing the differences between the groups I and II.

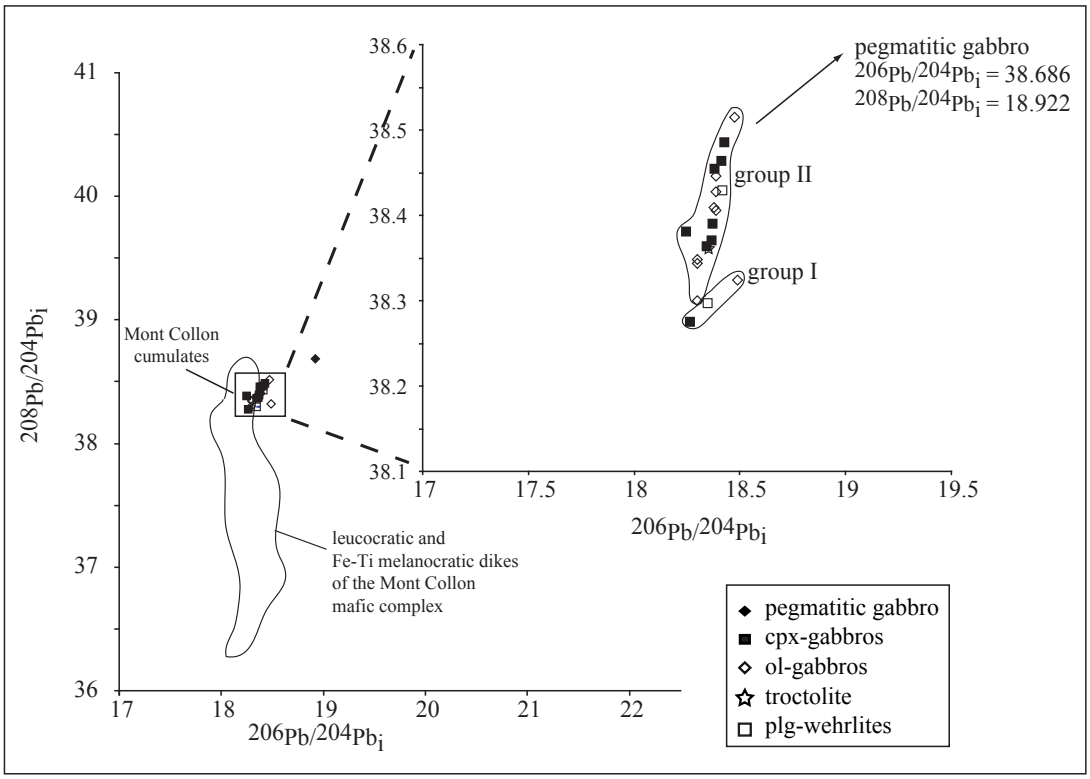

Fig. 50: $^{206}Pb/^{204}Pb_i$ - $^{208}Pb/^{204}Pb_i$ co-variation diagram for the Mont Collon cumulates showing the differences between the groups I and II. The pegmatitic gabbro MP4 is not shown.

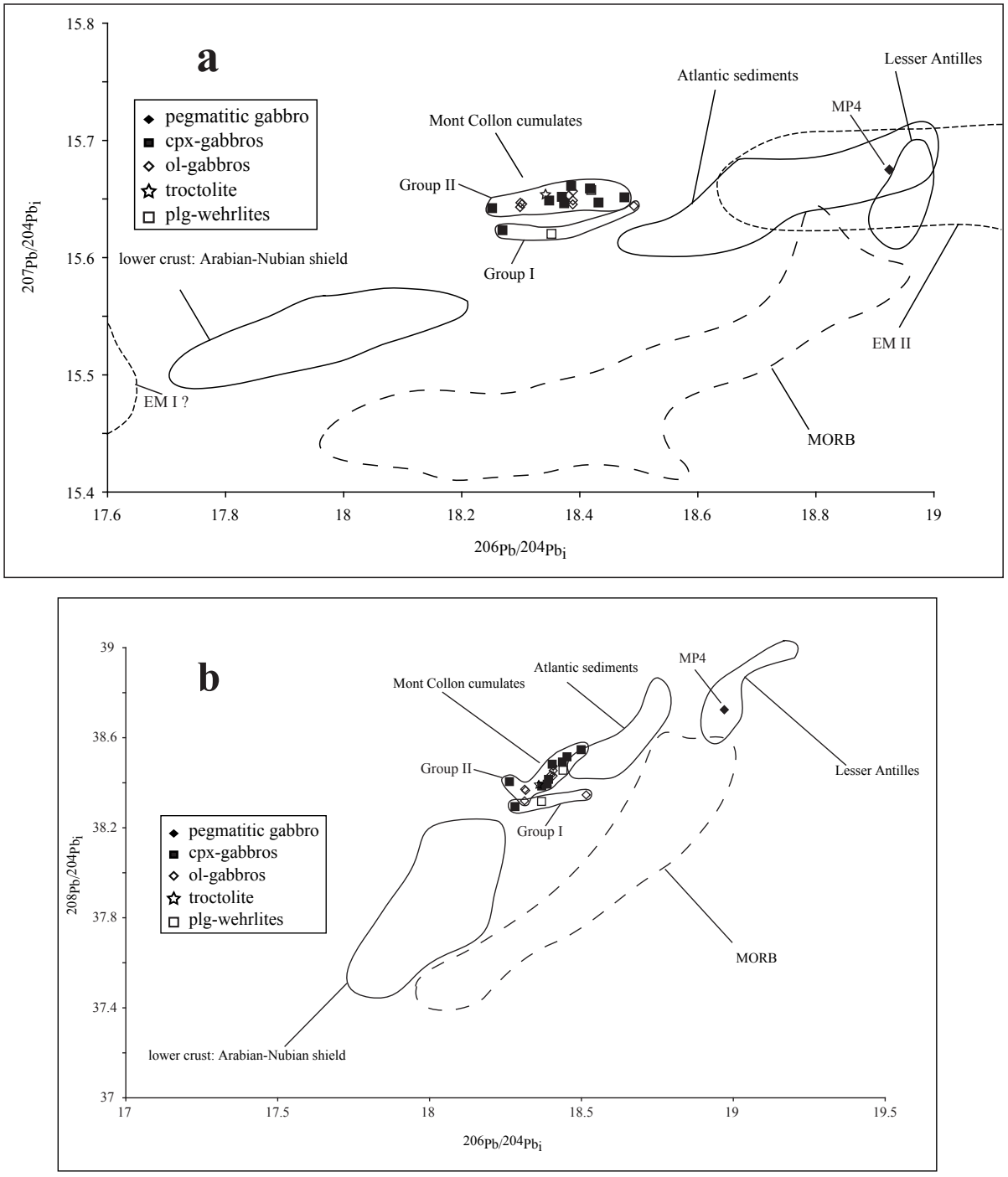

Fig. 51: a) $^{206}Pb/^{204}Pb_i$ - $^{207}Pb/^{204}Pb_i$ and b) $^{206}Pb/^{204}Pb_i$ - $^{208}Pb/^{204}Pb_i$ diagram for the Mont Collon cumulates. Lower crust of Arabian - Nubian shield (Bosch and Lancelot, 1990), MORB (White et al. 1987), Lesser Antilles island arc (White and Dupré, 1986; Davidson, 1987) and Atlantic sediments (Ben Othman et al., 1989). EM I and EM II fields after Zindler and Hart (1986).

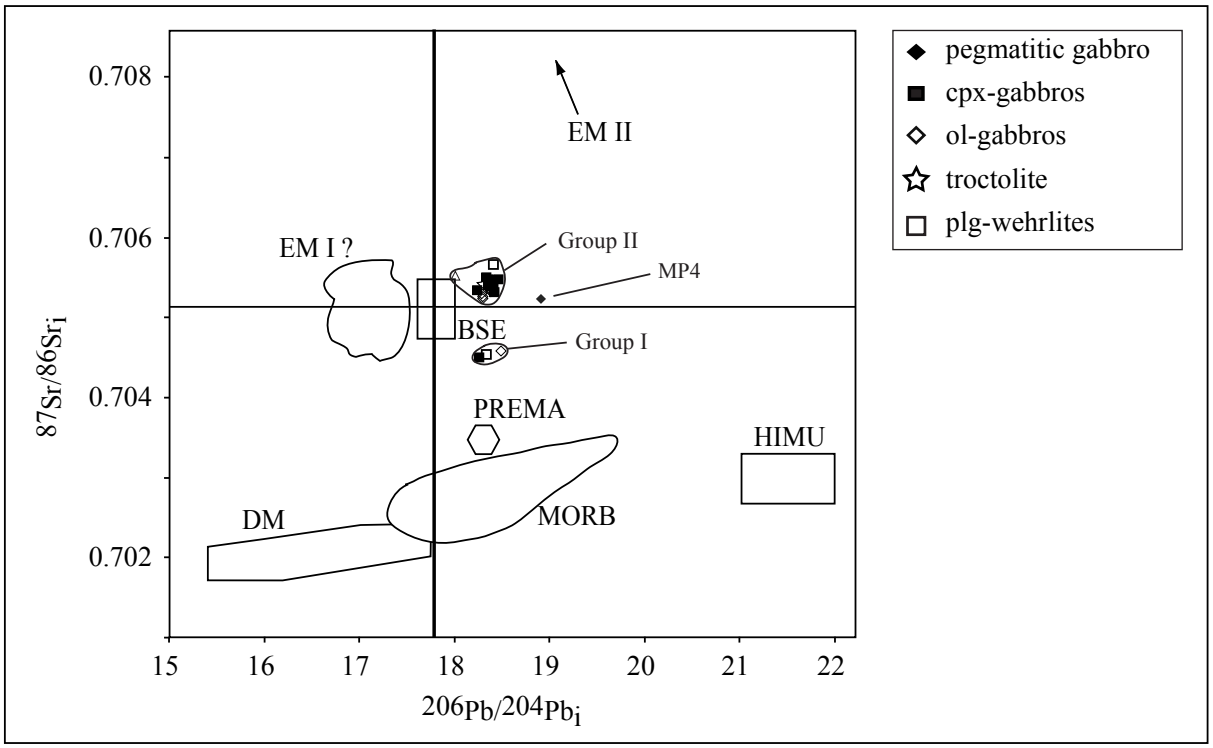

Fig. 52: $^{206}Pb/^{204}Pb_i$ - $^{87}Sr/^{86}Sr_i$ diagram for the Mont Collon cumulates. MORB, Depleted Mantle (DM), HIMU, PREMA and Bulk Silicate Earth (BSE) fields after Zindler and Hart (1986).

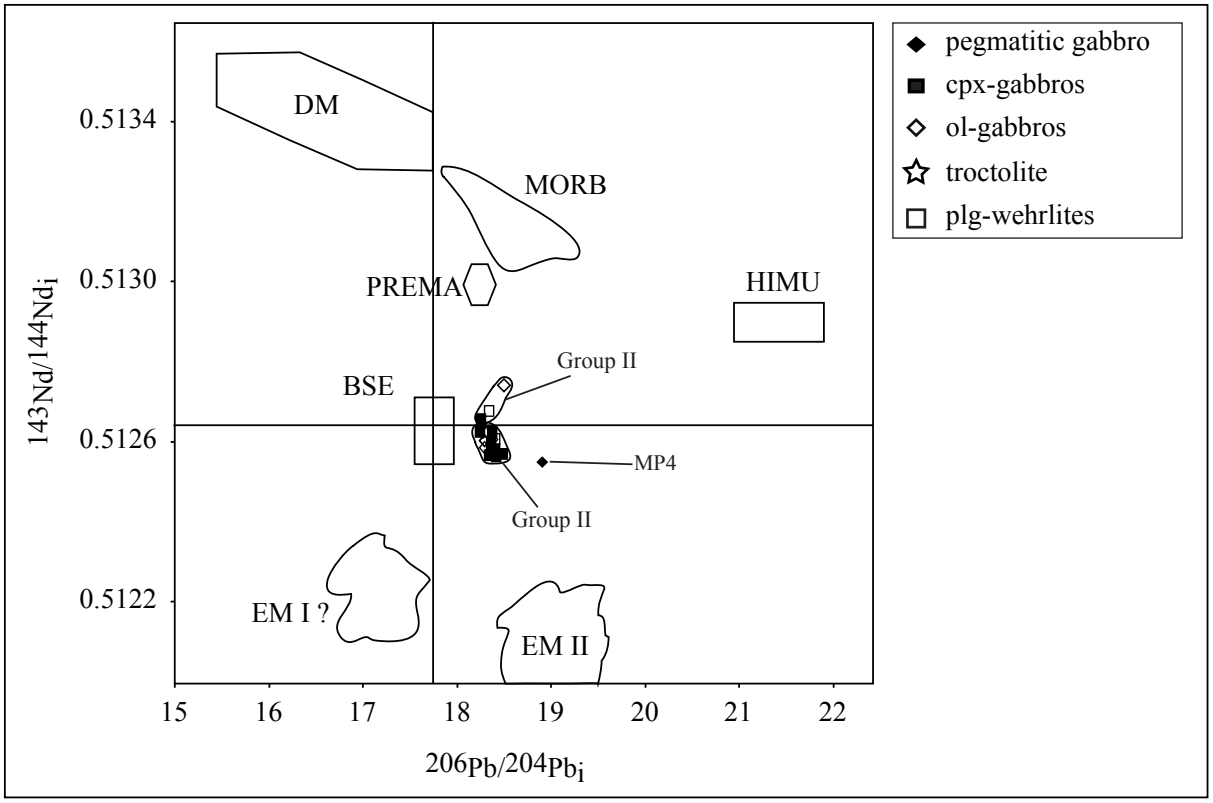

Fig. 53: $^{206}Pb/^{204}Pb_i$ - $^{143}Nd/^{144}Nd_i$ diagram for the Mont Collon cumulates. MORB, DM, HIMU, PREMA and BSE fields after Zindler and Hart (1986).

5.3. The leucocratic dikes

5.3.1. Major- and trace-element chemistry

Major-element compositions of the quartz-rich pegmatites are very homogeneous with the exception of Al_2O_3 abundance. In contrast, the aplite compositions exhibit larger variations, especially for CaO, Al_2O_3 and K_2O contents (Fig. 54, Table 16).

The microgranodiorites display variable SiO_2 contents from the central part to the margin of the dike (67.1 - 72.8 wt%). This silica content increase is related to higher quartz modal composition at the margin compared to the central part. Despite identical mineralogical content, sample MP128 differs from the other microgranodiorites by its lower SiO_2 content (61.0 wt%). We explain this variable silica content by a use of a bad powder fraction for the major-element analysis. It is noteworthy that the powder fractions used for major-element analyses and trace-element and isotopic determinations are made with different grinders (tungsten-carbide and agathe grinder, respectively) and thus, trace-element and isotope are reliable. Moreover, the microgranodiorites differ in higher FeO* (1.56 - 3.36 wt%) and MgO (0.68 - 1.63 wt%) contents, from the other leucocratic dikes. This feature is mainly related to the presence of biotite (see chapter 2).

The anorthositic dikes exhibit intermediate compositions (SiO_2 ~ 60 wt%) and differ from the other leucocratic dikes by their higher K_2O (up to 1.42 wt%), Al_2O_3 (~21 wt%) and Na_2O (5.8-8.6 wt%) contents.

All leucocratic dikes are Mg-poor (MgO < 1.6 wt%, Table 16). That is why SiO_2 was chosen as differentiation index. The leucocratic dikes display more or less well-defined linear trends in Harker-type diagrams (oxides versus SiO_2; Fig. 54) with the exception of K_2O and Na_2O. For instance, the leucocratic dikes plots are scattered in the K_2O-SiO_2 diagram. This is likely related to the orthoclase abundance relative to quartz or variable degrees of alteration.

Table 16: Whole-rock major-element compositions of the Arolla orthogneisses and the dikes exposed in the Mont Collon mafic complex (in wt%)

Rock types	orthogneiss		Qz-rich pegmatites		microgranodiorite				aplites			anorthositic dikes		
Sample numbers	KAW1525	KAW1983	MP2	MP5	MP132b(rim)	MP128	FB1085	FB1089	MP173b	MP18b	MP141b	MP89	MP99	FB1087
SiO_2	68.0	54.1	61.0	73.3	72.8	61.0	67.1	69.8	70.8	66.9	75.4	60.5	60.3	60.6
TiO_2	0.41	0.83	0.14	0.16	0.20	0.27	0.49	0.31	0.04	0.02	0.11	0.36	0.12	0.05
Al_2O_3	14.8	17.8	22.1	14.9	14.4	20.7	15.6	15.5	15.0	17.5	13.6	22.4	20.7	22.9
FeO_T	3.7	8.1	0.87	0.78	1.77	1.87	3.36	2.72	0.60	0.71	0.95	0.28	0.74	0.24
MnO	0.08	0.18	0.01	0.02	0.03	0.02	0.05	0.04	0.02	0.02	0.01	0.01	0.02	0.01
MgO	1.28	3.25	0.63	1.00	0.61	1.63	1.24	0.68	0.21	0.55	0.31	0.14	0.84	0.20
CaO	2.4	6.1	6.7	4.6	2.7	6.6	5.1	3.7	9.1	8.2	1.4	5.3	8.1	4.8
Na_2O	3.8	3.3	5.6	4.5	3.6	5.4	4.2	4.5	3.2	4.5	4.4	7.8	5.8	8.6
K_2O	3.1	2.4	1.5	0.2	2.9	0.7	0.6	1.0	0.0	0.2	3.2	0.8	1.4	0.9
P_2O_5	0.11	0.20	0.11	0.11	0.07	0.43	0.17	0.08	0.09	0.02	0.04	0.20	0.03	0.01
LOI	1.45	2.61	1.34	0.54	0.94	1.31	1.47	0.98	1.15	0.86	0.60	0.81	1.27	1.04
Total	99.02	98.92	100.05	100.03	100.09	99.87	99.31	99.21	100.20	99.47	100.11	98.71	99.28	99.31
Mg#	0.0	0.0	56.5	0.0	37.9	60.9	39.7	30.9	38.0	57.7	36.5	0.0	66.9	59.8

Rock types	Fe-Ti melanocratic dikes				
Sample numbers	MP177	MP244a	MP244e	MP245a	MP249a
SiO_2	41.6	42.1	40.7	43.0	43.1
TiO_2	3.3	3.7	3.5	3.3	3.3
Al_2O_3	12.2	12.9	11.7	12.3	12.7
FeO_T	14.2	11.5	12.4	13.6	13.6
MnO	0.19	0.14	0.15	0.19	0.19
MgO	10.5	7.7	9.4	9.2	9.1
CaO	10.2	11.9	11.9	10.4	10.7
Na_2O	2.9	3.5	2.6	3.3	3.6
K_2O	0.51	0.41	0.65	0.57	0.57
P_2O_5	0.72	0.91	0.91	0.72	0.73
LOI	2.79	5.14	4.96	2.58	2.32
Total	99.14	99.96	99.03	99.20	100.04
Mg#	56.9	54.3	57.5	54.5	54.5

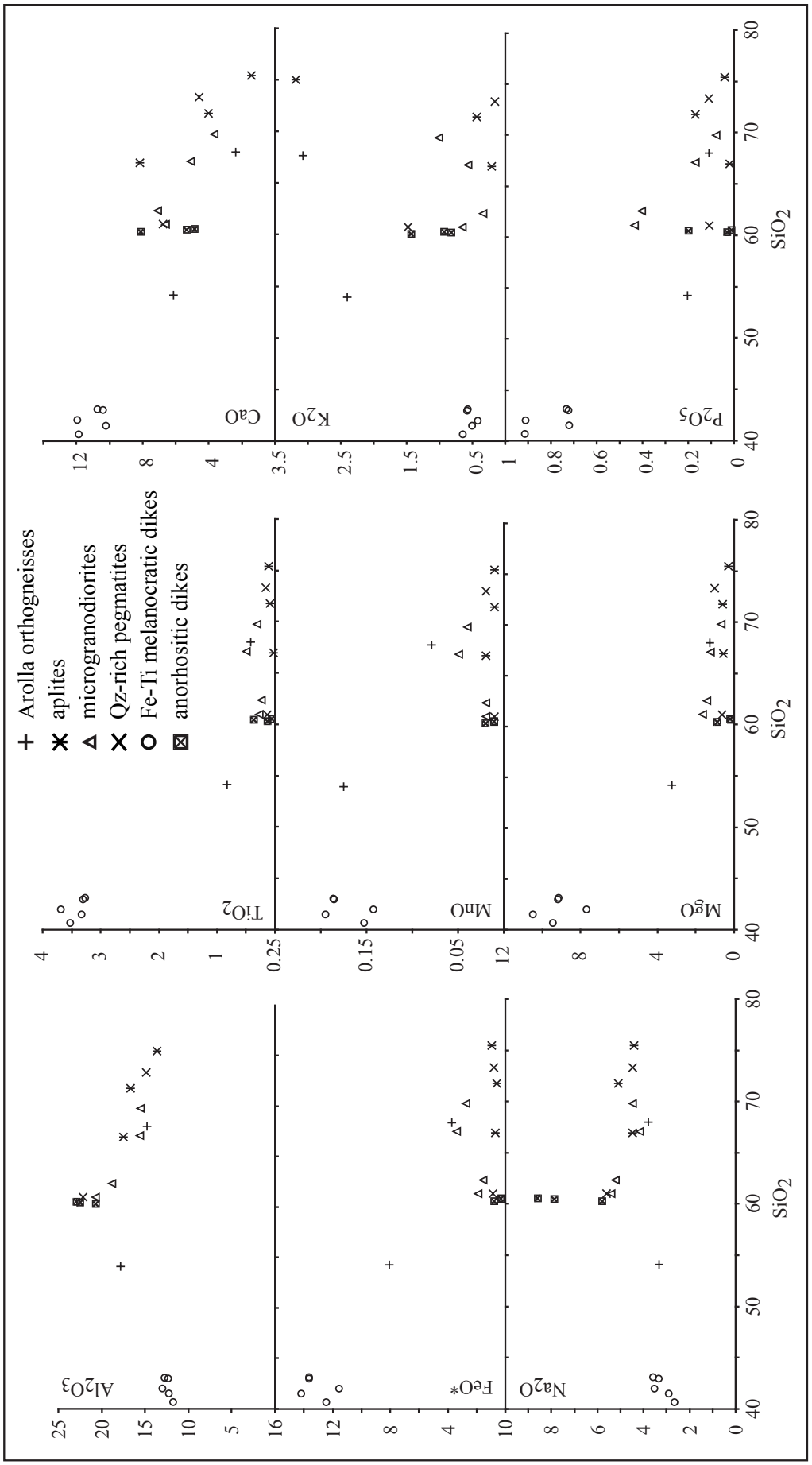

Fig. 54: Harker-type diagrams for major elements versus SiO_2 (in wt%) for the Arolla orthogneisses, the leucocratic and Fe-Ti melanocratic dikes.

5.3.2. Chondrite-normalized rare earth element patterns

All the leucocratic dikes show LREE-enriched patterns (Fig. 55, Table 17), but the LREE enrichment varies with the rock types and sometimes within a given rock type (i.e., pegmatites, microgranodiorites). Among the Qz-pegmatites, sample MP2 shows the highest LREE enrichment [$(La/Yb)_N$ = 177.31] of all the leucocratic dikes and a small Eu positive anomaly (Eu/Eu* = 1.29). The aplites show very homogeneous REE patterns with the exception of the Eu anomaly. One sample differs from the others by a marked negative Eu anomaly (Eu/Eu* = 0.62). The microgranodiorites exhibit the more diversified REE patterns, i.e. positive or negative Eu anomalies (Eu/Eu* = 0.53 - 1.49), variable LREE enrichments, [$(La/Yb)_N$ = 25.73 - 90.35]. These differences in the REE chemistry are likely related to the biotite abundance with respect to sanidine and andesine.

The LREE-rich patterns of the anorthositic dikes are not similar to those of Ca-rich plagioclase. This is due to the abundant apatite (up to 5 vol-%).

5.3.3. Primitive mantle-normalized multi-element plots

All the leucocratic dikes are characterized by Nb, (La/Nb = 1.39 - 8.06) Ta, and Ti negative anomalies and variable enrichments in large ion lithophile elements (LILE, Ba, Th, U), with the exception of a sample of aplitic dike, which is also characterized by a K negative anomaly (Fig. 56). This is probably related to an alteration process. Pegmatites, aplites and microgranodiorites exhibit also differences in the P, Zr and Hf contents. Some samples are characterized by P, Zr and Hf positive anomalies, other not. This is probably linked to the presence (variable modal amounts) or absence of apatite and zircon. The Pb positive anomaly of the anorthositic dikes can be attributed to the plagioclase abundance, as expected from the high distribution coefficients of lead in plagioclase.

5.3.4. Nd, Sr and Pb isotopic compositions

All the leucocratic dikes are characterized by negative εNd_i values that range between –1 and –6.6 and high $^{87}Sr/^{86}Sr$ initial ratios (0.70573 to 0.71005; $+83.5 < \varepsilon Sr_i < +22.2$; Fig. 57; Table 18). Such values are similar to those of upper continental crust. One sample (MP141, MP132b) shares with some cumulate gabbros similar εNd_i values (-1) that are the highest among the leucocratic dikes. However, the $^{87}Sr/^{86}Sr$ initial ratios of these two rocks differ significantly (0.70636 and 0.71005). This difference in the initial Sr ratios can be attributed to alteration or weathering processes. In the $^{143}Nd/^{144}Nd_i$ versus $^{87}Sr/^{86}Sr_i$ plot, the leucocratic dikes do not show a well-defined correlation trend.

Table 17: Whole-rock trace-element compositions of the Arolla orthogneisses and the dikes exposed in the Mont Collon mafic complex.

Rock types	Qz pegmatite		anorthositic dikes		microgranodiorites				aplites			Fe-Ti melanocratic dikes			Arolla orthogneisses	
Sample numbers	MP2	MP5	MP89	FB1087	MP132c	MP128	FB1085	FB1089	MP173b	MP18b	MP141b	MP177	MP245a	MP249a	KAW985	KAW1983
Cu*	6	n.d.	n.d.	5	13	3	9	6	6	8	4	61	70	62	n.d.	n.d.
S*	80	n.d.	n.d.	-	62	-	23	-	116	4	9	1351	410	483	n.d.	n.d.
Sc*	7	n.d.	n.d.	5	5	9	10	4	10	9	3	34	34	31	n.d.	n.d.
As*	-	n.d.	n.d.	-	4	-	7	-	-	3	-	5	-	-	n.d.	n.d.
V**	15	9	8	-	15	22	48	17	-	6	6	267	266	255	43	132
Cr**	8	12	6	2	6	10	13	-	3	6	3	256	281	249	3	13
Ni**	14	17	5	2	-	8	-	-	-	20	-	246	205	204	-	5
Ga**	26	14	19	20	18	25	18	18	15	19	16	24	25	24	18	23
Zn**	16	29	4	3	23	36	39	25	6	141	10	131	127	130	60	116
Co	13	5	2	2	3	8	8	2	12	2	10	50	59	54	5	13
Cs	0.82	0.10	0.23	0.27	0.64	0.72	0.14	0.26	0.15	0.26	0.47	0.43	0.25	0.42	1.13	1.19
Rb	47	4	19	23	66	24	10	15	1	15	115	3	3	0	100	84
Ba	275	84	161	169	232	113	64	101	14	101	821	92	130	174	654	317
Th	14.67	6.91	20.69	30.14	20.73	12.25	10.63	4.73	10.98	4.73	4.26	3.84	3.89	3.95	7.99	5.79
U	0.88	2.32	6.49	6.33	2.54	2.11	4.17	0.82	0.65	0.82	0.92	1.30	1.35	1.29	1.47	2.35
Nb	11.50	8.98	7.47	10.43	7.97	6.66	5.53	2.68	13.30	2.68	4.96	69.98	69.72	70.90	12.93	12.80
Ta	0.66	1.66	0.99	1.04	0.53	0.57	0.40	0.26	0.89	0.26	0.33	3.94	4.27	4.22	0.67	1.44
Pb	6.07	5.01	3.97	4.14	13.07	14.32	10.38	5.32	5.52	5.32	11.11	2.01	1.54	2.85	9.37	11.87
Sr	492	442	621	612	127	541	354	222	82	222	143	443	528	735	191	261
Zr	20.0	89.0	272.8	349.9	255.5	42.4	23.9	45.2	22.8	45.2	26.7	290.2	292.2	283.8	191.5	190.7
Hf	0.60	2.39	7.07	8.42	6.66	1.34	0.75	1.67	0.72	1.67	0.88	5.87	6.30	5.96	4.54	5.57
Y	4.0	7.8	19.4	23.6	18.0	10.7	7.9	3.7	11.2	3.7	9.7	29.8	31.3	31.5	27.2	50.2
La	61.40	4.99	60.17	82.29	40.35	51.65	17.02	9.53	18.48	9.53	10.61	35.44	35.56	36.94	31.62	14.97
Ce	108.64	9.15	121.38	162.90	88.03	97.92	34.29	19.10	36.64	19.10	22.26	72.77	76.41	77.76	62.05	40.05
Pr	11.13	1.14	13.17	18.04	9.26	11.25	4.56	2.34	4.35	2.34	2.65	9.06	9.45	9.45	7.32	6.16
Nd	35.46	4.23	42.79	58.82	34.24	39.80	18.35	8.55	17.07	8.55	9.41	37.99	38.55	38.89	26.56	27.43
Sm	4.58	1.09	7.07	9.58	6.13	6.78	4.43	1.81	3.64	1.81	2.03	8.20	8.53	8.55	5.20	7.83
Eu	1.41	0.38	1.07	1.30	0.91	1.46	1.14	0.78	0.70	0.78	0.71	2.54	2.85	2.85	0.91	1.31
Gd	2.45	1.17	5.28	6.89	4.57	4.95	3.39	1.41	3.31	1.41	1.88	7.69	7.78	7.97	5.14	8.15
Tb	0.25	0.19	0.67	0.84	0.57	0.53	0.39	0.17	0.44	0.17	0.25	1.13	1.14	1.14	0.76	1.43
Dy	0.87	1.09	3.39	4.00	2.93	2.24	1.68	0.75	2.12	0.75	1.42	5.73	6.00	5.90	4.39	8.51
Ho	0.13	0.22	0.64	0.76	0.56	0.35	0.27	0.13	0.38	0.13	0.29	1.02	1.07	1.10	0.90	1.80
Er	0.32	0.60	1.69	2.04	1.62	0.83	0.63	0.30	0.94	0.30	0.83	2.60	2.83	2.81	2.54	5.29
Yb	0.25	0.55	1.76	1.97	1.47	0.57	0.39	0.37	0.67	0.37	0.70	1.93	2.03	2.06	2.27	4.90
Lu	0.04	0.08	0.28	0.31	0.24	0.08	0.05	0.06	0.09	0.06	0.10	0.26	0.29	0.27	0.32	0.71

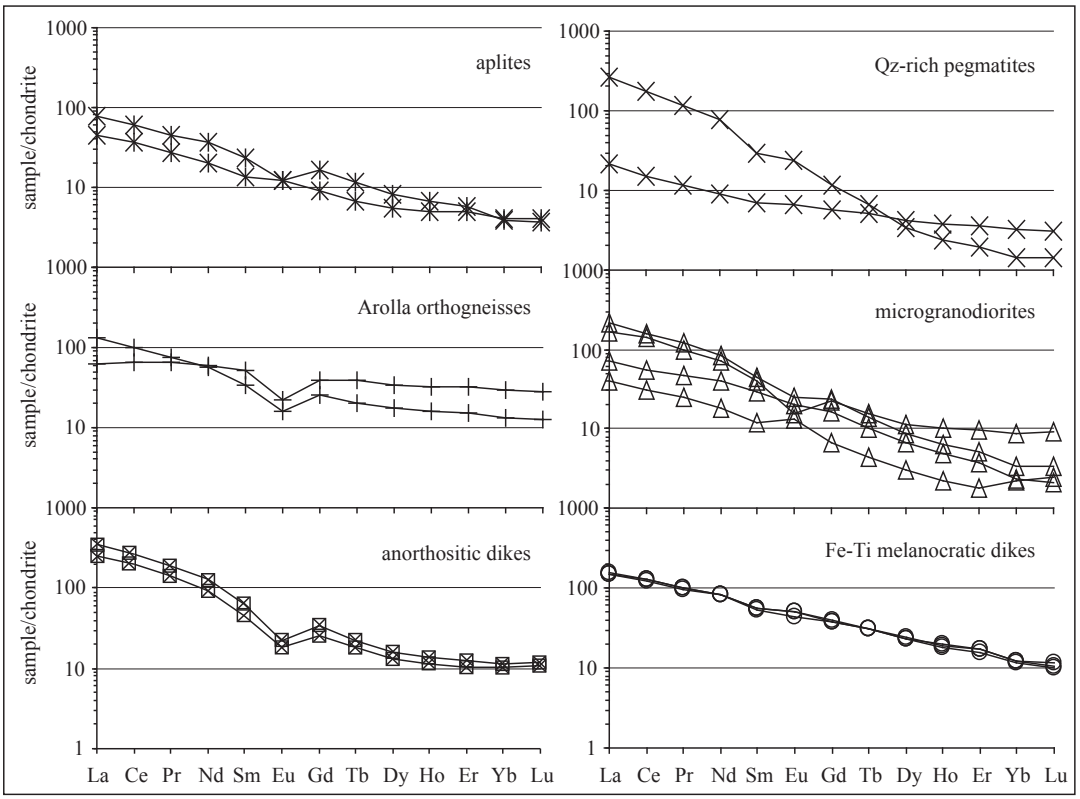

Fig. 55: Chondrite normalized REE content of whole-rocks of the Mont-Collon leucocratic and Fe-Ti melanocratic dikes and the Arolla orthogneisses. Normalization to the C1 chondrite (Sun and McDonough, 1989).

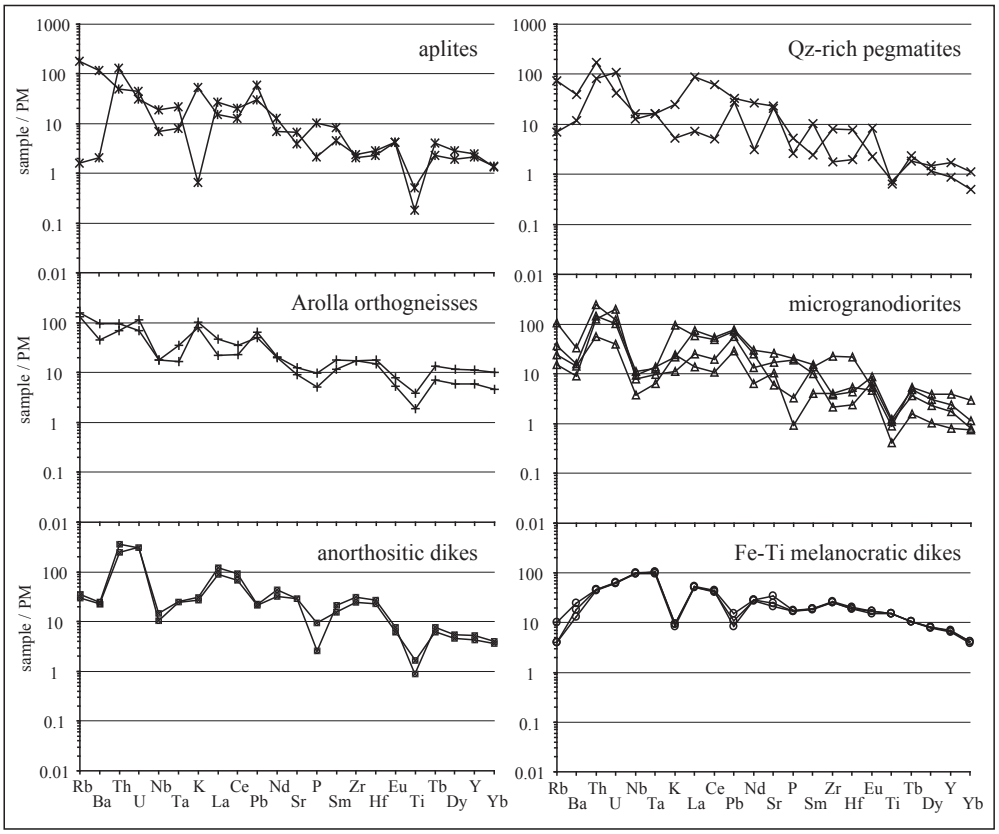

Fig. 56: Extended normalized trace-element plots of the Mont Collon leucocratic, Fe-Ti melanocratic dikes and the Arolla orthogneisses. Normalization after Sun and McDonough (1989).

Table 18a: Nd and Sr isotopic compositions of the Arolla orthogneisses and the dikes exposed in the Mont Collon mafic complex.

Sample type	Sample number	Age (Ma)	$^{143}Nd/^{144}Nd$	2σ	$^{143}Nd/^{144}Nd_i$	εNd_i	$^{87}Sr/^{86}Sr$	2σ	$^{87}Sr/^{86}Sr_i$	εSr_i
Qz pegmatite	MP2	282	0.51209	0.000002	0.51194	-6.4	0.70945	0.000017	0.70834	+59.2
microgranodiorites	MP128	282	0.51213	0.000008	0.51194	-6.6	0.70847	0.000012	0.70708	+41.3
	MP132b	282	0.51239	0.000005	0.51219	-1.6	0.71160	0.000008	0.71005	+83.5
aplites	MP18b	282	0.51224	0.000007	0.511972	-5.9	0.70597	0.000015	0.70573	+22.2
	MP141	282	0.51246	0.000003	0.51222	-1.0	0.71576	0.000013	0.70636	+31.2
	MP173	282	0.51223	0.000004	0.51199	-5.6	0.70718	0.000007	0.70673	+36.4
Arolla orthogneisses	KAW985	289	0.51232	0.000006	0.51209	-3.4	0.71434	0.000011	0.70808	+55.7
	KAW1983	289	0.51241	0.000005	0.51208	-3.7	0.71218	0.000011	0.70837	+59.8
Fe-Ti melanocratic dikes	MP177	259	0.51288	0.000003	0.51266	+7.0	0.70298	0.000011	0.70292	-18.2
	MP245a	259	0.51291	0.000003	0.51268	+7.4	0.70305	0.000007	0.70297	-17.3
	MP249b	259	0.51291	0.000005	0.51268	+7.4	0.70301	0.000009	0.70301	-16.9

Table 18b: Pb isotopic compositions of the Arolla orthogneisses and the dikes exposed in the Mont Collon mafic complex.

		measured Pb ratios										corrected Pb ratios		
Sample type	**Sample number**	**206/204**	2σ	**207/204**	2σ	**208/204**	2σ	**207/206**	2σ	**208/206**	2σ	**$206/204_i$**	**$207/204_i$**	**$208/204_i$**
Qz-rich pegmatite	**MP2**	18.563	0.010	15.680	0.010	38.557	0.011	0.845	0.002	2.077	0.003	18.145	15.662	36.348
microgranodiorites	**MP128**	18.719	0.003	15.689	0.005	39.412	0.006	0.838	0.003	2.105	0.003	18.283	15.666	38.623
	MP132b	18.585	0.002	15.665	0.004	39.660	0.005	0.843	0.002	2.133	0.003	18.016	15.635	38.189
aplites	**MP18b**	18.897	0.011	15.675	0.010	38.784	0.011	0.830	0.002	2.052	0.003	18.554	15.663	36.958
	MP141	18.379	0.003	15.646	0.005	38.450	0.006	0.851	0.002	2.092	0.003	18.132	15.633	38.109
	MP173	18.549	0.004	15.676	0.004	38.906	0.005	0.845	0.003	2.098	0.004	18.196	15.655	37.067
Fe-Ti melanocratic dikes	**MP177**	19.980	0.005	15.651	0.007	39.305	0.008	0.783	0.003	1.967	0.004	18.111	15.549	37.507
	MP249b	19.815	0.004	15.630	0.005	39.035	0.007	0.789	0.002	1.970	0.004	18.496	15.557	37.733

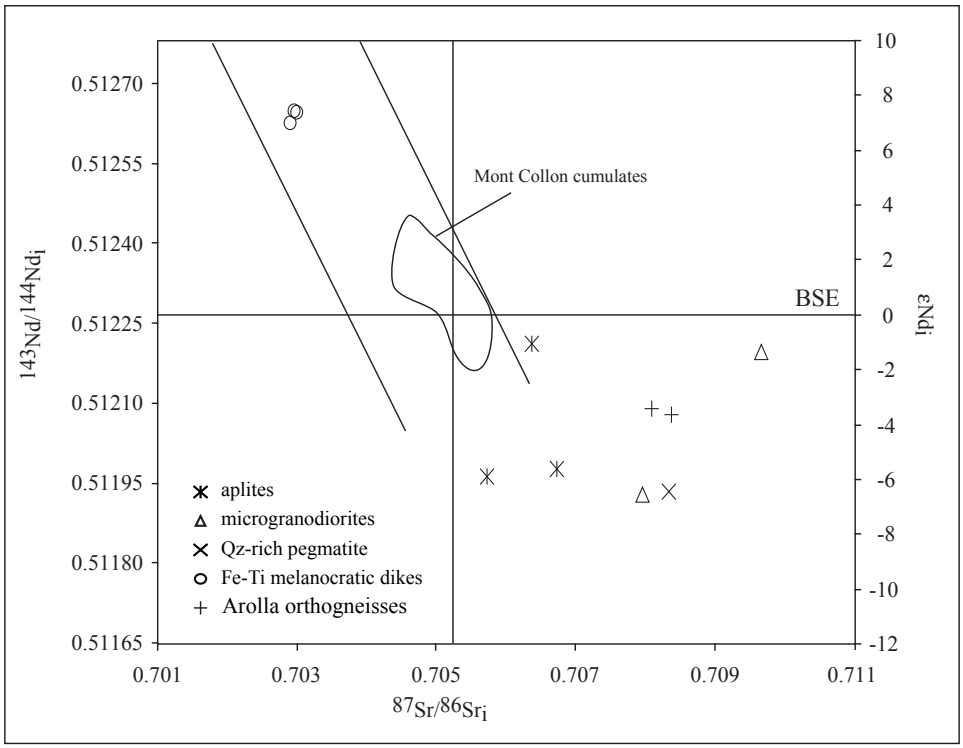

Fig. 57: εNd_i, $^{143}Nd/^{144}Nd_i$ and $^{87}Sr/^{86}Sr_i$ diagram for the Arolla orthogneisses, the leucocratic and Fe-Ti melanocratic dikes. Also shown the compositional field of the Mont Collon cumulates.

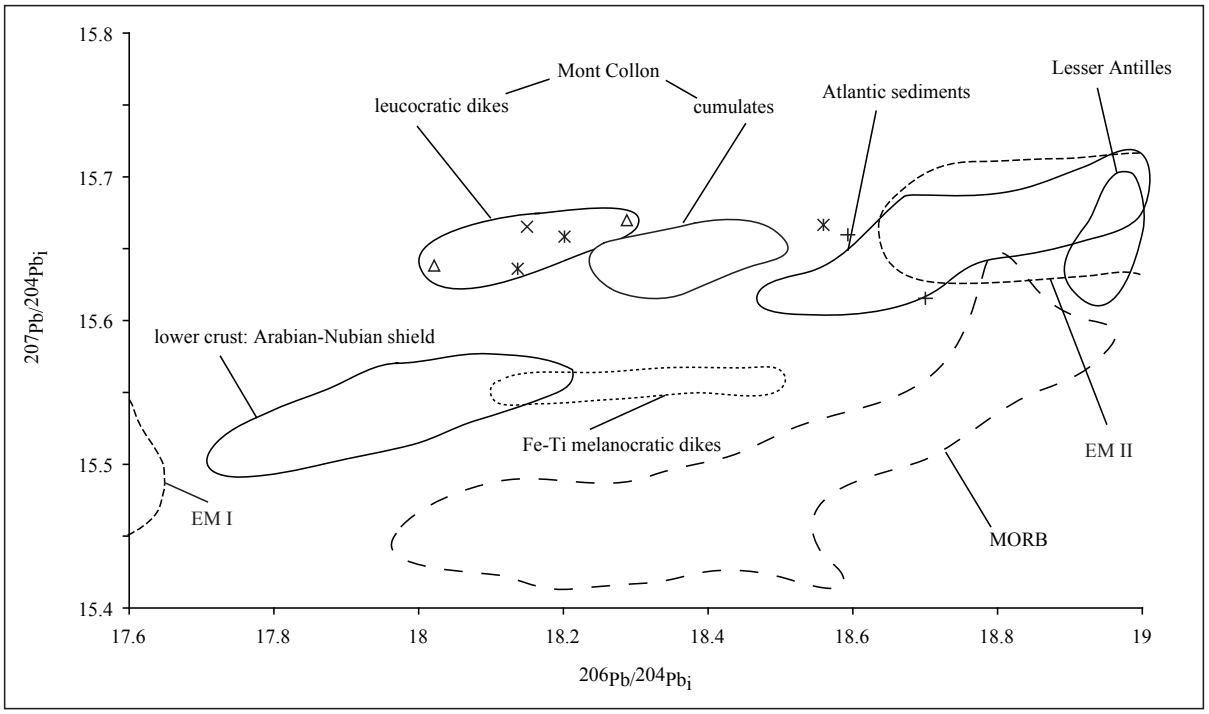

Fig. 58: $^{206}Pb/^{204}Pb_i$ - $^{207}Pb/^{204}Pb_i$ diagram for the leucocratic and Fe-Ti melanocratic dikes. Lower crust of Arabian - Nubian shield (Bosch and Lancelot, 1990), MORB (White et al., 1987), Lesser Antilles (White and Dupré, 1986 and Davidson, 1987), Atlantic sediments (Ben Othman et al., 1989). EM I and EM II fields after Zindler and Hart (1986). Also shown the compositional field of the Mont Collon cumulates. Same legend as figure 53.

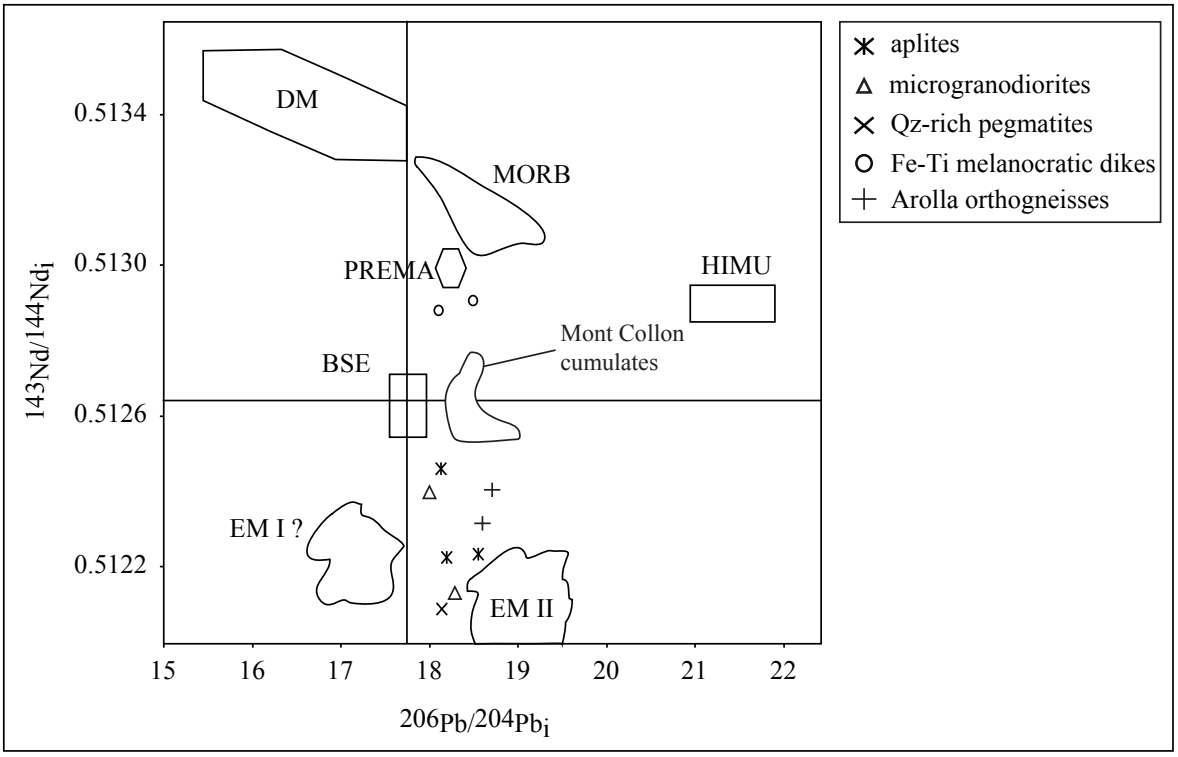

Fig. 59: $^{206}Pb/^{204}Pb_i$ - $^{143}Nd/^{144}Nd_i$ diagram the leucocratic and Fe-Ti melanocratic dikes. MORB, DM, HIMU, PREMA and BSE fields after Zindler and Hart (1986).

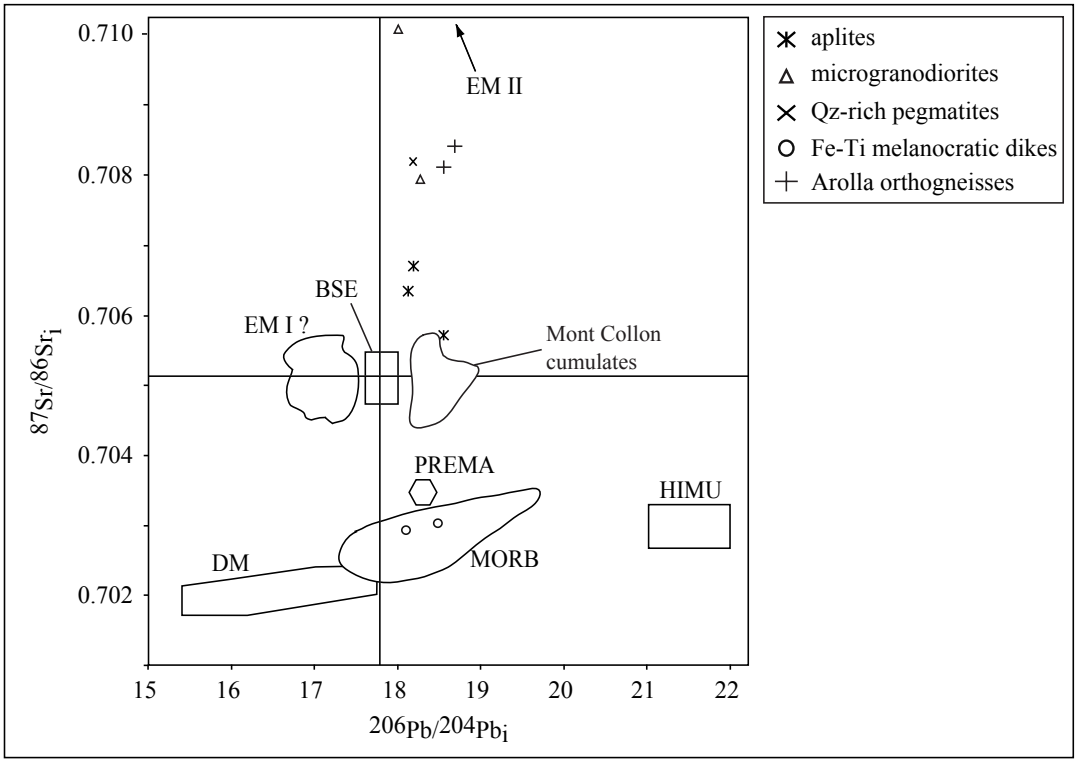

Fig. 60: $^{206}Pb/^{204}Pb_i$ - $^{87}Sr/^{86}Sr_i$ diagram the leucocratic and Fe-Ti melanocratic dikes. MORB, DM, HIMU, PREMA and BSE fields after Zindler and Hart (1986).

The Pb isotope compositions of the leucocratic dikes are heterogeneous and do not depend on the rock type. They fall within the field of the continental crust. In the $^{207}Pb/^{204}Pb_i$ versus $^{206}Pb/^{204}Pb_i$ diagram (Fig. 57, Table 18), the leucocratic dikes show a linear trend between the Bulk Silicate Earth (BSE) and Enriched Mantle II (EMII) fields. This is due to the rather high and homogeneous $^{207}Pb/^{204}Pb_i$ (between 15.635 and 15.666), while the $^{206}Pb/^{204}Pb_i$ ratios are more variable (between 18. .016 and 18.554). Similarly, in the $^{143}Nd/^{144}Nd_i$ and $^{87}Sr/^{86}Sr_i$ versus $^{206}Pb/^{204}Pb_i$ correlation diagrams (Fig. 59 and 60), the leucocratic dikes exhibit a linear trend between BSE and EMII. Among these dikes, one pegmatite and a microgranodiorite fall near the EMII field.

5.4. The Fe-Ti melanocratic dikes

5.4.1. Major- and trace-element chemistry

The Fe-Ti melanocratic dikes are SiO_2-undersaturated (40.7 - 43.1 wt%) and nepheline normative (*ne* = 6.5 - 9.0 %, Fig. 21). They have high FeO* (11.5 - 14.2 wt%; Fig. 54, Table 16), TiO_2 (~ 3 wt%), alkali ($3 < (Na_2O + K_2O)\ \% < 4$ wt%) and P_2O_5 (0.72 to 0.91 wt%) contents. $Na_2O + K_2O$ content is always lower than that of Al_2O_3 and Na_2O content always higher than that of K_2O ($4.1 < Na_2O/K_2O < 8.6$) . Al_2O_3 content decreases from the center part (12.9 wt%) to the margin (11.7 wt%) of the dikes, and is rather high for such low SiO_2 contents. The Al to (Na+K) molar ratios are comprised between 2 and 2.3. Thus, the Fe-Ti melanocratic dikes show features of metaluminous melts (Shand, 1951). Their Mg-numbers (Mg# = molar ratio (Mg / $Mg + Fe^{2+}$) x 100) range from 54 to 57 and remain relatively constant but show a slight negative correlation with SiO_2 (mean value of = 42.1 wt%). The Na_2O, ranging from 2.63 to 3.58 wt%, increases with SiO_2.

5.4.2. Chondrite-normalized rare earth element patterns

All the REE patterns of the Fe-Ti-rich melanocratic dikes are very similar and characterized by high contents (ΣREE_N ~ 700; Fig. 55), and important LREE enrichments (La_N/Yb_N = 12.56 - 13.19). They do not display Eu anomalies (Eu/Eu* = 1.0-1.1).

5.4.3. Primitive mantle-normalized multi-element plots

The Fe-Ti melanocratic dikes exhibit multi-element plots, very similar to those of alkaline mafic rocks (Fig. 56), with marked depletions on both ends of the plots, i.e. Rb and Ba and HREE and Y, respectively. In contrast with the leucocratic dikes and cumulates, the Fe-Ti melanocratic dikes do not show Nb and Ta negative anomalies. Their La/Nb ratio is less than 1. Moreover, they exhibit also K and Pb negative and Sr positive anomalies. The K negative anomaly suggests that the Fe-Ti melanocratic dikes belong to Na-rich alkaline rocks. They are slightly depleted in HREE and Y, which could indicate that they are typical of within-plate alkaline melts.

5.4.4. Nd, Sr and Pb isotope compositions

The Fe-Ti melanocratic dikes have the highest εNd_i values (~+7, , Table 18) and lowest $^{87}Sr/^{86}Sr_i$ ratios of all the Mont Collon igneous suites (Fig. 53, Table 18). This suggests that these melanocratic dikes are mantle-derived melts, without involvement of the continental crust (no crustal contamination). The εNd_i values of the dikes fall in the range of enriched OIB-type mantle source. In the εNd_i-$^{87}Sr/^{86}Sr_i$, the dikes plot in the mantle array. In the $^{206}Pb/^{204}Pb_i$-$^{207}Pb/^{204}Pb_i$ correlation diagram (Fig. 58), the dikes cluster near the MORB field, while in the $^{143}Nd/^{144}Nd_i$ and $^{87}Sr/^{86}Sr_i$ versus $^{206}Pb/^{204}Pb_i$ diagrams (Fig. 59 and 60), they plot below and in the MORB field, respectively.

5.4.5. Discussion on the Fe-Ti melanocratic dikes

Classifying the Fe-Ti melanocratic dikes is not evident for mineralogical and chemical reasons. Their mineralogy is typical for alkaline rocks, i.e. they contain alkaline calcic amphibole (kaersutite), a high modal proportion of apatite, and the clinopyroxene (with high Ti content) appears before plagioclase, in the crystallization sequence. The latter is in the range of albite-oligoclase (An_{5-15}). According the international nomenclature (Le Maitre, 2002), mafic rocks that contain Na-rich plagioclase should be called diorites or if they occur as dikes and are fine-grained, as it is the case here, microdiorites. But diorites are much richer in SiO_2 (55-57%), than our rocks, which are ultrabasic (42-43% SiO_2).

Chemically they have a metaluminous affinity (Al/Na+K molar ratio > 1) and a relatively low Mg-number (Mg# close to 55), typical for evolved liquids. Their Rare Earth Element contents are high (REE_N ~ 700; Fig. 55) and they exhibit important LREE enrichments (La_N/Yb_N = 12.56 - 13.19), and HREE and Y depletions (Fig. 56). They are also nepheline normative, indicating an alkaline tendency. However, their Nd, Sr and Pb radiogenic isotopes suggest that they derived from an asthenospheric mantle source (Fig. 57 to 60). This somehow contradictory

Table 19: Hf isotopic compositions of zircons extracted from the pegmatitic gabbro MP4 and the quartz pegmatite MP2. MP4/x and MP2/x refer to the zircon fractions used for the U/Pb dating.

Sample type and number	Fraction number	Age (Ma)	$^{176}Hf/^{177}Hf$	2σ	$^{176}Hf/^{177}Hf$ standard value	$^{176}Hf/^{177}Hf$ normalized	$^{176}Hf/^{177}Hf_i$	εHf_0	εHf_i	2σ
Pegmatitic gabbro MP4	**MP4/1**	284	0.28271	0.000004	0.28215	0.28272	0.28272	-1.7	+ 4.8	0.1
	MP4/2	284	0.28258	0.000003	0.28213	0.28261	0.28260	-5.8	+ 0.7	0.1
	MP4/3	284	0.28260	0.000003	0.28215	0.28261	0.28261	-5.7	+ 0.8	0.1
	MP4/4	284	0.28263	0.000003	0.28213	0.28266	0.28266	-4.0	+ 2.5	0.1
	MP4/5	284	0.28265	0.000006	0.28213	0.28268	0.28268	-3.3	+ 3.2	0.2
	MP4/6	284	0.28262	0.000005	0.28218	0.28260	0.28257	-6.0	+ 0.4	0.2
	MP4/7	284	0.28261	0.000002	0.28218	0.28260	0.28257	-6.2	+ 0.3	0.1
Quartz-rich pegmatite MP2	**MP2/1**	282	0.28257	0.000003	0.28215	0.28258	0.28258	-6.8	-0.3	0.1
	MP2/2	282	0.28253	0.000003	0.28215	0.28255	0.28254	-8.0	-1.6	0.1
	MP2/3	282	0.28254	0.000006	0.28213	0.28257	0.28257	-7.2	-0.8	0.2

Table 20: Re-Os isotopic compositions of the Mont Collon cumulates, the leucocratic and Fe-Ti melanocratic dikes and the Arolla orthogneisses.

Sample types	Sample number	Re (ppb)	error %	Os (ppb)	error %	$^{187}Os/^{188}Os$ spike corrected	$^{187}Re/^{188}Os$	$^{187}Os/^{188}Os_i$
Plg-wehrlite	FB1095	0.303	0.4	0.0035	1.3	2.88	87.52	2.46
Ol-gabbros	MP161	0.351	0.3	0.0014	1.7	14.62	245.81	13.46
	MP176 (d)	0.109	0.5	0.0015	0.5	2.67	75.00	2.31
Cpx-gabbros	MP134	0.131	0.6	0.0012	1.6	4.37	110.21	3.85
	MP157	0.662	0.4	0.0025	4.0	17.43	268.29	16.16
Pegmatitic gabbro	MP4 (d)	0.163	0.4	0.0015	1.3	8.13	108.20	7.62
Qz pegmatite	MP2	0.035	0.8	0.0015	0.8	1.55	23.35	1.44
granodiorite	MP128 (d)	0.013	1.3	0.0057	5.0	1.27	2.26	1.26
aplite	MP173	0.008	7.2	0.0005	1.7	1.36	16.62	1.28
Arolla orthogneiss	KAW1983 (d)	0.018	0.7	0.0012	1.1	1.38	14.60	1.31
Fe-Ti melanocratic dike	MP177 (d)	0.225	2.2	0.0200	0.3	0.53	11.28	0.47

Blank C1: 0.003 ppb Re (error: 11.8% and 0.28 pg Os (error < 1%). Blank C2: 0.01 ppb Re (error: 4.5% and 0.15 pg Os (error < 1%).

chemical signature is typical for alkaline lamprophyres (Rocks, 1991). Indeed, chemically, the Fe-Ti melanocratic dikes share many typical characteristics of camptonites. Both rock types share the mineralogical composition (clinopyroxene+kaersutite+plagioclase±olivine), major- and trace-element contents, i.e. low SiO_2 (< 45 wt%), high Fe, Ti and Ca contents (~12 wt%, ~3 wt% and ~10 wt%, respectively), high LREE, HFSE (Th, U) and LILE (Nb-Ta) contents. Typical camptonites display a significant K_2O content (up to 2 wt%), compared to the low K_2O (~ 0.5 wt%) of the Fe-Ti dikes. This feature is related to the presence of biotite in camptonite, which has not been recognized in the Fe-Ti dikes.

Alkaline lamprophyres have been found in many different geodynamic settings. They are emplaced either during convergent or distensive geodynamic contexts (Rocks, 1991), as well as in intraplate situation, and related either to lithospheric or asthenospheric mantle sources, according to their Nd, Sr and Pb isotopic signatures (Rocks, 1991; Debon and Zimmermann, 1993; Riley et al., 2003).

Another problem remains to be clarified: The high Na-content composition of the plagioclase is not in agreement with the findings of Dal Piaz et al. (1977), who mentioned a range between An_{70} and An_{55} for the plagioclase of apparently similar dikes in the Matterhorn area and a labradorite composition (An_{68}) from sample DBL 605 outcropping in the Dents de Bertol area. Nevertheless, in the complete absence of deuteric alteration in our samples (no epidote or sericite), we consider that the high Na-plagioclase is a magmatic feature. This plagioclase composition is in agreement with the low Mg# and high trace-element content of these dikes (evolved character).

5.5. The Arolla orthogneisses

5.5.1. Major- and trace-element chemistry

One sample of the Arolla orthogneiss (KAW1983, collection J.C. Hunziker) has a very low SiO_2 content (54.1 wt%; Table 16) compared to rocks of intermediate to acidic composition (Fig. 54) and especially to the other sample Arolla orthogneiss KAW985 (68.0 wt%). Moreover, the Arolla orthogneiss KAW1983 exhibits higher FeO_T, MgO and CaO contents (3.7-8.1, 1.28-3.25 and 2.4-6.1, respectively) than the other orthogneiss. The two samples were not collected in the same place. KAW985 (sample provided by J.C. Hunziker) was sampled near the Matterhorn and not in the vicinity of the Mont Collon intrusion whereas KAW1983 was collected in the host rocks of the complex. As for SiO_2, the two orthogneiss samples show differences in their major-element chemistry. These variations are probably due to variable mobility of elements during metamorphic processes or both orthogneisses could have different protoliths. We rather give preference to the second hypothesis, i.e. these protoliths could be a diorite for sample KAW1983 and a granite for sample KAW985.

5.5.2. REE and extended trace-element patterns and isotope ratios

The differences in major-element chemistry between the two Arolla orthogneisses appear also in their REE and extended trace-element patterns (Fig. 55 and 56, Table 17). The sample KAW985 displays a more fractionated REE pattern (La_N/Yb_N = 10.0) with respect to the other orthogneiss (La_N/Yb_N = 2.2). This difference is marked by LREE enrichment in the former ($\Sigma LREE_N$ = 402.7 ppm) compared with the orthogneiss KAW1983 ($\Sigma LREE_N$ = 303.4 ppm). Inversely, the orthogneiss KAW1983 is HREE-richer ($\Sigma HREE_N$ = 231.9 ppm) than the orthogneiss KAW985 ($\Sigma HREE_N$ = 119.9 ppm).

In spite of their differences, both samples are characterized by marked negative Eu anomalies (Eu/Eu* ~ 0.5), important LILE (Ba and Rb) enrichments, Nb-Ta and Ti negative and Zr-Hf, K and Pb positive anomalies. The positive Pb anomaly is correlated with the Th-U enrichment.

Moreover, Arolla orthogneisses have similar $^{143}Nd/^{144}Nd_i$ ratios (0.51208 - 0.51209), εNd_i values (ranging from -3.4 to -3.7) and $^{87}Sr/^{86}Sr_i$ ratios (0.70808 - 0.70837; Fig. 57). Lead isotopic compositions are also very similar. They plot close to the EMII field in the Nd ratio and $^{207}Pb/^{204}Pb_i$ versus $^{206}Pb/^{204}Pb_i$ correlation diagrams (Fig. 58), and they display Sr isotopic ratio and $^{206}Pb/^{204}Pb_i$ similar of those of microgranodiorite sample MP128 and the quartz-rich pegmatite MP2.

5.6. Hf and Re-Os isotopes of the Mont Collon igneous suites

5.6.1. Hf isotopes

The U/Pb-dated zircon fractions have also been used for Hf isotopes determinations (Fig. 61, Table 19). The zircon Hf data plot in the εHf_i vs. time (Ma) diagram are aligned (because of their similar ages) but, the lower εHf_i of the pegmatitic dike suggest that the latter are more contaminated by the upper crust than the pegmatitic gabbro.

5.6.2. Re-Os isotopes

The Mont Collon cumulate rocks seem to offer valid samples in order to determine Osmium concentrations and isotopic ratios. The Re-Os isotope system differs from the Nd-Sr and Pb ones in that the daughter product Os is highly compatible in the residual mantle during partial melting, whereas the parent Re is incompatible. Thus, melting lowers the Re-Os ratios in the residue. The samples have been analyzed twice because the first set of analyses produced

very low Os contents. Unfortunately, the second data confirm the extremely low Os contents of the cumulates (Table 20), melanocratic and leucocratic dikes. Thus, $^{187}Os/^{188}Os_i$ isotopic ratios (as well as the deviations compared to the CHUR, i.e. the γOs parameter) are not interpretable in term of signatures of mantle or crustal source(s). We can suggest a few hypotheses to explain these very low Os contents, such as the formation of layers rich in minerals with strong affinities for Os, as olivine chromite and sulfide. Such horizons could have precipitated at the base of the intrusion, which is not outcropping or at lower surface level.

Cumulative rocks and Fe-Ti melanocratic dikes display similar ^{187}Re content (0.109 < Re < 0.662 ppb and Re = 0.225 ppb respectively, Table 20). Thus, Re contents could indicate that this element displays the same content in the both sources of the melanocratic dikes and cumulates. Os content is higher by one order of magnitude in melanocratic dikes (^{188}Os = 0.0199). However, as for cumulates, the γOs is also useless, as well as the $^{187}Os/^{188}Os_i$, in view of their very high $^{187}Re/^{188}Os$ ratio.

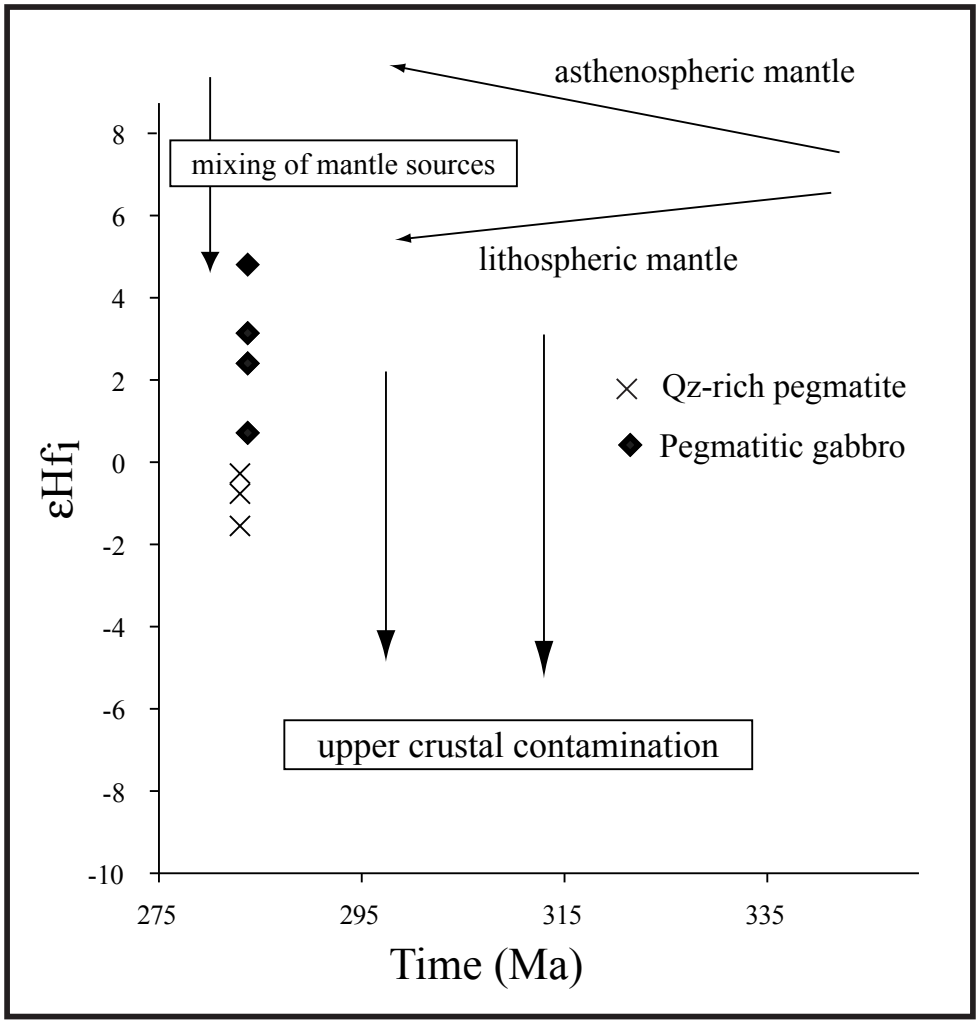

Fig. 61: εHf_i vs. Time (Ma) co-variation diagram for zircon fractions extracted from the dated pegmatitic gabbro (MP4) and the quartz-rich pegmatite (MP2). Arrows refer to general tendencies toward mantellic or crustal reservoirs (after Stille and Schaltegger, 1996).

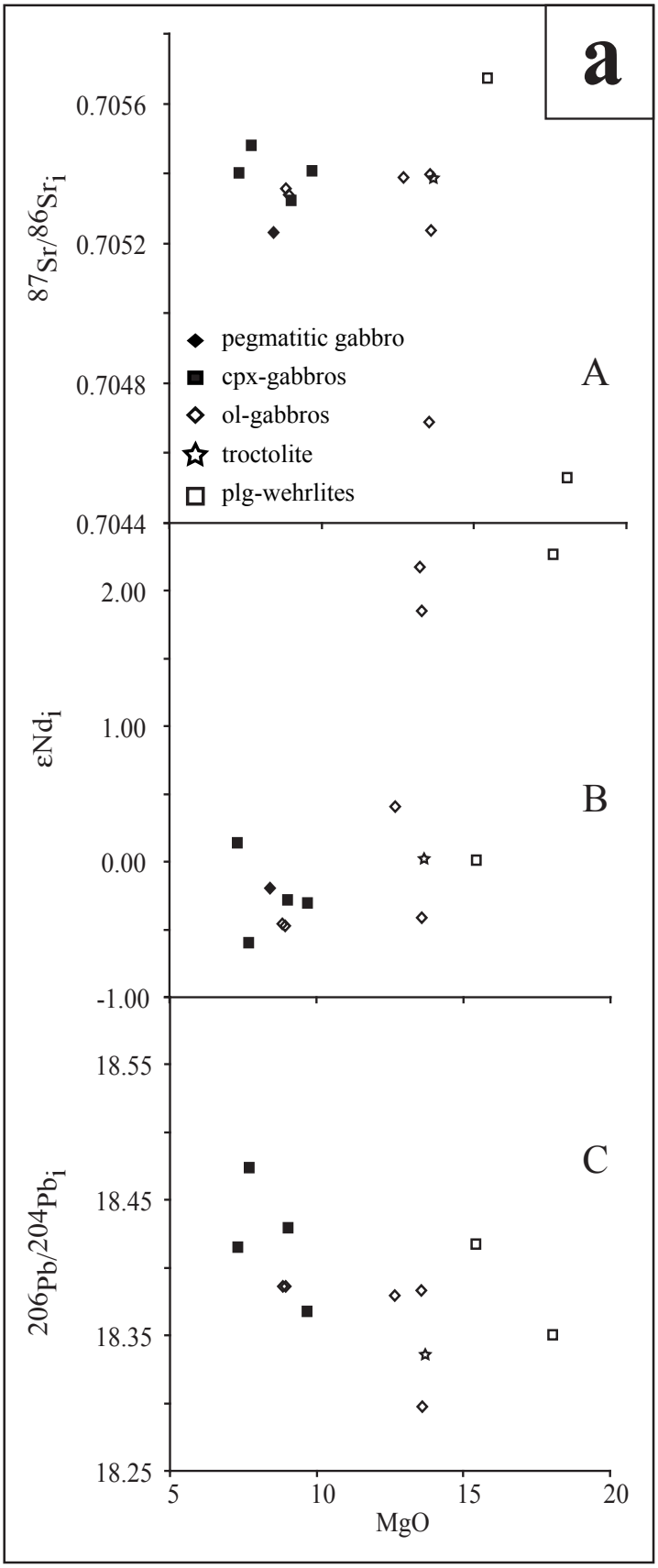

Fig. 62a: Variations diagrams between MgO and $^{87}Sr/^{86}Sr_i$ (A), εNd_i (B) and $^{206}Pb/^{204}Pb_i$ (C) for the Mont Collon cumulates.

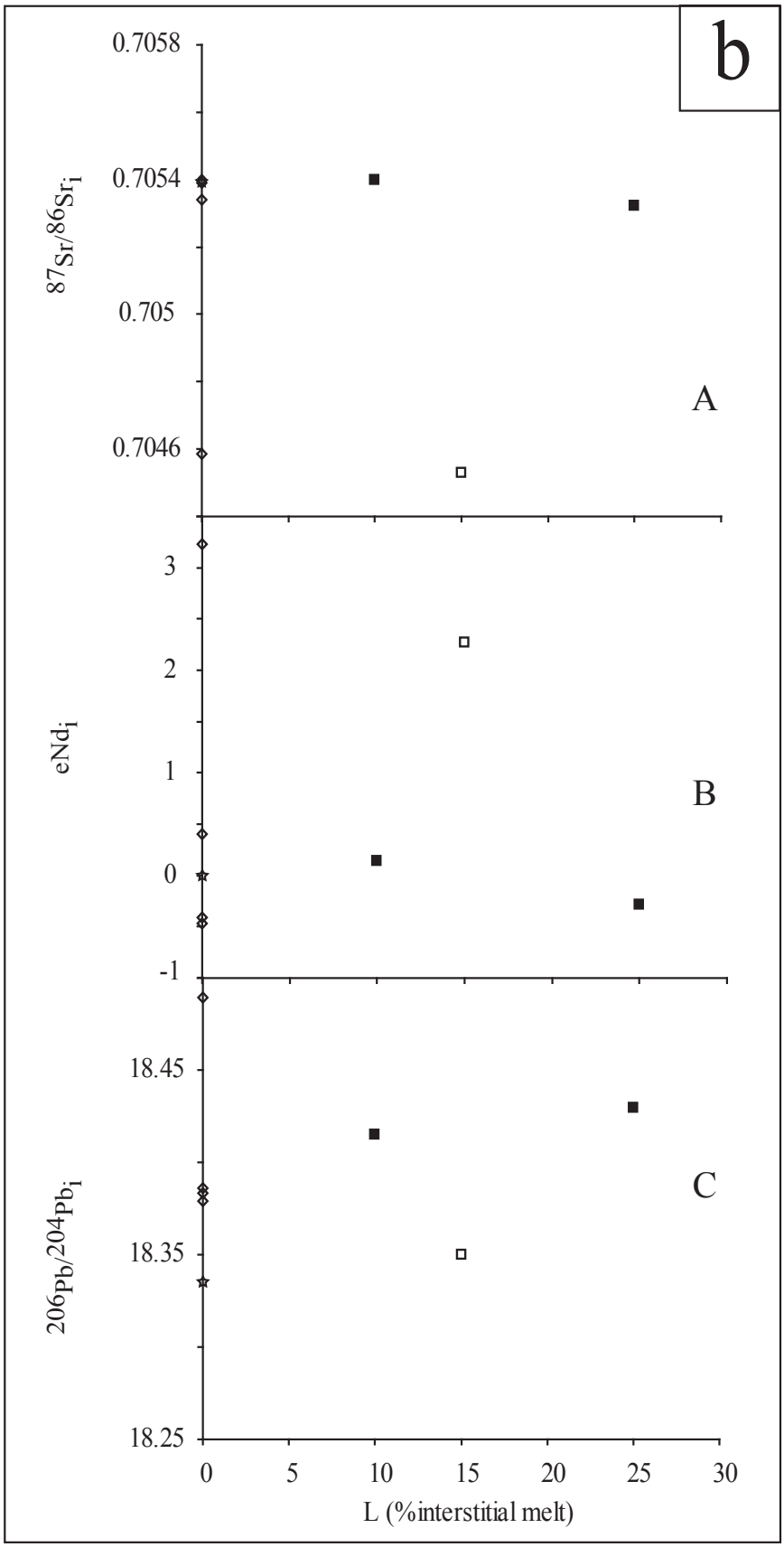

Fig. 62b: Variations diagrams of $^{87}Sr/^{86}Sr_i$ (A), εNd_i (B) and $^{206}Pb/^{204}Pb_i$ (C) as a function of L (% of interstitial melt) for the Mont Collon cumulates.

5.7. Discussion: Nature of the sources and igneous processes linked to the genesis of the Mont Collon cumulates

5.7.1. Assimilation process and influence of the interstitial melt

The cumulate rocks sampled along the Dents de Bertol cliff (group II, see Fig. 49) have remarkably homogeneous εNd_i in spite of the wide range of the MgO contents of the cumulate rocks. Similarly, the Sr and Pb isotopic variations are not linked to the MgO abundances (Fig. 62a). As expected, we assume that the isotopic compositions do not depend on the fractionation degree of the cumulates. We have shown in chapter 5, that the cumulates were characterized by the presence of a LREE and Zr- and Hf-enriched interstitial trapped liquid. The abundance of the trapped interstitial liquid is correlated positively with the modal percentage of amphibole (Fig. 38; see chapter 4). Thus, the incompatible trace-element contents (LREE, Zr, Hf, Rb, Ba, Zr and Y) of the whole rocks and minerals (clinopyroxene, plagioclase and amphibole) depend more or less exclusively on the abundance of the interstitial trapped liquid. They have been significantly increased, in relation to the abundance of trapped liquid. Figures 38 and 41 (see chapter 4) illustrate the well-defined positive correlations between interstitial melt (L) and some incompatible trace elements (Zr, LREE) and the percentage of amphibole. No correlation exists between the abundance of interstitial liquid in cumulates and the initial Nd, Sr and Pb (Fig. 62b). Similar observations can be made for group I. Thus, the variations of the Nd-Sr and Pb isotopic initial ratios are not linked to the presence of the interstitial melt.

The Mont Collon cumulates Nd, Sr and Pb isotopic compositions suggest that these rocks derived from partial melting of an enriched mantle source. Moreover, these cumulates exhibit systematic Nb and Ta negative anomalies, suggesting that this feature is (i) linked to the source composition, (ii) derive from the partial melting of this source (Nb-Ta melt depletion) or (iii) implies the involvement of continental crustal material. In addition, whether a crustal continental component influences the isotopic and trace-element composition of the cumulate, could be related to assimilation or mixing processes or source contamination.

5.7.2. Assimilation-Fractional Crystallization (AFC) and mixing modeling

We carried out an AFC model to confirm or invalidate the possible effects of assimilation during the cumulate fractionation of the Mont Collon mafic melt. For this model, we have selected samples MP152 and KAW1983 as mafic and crustal end-members. Sample MP152 is an ol-gabbro, which is characterized by the highest $\varepsilon Nd_i = +1.9$ value of group II. KAW1983 ($\varepsilon Nd_i = -3.7$) was collected in the Arolla orthogneiss and we assume that it represents the Mont Collon host rocks. Group I rocks have not been considered in this model because they

do not belong to the continuous exposure of the Dents de Bertol sequence. AFC equations and procedure are from De Paolo (1981). The resulting AFC parameters are (i) r, the ratio of the assimilation rate to the fraction of melt remaining, and (ii) F, the fraction of remaining melt. We obtained the values r = 0.7 and F ~ 0.95 (Fig. 63). These values seem to be unrealistic to explain the isotopic compositions of the cumulates by an AFC model with the assumption that the Arolla orthogneisses are the original country rocks of the Mont Collon mafic complex. A very high degree of crustal contamination during the crystallization of cumulates has to be invoked to reach the Sr isotopic compositions of the cumulates with such r-F parameters. Thus, we infer that these calculations fail to reproduce a realistic assimilation-fractional crystallization process. We can assume that assimilation of wall-rock does not represent the main process which could explain the variations of the isotopic composition of Mont Collon cumulative rocks.

Mixing modeling (equations after Langmuir et al., 1978) has been performed using the following mantle (Nd =8 ppm, Sr = 120 ppm, εNd = +7 and $^{87}Sr/^{86}Sr$ =0703; values from Voshage et al., 1990) and crustal (Nd = 40 ppm, Sr = 220 ppm, εNd = -10 and $^{87}Sr/^{86}Sr$ =0715 for the metapelitic Kinzigite Formation of the Ivrea zone, which is thought to be exposed lower crust; values from Voshage et al., 1990) end-members. The obtained mixing curve (Fig. 64) shows that the Nd and Sr isotopic compositions of the Mont Collon mafic cumulates could be

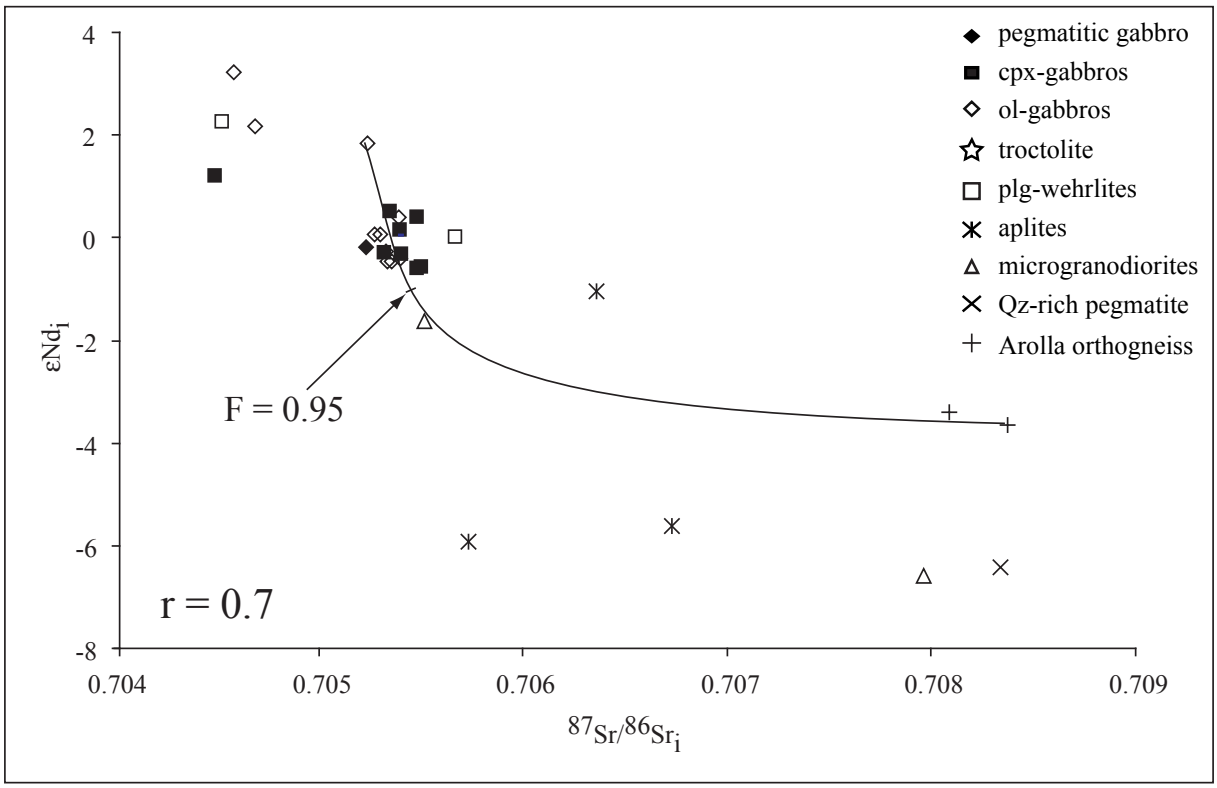

Fig. 63: εNd_i vs. $^{87}Sr/^{86}Sr_i$ diagram for Mont Collon cumulates and acid rocks. Calculated AFC path after the equations of de Paolo (1981). Fractionated assemblages: 45% cpx , 40% plg, 13% ol and 2% amph. $D_{min/M}$ identical to those of the in-situ crystallization modeling (see Table 11).

explained by mixing the mantellic end-member with less than 15% of the crustal end-member. This leads to the conclusion that the Mont Collon mafic cumulates show some effect of crustal contamination. Nevertheless, the mixing curve in figure 64 shows that this contamination is very much weaker in group I samples (between 5 and 10%) than those of group II (between 10 and 15%). Comparison with other mafic complexes (e.g. Finero External Gabbro Unit, Ivrea zone; Lu et al. 1997) or peridotitic massifs exposed in the Alps (Balmuccia, Ivrea zone; Lu et al. 1997) show that similar mixing modeling indicates that in the Finero gabbro suffered very minor contamination by the surrounding crust (less than 10%, Lu et al., 1997), whereas the Balmuccia peridotite massif has been pervasively metasomatized by crust-derived fluids, which led to the crystallization of phlogopite and the development of crustal-type (negative) εNd values.

The Mont Collon cumulates and their mineral components (i.e. clinopyroxene and plagioclase with the exception of the interstitial amphibole, which has a high affinity for Nb) are characterized by U-Th enrichment and Nb-Ta negative anomalies. The significance of this systematic Nb-Ta anomaly could be explained by either crustal contamination of the melt or presence of this anomaly in the mantle source of the Mont Collon mafic cumulates.

The composition of the lower crust was mostly deduced from granulitic rocks, exposed at the surface by regional tectonic processes. Xenoliths perhaps provide a better direct sampling of the lower crust, but they are rare. Average lower crust is MgO and Al_2O_3-rich (7.1 and 16.6 wt%, respectively) according to Rudnick and Fountain (1995) or slightly less enriched in these elements (5.2 and 15.5 wt%, respectively; Fig. 65) according to Wedepohl (1995). The lower crust is LREE-enriched (20 times the chondritic values of Sun and McDonough, 1989). It exhibits also enrichment in HFSE (Th, U) and LILE (Pb, Sr, Ba, Rb and K) but a flat primitive mantle normalized pattern for the other incompatible trace elements (HREE, Zr, Hf and Y). Compared to the CLM (Fig. 65), the lower crust has similar Nb and Ta contents (McDonough, 1990; Downes, 2001), but higher abundances in incompatible elements such as Th, U and LREE. Thus, U and Th enrichment in the cumulates could be related to contamination of the Mont Collon mafic magma by the lower crust during its ascent.

Nevertheless, we cannot rule out the possibility that the mantle source of the Mont Collon mafic cumulates could be metasomatized by (ancient?) subducted-related fluids with crystallatization of Nb-rich minerals (e.g. rutile). Subsequent melting of this mantle would have retained Nb and Ta in the rutile. Thus, we could also generate the observed systematic Nb-Ta negative anomaly by this process.

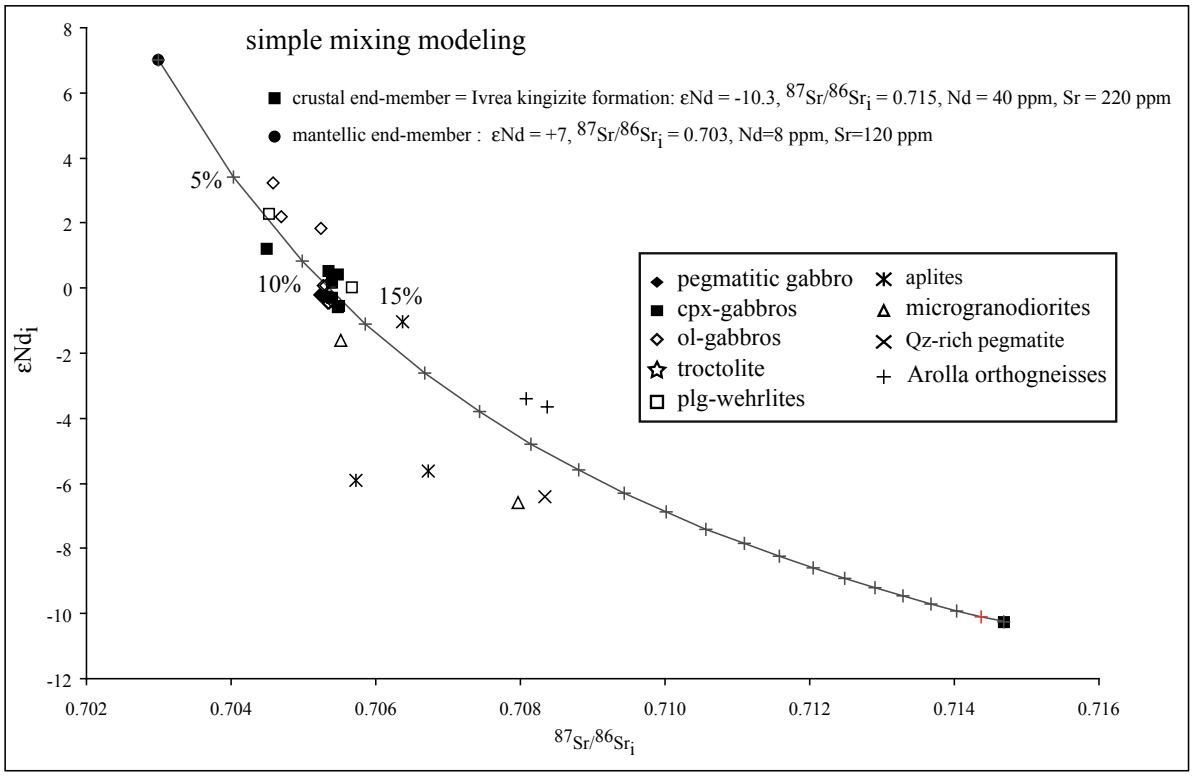

Fig. 64: Simple mixing model curve using the εNd_i vs. $^{87}Sr/^{86}Sr_i$ isotopic composition of the Mont Collon mafic cumulates. The compositions of the mantellic and crustal end-members are given within the diagram (after Voshage et al., 1990).

5.7.3. Mantle source contamination by crustal material(s)

5.7.3.1. Composition of the subcontinental lithospheric mantle

Databases on spinel and garnet peridotite and harzburgite xenoliths (McDonough, 1990; Griffin et al., 2003) are used to constrain the composition of the subcontinental lithospheric mantle (CLM) and demonstrate the secular evolution of its composition. Garnet peridotite xenoliths from Australia, South Africa or Siberian cratons display relatively lower concentrations in some elements (e.g. HREE, Sc, Ca, Mn or Fe) than spinel peridotite of the same locations. These differences are mainly ascribed to regional or age variations between Archean and post-Archean lithospheric mantle. The main process that controls the geochemistry of the CLM is the extraction of basaltic liquid by partial melting, mainly observed in major-element (TiO_2, Al_2O_3 or CaO vs. MgO) variations (Frey and Green, 1975; Ottonello et al., 1984 and Frey et al., 1985). Variations from this model could reflect other processes of trace-element and isotope enrichment or depletion, such as metasomatism processes by subduction-related or carbonatitic melt or fluid (Lu et al., 1997; Lenoir et al., 1997), recycled crustal materials (e.g. Rosenbaum et al., 1997). Other studies based on the comparison between mantle xenoliths and peridotitic massifs tectonically emplaced during Variscan and Alpine orogenies in the Central and Western

Alps (Downes, 2001) show that both the mantle xenoliths exhumed by lavas and the peridotitic massifs (e.g. Ronda, Ivrea, Pyrénées) present similar compositions. The most frequently observed mineralogy consists of anhydrous spinel peridotite with subordinate harzburgite. Such mineralogies and their corresponding major-element and incompatible trace-element compositions are thought to reflect the shallow subcontinental lithospheric mantle (SCLM) composition. In Central and Western Alps, the SCLM is LREE enriched (by metasomatism) or depleted (basaltic melt extraction) relative to the primitive mantle with Nb-Ta positive anomalies (Fig. 65; Table 21). The latter feature is not observed in the extended primitive-mantle normalized plots of the Mont Collon cumulative rocks (Fig. 32). Thus, the trace-element geochemical characteristics of the Mont Collon cumulate cannot be related solely to the partial melting of the CLM. According to numerous publications (e.g. McDonough, 1990; Kalt et al., 1997; Downes, 2001; Cannic et al., 2002), the CLM is characterized by a large range of Nd and Sr initial ratios that fall also in the range of OIB-type enriched mantle. Thus, it appears difficult on the basis of Nd, Sr and Pb isotopic data only, to assume that the mantle source of the Mont Collon cumulates is an enriched asthenospheric or a subcontinental lithospheric mantle. We think that other arguments are needed to determine what type of mantle was the source of the cumulates, i.e. the nature of the crustal component involved at the source of the Mont Collon cumulates or the tectonic features linked to the Mont Collon emplacement.

5.7.3.2. Potential composition of the source contaminant

Data from the Lesser Antilles island arc are useful to discriminate a potential contamination by a continental terrigenous sediment component. Terrigenous sediments display high $^{207}Pb/^{206}Pb$ and $^{87}Sr/^{86}Sr$ ratios. Davidson (1987) postulated that the Lesser Antilles island arc magmas have been contaminated at crustal levels by a sedimentary component intercalated within the Caribbean plate. Because in the Lesser Antilles, the subducted sediments display higher Pb isotopic signatures than Atlantic sediments, White and Dupré (1986) and Davidson (1987) suggested that they contain a terrigenous component derived from the erosion of the Precambrian Venezuela shield area.

In Pb-Pb correlation diagrams (Fig. 51), the Mont Collon cumulates cluster close to the field of the Atlantic sediments. Thus, sediments geochemically similar to those of the Atlantic could represent the crustal component involved in the genesis of the Early Permian mafic magmas. However, the geodynamic setting of the Mont Collon complex is not that of an Andean-type margin and the sediments input cannot be related to the subduction of an oceanic plate. Thus, the sedimentary component must be searched in the lithospheric mantle. The process to call for the presence of recycled sediments in the lithospheric mantle must be an old subduction process, i.e., 900 Ma as suggested by Stille and Schaltegger (1996) or during the Palaeo-Tethys subduction (the multi-stage eclogite-facies metamorphism is dated at 425-395 Ma, i.e. Silurian., Paquette et al., 1989).

	lower crust	CLM
Rb	11	1.9
Ba	259.0	33.0
Th	6.6*	0.7
U	0.9*	0.1
Nb	5	4.8
Ta	0.6	0.4
K	4980	448
La	8	2.6
Ce	20	6.3
Pb	4.2	0.2
Nd	11	2.7
Sr	348	49
P	436.0	244.2
Sm	2.8	0.5
Zr	68	21.0
Hf	1.9	0.3
Eu	1.1	0.2
Ti	4792	539
Tb	0.5	0.1
Dy	3.1	0.5
Y	16	4.4
Yb	1.5	0.3

Table 21: Trace-element compositions of the lower crust (after Rudnick and Fountain, 1995) and the subcontinental lithospheric mantle (McDonough, 1990).

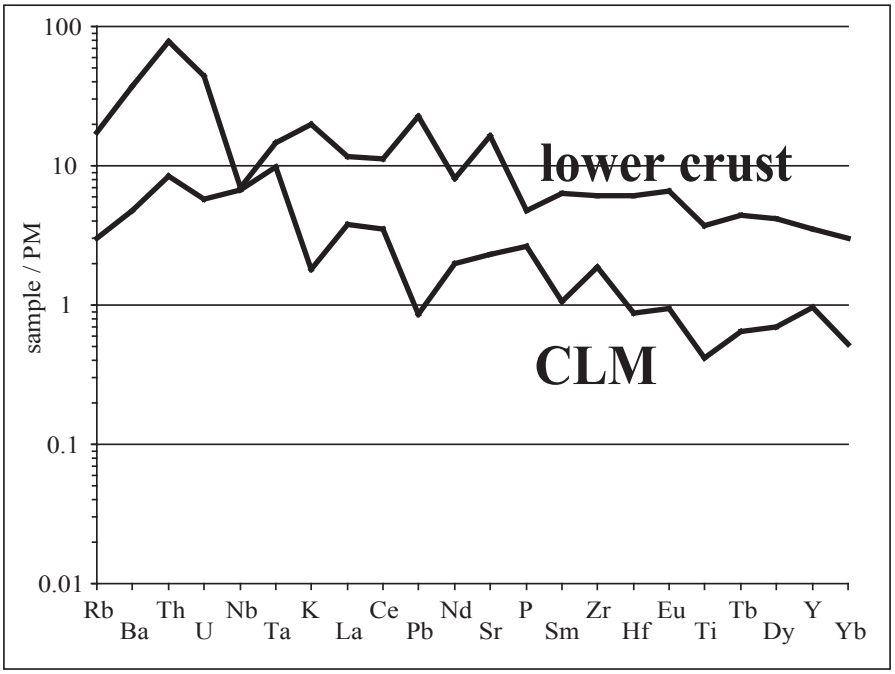

Fig. 65: Primitive mantle-normalized patterns of the lower crust and the subcontinental lithospheric mantle (CLM). Normalization values after Sun and McDonough (1989).

5.8. Could the Arolla orthogneisses be the source of the leucocratic dikes ?

Like the ultramafic and mafic cumulates, the leucocratic dikes display a more or less pronounced Nb-Ta, Zr-Hf and Ti negative anomalies (Fig. 56), a distinctive feature considered as typical of subduction-related magmas (e.g. Pearce, 1983). However, unlike arc-related magmas, all the intermediate to acidic rocks display a more or less pronounced Ba trough relative to the adjacent Rb and Th (-U). Moreover, microgranodioritic dikes are the most Th- and U-enriched among the leucocratic rocks. As discussed in the chapter 7, a subduction-related tectonic setting has never been invoked for the Early Permian magmatism. Thus, the Nb-Ta, Zr-Hf and Ti negative anomalies are not directly related to a subduction tectonic setting but could be related to upper crustal contamination or to the characteristics of the source. Moreover, the Rb and Th enrichments have not to be considered as features of alteration overprint. Rb and Ba show comparable mobility. Th is considered to be immobile in aqueous fluids (Pearce, 1983). So, Ba and Rb have similar behaviors. Consequently, the Ba depletion likely represents a primary magmatic characteristic rather than a consequence of weathering or hydrothermal overprints. Such Rb and Th enrichment relative to Ba is also observed in crustal contaminated volcanic rocks of Southern Alps (Rottura et al., 1998) and in the Pyrenees (Innocent et al., 1994).

The negative εNd_i, high initial Sr and Pb isotopic ratios of the leucocratic dikes (Fig. 57) are more or less similar to those of the Arolla orthogneisses and the upper continental crust. This suggests that the leucocratic dikes could derive from the melting of the Arolla gneisses which are slightly older than the dikes (i.e. ~ 289 Ma, see chapter 4).

Furthermore, the Hafnium isotopic ratio of the Qz-pegmatite clearly suggests the contribution of an upper crustal component in their genesis. Among the leucocratic dikes, some samples have higher Sr ratios than those of Arolla gneisses. This difference could be explained by the presence of fluids, characterized by higher Sr isotopic ratios than the Arolla orthogneisses.

Among the leucocratic dikes, the anorthositic dikes are probably not related to the re-melting of the Arolla orthogneisses. Some characteristics point to an origin from late fractionated products of the Mont Collon mafic cumulates. They display major- and trace-element contents compatible with derivation from residual melt, such as high Al and LREE contents (Fig. 54 and 55). Zircon and apatite (i.e. LREE-bearing minerals) are refractory phases during melting of orthogneiss. Consequently, the resulting melt would be less LREE-enriched than the anorthositic dikes. Moreover, experimental studies have shown that melting of metasediments or orthogneisses cannot generate feldspathic and quartz-free dikes. Consequently, anorthositic dikes are most probably late differentiation products of the Mont Collon cumulates.

5.9. Fe-Ti melanocratic dikes: the late Permian episode

The youngest Fe-Ti melanocratic dikes exhibit clearly distinct characteristics from those of the cumulates and leucocratic dikes. These melanocratic dikes show high incompatible trace-element enrichments (e.g. LREE, Nb-Ta, Th-U) whereas other elements such as K or Pb show marked negative anomalies. The high incompatible trace-element enrichment and the relatively strong LREE/HREE fractionation (La_N/Yb_N = 12 - 13, Fig. 55) suggest that they could be the products of low degree partial melting of an enriched mantle source or more probably they are highly fractionated melts, considering compositional characteristics, such as their rather low bulk rock Mg# (54.3-57.5). They are also depleted in HREE and Y that could be interpretded as a partial melting starting in the garnet stability field.

According to their isotopic Nd, Sr and Pb (εNd_i = +7 and $^{87}Sr/^{86}Sr_i$ = 0.703; Fig. 57 and 54) signatures, the OIB type mantle source of these dikes is more depleted than that of the Mont Collon cumulates and could be the asthenospheric mantle. The rather low $^{87}Sr/^{86}Sr_i$ and Pb initial ratios rule out a crustal contamination.

5.10. Conclusion: the early Permian and late Permian magmatic episodes

The Nd and Sr isotopic chemistry of the Mont Collon cumulates suggests that these rocks derived from the melting of an enriched mantle source (i.e., lithospheric or asthenospheric), although recycled oceanic sediments in the subcontinental lithospheric mantle have to be invoked to explain the Pb isotopic signatures. The systematic Nb and Ta negative anomalies that characterize the Mont Collon cumulates is commonly interpreted as a feature of subducted-related magmas or fluids. However, no contemporaneous subduction of oceanic lithosphere is considered to occur in the early Permian in the Variscan belt. We have shown in a previous section that the Nb-Ta negative anomaly could also be related to crustal contamination. In an intra-continental break-up tectonic setting, specific conditions occurred to obtain «pseudo-calc-alkaline liquids» (this term was introduced by Pin and Marini, 1993).

Similar mafic intrusions in the Alps, e.g. central-eastern Southern Alps mafic intrusions and volcanic districts (Rottura et al., 1998) or the Sondalo gabbroic complex (Tribuzio et al., 1999) are also thought to originate from the melting of lithospheric mantle in the spinel peridotite stability field. These mafic complex all underwent significant crustal contamination and the isotopic composition of their sources are inferred from mixing and/or AFC modeling. Nevertheless, the possible mantle source of the Sondalo complex is supposed to be a NMORB-type mantle, similar to those of the Internal Ligurides ophiolites (Rampone et al., 1996 and 1998).

The Fe-Ti melanocratic dikes are probably the first indication that the subcontinental lithospheric mantle has been reduced in thickness beneath the collapsed Variscan belt and that the asthenosphere reaches the conditions for partial melting. Similar dikes are also exposed in the Braccia gabbro-Val Malenco but their ages and isotopic compositon are not well constrained. But, according to Hermann et al. (2001), these dikes could have the same early Permian crystallization age than that of the surrounding gabbros.

Chapter 6: Geodynamic reconstructions

Chapter 6: Geodynamic reconstructions

6.1. Introduction

The collapse of the mountain belts represents an important feature of post-collisional orogenic stages. Several models have been proposed to explain the tectonic setting, which led to the collapse of the Variscan belt (Malavieille, 1993; Schaltegger and Corfu, 1995; Stampfli, 1996; Ziegler et al., 2001). The accretion of the Huns superterranes and thickening of the Variscan lithosphere occurred mainly during the Devonian and Carboniferous. This episode is rapidly followed by the subduction of the Palaeo-Tethys mid-oceanic ridge (Stampfli, 1996). Extension was associated with a fundamental change, in the regional stress field affecting Western and Central Europe, at the Westphalian-Stephanian boundary. This change was coincident with the termination of orogenic activity in the Variscan foldbelt, followed by major dextral translation between North Africa and Europe. Consequently, after the major Carboniferous Variscan collisional event (Fig. 66), the European Variscan belt underwent repeated intra-continental post-convergence distensive events during the upper Palaeozoic (Matte, 1986; Burg et al., 1994). A first extensional event occurred between the late Visean and the late Westphalian, but extensional processes are not generalized to the whole belt. Inversely, the second distensive episode affected the entire Variscan belt at the late Carboniferous-Permian boundary and led to the complete collapse of the chain.

During the late Carboniferous and Permian, the northern Europe experienced a widespread mafic and acid magmatic activity, associated with a major episode of extensional tectonics (Fig. 67). As proposed by Schaltegger (1997) for the central and western Alpine belt (Austroalpine nappe system, Penninic realm), magmatism could be subdivided into three main events. These observations could be extended through the whole Variscan chain remnants in the Southern Alps, Pyrenees, Corsica, Sardinia or Esterel massif (southeast France).

The Carboniferous magmatism displays mainly high-K and -Mg calc-alkaline affinities (e.g. Internal Crystalline Massifs, Sesia Lanzo zone) or both calc-alkaline and alkaline characteristics (e.g. External Crystalline Massifs). These magmatic suites are characterized by negative εNdi values, showing that melts originating in the lithospheric mantle were affected by substantial crustal contamination.

At the late Carboniferous-early Permian boundary, magmatic activity was also widespread in the Alpine, Corsican/Sardinian and Pyrenean Variscan basement and was represented by numerous granitoids (e.g. Bonin et al., 1993) and scarce mafic complexes (e.g. Hermann et al., 2001; Tribuzio et al., 1999). The geochemical characteristics of volcanic and plutonic rocks resemble closely those of (high-K) calc-alkaline subduction-related magmatism, with still more or less marked Nb-Ta negative anomaly and εNd_i close to the Bulk Silicate Earth values or weakly negative.

Magmas emplaced during the middle and late Permian (after ~ 270 Ma) display mainly alkaline affinities as observed in the Pyrénées (e.g. upper Permian Anayet fifth episode and volcanic suites; Innocent et al., 1994). These volcanic rocks have positive εNdi values, indicating a reduced involvement of the continental crust and the significant implication of asthenospheric mantle.

Nevertheless, we have to mention the occurrence of middle Permian transitional magmas in the Estérel massif (eastern Provence, France; Poitrasson and Pin, 1998), which still exhibit some calc-alkaline characteristics (Nb-Ta negative anomaly) and εNd_i values near 0, like the Mont Collon cumulates. The youngest transitional tholeiitic melts observed in this area are represented by the basalts of the bassin d'Agay and the trachytes of the Batteries des Lions (ca. 250 Ma, Lapierre et al., 1999), which also display Nb-Ta negative anomalies and εNd_i ratios close to the Bulk Earth. Thus, between the Carboniferous and the late Permian, the increase of the εNd_i values, the transition from Nb-Ta negative to positive anomaly and the evolution from calc-alkaline (or subalkaline) to alkaline melt may reflect an increasing contribution of the asthenosphere and a .decreasing role of the lithospheric mantle and/or crustal contamination.

The goal of this chapter is to integrate available geodynamic concepts with ages, P/T calculations and geochemical data obtained on the Mont Collon mafic complex in order to integrate this mafic complex in a regional tectonic context and to constrain the late Variscan orogenic evolution. When taking into account the ages and the geochemical characteristics of the Mont Collon cumulates and the Fe-Ti melanocratic dikes, the tectonic settings responsible for their emplacement have to be clearly different. The crystallization ages obtained on the Mont Collon cumulates and the Fe-Ti melanocratic dikes relate these magmatic events to distinct stages of the Variscan orogenic evolution, separated by approximately 25 Ma. Moreover, the Mont Collon cumulates and Fe-Ti melanocratic dikes have distinct geochemical characteristics (major- and incompatible trace-element contents and isotopes). The variation in the Nd, Sr and Pb isotopic signatures among the cumulates and Fe-Ti melanocratic dikes suggests the participation of at least two distinct components in the mantle source, i.e. the subcontinental lithospheric mantle with an isotopic signature modified by recycled oceanic sediments, and 25 Ma later, an increasing role of the asthenospheric mantle. Evidently, the tectonic environment inducing the partial melting of these two mantle types is the extension of the crust and/or the lithosphere, but the switch between lithospheric to asthenospheric mantles could happen in various ways. Thus, we propose here several hypotheses to explain the partial melting of lithospheric and asthenospheric mantles during the late stages of the Variscan orogeny.

6.2. The collapse stages of the Variscan belt

Various hypotheses have been proposed to explain the collapse of the Variscan belt, by comparison with other belts, i.e. the North American Pacific Coast and a Basin and Range model, the Himalaya belt and a Tibetan plateau evolution or the South American Cordillera and an Andean-type model. Moreover, several extensional periods have been recognized at the late Visean-Westphalian and the late Carboniferous-early Permian to late Permian.

From late Visean to Westphalian (Fig. 66), a first extensional period took place in the Variscan belt and is characterized by sub-parallel ductile strike-slip faulting. This first extensional tectonic episode occurred, while the tectonic convergence prevailed at the scale of the whole orogen (Matte, 1986 and 2001). For instance, pre-330 Ma volcano-sedimentary sequences located in the Aar massif (Bifertenfirn formations) are ascribed to this first distensive episode. They were deposited in relatively small transtensional or extensional basins with some marine and estuarine influences (Schaltegger and Corfu, 1995). Although the age and the lifetime of these small basins are unknown, they could be related to similar late Visean (between 345 and 335 Ma) volcanic and sedimentary deposits of the Southern Vosges (Schaltegger et al., 1996). They probably mark the development of back-arc basins related to the subduction of the Palaeo-Tethys. Between late Visean and Westphalian times, according to Stampfli (1996), the opening of back-arc basins was followed by the diachronous subduction of the Palaeo-Tethys mid-oceanic, along the Variscan belt. It is noteworthy that the subduction of the Palaeo-Tethys mid-oceanic ridge below the Eurasian margin probably protracted up to the Permian (remnants of Permian MORB accretion in Iran, Ruttner, 1993). Such a tectonic environment suggests an analogy between the late collisional stages of the Variscan orogen and an Andean-type orogeny. The Andean-type model would better fit for the Variscan orogen evolution up to the Westphalian (Stampfli, 1996) than a Tibetan plateau evolution (Ménard and Molnar, 1988) in term of width of the belt (300-400 km for the Variscan belt compared to the 1000 km of the Tibetan plateau), amplitude of uplift and timing.

Recent geodynamic reconstructions (Ziegler and Stampfli, 2001; Stampfli and Borel, 2002) suggest that the late Carboniferous-early Permian post-orogenic extension of the European Variscan orogeny is probably induced by the roll-back effect of the still subducting Palaeo-Tethys oceanic slab on the eastern side of the Variscan belt (Fig. 3 and 67). Thus, the Andean-type tectonic, which prevailed during the Visean-Westphalian, was probably followed by a Basin and Range situation, as proposed by Schaltegger and Corfu (1995) and Stampfli (1996). Nevertheless, a Basin and Range geodynamic context is connected with the evolution of an active margin and not with a continent-continent collision as it is the case for the Variscan belt. Using this active margin analogy, the general extension and magmatism, which affected the Variscan belt during the late Carboniferous-early Permian, can certainly be compared to a Basin and Range tectonic context. Schaltegger and Corfu (1995) proposed a Basin and

Range model according to the magmatic activity observed during the late Carboniferous-early Permian. Despite Stampfli (1996) agreed, with caution, with the Basin and Range model for the general collapse of the Variscan belt, tectonic studies (Lorenz and Nicholls, 1984) showed that the Variscan orogenic collapse was accompanied by dextral shear component and/or dextral faulting along continental transcurrent discontinuities. Thus, a Basin and Range model could not be strictly applied to the late Variscan tectonic environment. From late Carboniferous to Autunian, the distension is essentially transverse compared to the general stretching direction of the belt and related to the main generalized collapse evolution of the Variscan belt (Malavieille, 1993). This extensional period is mainly responsible of the formation of the Stephanian (like the Zone Houillère) and early Permian basins (Burg et al., 1990).

Stampfli and Borel (2002) infer that the Permian mafic complexes are related to a subduction tectonic setting. Conversely, we have shown in the previous chapter that the «calc-alkaline» subduction-related Nb-Ta negative anomaly resulted rather from source signature or contamination by a crustal component. Moreover, geochronological investigations indicate a significant time span between the Variscan subduction event and the intrusion of the mafic complexes. For instance, the Variscan eclogites from the Austroalpine Ötztal (Eastern Alps) yield Sm-Nd mineral isochrons of about 360-350 Ma for the eclogite-facies metamorphic overprint (Miller and Thöni 1995).

6.3. Thermal input and melting of various mantle types

6.3.1. The Mont Collon mafic cumulates

We have shown that the 284 Ma-old Mont Collon mafic complex is not unique in the Austroalpine domain (e.g. Val Malenco, Ivrea-Verbano zone, Sondalo; chapter 4, Fig. 48). Available structural data indicate that the emplacement of these mafic complexes was associated with an extensional tectonic regime (Quick et al. 1994; Hermann et al. 1997). The isotopic data (Pb, Nd, and Sr) show that the subcontinental lithospheric mantle (previously contaminated by recycling of oceanic sediments) could be the most suitable source for the Mont Collon cumulates magmas. We could propose some hypotheses based on those provided by available articles. Several tectonic processes could provide enough heat for partial melting of the lithospheric mantle. Melting might be initiated by various processes such as (i) lithospheric mantle root detachment, which could induce the asthenosphere upwelling and heat input at the base of the lithosphere (Fig. 68) and/or (ii) simple adiabatic decompression, delamination of the subcontinental lithospheric mantle by thermal erosion and heat input by asthenosphere upwelling (Fig. 69). Recent modeling on delamination and detachment of lithospheric root have been proposed by Schott and Schmeling (1998) and applied to the Himalayan and Variscan belts, showing that conditions of delamination and detachment of lithospheric root

Late-collisional stage late Visean - 340 Ma

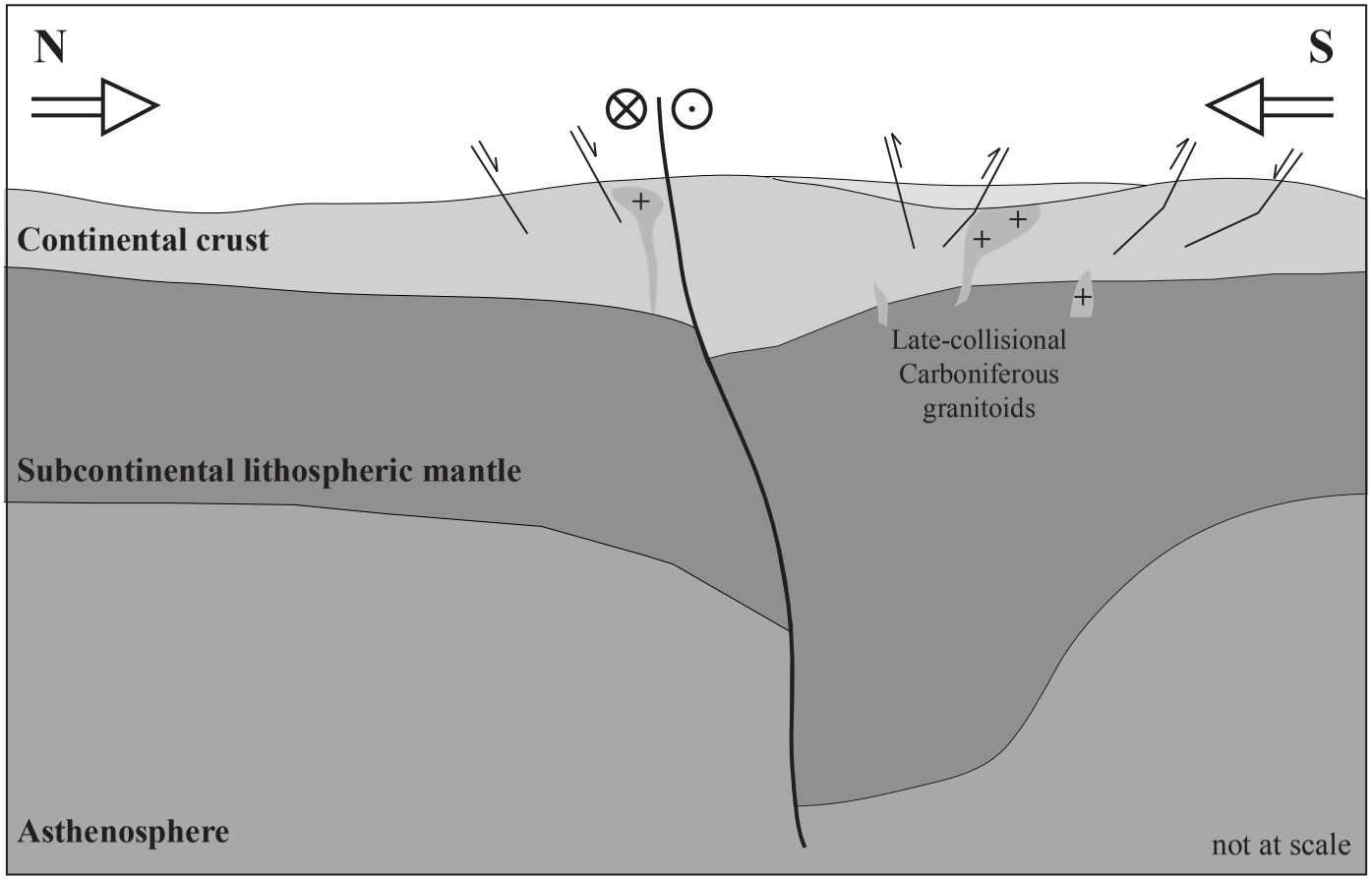

Fig. 66: Simplified cross-section of the Variscan belt after its structuration around 340 Ma (after Schaltegger, 1997; Matte, 1986).

is an appropriate hypothesis, during late orogenic phases of the Variscan belt. Detachment of the Variscan lithospheric root is suggested by Spiess et al. (2001) between 343 ± 2 Ma (according to the metamorphic decompressionnal growth of garnets in micaschists of Ötztal, Eastern Alps; Schweigl, 1995) and 320 Ma (Rb/Sr white micas age cooling of this previous micaschists). This hypothesis was also proposed by Schaltegger (1997) to explain de variations in the magmatic affinities and isotopic signatures of plutons and volcanites and the occurrence of distinct magmatic pulses, despite he suggested that the lithospheric root detachment occurred at the Permo-Carboniferous boundary (around 300 Ma). So, lithospheric mantle root probably occurred during the Carboniferous, but with an upper age limit of 320 Ma. Thus, upwelling of hot asthenospheric mantle could provide enough heat for lithospheric mantle partial melting. Consequently, the partial melting processes at the origin of the Mont Collon cumulates parental melt would not directly be linked to the lithospheric root detachment, but rather to delamination processes (i.e. thermal erosion) induced by the asthenopshere convection and subsequent adiabatic decompression in the mantle.

6.3.2. The Fe-Ti melanocratic dikes

Following the palinspastic reconstructions of Stampfli and Borel (2002), the Variscan belt has completely collapsed at the late Permian (Fig. 70). Mid- to late Permian alkaline dikes geochemically similar to the Fe-Ti melanocratic dikes exposed in the Mont Collon mafic complex were also found in Western Alps (e.g. Val Malenco) or in the Pyrenees. Large swarm of dikes crosscut plutons and pre-Permian Palaeozoic sedimentary sequences in the Pyrenean Axial Zone (Debon and Zimmermann, 1993 and ref. therein; Innocent et al., 1994). Other occurrences of late Permian alkaline dikes are reported by Zheng et al. (1991), Poitrasson and Pin (1998) and Lapierre et al. (1999) in the Mediterranean domain (Esterel massif, eastern Provence, France), but their argon dating have to be taken cautiously considering the highly altered character of the dikes, as reported by Zheng et al. (1991). These dikes are thus also related to the late Variscan distensive stages.

Isotopic and incompatible trace-element characteristics of the alkaline Fe-Ti dikes suggest that they are the products of the melting of the asthenospheric mantle (Fig. 71). The later emplacement of alkali magmas (i.e. the Fe-Ti dikes) implies that the underlying asthenospheric mantle reached the conditions of partial melting. Moreover, the continental crustal contribution is indeed absent from the chemical characteristics of the Fe-Ti melanaocratic dikes. Then, the alkaline melts preserve their geochemical characteristics (Nb-Ta positive anomaly) and isotopic signatures (positive εNd_i and low $^{87}Sr/^{86}Sr_i$ ratios).

Different geodynamic processes were proposed to explain the transition between within-plate continental transitional (or tholeiitic) melts and alkaline mantle magmas in the Variscan belt at the middle and late Permian. In the Pyrenees Range, Vissers (1992) and Vissers et al. (1993) proposed the development of a gravitationally unstable lithospheric root, which consequently detached and were replaced by the upwelling of the asthenosphere producing

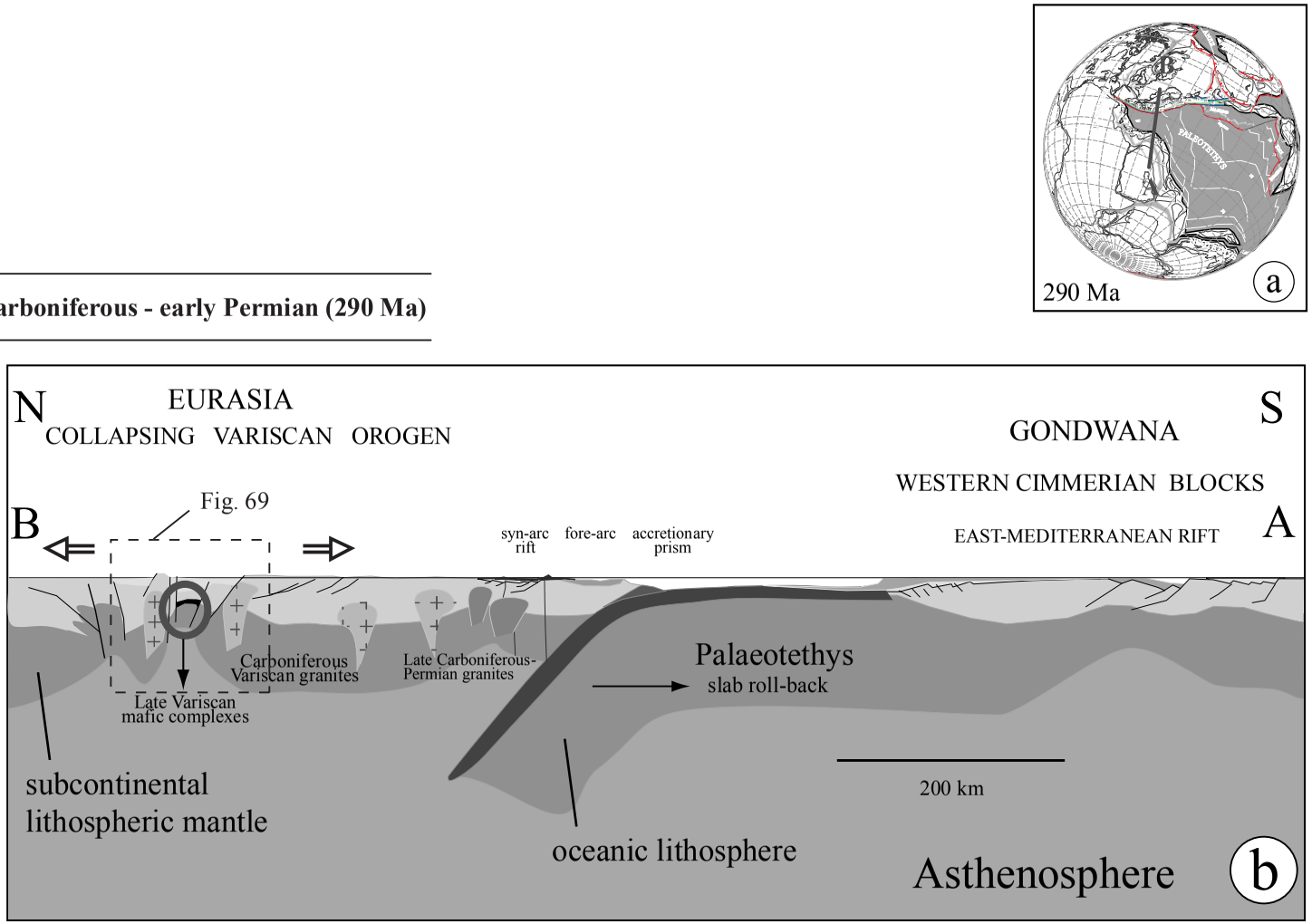

Fig. 67: a) Geodynamic reconstruction at the Carboniferous - early Permian boundary (after Stampfli and Borel, 2002) with a schematic cross-section b (at the lithospheric scale) through the Eurasia and Gondwana terranes at 290 Ma showing the roll-back of the Palaeotethys slab, the collapsing Variscan belt and the possible zone of emplacement of the late Permian Mont Collon mafic complex (after Stampfli, 1996). Also shown the area of the figure 65.

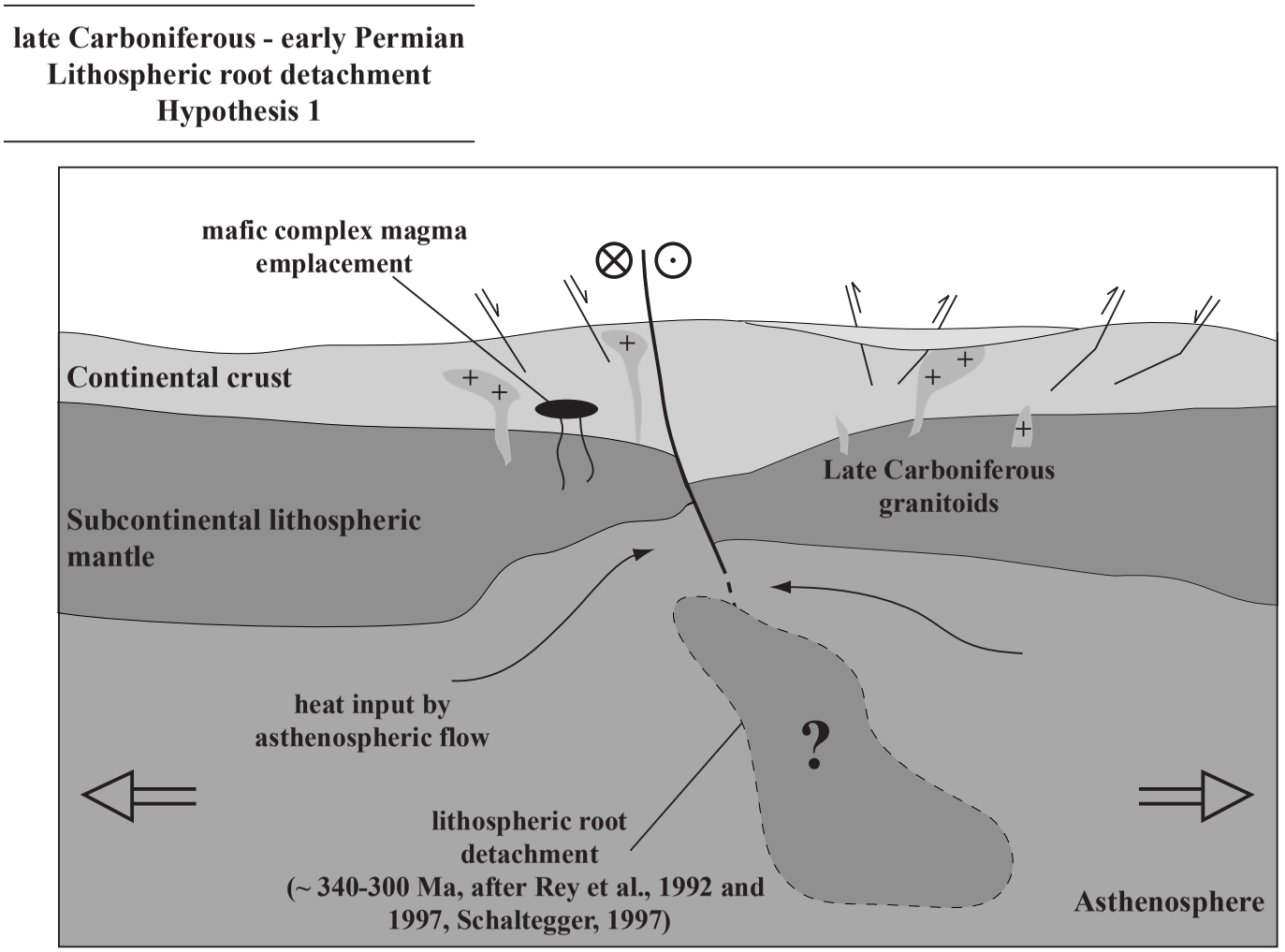

Fig. 68: Hypothetical cross-section through the lithosphere in the Variscan belt at 284 Ma. The hypothesis of a lithospheric root detachment are based on Rey et al. (1992 and 1997), Schaltegger (1997), Schott and Schmeling (1998) and Spiess et al. (2001).

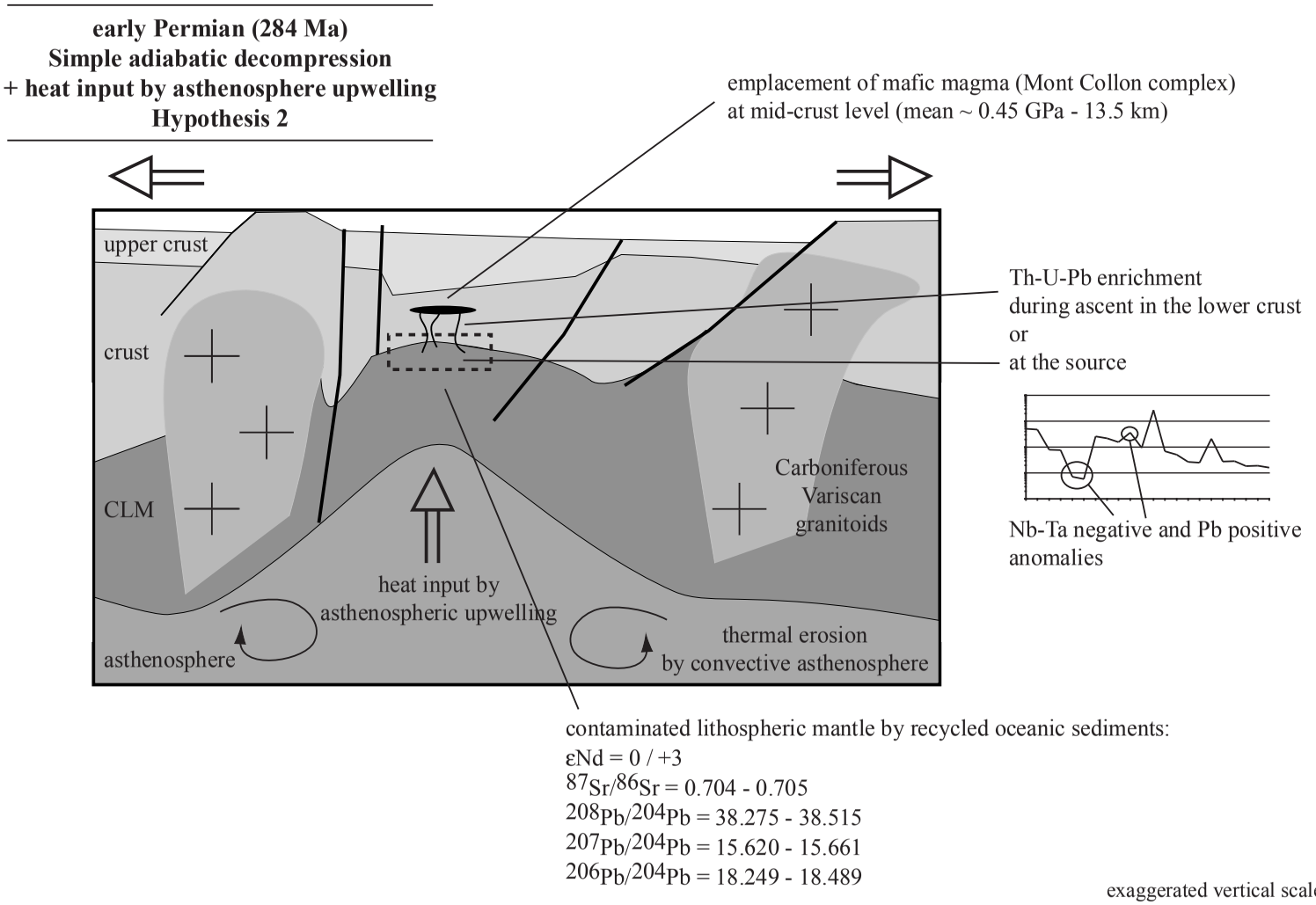

Fig. 69: Other possible model for the heat input at the base of the subcontinental lithospheric mantle for generating basic magmas during the Variscan belt distensive episode (at 284 Ma). Also shown a representative extended pattern (normalization after Sun and Mc Donough, 1989) and a recall of the range of Nd, Sr and Pb isotopic compositions of the Mont Collon cumulates (this study).

late Permian (265 - 260 Ma)

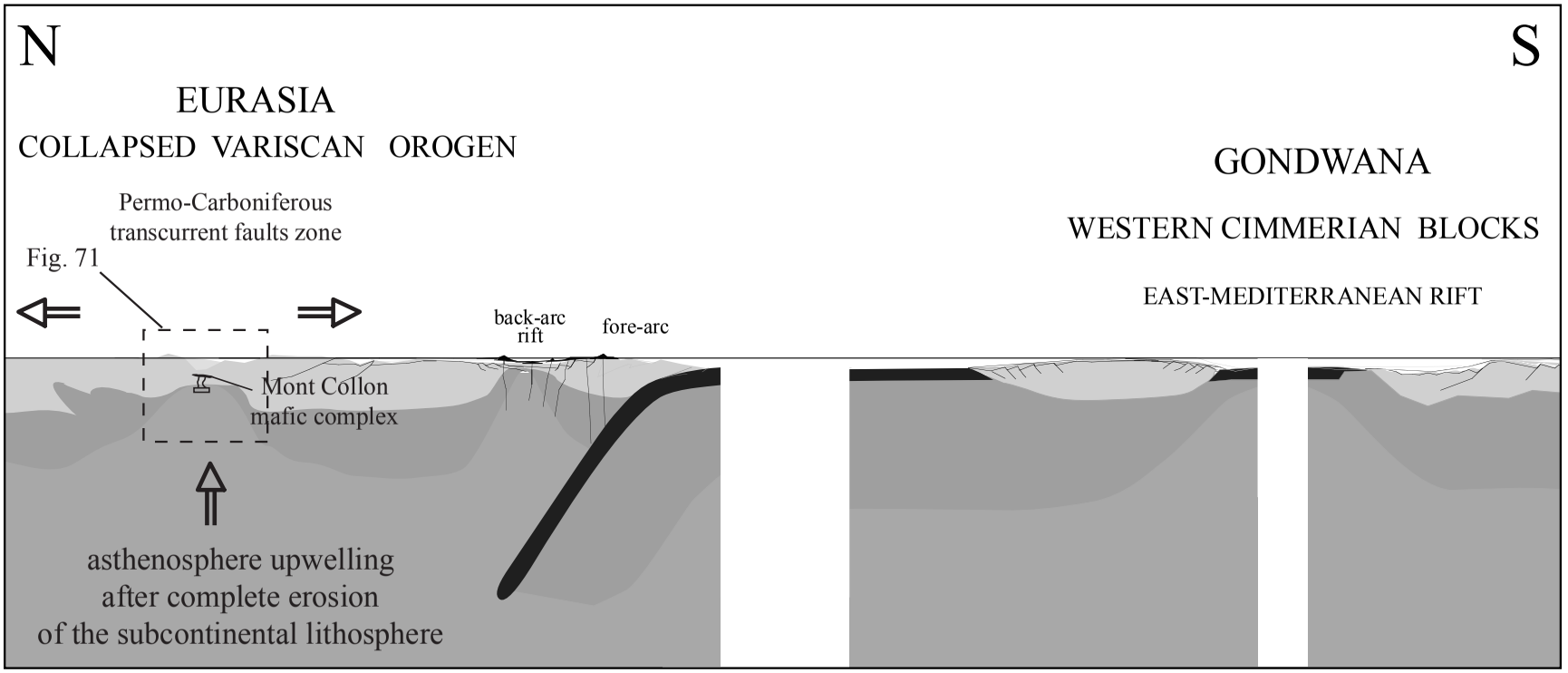

Fig. 70: Cross-section at lithospheric scale through the collapsed Variscan belt and the Mediterranean rift at the Middle Permian (simplified after Stampfli, 1996). Also shown the area of the figure 67.

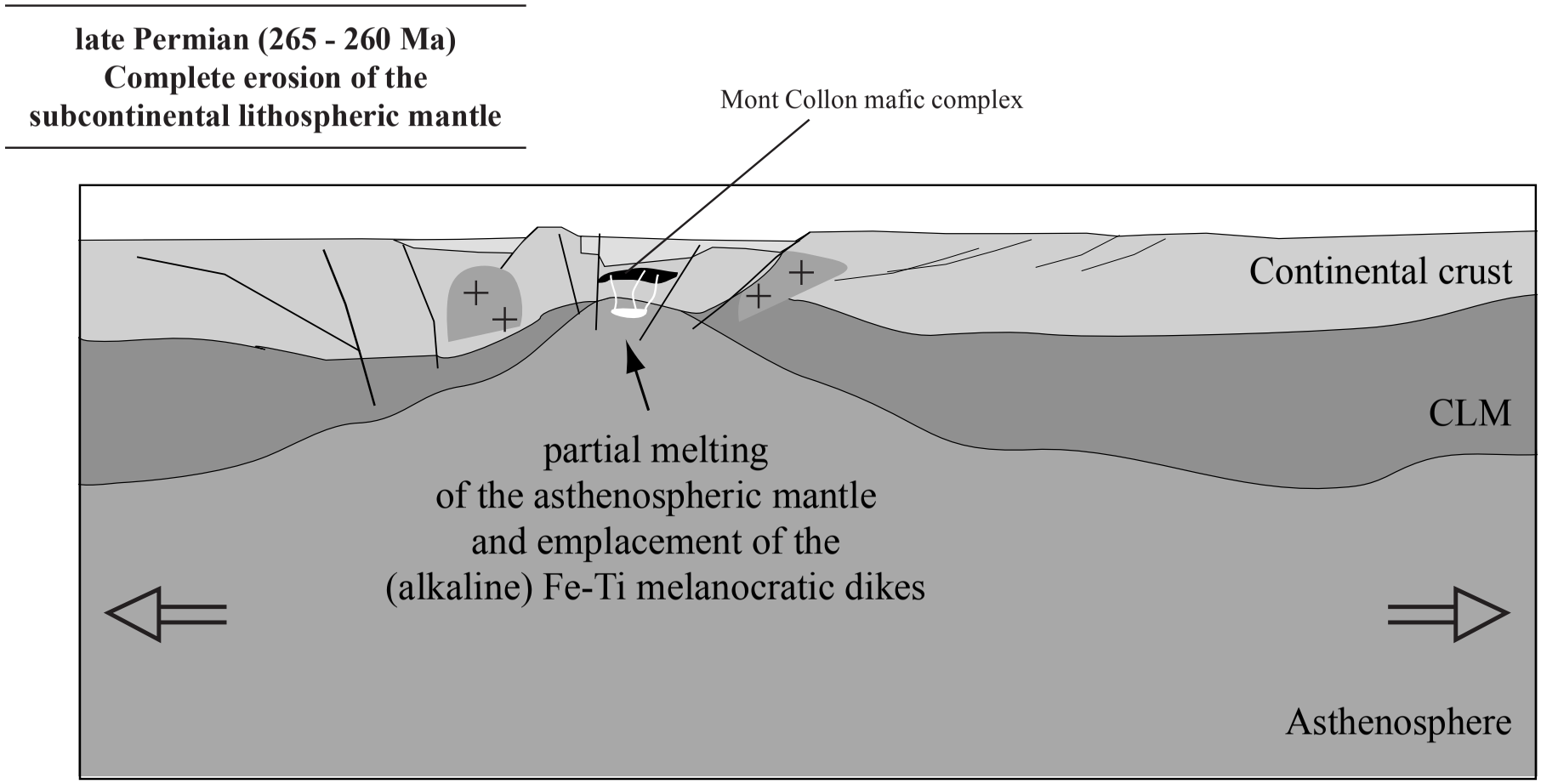

Fig. 71: Profile of the collapsed Variscan belt at the late Permian (265 -260 Ma) showing the possible zone of mantle melting and generation of the Fe-Ti melanocratic dikes.

alkaline mantle-derived magmas. If we suppose that lithospheric root detachment occurred, this process occurred earlier in the Variscan history (see above). Thus, we rather agree with the hypothesis of Innocent et al. (1994 and references therein), which suggested the progressive thinning and finally complete erosion of the lithospheric mantle. The complete disappearance of the subcontinental lithospheric mantle was probably triggered off by the thermal erosion induced by convection in the underlying asthenospheric mantle (Fig. 71).Adiabatic upwelling of the asthenospheric mantle led to its partial melting. These processes lead to the «asthenospherization» of this part of the Variscan belt.

6.4. General conclusions

In a time span of 25 Ma, the mantle source of the magmatism occurring in the Dent Blanche nappe evolves, pointing to an increasing thermal gradient and the final implication of the asthenospheric mantle. Extension is induced by the roll-back effect of the distant Palaeo-Tethys subduction zone, although gravitational collapse has probably to be taken into account and associated to subduction pull forces in extensional processes. We exclude a lithospheric mantle root detachment at 280 Ma and we give preference to the delamination of the subcontinental lithospheric mantle by thermal erosion and decompressionnal melting (Fig. 71). The thermal erosion of the subcontinental lithospheric mantle, induced by the convection of the underlying asthenosphere was certainly active during the melting of the subcontinental lithospheric mantle. This process is consistent with the tectonic environment that led to the generation of the Fe-Ti melanocratic dikes asthenosphere-derived melts. They are the markers of the evolution from transitional to alkaline magmatism and their ages constitute possibly an upper limit age for the collapse of the Variscan belt in the Western Alps. This chronological switch from transitional melts to asthenospheric alkaline products seems to be common during the late-Variscan stages, as shown by the widespread similar dikes in all the European Variscan realms. The complete restructuration of the lithosphere was thought to be completed close to 200 Ma (Innocent et al., 1994), while the final closure of the Palaeo-Tethys in the Tethyan domain was achieved during the Cimmerian (Triassic to Jurassic) orogenic cycle (Innocent et al., 1994; Stampfli and Borel, 2002). The overall tectono-magmatic evolution is interpreted in a scenario of post-collisional thinning and restoration to normal size of a thickened continental lithosphere. The latter re-equilibrates through root detachment, delamination and thermal erosion of the lithospheric mantle.

This study of Mont Collon mafic complex provides new insights into the mineralogical and geochemical characteristics of this well-preserved early Permian layered mafic intrusion and the geochemistry of magmas related to the Carboniferous - early Permian and late Permian tectonic episode of the Variscan belt.

This work has produced important new data on the Mont Collon mafic complex:

i) the field study, which allowed us to discriminate three major rock suites, i.e. the mafic cumulates, the leucocratic and the Fe-Ti melanocratic dikes.

ii) U/Pb and $^{40}Ar/^{39}Ar$ dating on mafic and acid pegmatitic rocks and the Fe-Ti melanocratic dikes, respectively,

iii) major- and trace-element analyses on whole rocks and minerals in order to model the differentiation process of the cumulates,

iv) isotopic analyses showing that several types of isotopes (Nd, Sr, Pb and Hf) are necessary to discriminate the source signature, the contamination processes (at the source or during the ascent of magmas), each isotope providing specific informations.

Compiling all the data enable to propose geodynamic reconstructions at the Carboniferous - early Permian boundary and at the middle Permian.

The major rock suites recognized during the field work are (i) the mafic rocks i.e. the cumulates (wehrlites, plg- wehrlites, ol- and cpx-gabbros, troctolite and anorthosite) and pegmatitic gabbros, (ii) the leucocratic dikes (quartz-rich pegmatites, aplites, granodiorites and anorthositic dikes) and (iii) the Fe-Ti melanocratic dikes.

The crystallization ages of the Mont Collon cumulates (ca. 284 Ma), the widespread leucocratic dikes exposed in the complex (ca. 282 Ma) and, the Fe-Ti melanocratic dikes (ca. 260 Ma) allow us to infer that two major magmatic events occurred in this area in 20 Ma. These data are crucial for the understanding of the magmatic activity because they show that the collapse episode of the Variscan belt is a long-lasting tectonic event.

The fact that the majority of the rocks present in the Mont Collon mafic complex are cumulates (~95 vol-%) and that, therefore, we could not use methods on major and incompatible trace elements classically applied to the magmatic representative liquids, show well that it is necessary to take care of erroneous interpretations based on binary covariation diagrams (e.g. correlations between incompatible trace-element ratios) or partial melting equations, which can only apply to volcanic rocks. Nevertheless, coupling an *in-situ* crystallization model with Nd, Sr and Pb isotopic geochemistries permit us to understand the differentiation processes at the origin of the cumulates, i.e. (i) the involvement of an LREE-rich interstitial melt during crystallization of cumulates influences in an considerably way the trace-element contents and behaviors in whole rocks and minerals, (ii) the trace-element characteristics of the parental liquid show that transitional melts are not restricted to oceanic environments but also to continental settings, (iii) the subcontinental lithospheric mantle previously contaminated by oceanic sediments is a suitable source for mafic magmas and, (iv) the widespread Nb-Ta negative anomaly results from subcontinental lithosphere or the crustal contamination by crustal component rather than be related to melting in subduction-type tectonic environment.

The second magmatic mafic event occurring in the Mont Collon mafic complex is represented by the emplacement of alkaline melts (i.e. the Fe-Ti melanocratic dikes). These geochemically contrasted dikes indicate the melting of asthenospheric mantle.

Thus, each magmatic episode (early Permian and late Permian) is characterized by distinct geochemical signature related to distinct geodynamic environment.

References

References

Avigad, D., Chopin, C., Goffé, B. and Michard, A. (1993): Tectonic model for the evolution of the western Alps. Geology, 21: 659-662.

Ayrton, S., Bugnon, C., Haarpaintner, T., Weidmann, M. and Frank, E. (1982): Geology of the front of the Dent-Blanche Nappe in the Mont-Dolins region, Valais. Eclogae geol. Helv., 75(2): 269-286.

Ballèvre, M., Kienast, J.R., and Vuichard, J.P. (1986): La «nappe de la Dent blanche» (Alpes Occidentales): deux unités austroalpines indépendantes. Eclogae geol. Helv., 79: 57-74.

Beattie, P. (1994): Systematic and energetic of trace-element partitioning between olivine and silicate melts: Implication for the nature of mineral/melt partitioning. Chem. Geol., 117: 57-71.

Ben Othman, D., W. M. White, and J. Patchett (1989): The geochemistry of marine sediments, island arc magma genesis, and crust-mantle recycling, Earth Planet. Sci. Lett., 94, 1-21.

Barnes, S.J. (1986): The effect of trapped liquid crystallization on cumulus mineral compositions in layered intrusions. Contrib. Mineral. Petrol., 93: 524-531.

Barrat, J.A., Keller. F, Amosse, J., Taylor, R.N., Nesbitt, R.W. and Hirata, T. (1996): Determination of rare earth elements in sixteen silicate reference samples by ICP-MS after Tm addition and ion exchange separation. Geostand. Newslett., 20(1): 133-139.

Belka, Z., Valverde-Vaquero, P., Dörr, W., Ahrendt, H., Wemmer, K., Franke, W. and Schäfer, H.J. (2002): Accretion of first Gondwana-derived terranes at the margin of Baltica. In: Winchester, J.A., Verniers, J. and Pharaoh, T.C. (Eds.): Palaeozoic amalgamation of Central Europe. Spec. Publ. Geol. Soc. London, 201: 19–36.

Bigi, G., Castellarin, A., Coli, M., Dal Piaz, G.V., Sartori, R., Scandone, P. and Vai, G.B. (1990): Structural model of Italy 1:500000, sheet 1. C.N.R., Progetto Geodinamica, SELCA, Firenze.

Bistacchi, A., Dal Piaz, G.V., Massironi, M., and Balestrieri, M.L. (2001): The Aosta-Ranzola extensional fault system and Oligocene-Present evolution of the Austroalpine-Penninic wedge in the northwestern Alps. Int. J. Earth Sci., 90: 654-667

Bonin, B. Brändlein, P., Bussy, F., Desmons, J., Eggenberger, U., Finger, F., Graf, K., Marro, Ch., Mercolli, R., Oberhänsli, R., Ploquin, A., von Quadt, A., von Raumer, J.F., Schaltegger, U., Steyrer, H.P., Visonà, D. and Vivier, G. (1993): Late Variscan magmatic evolution of the Alpine basement. In: J.F. von Raumer and F. Neubauer (eds): Pre-Mesozoic geology in the Alps, Springer-Verlag: 171-202.

Boriani, A. and Villa, I.M. (1997): Geochronology of regional metamorphism in the Ivrea-Verbano Zone and Serie dei Laghi, Italian Alps. Schweiz. Mineral. Petrogr. Mitt., 77(3): 381-401.

Bosch, D. and Lancelot, J.R. (1990): A Pan-African age for the HP-HT granulite gneisses of Zabargad island: implications for the early stages of the Red Sea rifting. Earth Planet. Sci. Lett., 107: 539-549.

Bucher, K., Dal Piaz, G.V., Oberhansli, R, Gouffon, Y., Martinotti, G. and Polino, R. (2003): Blatt 1347 Matterhorn. Geol. Atlas Schweiz, 1/25 000, Karte: 107.

Bucher, K., Dal Piaz, G.V., Oberhansli, R, Gouffon, Y., Martinotti, G. and Polino, R. (2004): Blatt 1347 Matterhorn. Geol. Atlas Schweiz, 1/25 000, Erlut.: 107.

Burg, J.P., Brun, J.P. and van den Driessche, J. (1990): Le sillon Houiller du Massif Central français: faille de transfert pendant l'amincissement crustal de la chaîne varisque ? C. R. Acad. Sci., 311: 147-152.

Burg, J.P., van den Driessche, J. and Brun, J.P. (1994): Syn- to post-thichening extension: mode and consequences. C. R. Acad. Sci., 319: 1019-1032.

Bussy, F. (1990): Pétrogenèse des enclaves microgrenues associées aux granitoïdes calco-alcalins: exemple des massifs varisque du Mont-Blanc (Alpes occidentales) et miocène du Monte Capanne (Ile d'Elbe, Italie). Mém. Univ. Lausanne, 7: 309 pp.

Bussy, F. and von Raumer, J. (1993): U/Pb dating of Paleozoic events in the Mont-Blanc crystalline massif, Western Alps. Terra Abstr., 5(1): 382-383.

Bussy, F. and Cadoppi, P. (1996): U/Pb zircon dating of granitoids from the Dora-Maira massif (western Italian Alps). Schweiz. Mineral. Petrogr. Mitt., 76(2): 217-233.

Bussy, F. and Hernandez, J. (1997): Short-lived bimodal magmatism at 307Ma in the Mont Blanc/Aiguilles Rouges area: combination of decompressional melting, basaltic underplating and crustal fracturing. Quad. Geodin. Alpina Quat. 4:22.

Bussy, F., Venturini, G., Hunziker, J.C., and Martinotti, G. (1998): U/Pb ages of magmatic rocks of the western Austroalpine Dent Blanche-Sesia Unit. Schweiz. Mineral. Petrogr. Mitt., 78: 163-168.

Bussy, F., Hernandez, J. and von Raumer, J. (2000): Bimodal magmatism as a consequence of the post-collisional readjustment of the thickened Variscan continental lithosphere (Aiguilles Rouges-Mont Blanc massifs, western Alps). Trans. Royal Soc. Edinburgh, 91: 221-233.

Cannic, S., Lapierre, H., Monié, P., Briqueu, L. and Basile, C. (2002): Late orogenic evolution of the Variscan lithosphere: Nd isotopic constraints from the western Alps. Schweiz. Mineral. Petrogr. Mitt., 82: 77-99.

Claeson, D.T. (1998): Coronas, reaction rims, symplectites and emplacement depth of the Rymmen gabbro, Transscandinavian Igneous Belt, southern Sweden. Mineral. Mag., 62(6): 743-757.

Compagnoni, R., Dal Piaz, G.V., Hunziker, J.C., Gosso, G., Lombardo, B. and Williams, P.F. (1977): The Sesia-Lanzo Zone, a slice of continental crust with Alpine high pressure-low temperature assemblages in the western Italian Alps. Rend. Soc. It. Min. Petrol., 33(2): 281-334.

Cortiana, G., Dal Piaz, G.V., Del Moro, A., Hunziker, J.C., and Martin, S. (1998): $^{40}Ar/^{39}Ar$ and Rb/Sr dating of the Pillonet klippe and Sesia-Lanzo basal slice in the Ayas valley and evolution of the Austroalpine-Piedmont nappe stack. Mem. Sci. Geol., 50: 177-194.

Costa, S and Caby, R. (2001): Evolution of the Ligurian Tethys in the Western Alps; Sm/Nd and U/Pb geochronology and rare earth element geochemistry of the Montgenèvre Ophiolite (France). Chem. Geol., 175(3-4): 449-466.

Coward, M.P., Dietrich, M. and Park, R.G. (1989): Alpine tectonics. Geol. Soc. Spec. Publ., 45: 450 pp.

Dal Piaz, G.V., De Vecchi, G., and Hunziker, J.C. (1977): The Austroalpine layered gabbros of the Matterhorn and Mt. Collon-Dents de Bertol. Schweiz. Mineral. Petrogr. Mitt., 57: 59-88.

Dal Piaz, G.V., Hunziker, J.C. and Martinotti, G. (1972): La zona Sesia-Lanzo e l'evolutione tettonico-metamorfica delle Alpi nordoccidentali interne. Mem. Soc. Geol. It., 11: 433-466.

Dal Piaz, G.V. (1993): Evolution of Austro-Alpine and Upper Penninic basement in the Northwestern Alps from variscan convergence to post-variscan extension. In: von Raumer, J.F., and Neubauer, F. (eds.): Pre-Mesozoic Geology in the Alps, Springer-Verlag: 327-344.

Dal Piaz, G.V. (1999): The Austroalpine-Piedmont nappe stack and the puzzle of Alpine Tethys. Mem. Sci. Geol., 51: 155-176.

Dal Piaz, G.V. (2001): Geology of the Monte Rosa massif: historical review and personal comments. Schweiz. Mineral. Petrogr. Mitt., 81: 275-303.

Dalrymple, G.B, Alexander, E.C, Lanphere, M.A and Kraker, G.P. (1981): Irradiation of samples for $^{40}Ar/^{39}Ar$ dating using the Geological Survey TRIGA reactor. U. S. Geol. Survey Prof. Paper: 55.

Davidson, J.P. (1987): Crustal contamination versus subduction zone enrichment: examples from the Lesser Antilles and implications for mantle source compositions of island arc volcanics. Geochim. Cosmochim. Acta, 51 2185-2198.

Debon, F., and Zimmermann, J.L. (1993): Mafic dykes from some plutons of the western Pyrenean Axial Zone (France, Spain): markers of the transition from late-Hercynian to early-Alpine events. Schweiz. Mineral. Petrogr. Mitt., 73, 421-433.

Debon, F., Cocherie, A., Ménot, R.-P., Vivier, G. and Barfety, J.-C. (1994): Datation du plutonisme magnésien varisque des massifs cristallins externes des Alpes : l'exemple du Granite des Sept Laux (Massif de Belledonne, France). C. R. Acad. Sci. t. 318, Série II, 1497-1504.

Deer, W.A., Howie, R.A. and Zussmann, J. (1992): An introduction to the rock-forming minerals, 1. Ed.: Longman, 696 pp.

de Gracianski, P.C.(1993): Basement-cover relationship in the Western Alps. Constraints for the pre-Triassic reconstructions. In: von Raumer, J.F. and Neubauer, F. (eds.): Pre-Mesozoic Geology in the Alps, Springer-Verlag: 7-28.

Diehl, E.A., Masson, R. and Stutz, A.H. (1952): Contributi alla conoscenza del ricoprimento Dent Blanche. Mem. Ist. Geol. Min. Univ. Padova, 17: 53.

de Paolo, D.J: (1981): Trace-element and isotopic effect of combined wallrock assimilation and fractional crystallization. Earth Planet. Sci. Lett., 53: 189-202.

del Moro, A. and Notarpietro, A. (1987): Rb/Sr geochemistry of some Hercynian granitoids overprinted by eo-Alpine metamorphism in the Upper Valtellina, Central Alps. Schweiz. Mineral. Petrogr. Mitt., 67: 295-306.

Downes, H. (2001): Formation and modification of the shallow subcontinental lithospheric mantle: a review of geochemical evidence from ultramafic xenolith suites and tectonically emplaced ultramafic massifs of Western and Central Europe. J. Petrol, 42(1): 233-250.

Elter, G. (1960): La zona pennidica dell'alta e media valle d'Aosta e le unita limitrofe. Mem. Ist. Geol. Min. Univ. Padova, 22: 113.

Engi, M., Scherrer, N.C., and Burri, T. (2001): Metamorphic evolution of pelitic rocks of the Monte Rosa nappe: Constraints from petrology and single grain monazite age data. Schweiz. Mineral. Petrogr. Mitt., 81, 305-328.

Frey, F.A. (1969): Rare earth abundances in a high-temperature peridotite intrusion. Geochim. Cosmochim. Acta, 33(11): 1429-1447.

Frey, F.A. and Green, D.H. (1975): The mineralogy, geochemistry and origin of lherzolite inclusions in Victorian basanites. Geochim. Cosmoch. Acta, 38: 1023-1059.

Frey, F.A., Suen, J. and Stockman, H.W. (1985): The Ronda high temperature peridotite: geochemistry and petrogenesis. Geochim. Cosmoch. Acta, 49: 2469-2491.

Garuti, G., Bea, F., Zaccarini, F. and Montero, P. (2001) : Age, geochemistry and petrogenesis of ultramafic pipes in the Ivrea Zone, NW Italy. J. Petrol., 42(2): 433-457.

Grantham, G.H., Thomas, R.J., Eglington, B.M., de Bruin, D., Atanasov, A. and Evans, M.J. (1993): Corona textures in Proterozoic olivine melanorites of the Equeefa Suite, Natal Metamorphic Province, South Africa. Mineral. Petrol., 49: 91-102.

Green, D.H. and Ringwood, A.E. (1967): The genesis of basaltic magmas. Contrib. Mineral. Petrol., 15(2): 103-190.

Grieve, R.A.F. and Gittins, J. (1975): Composition and formation of coronas in the Hadlington Gabbro, Ontario, Canada. Canad. J. Earth Sci., 12(2): 289-299.

Griffin, W.L., O'Reilly, S.Y., Abe, N., Aulbach, S., Davies, R.M., Pearson, N.J., Doyle, B.J. and Kivi, K. (2003): The origin and evolution of Archean lithospheric mantle. Prec. Research, 127: 19-41.

Hack, P.J., Nielsen, R.L. and Dana Johnston, A. (1994): Experimentally determined rare earth elements and Y partitioning behavior between clinopyroxene and basaltic liquids at pressures up to 20 kbar. Chem. Geol., 117: 89-105.

Hammarstorm, J.M. and Zen, E. (1986): Aluminum in hornblende: an empirical igneous geobarometer. Amer. Mineral., 71: 1297-1313.

Hansmann, W., Hermann, J. and Müntener, O. (1996): U/Pb dating of zircons from the Fedoz gabbro, an intrusion located at the crust/ mantle boundary. Schweiz. Mineral. Petrogr. Mitt., 76(1): 116-117.

Hansmann, W., Müntener, O. and Hermann, J. (2001). U-Pb zircon geochronology of a tholeiitic intrusion and associated migmatites at a continental crust-mantle transition, Val Malenco, Italy. Schweiz. Mineral. Petrogr. Mitt., 81(2): 239-255.

Hauri, E.K., Wagner, T.P. and Grove, T.L. (1994): Experimental and natural partitioning of Th, U, Pb and other trace elements between garnet, clinopyroxene and basaltic melt. Chem. Geol., 117: 149-166.

Hegner, E., Kölbl-Ebert, M. and Loeschke, J (1998): Post-collisional Variscan lamprophyres (Black Forrest): $^{40}Ar/^{39}Ar$ phlogopite dating, Nd, Pb, Sr isotopes, and trace-element characteristics. Lithos, 45: 395-412.

Hermann, J., Müntener, O., Trommsdorff, V. and Hansmann, W. (1997): Fossil crust-to-mantle transition, Val Malenco, (Italian Alps). J. Geophys. Res., 102(B9): 20123-20132.

Hermann, J., Müntener, O. and Günther, D. (2001): Differentiation of mafic magma in a continental crust-to-mantle transition zone. J. Petrol., 42(1): 189-206.

Holland, T.J.B. and Blundy, J.D. (1994): Non-ideal interactions in calcic amphiboles and their bearing on amphibole-plagioclase thermometry. Contrib. Mineral. Petrol., 116: 433-447.

Hunziker, J.C. (1974): Rb-Sr and K-Ar age determinations and the Alpine tectonic history of the Western Alps. Mem. Ist. Geol. Min. Univ. Padova, 31: 55 pp.

Hunziker, J.C., Desmons, J. and Martinotti, G. (1989): Alpine thermal evolution in the Central and Western Alps. In: Coward, M.P., Dietrich, M. and Park, R.G. (eds): Alpine tectonics. Geol. Soc. Spec. Publ., 45: 353-367.

Hunziker, J.C., Desmons, J. and Hurford, A.J. (1992): Thirty-two years of geochronological work in the Central and Western Alps; a review of seven maps. Memoires de Geologie Lausanne, 13: 59 pp.

Holloway, J.R. and Burnham, C.W. (1972): Melting relations of basalt with equilibrium water pressure less than total pressure. J. Petrol., 13: 1-29.

Innocent, C., Briqueu, L., and Cabanis, B. (1994): Sr-Nd isotope and trace-element geochemistry of late Variscan volcanism in the Pyrenees: magmatism in post-orogenic extension ? Tectonophysics, 238: 161-181.

Irvine, T.N. and Baragar, W.R.A. (1971): A guide to the chemical classification of the common volcanic rocks. Canad. J. Earth Sci., 8(5): 523-548.

Irving, A.J. and Frey, F.A. (1984): Trace-element abundances in megacrysts and their host basalts; constraints on partition coefficients and megacryst genesis. Geochim. Cosmochim. Acta, 48(6): 1201-1221.

Jaffrey, A.J., Flynn, F.K., Glendenin, L.E., Bentley, W.C., and Essling, A.M. (1971): Precision measurements of half-lives and specific activities of ^{235}U and ^{238}U: Physical Review, C4, 1889-1906.

Johnson, M.C. and Rutherford, M.J. (1989): Experimental calibration of the aluminum-in-hornblende geobarometer with application to Long Valley Caldera (California) volcanic rocks. Geology, 17(9): 837-841.

Kalt, A;, Hegner, E. and Satir, M. (1997): Nd, Sr and Pb isotopic evidence for diverse lithospheric mantle sources of East African Rift carbonatites. Tectonophysics, 278: 31-45.

Krogh, T.E. (1973): Improved accuracy of U/Pb zircon ages by the creation of more concordant system using an air abrasion technique. Geochim. Cosmochim. Acta, 46: 637-649.

Krogh, T.E. (1982): A low-contamination method for hydrothermal decomposition of zircon and extraction of U and Pb for isotopic age determinations: Geochim. Cosmochim. Acta, 37: 485-494.

Lapierre, H., Basile, C. and Dupuis, V. (1999): Basaltes et trachytes permiens de l'Estérel (SE France): une série tholéiitique transitionnelle épanchée pendant l'amincissement lithosphérique. Bull. Soc. géol. France, 170(2): 253-265.

Langmuir, C.H. (1989): Geochemical consequences of in situ crystallization. Nature, 340(6230): 199-205.

Langmuir, C.H., Vocke, R.D., Hanson, G.N. and Hart, S.R. (1978): A general mixing equation with applications to iceland basalts. Earth Planet. Sci. Lett., 37: 380-392.

Leake, B.E, Woolley, A.R., Arps, C.E.S., Birch, W.D., Gilbert, M.C., Grice, J.D., Hawthorne, F.C., Kato, A., Kisch, H.J., Krivovichev, V.G., Linthout, K., Laird, J., Mandarino, J.A., Maresch, W.V., Nickel, E.H., Rock, N.M.S., Schumacher, J.C., Smith, D.C., Stephenson, N.C.N., Ungaretti, L., Whittaker, E.J.W. and Guo, Y. (1997): Nomenclature of amphiboles; report of the subcommittee on amphiboles of the International Mineralogical Association, Commission on New Minerals and Mineral Names. Canad. Mineral., 35(1): 219-246.

Lenoir, X., Dautria, J.M. and Bodinier, J.L. (1997): Les enclaves mantelliques protogranulaires du Forez: témoins de l'érosion lithosphérique en bordure de panache du Massif Central. C. R. Acad. Sci., 325: 235-241.

Leterrier, J. (1972): Etude pétrographique et géochimique du massif granitique de Quérigut (Ariège). Thèse de Doctorat d'Etat, Université de Nancy, 320 pp.

Lindsey, D.H. (1983): Pyroxene thermometry. Am. Mineral., 68: 477-493.

Lorenz, V. and Nicholls, I.A. (1984): Plate and intraplate processes of Hercynian Europe during the late Paleozoic. Tectonophysics, 107: 25-56.

Loucks, R.R. (1996): A precise olivine-augite Mg-Fe exchange geothermometer. Contrib. Mineral. Petrol., 125: 140-150.

Lu, M., Hofmann, A.W., Mazzucchelli, M. and Rivalenti, G. (1997): The mafic-ultramafic complex near Finero (Ivrea-Verbano Zone), ii. Geochronology and isotope geochemistry. Chem. Geol., 140: 223-235.

Ludwig, K.R. (1998): Isoplot: a plotting and regression program for radiogenic-isotope data. U.S. Geol. Survey, Open File Re, 91-445, 43 pp.

Malavieille, J. (1993): Late orogenic extension in mountain belts: insight from the Basin and Range and the late Paleozoic Variscan belt. Tectonics, 12: 1115-1130.

Marroni, M., Molli, G., Montanini, A. and Tribuzio, R. (1998): The association of continental crust rocks with ophiolites in the Northern Apennines (Italy); implications for the continent-ocean transition in the western Tethys. Tectonophysics, 292(1-2): 43-66.

Matte, P. (1986): La chaîne varisque parmi les chaînes paléozoïques péri-Atlantique, modèle d'évolution et position des grand blocs continentaux au Permo-Carbonifère. Bull. Soc. Géol. France, 8: 9-24.

Matte, P. (2001): The Variscan collage and orogeny (480-290 Ma) and the tectonic definition of the Armorica microplate: a review. Terra Nova, 13: 122-128.

Martinotti, G., and Hunziker, J.C. (1984): The Austroalpine system in the Western Alps: a review. Mem. Soc. Geol. It., 29: 233-250.

McDougall, I. And Harrison, T.M. (1988): Geochronology and thermochronology by the $^{40}Ar/^{39}Ar$ method. Oxford Monograph on Geology and Geophysics n°9, 212 pp.

McDonough, W.F. (1990): Constraints on the composition of the continental lithospheric mantle. Earth Planet. Sci. Lett. 101: 1-18.

McKenzie, D. and O'Nions, R.K. (1991): Partial melt distributions from inversion of rare earth element concentrations. J. Petrol., 32(5): 1021-1091

Miller, C. and Thöni, M. (1995): Origin of eclogites from the Austroalpine Ötztal basement (Tirol, Austria): geochemistry and Sm-Nd vs. Rb--Sr isotope systematics. Chem. Geol., 122: 199-225.

Ménard, G. and Molnar, P. (1988): Budget of crustal shortening and subduction of continental crust in the Alps. Nature, 334: 235-237.

Ménot, R.-P., von Raumer, J.F., Bogdanoff, S., and Vivier, G. (1994): Variscan basement of the Western Alps : the external Crystalline Massifs. In: von Raumer, J.F., and Neubauer, F. (eds.): Pre-Mesozoic Geology in the Alps, Springer-Verlag: 458-466.

Monjoie, P., Bussy, F., Lapierre, H., Schaltegger, U., Pfeifer, H.-R. and Mulch, A. Precise U/Pb and $^{40}Ar/^{39}Ar$ dating of the layered Permian Mafic Complex of the Mont Collon (Western Alps, Wallis, Switzerland). Submitted to Schweiz. Mineral. Petrogr. Mitt.

Monjoie, P., Bussy, F., Lapierre, H., and Pfeifer, H.-R. (2003): Modeling of *in-situ* crystallization processes in the Permian layered intrusion of the Mont Collon (Dent Blanche nappe, western Alps). Submitted to Lithos.

Morimoto, N., Fabries, J., Ferguson, A.K., Ginzburg, I.V., Ross, M., Seifert, F.A., Zussman, J., Aoki, K. and Gottardi, G (1988): Nomenclature of pyroxenes. Mineral. Petrol., 39(1): 55-76.

Mulch, A., Rosenau, M., Doerr, W. and Handy, M.R. (2002): The age and structure of dikes along the tectonic contact of the Ivrea-Verbano and Strona-Ceneri zones (Southern Alps, northern Italy, Switzerland). Schweiz. Mineral. Petrogr. Mitt., 82(1): 55-76.

Müntener, O., Hermann, J. and Trommsdorff, V. (2000): Cooling history and exhumation of lower crustal granulite and upper mantle (Malenco, Eastern Central Alps). J. Petrol., 41(2): 175-200.

Nesbit, H.W. and Young, G.M. (1989): Formation and diagenesis of weathering profiles. J. Geol., 97: 129-147.

Nimis, P., and Ulmer, P. (1998): Clinopyroxene geobarometry for magmatic rocks Part 1: An extend structural geobarometer for anhydrous and hydrous, basic and diorite systems. Contrib. Mineral. Petrol., 133: 122-135.

Nimis, P. (1995): A clinopyroxene geobarometer for basaltic systems based on crystal-structure modeling. Contrib. Mineral. Petrol., 121: 115-125.

Olsen, S.N., Johnson, C.M., Beard, B. and Baumgartner, L.P. (200): New U/Pb zircon data and constraints on the age and mode of migmatization in the Aar Massif, Central Alps. European J. Mineral., 12(6): 1245-1260.

Ottonello, G. Ernst, W.G. and Joron, J.L. (1984): Rare earth and 3d transition element geochemistry of peridotitic rocks: I. Peridotites from the Western Alps. J. Petrol., 25: 343-372.

Paquette, J.-L., Ménot, R.-P. and Peucat, J.J. (1989): REE, Sm-Nd and U/Pb zircon study of eclogites from the Alpine External Massifs (Western Alps): evidence for crustal contamination. Earth Planet. Sci. Lett., 96: 181-198.

Pearce, J.A. (1983): Role of the sub-continental lithosphere in magma genesis at active continental margins. In Hawkesworth, C.J. and Norry, M.J.: Continental basalts and mantle xenoliths. Shiva Publ., Nantwich (United Kingdom): 230-249.

Pin, C (1986): Datation U/Pb sur zircons a 285 Ma du complexe gabbro-dioritique du Val Sesia-Val Mastallone et âge tardi-hercynien du metamorphisme granulitique de la zone Ivrea-Verbano (Italie), C. R. Acad. Sci. Série II, 303(9): 827-830.

Pin, C Marini, F. (1993): Early Ordovician continental break-up in Variscan Europe; Nd-Sr isotope and trace-element evidence from bimodal igneous associations of the southern Massif Central, France. Lithos, 29(3-4): 177-196.

Pfiffner, O.A. (1993): The structure of the Alps: an introduction. In: von Raumer, J.F. and Neubauer, F. (eds.): Pre-Mesozoic Geology in the Alps, Springer-Verlag: 3-6.

Poitrasson, F. and Pin, C (1993): Extreme Nd isotope homogeneity in a large rhyolitic province: the Esterel massif, southeast France. Bull. Volcano., 60: 213-223.

Quick, J.E.,Sinigoi, S. and Mayer, A. (1994): Emplacement dynamics of a large intrusion in the lower crust, Ivrea-Verbano, northern Italy. J. Geophys. Res., 99(B11): 21559-21573.

Rampone, E., Hofmann, A.W., Piccardo, G.B.; Vannucci, R., Bottazzi, P. and Ottolini, L. (1996): Trace-element and isotope geochemistry of depleted peridotites from an N-MORB type ophiolite (Internal Liguride, N. Italy). Contrib. Mineral. Petrol., 123: 61-76.

Rampone, E., Hofmann, A.W., and Raczek, I. (1998): Isotopic contrasts within the Internal Liguride ophiolite (N. Italy): the lack of a genetic mantle-crust link. Earth Planet. Sci. Lett., 163: 175-189.

Ramsay, J.G., (1967): Folding and fracturing of rocks. Ed.: McGraw-Hill, New York, 568 pp.

Renne, P.R. Swisher, C.C., Deino, -A.L. Karner, D., Owens, T. and DePaolo, D. (1998): Intercalibration of standards, absolute ages and uncertainties in $^{40}Ar/^{39}Ar$ dating. Chem. Geol., 145(1-2): 117-152.

Rey, P., Burg, J.P. and Caron, J.M. (1992): Middle to late Carboniferous extension in the Variscan belt: structural and petrological evidences from the Vosges massif (eastern France). Geodinam. Acta, 5: 17-36.

Rey, P., Burg, J.P. and Casey, M. (1997): The Scandinavian Caledonides and their relationship to the Variscan belt. In: Burg, J.P. and Ford, M. (eds): Orogeny through time. Spec. Publ. Geol. Soc. London, 121: 179-200.

Riley, T.R., Leat, P., Storey, B.C., Parkinson, I.J. and Millar, I.L. (2003): Ultramafic lamprophyres of the Ferrar large igneous province: evidence for a HIMU mantle component. Lithos, 66: 63-76.

Rivalenti, G., Garuti, G., Rossi, A., Siena, F., and Sinigoi, S. (1980): Existence of different peridotite types and of a layered igneous complex in the Ivrea Zone of the Western Alps. J. Petrol., 22: 127-153.

Rosenbaum, J.M., Wislon, M. and Downes, H. (1997): Enrichment of the Pannonian-Carpathian mantle: Pb-Sr-Nd isotopes and trace-element constraints. J. Geophys. Res., 102: 275-288.

Rottura, A., Bargossi, G.M., Caggianelli, A., Del Moro, A., Visòna, D. and Tranne, C.A. (1998): Origin and significance of the Permian high-K calc-alkaline magmatism in the central-eastern Alps, Italy. Lithos, 45: 329-348.

Rubatto, D. and Gebauer, D. (1997): The Bonze Unit (Sesia-Lanzo Zone, Western Alps): a gabbroic early Carboniferous intrusion that recorded Hercynian and Alpine metamorphism. Abstract 3rd workshop on Alpine geol. Studies, Quad. Geodin. Alps E. Quatern. 4: 106-107.

Rubatto, D., Schaltegger, U., Lombardo, B., Colombo, F. and Compagnoni, R. (2001): Complex Paleozoic magmatic and metamorphic evolution in the Argentera Massif (Western Alps) resolved with U/Pb dating.. Schweiz. Mineral. Petrogr. Mitt., 81(2): 213-228.

Rudnick, R.L., and Fountain, D.M. (1995): Nature and composition of the continental crust: a lower crustal perspective. Rev. Geophys., 33: 267-309.

Ruttner, A.W. (1993): Southern borderland of Triassic Laurasia in NE Iran. Geol. Rundsch., 82: 110-120.

Schaltegger, U. (1994): Unravelling the pre-Mesozoic history of the Aar-Gotthard massifs (Central Alps) by isotopic dating: a review. Schweiz. Mineral. Petrogr. Mitt., 74: 41-51.

Schaltegger, U. (1997): Magma pulses in the Central Variscan belt: episodic melt generation and emplacement during lithospheric thinning. Terra Nova, 9: 242-245.

Schaltegger, U. and Corfu, F. (1992): The age and source of the late Hercynian magmatism in the Central Alps: evidence from precise U/Pb ages and Hf initial isotopes. Contrib. Mineral. Petrol., 111: 329-344.

Schaltegger, U. and Corfu, F. (1995): Late Variscan «Basin and Range» magmatism and tectonics in the Central Alps: evidence from U/Pb geochronology. Geodinam. Acta, 8(2): 82-98.

Schaltegger, U., Schneider, J.-L., Maurin, J.-C. and Corfu, F. (1996): Precise U/Pb chronometry of 345-340 Ma old magmatism related to syn-convergence extension in the southern Vosges (central Variscan Belt). Earth Planet. Sci. Lett., 144(3-4): 403-419

Schaltegger, U., Fanning, C.M., Gunther, D., Maurin, J.-C., Schulmann, K. and Gebauer, D. (1999): Growth, annealing and recrystallization of zircon and preservation of monazite in high-grade metamorphism; conventional and in-situ U/Pb isotope, cathodoluminescence and microchemical evidence. Contrib. Mineral. Petrol., 134(2-3): 186-201.

Schmidt, M.W. (1992): Amphibole composition in tonalite as a function of pressure: an experimental calibration of the Al-in-hornblende barometer. Contrib. Mineral. Petrol., 110: 304-310.

Schott, B. and Schmeling, H. (1998): Delamination and detachment of a lithospheric root. Tectonophysics, 296: 225–247.

Sergeev, S.A. and Steiger, R.H. (1993): High-precision U/Pb single zircon dating of Variscan and Caledonian magmatic cycles in the Gotthard massif, Central Alps. Terra Abstr., 5: 394-395.

Schweigl, J. (1995): Neue geochronologische und isotopengeologische Daten zur voralpidischen Entwicklungsgeschichte im Ötztal kristallin (Ostalpen). Jahrb. Geol. Bund., 138: 131–149.

Shand, S.J. (1951): Eruptive rocks their genesis, composition, classification, and their relation to ore deposits. New York, Hafner Publishing Company, 488 pp.

Sinigoi, S., Quick, J.E., Clemens-Knott, D., Mayer, A., Demarchi, G., Mazzucchelli, M., Negrini, L., Rivalenti, G. (1994): Chemical evolution of a large mafic intrusion in the lower crust, Ivrea-Verbano Zone, northern Italy. J. Geophys. Research, 99(B11): 21 575-21 590.

Skulski, T., Minarik, W.G. and Watson, E.B. (1994): High-pressure experimental trace-element partitioning between clinopyroxene and basaltic melts. Chemical Geology, 117(1-4): 127-147.

Smith, J.V. and Brown, W.L. (1988): Feldspar minerals. Vol. 1: Crystal structures, physical, chemical, and microtextural properties. 2nd ed. Springer-Verlag, Berlin, 828 pp.

Spiess, R., Bertolo, B. Borghi, A. and Tinor Centi, M. (2001): Crustal–mantle lithosphere decoupling as a control on Variscan metamorphism in the Eastern Alps. Austral. J. of Earth Sci., 48: 479–486.

Spillman, P. and Büchi, H. (1993): The pre-Alpine basement of the lower Austroalpine nappes in the Bernina Massif (Grisons, Switzerland; Valtellina, Italy). In: von Raumer, J.F., and Neubauer, F. (eds.): Pre-Mesozoic Geology in the Alps, Springer-Verlag: 457-468.

Springer, W. and Seck, H.A. (1997): Partial fusion of basic granulites at 5 to 15 kbar: implications for the origin of TTG magmas. Contrib. Mineral. Petrol., 127: 30-45.

Stampfli, G.M. (1996): The Intra-Alpine terrain. A Paleotethyan remnant in the Alpine Variscides. Eclogae geol. Helv., 89: 13-42.

Stampfli, G.M., and Borel, G.D. (2002): A plate tectonic model for the Paleozoic and Mesozoic constrained by dynamic plate boundaries and restored synthetic oceanic isochrons. Earth Planet. Sci. Lett., 196: 17-33.

Steck, A. (1980): Deux directions principales de flux synmetamorphiques dans les Alpes centrales. Bull. Soc. Vaudoise Sci. Nat., 75(2-358): 141-149.

Steck, A. and Hunziker, J.C. (1994): The Tertiary structural and thermal evolution of the Central Alps; compressional and extensional structures in an orogenic belt. Tectonophysics. 238(1-4): 229-254.

Steiger, R.H. and Jaeger, E (1977): Subcommission on geochronology; convention on the use of decay constants in geo- and cosmochronology. Earth Planet. Sci. Lett., 36(3): 359-362.

Stille, P. and Schaltegger, U. (1996): The lithospheric mantle beneath Centra Europe: Nd isotopic constraints for its late Proterozoic enrichment and implications for early crustal evolution. Geophysical Monography: Earth process: reading the isotopic code. Ed: American Geophysical Union, 95: 269-276.

Stille, P., Unruh, D.M. and Mitsunobu, T. (1986): Sr, Nd, and Hf isotopic constraints on the origin of Hawaiian basalts and evidence for a unique mantle source. Geochim. Cosmochim. Acta, 50(10): 2303-2319.

Sun, S.S., Nesbitt, R.W. and Sharaskin, A.Y. (1979): Geochemical characteristics of Mid-Ocean Ridge Basalts. Earth Planet. Sci. Lett., 44: 119-138.

Sun, S.S. and McDonough, W.F. (1989): Chemical and isotopic systematics of oceanic basalts: implications for mantle composition and processes. Spec. Publ. Geol. Soc., 42: 313-345.

Thompson, R.N. (1984): Dispatches from the basalt front. 1. Experiments. Proc. Geol. Ass., 95: 249-262.

Tribuzio, R., Thirlwall, M.F., and Messiga, B. (1999): Petrology, mineral and isotope geochemistry of the Sondalo gabbroic complex (Central Alps, Northern Italy): implications for the origin of post-Variscan magmatism. Contrib. Mineral. Petrol., 136: 48-62.

Venturini, G., Hunziker, J.C., and Pfeifer, H.-R. (1996): Geochemistry of mafic rocks in the Sesia zone (Western Alps): New data and interpretations. Eclogae geol. Helv., 89: 369-388.

Vissers, R.L.M. (1992): Variscan extension in the Pyrenees. Tectonics, 11: 1369-138.

Vissers, R.L.M., De Jong, A.C. and Wortel, M.J.R. (1993): Late Variscan extension in the Pyrenees: geological constraints and a thermal model study. In: Seranne, M. and Malavieille, J. (eds): Late orogenic extension in mountain belts; international meeting. Doc. BRGM, 219: 207.

von Raumer, J.F. (1998): The Palaeozoic evolution in the Alps - from Gondwana to Pangea. Geol. Rundschau, 87: 407-435

von Raumer, J.F., and Ménot, R.-P. (1989): Evolution paléozoïque du socle ouest-alpin et place des Massifs Cristallins Externes dans l'orogène Varisque. C. R. Acad. Sci. Serie 309: 397-402.

von Raumer, J.F., Ménot, R.-P., Abrecht, J., and Biino, G. (1993): The Pre-alpine evolution of the External massifs. In: von Raumer, J.F. and Neubauer, F. (eds.): Pre-Mesozoic Geology in the Alps, Springer-Verlag: 221-240.

von Raumer, J.F. and Neubauer, F. (1993): Late Precambrian and Palaeozoic evolution of the Alpine basement - An overview. In: von Raumer, J.F. and Neubauer, F. (eds.): Pre-Mesozoic Geology in the Alps, Springer-Verlag: 625-640.

von Raumer, J.F., Stampfli G.M. and Bussy, F. (2003): Gondwana-derived microcontinents - the constituents of the Variscan and Alpine collisional orogens. Tectonophysics, 6832: 1-16.

Voshage, H., Hofmann, A.W., Mazzucchelli, M., Rivalenti, G., Sinigoi, S., Raczek, I., Demarchi, G., (1990): Isotopic evidence from the Ivrea Zone for a hybrid lower crust formed by magmatic underplating. Nature, 347: 731-736.

Wedepohl, K.H. (1995): The composition of the continental crust. Geochim. Cosmochim. Acta, 59: 1217-1239.

Weidmann, M. and Zaninetti, L. (1974): New data on the Mont Dolin Series (Dent Blanche Nappe, Valais); description of Triassic foraminifera. Eclogae geol. Helv., 67(3): 597-603.

White,W.M. and Dupré, B. (1986): Sediment subduction and magma genesis in the Lesser Antilles: isotopic and trace-elements constrains. J. Geophys. Res., 91: 5927-5941.

White,W.M., Hofmann, A.W. and Pulchet, H. (1987): Isotope geochemistry of Pacific Mid-Ocean Ridges basalt. J. Geophys. Res., 92(B6): 4881-4894.

Wood, B.J. and Blundy, J.D. (1997): A predictive model for rare earth element partitioning between clinopyroxene and anhydrous silicate melt. Contrib. Mineral. Petrol., 129: 166-181.

Zheng, J.S., Mermet, J.F., Toutin-Morin, N, Hanes, J., Gondolo, Morin, R. and Fédaud, G. (1991): Datation $^{40}Ar/^{39}Ar$ du magmatisme et des filons minéralisés permiens en Provence orientale (France). Geodinam. Acta, 5: 203-215.

Zindler, A. and Hart, S.(1986): Chemical geodynamics. Ann. Rev. Earth Planet. Sci., 14: 493-571.

Ziegler, P.A. and Stampfli, G.M. (2001): Late Paleozoic and early Mesozoic plate boundary reorganisation: collapse of the Variscan orogen and opening of the Neotethys. In: Cassinis (eds): The continental Permian o the Southern Alps and Sardinia (Italy). Regional reports and general correlations. Ann. Mus. Civ. Sci. Nat., Brescia, 17-34.

Figure captions

Appendices

Appendix 1: Figure captions

Table captions

Appendix 2: Table captions.

Table 1: Representative major-element compositions of clinopyroxenes from wehrlites, plg-wehrlites, troctolite, ol- and cpx-gabbros and anorthosite used to the geobarometric calculations.

Subtitle: Structural formula based on 4 cations, (n.d.): not determined. p26

Table 2: Representative major-element compositions of olivines from plg-wehrlites, troctolite, ol-gabbros.

Subtitle: Structural formulae based on 3 cations. Olivines from wehrlites are all serpentinized and not included in this table. p27

Table 3: Representative major-element compositions of plagioclases from plg-wehrlites, troctolite, ol- and cpx-gabbros and anorthosite.

Subtitle:Structural formula based on 5 cations. p28

Table 4: Representative major-element compositions of amphiboles from wehrlites, plg-wehrlites, troctolite, ol- and cpx-gabbros and anorthosite. Amphibole names after Leake et al. (1997).

Subtitle: Structural formula based on 23 oxygens. p29

Table 5: Representative major-element compositions of k-feldspars from leucocratic dikes exposed in the Mont Collon mafic complex.

Subtitle: Structural formula based on 5 cations. p36

Table 6: Representative major-element compositions of kaersutites from Fe-Ti melanocratic dikes exposed in the Mont Collon mafic complex. Amphibole names after Leake et al. (1997).

Subtitle: Structural formula based on 23 oxygens. p37

Table 7: Representative major-element compositions of clinopyroxenes from Fe-Ti melanocratic dikes exposed in the Mont Collon mafic complex.

Subtitle: Structural formula based on 4 cations. p38

Table 8a-c: Representative major-element compositions of whole-rocks (wehrlites, plg-wehrlites, troctolite, ol- and cpx-gabbros pegmatitic gabbros and anorthosite). p56-57-58

Table 9a-c: Representative trace-element analyses of whole-rocks (wehrlites, plagioclase-wehrlites, troctolite, olivine-gabbros, clinopyroxene-gabbros and anorthosite). (*) XRF trace-element analysis using classical «short time» procedure. (**) XRF analysis using «Rhodes» long time procedure. (-): under detection limits. (n.d.): not determined. Other trace elements have been analyzed by ICPMS. p66-67-68

Table 10: Trace-element contents of the minerals used to constraint the in-situ crystallization model (in ppm).

Subtitle: (-): under detection limits. (n.d.): not determined. p72

Table 11: Calculated with the method of Wood and Blundy, 1997 (a) and published (b) partition coefficients between clinopyroxene and melt (lower and upper values are given when available). p82

Table 12: Major- (in wt% oxides) and trace-element (in ppm) compositions of dated rocks. p95

Table 13: Major- and trace-element analyses of the $^{40}Ar/^{39}Ar$ dated kaersutites (wt%). The structural formulae are calculated on the basis on 23 oxygens. p96

Table 14: Analytical isotopic results U/Pb: *: radiogenic Pb, a) frg = fragment, ndl = needle, pr = prism, b) in mol-% relative to total radiogenic Pb, c) corrected for spike Pb and for fractionation, d) corrected for fractionation, spike, U and Pb blanks and initial common lead, error estimates (95% confidence level) refer to the last significant digits of the isotopic ratios and reflect the reproducibility of standards, measurement errors and uncertainties in the common lead correction. [-] refers in the text to the label of analyzed zircon grain or fractions. p98

Table 15a: Nd and Sr isotopic compositions of the Mont Collon cumulate groups I and II (plg-wehrlites, ol- and cpx-gabbros, troctolite and anorthosite) and the pegmatitic gabbro MP4. p105

Table 15b: Lead isotopic compositions of the Mont Collon cumulate groups I and II (plg-wehrlites, ol- and cpx-gabbros, troctolite and anorthosite) and the pegmatitic gabbro MP4. p106

Table 16: Whole-rock major-element compositions of the Arolla orthogneisses and the dikes exposed in the Mont Collon mafic complex (in wt%). p111

Table 17: Whole-rock trace-element compositions of the Arolla orthogneisses and the dikes exposed in the Mont Collon mafic complex. p114

Table 18a: Nd and Sr isotopic compositions of the Arolla orthogneisses and the dikes exposed in the Mont Collon mafic complex. p116

Table 18b: Pb isotopic compositions of the Arolla orthogneisses and the dikes exposed in the Mont Collon mafic complex. p117

Table 19: Hf isotopic compositions of zircons extracted from the pegmatitic gabbro MP4 and the quartz pegmatite MP2. MP4/x and MP2/x refer to the zircon fractions used for the U/Pb dating. p122

Table 20: Re-Os isotopic compositions of the Mont Collon cumulates, the leucocratic and Fe-Ti melanocratic dikes and the Arolla orthogneisses.

Subtitle: Blank C1: 0.003 ppb Re (error: 11.8% and 0.28 pg Os (error < 1%). Blank C2: 0.01 ppb Re (error: 4.5% and 0.15 pg Os (error < 1%). p122

Appendices

Appendix 3: Major- and trace-element analytical procedures.

Major and some trace elements were analyzed with a Philips PW 2400 XRF spectrometer at the Centre d'Analyse Minérale (University of Lausanne, Switzerland) using melted and pressed pellets, respectively. Accuracy on major elements is close to 1% and detection limit is 0.5 ppm for trace elements. Trace elements (labeled * and **, see Tables 9) were analyzed using a short-time (15') and long-time «Rhodes» (180') procedures, respectively. To access the reproducibility and accuracy of the major- and trace-element measurements, BHVO-1 standard was analyzed for basic rocks and a set of G-2 (granite), STM (syenite), AGV (andesite), VH1, GSP (granodiorite), QLO (Qz latite), MFTH-A standards for acidic samples.

Whole-rock incompatible trace elements have been determined by inductively coupled plasma spectrometry (ICP-MS VG-PQ2+) at the Laboratoire de Géodynamique des Chaînes Alpines of the University J. Fourier (Grenoble, France), after acid dissolution, using procedures of Barrat et al. (1996). The accuracy on trace-element concentrations is better than 3% for all the REE based on various standards and sample duplicates.

Appendix 4: Mineral *in-situ* analytical procedures.

Mineral analyses were made on a Cameca SX50 electron microprobe at the Institute of Mineralogy and Geochemistry of the University of Lausanne. For clinopyroxene, the accelerating voltage used for measurements was 15 kV and the beam current was 20 nA and a magnification factor of 200000. For olivine, the accelerating voltage was 15 kV and the beam current was 30 nA and a magnification factor of 200000. For amphibole, the accelerating voltage was 15 kV and the beam current was 15 nA and a magnification factor of 20000. And for plagioclase, the accelerating voltage was 15 kV and the beam current was 10 nA and a magnification factor of 40000. For all minerals, the analytical error was given for a 2 confidence level. The detection limit is around 0.1 wt% for all elements.

Trace-element measurements on minerals were made by laser-ablation ICP-MS mass spectrometry using a 193 nm an Ar-F 193 nm Lambda Physics© Excimer laser coupled with a Perkin-Elmer6100DRC ICPMS. NIST610 and 612 glasses were used as external standards, Ca and Si as internal standards after microprobe measurements on the pit sites. Ablation pit size varied from 40 to 60 μm. BCR2 basaltic glass was regularly used as a monitor to check for reproducibility and accuracy of the system. Results were always within ± 10% of the certified values.

Appendix 5: Sampling and analytical procedures for whole-rock isotopic determinations and decay constants used for whole-rock isotopic corrections.

Twenty-two basic cumulates (two plg-wehrlite, a troctolite and, some ol- and cpx gabbros), the three Fe-Ti melanocratic dikes and one to three samples of each intermediate to acidic dikes were analyzed to define their isotopic compositions. These rocks were selected on the basis of the petrographic and major- and trace-element studies. Two types of leaching were intended to suppress organic matter, carbonates and the altered components. For Nd and Sr isotope measurements, the first «classical» leaching for enriched samples is completed in 2.5 *N* HCL and 3 drops of 48% HF (24 *N*) in pre-cleaned Savillex© closed beaker for at 70°C for 10 minutes after 10 minutes in an ultrasonic tank. The floating residue was removed and the sample was rinsed with ultra-pure distilled water, placed in ultrasonic tank, and then heated 10 minutes at 70°C. This treatment was repeated a second time after evaporation. For rocks supposed to be Nd and Sr depleted, the first part of the leaching was conducted using 6 *N* HCL and 10 drops of 48% HF (24 *N*). The second one is identical with the classical leaching, but without using HF acid. After leaching procedures, the samples were evaporated to dryness and the residual solid was digested for 48 hours in a mixture of 9ml HNO_3 (13 *N*) and 10 drops of 48% HF (24 *N*). Some samples containing zircons were dissolved under pressure. After evaporation and centrifugation, Sr and Nd were separated using standard ion exchange techniques. The isotopic Sr ratios were measured on a fully automated V.G. Sector mass spectrometer at the ISTEEM (Montpellier, France) and the Nd compositions on a Finnigan 261 mass spectrometer at the University of Paul Sabatier-Toulouse 3 (France). For Pb isotope measurements, the leaching is completed in 2.5 *N* HCL in pre-cleaned Savillex© closed beaker during 10 minutes in a heated ultrasonic tank. The samples were centrifuged during 10 minutes and the floating residue was removed. The sample was rinsed with ultra-pure distilled water, placed in ultrasonic tank, and then centrifuged a second time. The floating H_2O was then removed and the sample dried before separation using standard ion exchange technique.

To establish the reproducibility and accuracy of the Sr measurements, NBS 987 standard was repeatedly run (12 times) with an average value being 0.710240 for a precision better than ± 0.000026 (2σ). $^{87}Sr/^{86}Sr$ ratio was corrected for mass discrimination by normalizing to the $^{87}Sr/^{86}Sr$ value of 0.1194. To assess the accuracy of the Nd composition measurements, the JMC 361 international standard was analyzed repeatedly (8 times), the average value being 0.5119597 with an error of ± 0.000003 (2σ). $^{144}Nd/^{143}Nd$ ratios were normalized to a $^{144}Nd/^{143}Nd$ value of 0.7219. The Pb measurements were conducted on the Plasma 54 mass spectrometer of the Ecole Normale Supérieure de Lyon (France). Lead data were calibrated against NBS 981 standard with a mass discrimination factor of 0.0192 ± 0.0016 a.m.u.

Appendix 6: summary of the textures, mineralogies and modal proportions of the Mont Collon cumulates and the pegmatitic gabbros (Table 22).

Rock types	Texture	Magmatic mineralogy	Modal %
werhlite	ad- to mesocumulate	ol + cpx + amph	55 - 60 : 30 - 35 : 0 - 5
troctolite	ortho- to mesocumulate	ol + plg ± cpx ± amph (± cor opx)	33 - 35 : 60 - 62 : ~ 3 ~ 1
plg werhlite	ortho- to mesocumulate	ol + cpx + plg ± amph (± cor opx)	30 - 35 : 40 - 50 : 15 - 20 : ~5
olivine gabbro	ortho- to mesocumulate	ol + cpx + plg ± amph (± cor opx)	15 - 20 : 28 - 35: 35 - 47 : 2 - 7
clinopyroxene gabbro	ortho- to mesocumulate	cpx + plg ± amph	52 - 55 : 38 - 44 : 3 - 8.5
pegmatitic gabbro	pegmatitic	plg + amph	40 - 45 : 5 5- 60
anorthosite	adcumulate	plg ± cpx ± amph	95 : 4 - 5 : ~ 1

Appendix 7: Analytical data of $^{40}Ar/^{39}Ar$ dating of the Fe-Ti melanocratic dike MP177 (Table 23).

Run ID	T°C	^{40}Ar(moles)	error	^{39}Ar(moles)	error	^{38}Ar(moles)	error	^{37}Ar(moles)	error
Sample MP177									
22UL-32BCTD	850	7.22296E-13	1.59192E-15	5.54999E-16	1.16944E-17	5.29121E-16	5.76265E-18	5.49639E-16	2.92321E-17
22UL-32CCTD	950	4.15585E-13	9.04168E-16	3.18172E-16	3.52084E-18	3.09431E-16	3.44612E-18	8.86342E-16	1.79148E-17
22UL-32DCTD	980	2.03901E-13	5.91343E-16	3.53536E-16	3.04995E-18	2.13404E-16	2.55680E-18	2.80043E-15	2.11656E-17
22UL-32ECTD	1000	1.67107E-13	5.92250E-16	5.24231E-16	3.39665E-18	2.68004E-16	3.17114E-18	6.45511E-15	3.23436E-17
22UL-32FCTD	1010	1.21793E-13	3.18269E-16	4.29095E-16	3.26015E-18	2.06487E-16	2.49196E-18	5.72037E-15	2.27035E-17
22UL-32GCTD	1020	9.63745E-14	2.41554E-16	4.78377E-16	3.09272E-18	1.81440E-16	2.21663E-18	4.89434E-15	1.92485E-17
22UL-32HCTD	1030	9.03688E-14	2.56676E-16	5.54892E-16	4.62154E-18	1.85330E-16	2.52704E-18	5.07214E-15	2.02804E-17
22UL-32ICTD	1040	1.01274E-13	2.12609E-16	8.35958E-16	3.71390E-18	2.28345E-16	2.59780E-18	6.74689E-15	2.40131E-17
22UL-32JCTD	1050	1.08330E-13	2.30839E-16	1.00648E-15	3.35565E-18	2.35949E-16	2.88105E-18	7.74296E-15	2.21212E-17
22UL-32KCTD	1061	1.36897E-13	2.61367E-16	1.50303E-15	3.34352E-18	2.63567E-16	2.88741E-18	9.70701E-15	2.16421E-17
22UL-32LCTD	1070	1.38470E-13	2.40505E-16	1.62952E-15	3.29019E-18	2.45843E-16	2.99993E-18	9.40346E-15	2.40501E-17
22UL-32MCTD	1080	1.65890E-13	2.97920E-16	2.19574E-15	4.73152E-18	2.75206E-16	3.78031E-18	1.17214E-14	2.48488E-17
22UL-32NCTD	1090	2.11886E-13	3.00635E-16	3.03386E-15	4.70868E-18	3.25447E-16	3.50593E-18	1.57817E-14	3.13498E-17
22UL-32OCTD	1100	2.54795E-13	5.05397E-16	3.95082E-15	4.88768E-18	3.78112E-16	5.34182E-18	1.99773E-14	4.35514E-17
22UL-32QCTD	1150	2.57791E-12	2.19949E-15	4.63901E-14	2.13770E-17	4.26999E-15	4.58051E-17	2.44881E-13	2.02065E-16
22UL-32RCTD	1175	5.29947E-13	4.74089E-16	7.85611E-15	7.80242E-18	7.47145E-16	7.55456E-18	4.10673E-14	4.80759E-17
22UL-32SCTD	1200	1.46028E-13	4.89798E-16	9.80890E-16	4.65991E-18	1.35330E-16	3.03103E-18	4.78894E-15	2.61930E-17
22UL-32TCTD	1250	1.75742E-13	7.05673E-16	6.95324E-16	3.53728E-18	1.37751E-16	2.83885E-18	2.91253E-15	2.75644E-17
22UL-32UCTD	1282	1.46441E-13	5.80160E-16	3.76679E-16	4.17404E-18	1.05058E-16	2.77286E-18	1.02225E-15	2.09279E-17
22UL-32VCTD	1400	7.65261E-13	9.17143E-16	7.87235E-15	1.04445E-17	8.66271E-16	9.34071E-18	4.33364E-14	1.04316E-16
22UL-32WCTD	1500	4.12648E-13	1.36915E-15	7.94685E-16	3.22462E-18	2.80240E-16	3.37733E-18	2.50890E-15	2.16292E-17
22UL-32XCTD	1601	3.34705E-13	1.68017E-15	1.48969E-16	4.78489E-18	2.11021E-16	4.20884E-18	0.00000E+00	0.00000E+00

Run ID	^{36}Ar(moles)	error	37/39	40*/39	%^{40}Ar*	App. Age	2s
Sample MP177							
22UL-32BCTD	2.44165E-15	2.79442E-18	9.90344E-01	1.42914E+00	1.00000E-01	7.7	435.2
22UL-32CCTD	1.40163E-15	2.28557E-18	2.78573E+00	4.60449E+00	3.00000E-01	24.8	243.2
22UL-32DCTD	6.63470E-16	1.76570E-18	7.92121E+00	2.33357E+01	3.90000E+00	122.5	84.7
22UL-32ECTD	4.93750E-16	1.92740E-18	1.23135E+01	4.30382E+01	1.30000E+01	219.8	36.7
22UL-32FCTD	3.40578E-16	1.44908E-18	1.33313E+01	5.25069E+01	1.77000E+01	264.7	33.8
22UL-32GCTD	2.54510E-16	1.49387E-18	1.02311E+01	4.64993E+01	2.23000E+01	236.3	22.0
22UL-32HCTD	2.18029E-16	1.39384E-18	9.14076E+00	4.88223E+01	2.91000E+01	247.4	20.0
22UL-32ICTD	2.09335E-16	1.47607E-18	8.07085E+00	4.89738E+01	3.94000E+01	248.1	9.9
22UL-32JCTD	1.94876E-16	1.47854E-18	7.69313E+00	5.22316E+01	4.74000E+01	263.4	7.5
22UL-32KCTD	2.06827E-16	1.44211E-18	6.45831E+00	5.19208E+01	5.59000E+01	262.0	5.1
22UL-32LCTD	1.90762E-16	1.46560E-18	5.77070E+00	5.17134E+01	5.98000E+01	261.0	4.6
22UL-32MCTD	1.90208E-16	1.43026E-18	5.33823E+00	5.11677E+01	6.66000E+01	258.4	3.8
22UL-32NCTD	1.97117E-16	1.47498E-18	5.20185E+00	5.18331E+01	7.31000E+01	261.6	3.1
22UL-32OCTD	1.91971E-16	1.40695E-18	5.05651E+00	5.12804E+01	7.83000E+01	259.0	2.8
22UL-32QCTD	8.20937E-16	1.87916E-18	5.27873E+00	5.15464E+01	9.13000E+01	260.2	2.0
22UL-32RCTD	4.52265E-16	1.66319E-18	5.22744E+00	5.16395E+01	7.54000E+01	260.6	2.5
22UL-32SCTD	3.31495E-16	1.60334E-18	4.88224E+00	5.00938E+01	3.31000E+01	253.4	12.5
22UL-32TCTD	4.85132E-16	1.79914E-18	4.18874E+00	4.74624E+01	1.85000E+01	240.9	24.1
22UL-32UCTD	4.51154E-16	2.07820E-18	2.71385E+00	3.52859E+01	9.00000E+00	182.1	66.3
22UL-32VCTD	1.25785E-15	2.47550E-18	5.50488E+00	5.12480E+01	5.18000E+01	258.8	4.2
22UL-32WCTD	1.26178E-15	3.42853E-18	3.15710E+00	5.07558E+01	9.70000E+00	256.5	44.7
22UL-32XCTD	1.12621E-15	3.60794E-18	0.00000E+00	1.27376E+01	6.00000E-01	67.9	1093.4

Appendix 8: U/Pb zircon data of the Brandjispitz mafic complex.

During this study, we planned to compare the Mont Collon mafic complex with the comparable Brandjispitz mafic intrusion. This massif is located in the Turtmantal (Wallis, Switzerland).

The choice of this massif was based on previous diploma studies (Chabloz, 1999). Moreover, the Turtmantal is very close to the Val d'Hérens and this proximity with the Mont Collon massif was one of the first criteria of choice. The mineralogical, petrological and geochemical characteristics indicate that the Brandjispitz massif is similar to the Mont Collon complex. Nevertheless, the U/Pb zircon age on a pegmatitic gabbro sampled at the northern base of the intrusion clearly indicates that the Brandjispitz massif was late Cambrian (upper intersect at 503 Ma). This age was interpreted as the crystallization age of the massif. This age will be probably integrated in a next publication by François Bussy.

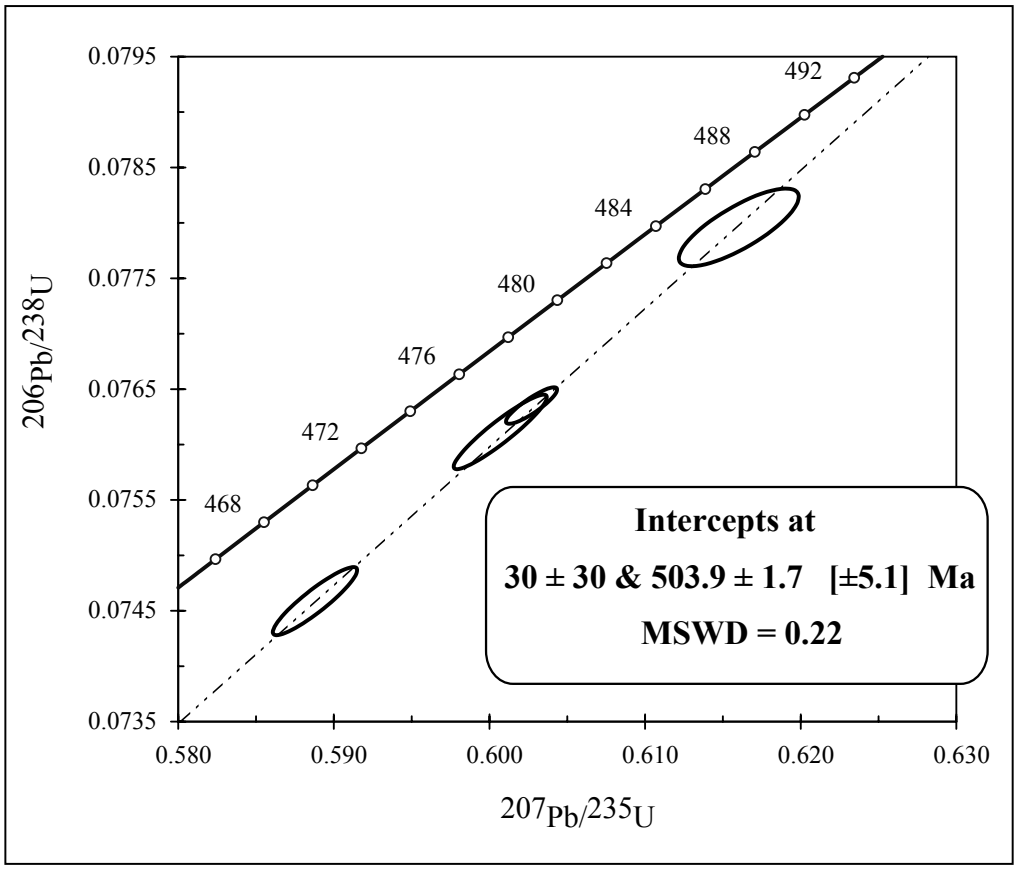

Fig. 72: U/Pb Concordia diagram for 1 to 3-grain zircon fractions of a pegmatitic gabbro outcropping at the Brandjispitz massif (Turtmanntal, Dent Blanche nappe, Wallis, Switzerland). Error ellipses are given at the 2σ confidence level.

Appendix 9: List of abbreviations:

Minerals:

- clinopyroxene: cpx
- orthopyroxene: opx
- olivine: ol
    - Fo: forsterite content
- plagioclase: plg
- alkaline feldspar: K-fd
- amphibole: amph
    - kaersutite: kaer
    - pargasite: prg
- quartz: Qz
- biotite: bio
- spinelle: sp
- ilmenite: ilm
- magnetite: mgt

Elements:

- REE: Rare Earth Element
    - LREE: Light Rare Earth Element
    - HREE: Heavy Rare Earth Element
- LILE: Large Ion Lithophile Element
- HFSE: High Field Strength Element

Mantle reservoirs:

- BSE: Bulk Silicate Earth
- PREMA: Prevalent Mantle
- PM: Primitive Mantle
- EM I and II: Enriched Mantle I and II
- HIMU: high μ (mantle reservoir which is highly Pb radiogenic)
- DM: Depleted Mantle
- MORB: Mid-Ridge Oceanic Basalt (with T = Transitional)
- OIB: Ocean Island Basalt
- (S)CLM: (Sub)Continental Lithospheric Mantle

Table 24: Sample location of the Mont Collon studied rocks. Coordinates are given using the Swiss reference grid. All rocks have been sampled in place, if not specified within brackets.

Sample	Rock type	Swiss coordinates sampling
MP2	Qz pegmatite	605750 / 93420
MP4	pegmatitic gabbro	605500 / 092800
MP5	Qz pegmatite	605750 / 934200
MP18b	aplite	605850 / 928500
MP46	ol-gabbro	605680 / 933300
MP89	anorthositic dike	605800 / 934200
MP99	anorthositic dike	605200 / 927560
FB1085	microgranodiorite	605470 / 093460
FB1087	anorthositic dike	60570 / 093320
FB1089	microgranodiorite	605470 / 093550
FB1090	ol-gabbro	near FB1085
FB1091	ol-gabbro	near FB1090 (scree)
FB1092	cpx-gabbro	605525 / 093385
FB1093	ol-gabbro	605400 / 093200 (central moraine)
FB1094	plg-wehrlite	605450 / 092940 (scree: base Mont Collon)
FB1095	plg-wehrlite	605450 / 092940 (scree: base Mont Collon)
KAW1983	Arolla orthogneiss	599600 / 096100 (Pas de Chèvres)
KAW985	Arolla orthogneiss	616900 / 089250 (Matterhorn)
MP106	plg-wehrlite	605270 / 093280 (central moraine)
MP107	plg-wehrlite	605270 / 093280 (central moraine)
MP108	plg-wehrlite	605270 / 093280 (central moraine)
MP113	pegmatitic gabbro	605380 / 092900
MP120	cpx-gabbro	607470 / 941200 (3310 m)
MP122	cpx-gabbro	MP120 + 10 m to NW
MP124	cpx-gabbro	MP120 + 25 m to NW
MP125	ol-gabbro	MP120 + 30 m to NW
MP127	ol-gabbro	MP120 + 40 m to NW
MP128	microgranodiorite	MP120 + 47 m to NW
MP129	microgranodiorite	MP120 + 50 m to NW
MP130	microgranodiorite	MP120 + 55 m to NW
MP131	cpx-gabbro	MP120 + 60 m to NW
MP132b	microgranodiorite	MP120 + 65 m to NW
MP134	cpx-gabbro	MP120 + 80 m to NW
MP135	ol-gabbro	MP120 + 85 m to NW
MP136	ol-gabbro	MP120 + 105 m to NW
MP138	cpx-gabbro	607120 / 941900
MP141b	aplite	607120 / 941900
MP148	cpx-gabbro	MP138 + 33 m to NW
MP149	cpx-gabbro	607100 / 941700 (3150 m)
MP150	ol-gabbro	MP138 + 38 m to NW
MP151	aplite	MP138 + 40 m to NW
MP152	ol-gabbro	MP138 + 42 m to NW

Table 24: continued

Sample	Rock type	Swiss coordinates sampling
MP154	cpx-gabbro	607040 / 094160
MP155	plg-wehrlite	MP154 + 2 m to NW
MP156	ol-gabbro	MP154 + 4 m to NW
MP157	ol-gabbro	MP154 + 6 m to NW
MP159	ol-gabbro	MP154 + 13 m to NW
MP160	ol-gabbro	MP154 + 20 m to NW
MP161	ol-gabbro	MP154 + 22 m to NW
MP166	ol-gabbro	MP154 + 31 m to NW
MP168	cpx-gabbro	MP154 + 35 m to NW
MP169	cpx-gabbro	MP154 + 37 m to NW
MP171	cpx-gabbro	MP154 + 41 m to NW
MP173b	aplite	intruding MP171
MP176	ol-gabbro	604830 / 093840
MP177	Fe-Ti melanocratic dike	606440 / 093670
MP180	cpx-gabbro	607430 / 941800 (3225 m)
MP181	cpx-gabbro	MP180 + 8 m to NW
MP184	cpx-gabbro	MP180 + 27 m to NW
MP187	cpx-gabbro	MP180 + 40 m to NW
MP188	ol-gabbro	MP180 + 55 m to NW
MP189	cpx-gabbro	MP180 + 65 m to NW
MP190	ol-gabbro	MP180 + 80 m to NW
MP191	ol-gabbro	MP180 + 85 m to NW
MP192	cpx-gabbro	607250 / 094190
MP194	cpx-gabbro	MP192 + 10 m to NW
MP213	wehrlite	605650 / 093600
MP221	ol-gabbro	605500 / 092920
MP223	cpx-gabbro	MP221 + 10 m to E
MP225	cpx-gabbro	60552/92840 (moraine base MC)
MP227	ol-gabbro	605780 / 092850
MP230	cpx-gabbro	605590 / 092650
MP240	troctolite	60741 / 94550 (2930 m)
MP242	ol-gabbro	60714 / 94180 (3100 m)
MP243	wehrlite	60703 / 94250 (3130 m)
MP244a	Fe-Ti melanocratic dike	60700 / 93480 (2850 m)
MP244e	Fe-Ti melanocratic dike	60700 / 93480 (2850 m)
MP245a	Fe-Ti melanocratic dike	60725 / 93800
MP247	cpx-gabbro	606990 / 094600
MP249a	Fe-Ti melanocratic dike	60670 / 93500
MP265a	pegmatitic gabbro	606770 / 093270 (2800 m)
MP278	wehrlite	606830 / 093070 (2840 m)
MP285	anorthosite	60688 / 92860 (2780 m)

Plate 3a: Microphotographs of thin sections of cumulative rocks.

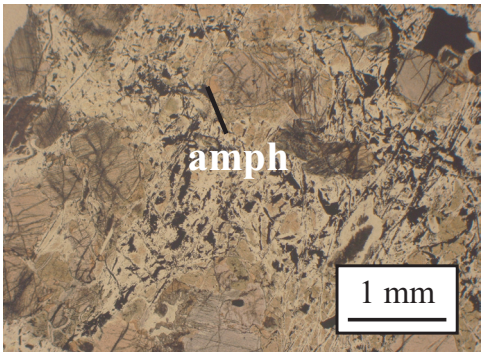

wehrlite (LN)

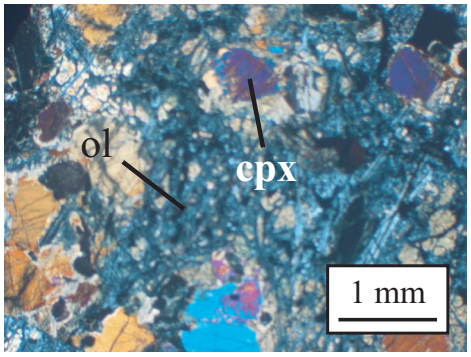

wehrlite (LP)

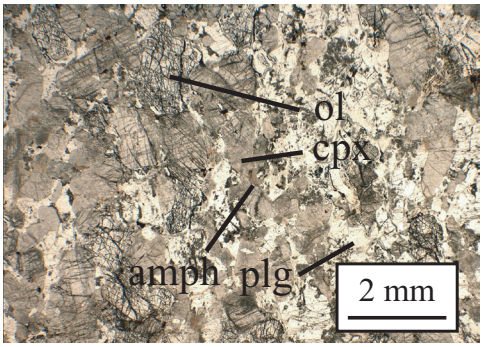

plagioclase-wehrlite (LN)

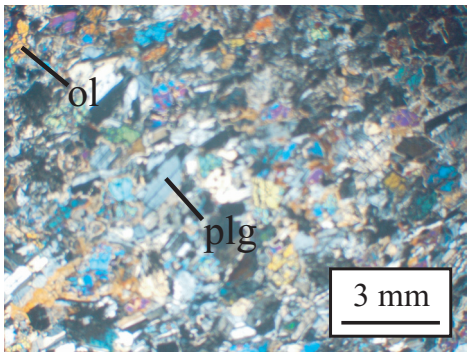

troctolite (LN)

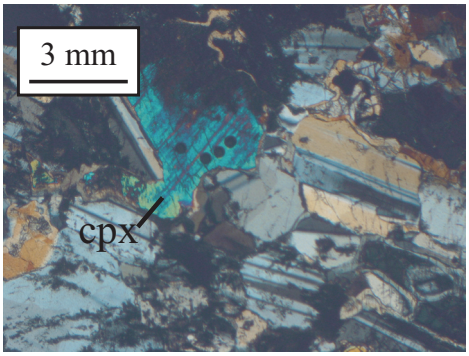

zoom cpx (troctolite, LP)

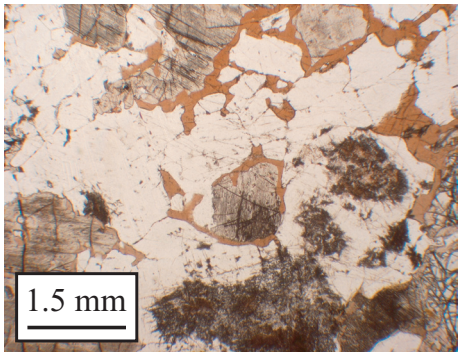

example of interstitial amphibole (ol-gabbro, LN)

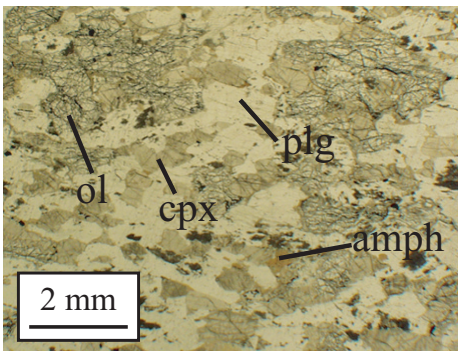

ol-gabbro (LN)

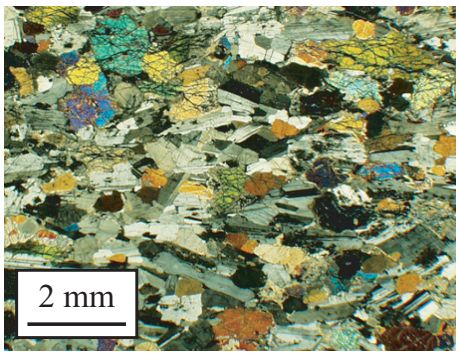

ol-gabbro (LP)

Plate 3b: Microphotographs of thin sections of cumulative rocks.

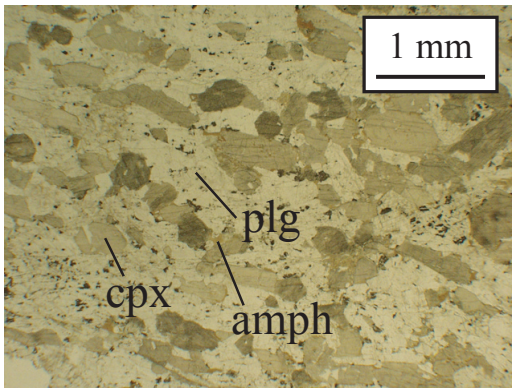

cpx-gabbro (LN)

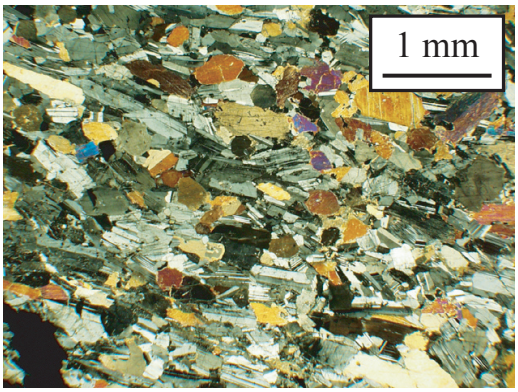

cpx-gabbro (LP)

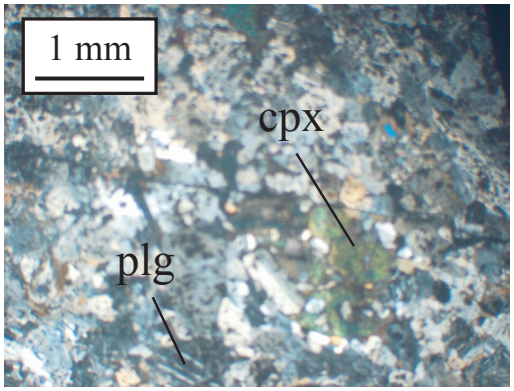

anorthosite (LP)

Plate 4: Microphotographs of thin sections of leucocratic and melanocratic dikes.

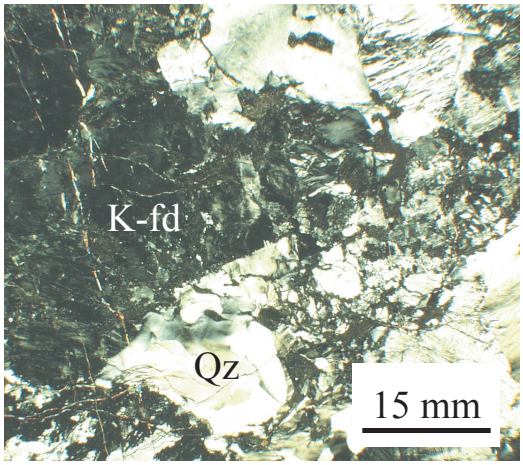

Qz-pegmatite (LN)

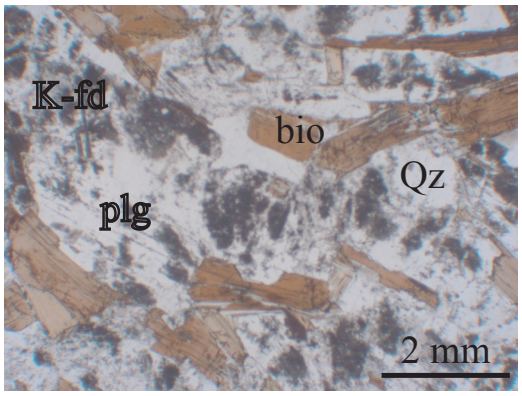

microgranodiorite (LN)

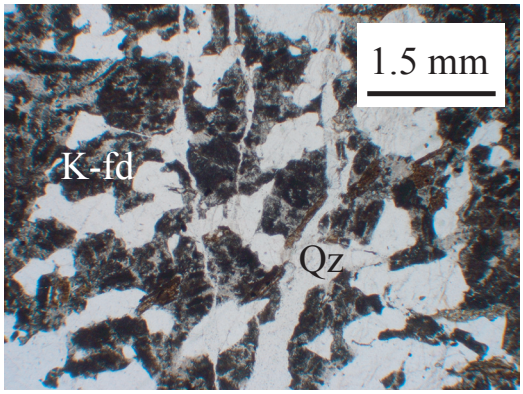

aplite (LN)

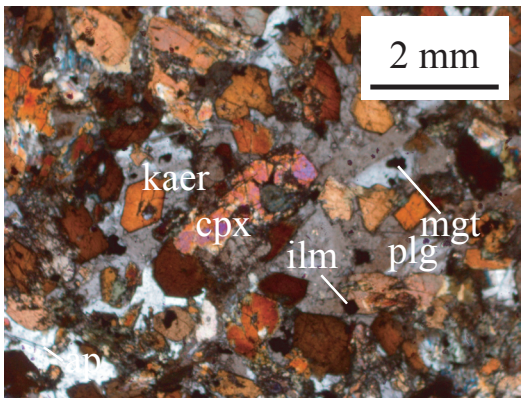

Fe-Ti melanocratic dike (LP)